Technische Universität München
Fakultät für Physik

Max-Planck-Institut für Physik
Werner-Heisenberg-Institut

Data Analysis for the CRESST Experiment: New Methods, improved Alpha Analysis, and Results on Light Dark Matter and Backgrounds

Philipp Martin Michael Bauer

Vollständiger Abdruck der von der Fakultät für Physik der Technischen Universität München zur Erlangung des akademischen Grades eines Doktors der Naturwissenschaften genehmigten Dissertation.

Vorsitzender: apl. Prof. Dr. Norbert Kaiser

Prüfende der Dissertation

1. Prof. Dr. Stefan Schönert
2. apl. Prof. Dr. Hubert Kroha

Die Dissertation wurde am 06.05.2020 bei der Technischen Universität München eingereicht und durch die Fakultät für Physik am 28.07.2020 angenommen.

ABSTRACT

The nature of dark matter is one of the big puzzles in modern physics. Indications for dark matter can be found throughout astrophysical observations, from the cosmic microwave background to the rotation speed of galaxies. In the prevalent ΛCDM model of cosmology, dark matter makes up about 26 % of the energy content of the observable universe and more than 80 % of its matter content. Several theoretically motivated candidates for dark matter are available, stemming from solutions to different problems in the standard model for particle physics. However, despite significant experimental efforts and advancements over the last decades, no clear evidence for any candidate has been found yet. The astrophysical evidence for dark matter as well as possible candidates are summarized in chapter 1 of this thesis.

Presented in chapter 1 are the different experimental approaches for the detection of dark matter. They can be broadly classified into three categories: collider experiments, indirect detection and direct detection. The CRESST experiment belongs to the third category. Its aim is the identification of dark matter particles by their scattering off nuclei of a target crystal. The challenges here lie in the extremely low expected rates and small transferred energies ($\mathcal{O}(\mathrm{eV} - \mathrm{keV})$).

CRESST tackles this problem with a cryogenic detector, operated around 15 mK, transition edge sensors (TES) and a SQUID based read-out. The low operation temperature reduces heat capacities to a point where a keV energy deposition results in an up to a few µK temperature increase. A TES is a very sensitive thermometer based on a superconductor in its transition from the super to the normal conducting phase. It converts the temperature increase into a resistance increase which in turn is read out by a magnetically coupled SQUID.

To be able to detect the extremely low rates, the CRESST experiment is located in an underground laboratory and encased in multiple layers of shielding material against environmental radioactivity. Furthermore, CRESST exploits the particle dependent scintillation of the $CaWO_4$ crystals it uses as its primary target. By adding a light detector, particle discrimination can be performed on an event by event basis, based on the detected amount of scintillation light. This reduces the dominating β/γ backgrounds even further. The experimental setup of CRESST is described in chapter 2.

This work focuses on two analyses carried out on the CRESST-II phase 2 and CRESST-III phase 1 data with an additional, supportive analysis reported in the appendix. While this includes a dark matter analysis of the recent CRESST-III phase 1 data, the main focus of the thesis lies on the understanding of backgrounds and detector effects.

Chapter 3 introduces the general steps that are required for a CRESST analysis, namely calculation of parameters, application of data selection criteria, energy reconstruction, determination of survival probability and, if applicable, dark matter limit calculation.

Chapter 4 deals with an α analysis of CRESST-II phase 2 data. An α analysis allows to determine precisely the internal contamination of target crystals from the three prevalent natural radioactive decay chains. The decays are fully embedded in the target crystal of a CRESST detector and thus produce mono-energetic peaks. This information is valuable input for simulation efforts to understand background contributions at low energies. Challenges arise from the high energies $\mathcal{O}(\mathrm{MeV})$ of α decays compared to the keV energies the detector is optimized for. Several steps were taken to tackle these challenges, culminating in improved precision and understanding of the observed α spectra compared to previous results from a subset of the same data. The results have already been used in an improved background simulation within the CRESST group.

Chapter 5 comprises the dark matter analysis and thereby the main result of the CRESST-III phase 1 measurement campaign. For the first time, data from the newly developed continuous data acquisition was analyzed. This allowed for a significantly improved way of determining the survival probability of dark matter events by simulating them directly on the saved data stream. Furthermore, the energy reconstruction is now based on the optimum filter method that offers an improved resolution compared to the previous standard event fit. Another novelty in CRESST-III phase 1 was the partial instrumentation of the holding structure with thermometers, allowing to identify certain types of background events.

The analysis focuses on one detector module with a nuclear recoil threshold of $30.1\,\mathrm{eV}$ which exceeds the $100\,\mathrm{eV}$ design goal by a factor of three. At low energies $\lesssim 200\,\mathrm{eV}$, an exponentially rising excess of events is observed that cannot be explained by the known backgrounds. This excess already severely limits the sensitivity in terms of dark matter particle-nucleon interaction cross-section in the corresponding mass range. Nonetheless, leading limits for dark matter masses between $160\,\mathrm{MeV}/c^2$ and $1.8\,\mathrm{GeV}/c^2$ could be derived by the CRESST group from the event spectra that were extracted in this work.

Special focus and further analysis effort are given to the identification of possible origins of the excess events. A crucial part in this regard is a full analysis of all event classes expected from the detector geometry. Different event classes are caused by energy depositions in the different parts of a detector module. The results of such an analysis with regard to the excess are also summarized in chapter 5, with the analysis itself described in appendix A.

This analysis revealed that the main target detects significant amounts of scintillation light from the scintillating holding structure which has not been observed to this extent in previous measurements. However, none of the investigated event types is a viable candidate for the excess.

ZUSAMMENFASSUNG

Eine der großen Herausforderungen der modernen Physik ist die Suche nach Dunkler Materie. Die Hinweise auf Dunkle Materie finden sich auf den verschiedensten Ebenen der Astrophysik, von der Rotationsgeschwindigkeit von Galaxien bis zur kosmischen Hintergrundstrahlung. Aus aktuellen Messungen ergibt sich, dass, basierend auf dem kosmologischen ΛCDM Modell, etwa 26 % des Energiegehalts des Universums in der Form von Dunkler Materie vorliegt, was etwa 80 % des gesamten Masseninhalts entspricht. Es gibt zahlreiche hypothetische, aus theoretische Betrachtungen abgeleitete Teilchen, die als Dunkle Materie in Frage kämen. Einige davon sind Bestandteil von Lösungen für gänzlich andere Probleme des Standardmodells der Teilchenphysik. Allerdings gibt es nach wie vor keine experimentellen Ergebnisse, die klar auf eines dieser Teilchen hinweisen würden. Die astrophysikalischen Hinweise auf Dunkle Materie und einige mögliche Kandidaten sind in Kapitel 1 zusammengefasst.

Desweiteren finden sich in Kapitel 1 auch die verschiedenen experimentellen Ansätze zur Suche nach Dunkler Materie. Diese lassen sich grob in drei Kategorien einordnen: Beschleunigerexperimente, indirekte Dunkle Materie-Suche und direkte Dunkle Materie-Suche, bei der auch das CRESST Experiment einzuordnen ist. CRESST versucht Dunkle Materie Teilchen über die Energie, die sie bei der Streuung an Atomkernen übertragen, nachzuweisen. Die großen Herausforderungen dabei sind die extrem geringe Rate, mit der solche Streuereignisse erwartet werden, und die geringen übertragenen Energien ($\mathcal{O}(\mathrm{eV} - \mathrm{keV})$).

Um die nötige Empfindlichkeit zu erreichen verwendet CRESST kryogene Detektoren, bei denen ein Kristall auf etwa 15 mK heruntergekühlt wird. Energieeinträge in den Kristall werden anhand der Temperaturänderung über ein Phasenübergangsthermometer (TES) und einen SQUID ausgelesen. Durch die geringe Temperatur ist die Wärmekapazität des Kristalls so gering, dass bereits Energieeinträge im Bereich von keV zu Temperaturänderungen bis zu wenigen µK führen. Ein TES ist ein sehr empfindliches, widerstandsbasiertes Thermometer, das den Phasenübergang eines Supraleiters von der supraleitenden zur normalleitenden Phase ausnutzt, um kleine Temperaturänderungen in messbare Widerstansänderungen zu übersetzen. Diese Widerstandsänderung wird wiederum durch den magnetisch gekoppelten SQUID ausgelesen.

Um die geringe erwartete Rate an Dunkle Materie-Interaktionen von Interaktionen durch natürliche Radioaktivetät und bekannte kosmische Strahlung unterscheiden zu können müssen diese so weit wie möglich abgeschirmt werden. Dazu befindet sich das CRESST Experiment in einem Untergrundlabor und die Detektoren sind von mehreren Schichten abschirmenden Materials umgeben. Ausserdem

sind CRESST-Detektoren durch die teilchenabhängige Szintillation des verwendeten $CaWO_4$ Kristalls in der Lage verschiedene Teilchenarten zu unterscheiden. Dadurch kann zwischen den für Dunkle Materie erwarteten Kernrückstößen und β/γ Interaktionen unterschieden werden, die den Großteil des verbleibenden radioaktiven Untergrunds ausmachen. Der experimentelle Aufbau von CRESST wird in Kapitel 2 beschrieben.

In der vorliegenden Arbeit werden zwei Analysen basierend auf den Daten von CRESST-II Phase 2 und CRESST-III Phase 1 präsentiert, außerdem eine zusätzliche Detailanalyse der CRESST-III Phase 1-Daten im Anhang. Der Fokus der Analysen liegt dabei vor allem auf dem Verständnis des Untergrunds und von Detektoreffekten. Außerdem ist die Dunkle Materie-Analyse der CRESST-III Phase 1 Daten beinhaltet. In Kapitel 3 werden die Grundlagen für die Analyse von CRESST Daten erklärt. Diese beinhalten die Berechnung verschiedener Parameter, die Kriterien zur Auswahl des abschließenden Datensets, die Energierekonstruktion für die aufgenommenen Interaktionen, die Berechnung der überlebenswahrscheinlichkeit von Dunkler Materie Interaktionen über die verschiedenen Schritte der Analyse hinweg und die Berechnung eines Ausschlusslimits für Dunkle Materie.

In Kapitel 4 wird die Alphaanalyse der CRESST-II Phase 2 Daten beschrieben. Eine Alphaanalyse ermöglicht es, die interne radioaktive Kontamination der untersuchten Kristalle durch Elemente aus den natürlichen Zerfallsreihen sehr präzise zu bestimmen. Aufgrund der kurzen Reichweite von Alphateilchen in Festkörpern kann die gesamte Energie eines Alphazerfalls im Kristall nachgewiesen werden. Dadurch ergibt sich für jeden Zerfallstyp ein klar identifizierbarer, monoenergetischer Peak im aufgenommenen Energiespektrum. Die daraus gewonnenen Informationen dienen unter anderem als Basis für Untergrundsimulationen, durch die auch der Untergrund bei niedrigen Energien besser verstanden werden kann. Die Herausforderungen bei der Alphaanalyse ergeben sich hauptsächlich durch die hohen Energien $\mathcal{O}$(MeV) für die der auf keV ausgelegte Detektor nicht geeignet ist. Durch neue und optimierte Analysetechniken konnte hier eine deutliche Verbesserung der Genauigkeit sowie des Verständnisses im Vergleich zu vorigen Analyseversuchen, die auf einem Teil des gleichen Datenset basierten, erreicht werden. Die Ergebnisse kamen bereits in einer verbesserten Untergrundsimulation der CRESST Gruppe zum Einsatz.

Kapitel 5 enthält die Dunkle Materie-Analyse und damit das zentrale Resultat der CRESST-III Phase 1 Messkampagne. Zum ersten Mal wurden hier Daten, die mit der neuen kontinuierlichen Datennahme aufgenommen wurden, analysiert. Dadurch konnte unter anderem die Wahrscheinlichkeit, dass ein Dunkle Materie-Streuereignisse in der Analyse korrekt behandelt wird, durch simulierte Ereignisse auf dem vollen Datenstrom bestimmt werden. Dies stellt eine deutliche Verbesserung zur Methodik vorheriger CRESST Analysen dar. Des Weiteren basiert die Energierekonstruktion jetzt auf einem sogenannten Optimalfilter, der eine bessere Auflösung als der bisher verwendete “Standard Event Fit” erreicht. CRESST-III Phase 1 verwendete außerdem zum ersten Mal eine teilweise instrumentierte

Halterung für den Detektorkristall. Diese ermöglicht es, bestimmte Arten von Untergrundereignissen besser zu identifizieren und zu verstehen.

Die Analyse konzentriert sich hauptsächlich auf ein einzelnes Detektormodul, das eine sehr niedrige Detektionsschwelle von 30.1 eV aufweist, etwa dreimal besser als die beim Design angestrebten 100 eV. In den analysierten Daten ist unterhalb von ungefähr 200 eV ein exponentieller Anstieg an Ereignissen hin zu kleinen Energien zu beobachten. Dieser Anstieg kann nicht durch die bekannten Untergründe erklärt werden, und schränkt die Emfindlichkeit des Experiments bei niedrigen Energien im Bezug auf Dunkle Materie bereits deutlich ein. Trotzdem konnte ein Ausschlusslimit für den Dunkle Materie - Nukleon Wechselwirkungsquerschnitt berechnet werden, das zu diesem Zeitpunkt für Dunkle Materie Massen zwischen $160\,\mathrm{MeV}/c^2$ and $1.8\,\mathrm{GeV}/c^2$ führend war.

Ein weiterer Fokus der Analyse sind mögliche Ansatzpunkte für den unerwarteten, ansteigenden Untergrund. Dafür ist eine vollständige Analyse aller Ereignisklassen, die sich aus dem Aufbau des Detektormoduls ergeben, essentiell. Die verschiedenen Ereignisklassen ergeben sich dabei aus Energiedepositionen in den verschiedenen Modulbauteilen. Diese Analyse wird in Anhang A beschrieben, die Ergebnisse im Hinblick auf den unerwarteten Untergrund werden in Kapitel 5 diskutiert.

Die Analyse der Ereignisklassen ergab unter anderem, dass der Detektorkristall auch in der Lage ist Licht von der ihn umgebenden, szintillierenden Halterstruktur zu detektieren. Dieser Effekt wurde bisher in dieser Ausprägung nicht beobachtet. Allerdings eignet sich keine der untersuchten Ereignisklassen als Erklärung für den unbekannten Untergrund. Dies liegt vor allem am Lichtdetektor, der es ermöglicht, die meisten der Eventklassen von Kernrückstößen zu unterscheiden.

Um Rahmen der Analyse konnten mehrere verschiedene Ursprünge für den unerwarteten Untergrund ausgeschlossen werden. Es wurden außerdem verschiedene Indizien mit Relevanz für die weitere Untersuchung des Phänomens gesammelt.

Contents

ABSTRACT ii

ZUSAMMENFASSUNG v

1. Dark Matter 1
- 1.1 Dark Matter Indications 1
  - 1.1.1 Velocity Distribution in Galaxy Clusters 1
  - 1.1.2 Galactic Rotation Curves 2
  - 1.1.3 Gravitational Lensing and the Bullet Cluster 2
  - 1.1.4 Cosmic Microwave Background (CMB) 4
- 1.2 Dark Matter Candidates 5
  - 1.2.1 Requirements 5
  - 1.2.2 WIMPs and the WIMP Miracle 6
  - 1.2.3 Hidden Sector Dark Matter 6
  - 1.2.4 Axion 7
- 1.3 The Search for Dark Matter 8
  - 1.3.1 Collider Production 9
    - 1.3.1.1 Detection Mechanism 9
    - 1.3.1.2 Experimental Approaches and Experiments 9
    - 1.3.1.3 Current Results 11
  - 1.3.2 Indirect Searches 11
    - 1.3.2.1 Detection Mechanism 11
    - 1.3.2.2 Experimental Approaches and Experiments 11
    - 1.3.2.3 Current Results 12
  - 1.3.3 Direct Searches 13
    - 1.3.3.1 Detection Mechanism 13
    - 1.3.3.2 Experimental Approaches and Experiments 17
    - 1.3.3.3 Current Results 20

2. The CRESST Experiment 23
- 2.1 Experimental Environment 23
- 2.2 CRESST Detector Modules 26
  - 2.2.1 Phonon-Light Particle Discrimination 26
  - 2.2.2 Generic Components 27
  - 2.2.3 Detector Response Model 29
  - 2.2.4 Realized Detector Designs 31
    - 2.2.4.1 Conventional Module 31
    - 2.2.4.2 Stick Holder Module 31

2.2.4.3 Instrumented Stick Module 32
2.3 Thermometers and Read-out Electronics 34
2.3.1 Transition Edge Sensors 34
2.3.1.1 Working Principle 34
2.3.1.2 Temperature Stabilization and Heaters 35
2.3.2 SQUID Resistance Measurement 35
2.3.3 Electronics 37
2.4 Data Acquisition and Triggering 40
2.4.1 Hardware Trigger based Acquisition 40
2.4.2 Continuous Acquisition and Optimum Triggering 40

3. Analysis Basics 43
3.1 General Information, Important Settings and Naming Conventions . 43
3.2 Parameter Gathering 45
3.2.1 Basic Parameters 45
3.2.2 Template Event Fit and Optimum Filtering Parameters . . . 46
3.2.2.1 Pulse Shape Determination 46
3.2.2.2 Standard Event Fit 49
3.2.2.3 Optimum Filtering 51
3.2.2.4 Linearity Limitations 54
3.2.3 Simulation related Parameters 56
3.3 Data Selection 57
3.3.1 Preselection on Files and Time Periods 57
3.3.1.1 Bad Files 57
3.3.1.2 Training and Blind Set 57
3.3.1.3 Rate Cut 57
3.3.1.4 Stability Cut 58
3.3.2 Selection Criteria for removing corrupted Pulses 58
3.3.2.1 Decaying Baselines 59
3.3.2.2 Flux Quantum Losses and SQUID Resets 59
3.3.2.3 Delta Spikes 60
3.3.2.4 Early Pulses and Pile-up 60
3.3.3 Background and Veto cuts 61
3.3.3.1 RMS 61
3.3.3.2 Muon Veto 62
3.3.3.3 Coincidence with other Detector Modules 62
3.3.3.4 Instrumented Holder Parts 62
3.4 Survival Probabilities 63
3.4.1 Life and Dead Time Estimate 63
3.4.2 Event Simulation - Hardware Trigger Data 63
3.4.3 Continuous Simulation - Continuous Data 64
3.5 Energy Calibration 64
3.5.1 Energy Calibration Sources 65
3.5.2 Peak Based Calibration 66

- 3.5.3 Heater Pulse Based Calibration 66
- 3.5.4 Dealing with Time Dependencies 67
- 3.5.5 Energy Calibrating in the Presence of Scintillation Light and a Light Detector 68
  - 3.5.5.1 Phonon Anti-quenching 68
  - 3.5.5.2 Calibration of the Light Detector 69
- 3.6 Light Yield, Band Fit, Particle Identification and Region of Interest 70
- 3.7 Limit Calculation 70
  - 3.7.1 Expected Dark Matter Spectrum 70
  - 3.7.2 Accounting for Analysis Systematics 71
  - 3.7.3 Yellin Method 73
  - 3.7.4 Likelihood Fit 75

4. CRESST-II Phase 2 Alpha Analysis 77

- 4.1 Introduction 77
  - 4.1.1 Relevance of Alpha Analyses for CRESST 77
  - 4.1.2 Radioactive Decay Chains and their Alpha Signature 78
    - 4.1.2.1 Decay Chains and Secular Equilibrium 78
    - 4.1.2.2 Alpha Cascades and Pile up 80
    - 4.1.2.3 Gamma Escape Lines 80
  - 4.1.3 Other Sources of MeV Energy Depositions 81
- 4.2 Analysis 83
  - 4.2.1 Measurement Setup 83
    - 4.2.1.1 Detectors 83
    - 4.2.1.2 Data Acquisition Settings 83
    - 4.2.1.3 Specific Limitations related to Alphas 85
  - 4.2.2 Parameter Gathering 85
    - 4.2.2.1 Important Basic Parameters 85
    - 4.2.2.2 Template Fit with high Truncation Limit 85
  - 4.2.3 Data Selection 88
    - 4.2.3.1 Pre-selection on Files and Time Periods 88
    - 4.2.3.2 Corrupted Pulses 88
    - 4.2.3.3 Veto Cuts 88
    - 4.2.3.4 Alpha Analysis specific Data Selection 88
  - 4.2.4 Survival Probabilities and Rate Calculation 90
  - 4.2.5 Energy Calibration 91
- 4.3 Results 93
  - 4.3.1 TUM40 93
  - 4.3.2 Lise 99
  - 4.3.3 VK28 103
- 4.4 Comparison with related Works 107
  - 4.4.1 Beta/Gamma and Alpha Backgrounds in CRESST-II Phase 2 [126] 107

4.4.2 Development of a Geant4 Based Electromagnetic Background Model for the CRESST Experiment [136] 109
4.4.3 High-Purity CaWO 4 Single Crystals for Direct Dark Matter Search with the CRESST Experiment [138] 109
4.5 Summary and Conclusions 109

5. CRESST-III Phase 1 Dark Matter Analysis 111
5.1 Primary Analysis 111
  5.1.1 Measurement Setup 111
    5.1.1.1 Detectors 111
    5.1.1.2 Data Acquisition Settings 112
    5.1.1.3 Data Sets 114
  5.1.2 Parameter Gathering 114
    5.1.2.1 Basic Parameters 114
    5.1.2.2 Standard Event Fit and Optimum Filter 114
  5.1.3 Data Selection 117
    5.1.3.1 Special Artifact Class - Baseline Jumps 117
    5.1.3.2 Preselection on Files and Time periods 118
    5.1.3.3 Corrupted Pulses 119
    5.1.3.4 Background and Veto Cuts 121
    5.1.3.5 Analysis Limitation Cuts 121
  5.1.4 Survival Probability 123
  5.1.5 Energy Calibration 123
  5.1.6 Light Yield and Band Fit 126
  5.1.7 Limit Calculation 127
  5.1.8 Uncertainty Considerations 127
    5.1.8.1 Scintillation Light Losses 127
    5.1.8.2 Position of the 11.27 keV Calibration Line 127
    5.1.8.3 Time Dependency of the Threshold 127
    5.1.8.4 Choice of the Heater Control Voltage Offset 128
    5.1.8.5 Final Results of Detector A 128
5.2 Investigation of the observed Excess Events 132
  5.2.1 Time Stability 132
  5.2.2 Crosscheck of the expected Number of Noise Triggers 132
  5.2.3 Baseline Jumps as Candidates for the observed Excess . . . 134
  5.2.4 Comparison to the Light Detector 134
    5.2.4.1 Analysis Steps 135
    5.2.4.2 Results of the Light Detector Analysis 136
  5.2.5 Comparison to the Gamma Calibration 139
  5.2.6 Comparison to other Detector Modules 139
    5.2.6.1 Detector Module E 140
    5.2.6.2 Detector Module J 141
    5.2.6.3 Detector Modules B,C,D 143
  5.2.7 Likelihood Compatibility Check 144

    - 5.2.8 Detector Module related Event Types . . . 148
        - 5.2.8.1 Results concerning Light Detection in the Phonon Channel . . . 148
        - 5.2.8.2 Electron/Gamma and Neutron Events as Excess Candidates . . . 149
        - 5.2.8.3 Instrumented Stick Events as Excess Candidates . . . 149
        - 5.2.8.4 Light Detector holding Stick Events as Excess Candidates . . . 150
        - 5.2.8.5 Foil Events as Excess Candidates . . . 150
- 5.3 Summary and Conclusions . . . 151

6. Summary and Outlook 153

APPENDICES 156

A. Event Class Analysis 157
- A.1 Introduction and Motivation . . . 157
- A.2 Pre-Analysis Knowledge . . . 157
- A.3 Parameter Gathering . . . 158
    - A.3.1 Basic Parameters . . . 158
    - A.3.2 Template Event Fit and Optimum Filtering Parameters . . . 158
- A.4 Data Selection . . . 159
    - A.4.1 Pre-selection on Files and Time Periods . . . 160
    - A.4.2 Basic Selection for the Event Class Analysis . . . 160
    - A.4.3 SQUID Resets and Flux Quantum Losses . . . 161
- A.5 Survival Probabilities . . . 161
- A.6 Energy Calibration . . . 161
- A.7 Light Yield, Band fits and Limit Calculation . . . 162
- A.8 Event Classes . . . 162
    - A.8.1 Total Event Population . . . 162
    - A.8.2 Main Absorber Events . . . 162
    - A.8.3 iStick Events . . . 165
    - A.8.4 Light Stick Events . . . 168
    - A.8.5 Low Energy Excess Light / Foil events . . . 171
    - A.8.6 Direct Light Detector Hits . . . 173
- A.9 Summary of the observed Event Rates . . . 174

B. Basic Event and Pulse Parameters 179
- B.1 Event Number . . . 179
- B.2 Time since Start . . . 180
- B.3 Light Yield . . . 180
- B.4 Testpulse Amplitude . . . 180
- B.5 Trigger Delay . . . 180
- B.6 Pulse Number . . . 180
- B.7 Baseline Offset . . . 181

B.8 Pulse Height and Peak Position 181
B.9 (Plain) FWHM of Baseline 182
B.10 Peak Onset 183
B.11 Peak Position - Onset 184
B.12 Risetime 184
B.13 Decaytime 185
B.14 Right - Left Baseline 185
B.15 Integral over PH 185
B.16 Baseline Gradient 186
B.17 Pile-up Voltage/RMS and Pile-up Time Width 187
B.18 Delta Voltage (-)/RMS 189
B.19 Heater Demand 189
B.20 Deadtime and Live Time 189
B.21 Trigger Amplitude (Continuous Acquisition only) 190

C. Co-57 Calibration Spectrum for $CaWO_4$ 191

D. Energy Patterns from internal Alpha Decays of the Natural Decay Chain 193

E. Alpha Analysis Data Selection Criteria 197

F. Fitted Amplitude Corrections for the Alpha Analysis 203
F.1 Correlation Mechanisms 203
F.2 Fitted Amplitude Corrections 205
F.3 Application to the Alpha Analysis of TUM40 205
F.4 Application to the Alpha Analysis of Lise and VK28 205

G. MCIII-1 Dark Matter Analysis Settings 209

Chapter 1

Dark Matter

The final goal of the efforts described in this thesis is the detection of **dark matter**, which is one of the most fundamental questions in physics today. To motivate this endeavor, in this chapter a number of indications for dark matter are summarized in section 1.1. Possible dark matter candidates derived from theoretical considerations are introduced in section 1.2. Different approaches to identify them and some of the related challenges are presented in section 1.3.

1.1 Dark Matter Indications

The idea of (yet) unobserved, i.e., "dark" matter has existed at least since the times of the ancient Greeks. Already in the 19th century, the idea of deriving the existence and position of a yet unobserved, so far "dark" mass by its gravitational influence led to the discovery of the planet Neptune [1].

The term dark matter, as understood today in physics, refers to the non-visible, gravitationally interacting mass made up of yet unknown particles comprising the majority of matter in the universe. This mass is required to explain several astronomical observations on galactic and cosmological length scales. Best estimates today give a ratio of about 1 to 5 between observable and dark matter within the ΛCDM model of the Universe. Apart from visible and dark matter, the energy content of the universe is dominated by the even more mysterious "**dark energy**" [2].

1.1.1 Velocity Distribution in Galaxy Clusters

The first conclusive observation that highlighted the need for dark matter in a modern sense was the application of the Virial theorem [3] to the measured velocity distribution of galaxies in the Coma Cluster [4][5].

The Virial theorem connects the mean kinetic energy $< T >$ in a stable system to its mean potential energy $< U >$. For a gravitational potential it yields that the average kinetic energy is half the gravitational potential energy and a simple, approximate relation between mass and velocity can be obtained.

Based on this relation, [4] and [5] concluded that the mass of the Coma cluster has to be significantly higher than expected from the observed luminosity. The calculations overestimated the discrepancy due to a too high value of the hubble constant available at that time. However, the general conclusion still stands [1].

1.1.2 Galactic Rotation Curves

For a gravitationally bound object on a spherical orbit, the velocity depends on the radius r of the orbit and the mass M contained within the orbit:

$$v^2 = G \cdot \frac{M}{r} \tag{1.1}$$

The visible, luminous mass of (spiral) galaxies is concentrated in the central region of the disc. Hence, the rotation velocity is expect to follow a $\sqrt{\frac{1}{r}}$ law when looking outside of the central bulge. Observation of galactic rotation curves, by contrast, show a constant or even slightly increasing velocity towards higher radii. Compare [6] and [7] for a review of methods and results. To explain this behavior an extended "dark" mass distribution is required as discussed in [8] for the M33 galaxy, displayed in figure 1.1.

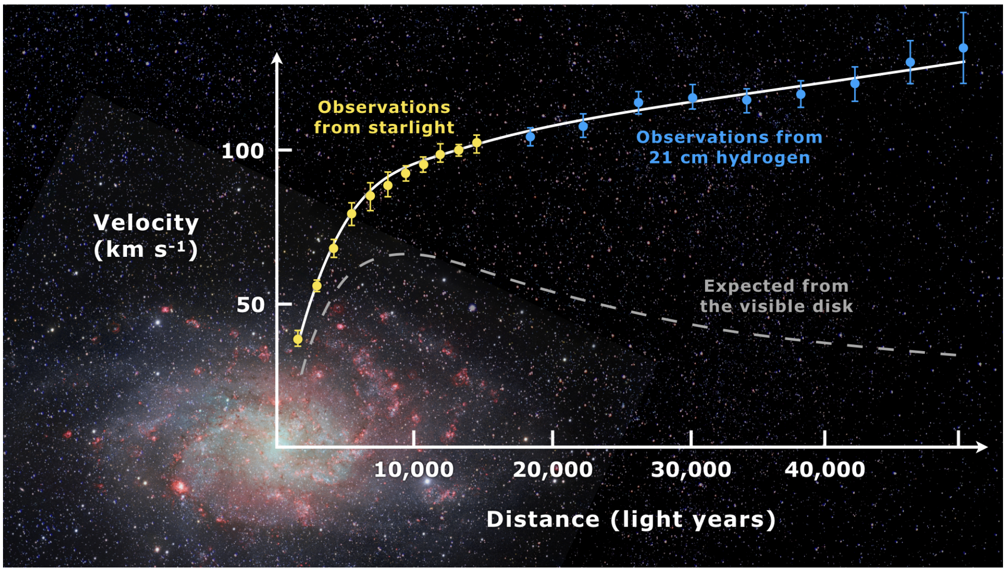

Figure 1.1: Measured and expected rotation curves for the M33 galaxy. The observed rotation curve cannot be explained by the visible matter alone. Picture taken from [9] with data from [8].

1.1.3 Gravitational Lensing and the Bullet Cluster

The path of light from distant astronomical objects can be changed by massive objects on it. This is a result of general relativity [10]. For sufficiently large masses this effect becomes clearly visible in the form that an observer can see multiple images of the same background object, shown schematically in figure 1.2a (strong lensing). If the effect is less pronounced it appears as a stretching of background objects around the massive object causing the lensing (weak lensing), schematically shown in figure 1.2b. In both cases, the mass and position of the foreground object can be inferred as suggested in [5]. For detailed reviews see [11] and [12].

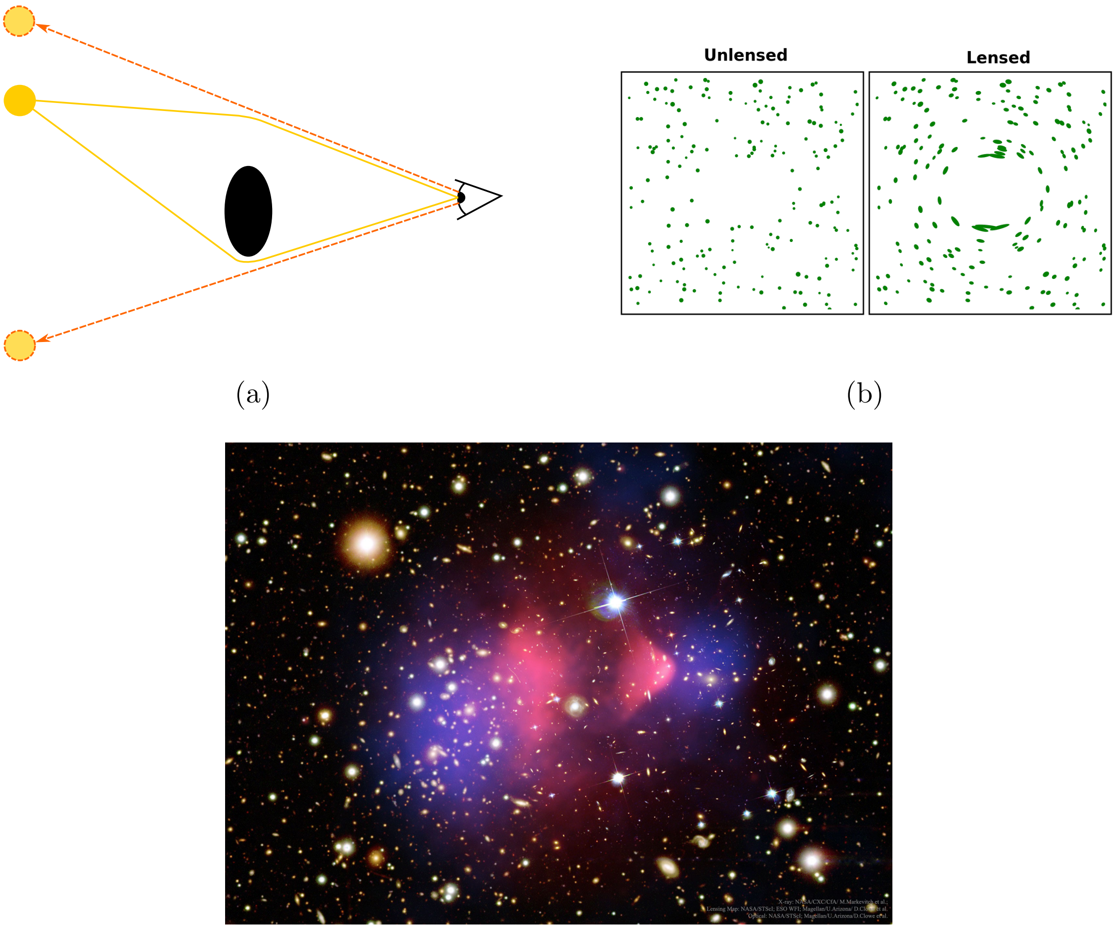

(a) (b)

(c)

Figure 1.2: a) Strong gravitational lensing: a massive foreground object bends the light (yellow lines) from a light source in the background (yellow circle) such that several light paths from the source to an observer are possible. For the observer, the background object appears at multiple apparent positions (orange dotted lines and circles) different from the real position of the background object. b) Weak gravitational lensing: less massive foreground objects do not produce multiple images or rings of background light sources but cause an elongation. This elongation can be evaluated on a statistical basis. Figure modified from [13]. c) Bullet cluster, the collision of two galaxy clusters lead to a separation of the gravitational mass (blue) and the main part of the luminescent matter in the form of gas (red). The gravitational mass is derived from gravitational lensing, the luminescent matter from x-ray images [14]. Picture from NASA [15].

An advantage of this method is that it is agnostic to the type of mass, as well as the physics within the mass. Therefore, it allows to directly probe the distribution of gravitational matter, most significantly in cases where it is not identical or congruent with the visible mass. This is the case in the so called “bullet cluster”. There, after the collision of two galaxy clusters, the two bulks of interacting, visible mass and the gravitational centers have separated [14], see figure 1.2c.

The misalignment between visible mass and gravitational centers is a strong indication for a dominant, weakly to non-interacting dark matter component that does not get slowed down by the collision. Other similar clusters exist, e.g., Abel 2744, albeit with a more complicated geometry [16].

1.1.4 Cosmic Microwave Background (CMB)

Current understanding of the evolution of the Universe is based on the ΛCDM model. In the ΛCDM model, the universe started out small, hot and uniform, then rapidly expanded and cooled down. The structure observed today has been seeded by random quantum fluctuations that were blown up to cosmic scales in a first, rapid expansion (inflation).

In the following slower expansion, the energy density of the Universe started high enough such that all baryonic matter was ionized. It formed an opaque photon-baryon plasma that acts like a compressible fluid, with dark matter gravitationally interacting in the background. This plasma started to oscillate due to the initial inhomogeneities, corresponding gravitational potentials and the pressure induced by the photons. The exact features of these oscillations depend on the composition of the Universe.

The ongoing expansion lead to further cooling of the Universe. At an age of the Universe of about 370 000 years, photon densities and energies are no longer sufficient to ionize the back-then forming neutral atoms. At that point, the Universe became transparent (decoupling). The now unhinderedly travelling photons correspond in their temperature to the baryonic mass distribution at that time. Therefore, they preserve a snapshot of the early Universe. These photons can be measured today as the **cosmic microwave background (CMB)**, red-shifted by the further expansion of the Universe to a temperature of about 2.725 K [17][18].

The CMB has been measured most precisely by satellite based experiments, starting with COBE [19], followed by WMAP [20] and, most recently, Planck [2]. A picture of the CMB anisotropies as measured by Planck is shown in figure 1.3a. Information about the Universe can, e.g., be derived by looking at the angular power spectrum of the inhomogeneities, compare figure 1.3c top. It captures the features of the aforementioned oscillations. For details see [2].

In total, the dark matter content of the Universe can be derived from the CMB measurements to be about 26%, with ordinary matter at only 5% of the total energy content of the Universe. The remaining 69% is attributed to the even less tangible dark energy [2][21].

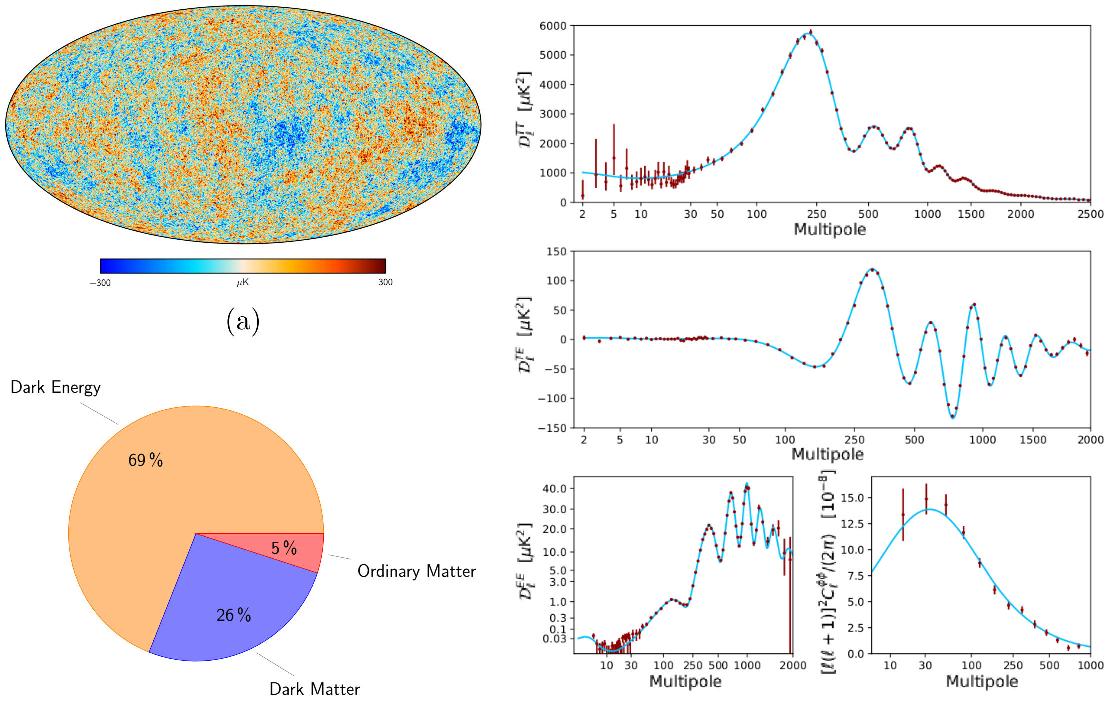

(a) (b) (c)

Figure 1.3: a) The anisotropies of the Cosmic microwave background (CMB) as measured by the Planck satellite displayed in a Mollweide projection of the sky. b) Composition of the Universe. Rounded values, taken from the Planck combined analysis with baryonic accoustic oscillations [2][22]. c) CMB power spectra measured by Planck. Angular power spectrum (top), the temperature-polarization cross-spectrum (middle), the E mode of polarization (bottom left) and the lensing potential (bottom right). Figures a and c from ESA and the Planck Collaboration [2][23][24].

1.2 Dark Matter Candidates

There are several dark matter candidates motivated by theoretical considerations, often as a solution to a different problem in physics. To be qualified as viable candidates, they have to fulfill certain requirements listed in section 1.2.1. A few examples are presented in sections 1.2.2 to 1.2.4. The content of this section is compiled from reviews [21],[25],[26] and [27].

1.2.1 Requirements

A viable dark matter candidate requires:

- **Production mechanism**: The observed dark matter abundance has to be created in the early Universe. Commonly this is achieved through a freeze in/out process. In such a process, an interaction between the dark matter and the baryons/photons leads to an equilibrium between dark matter production and annihilation at high energies and densities. When the energy and dark matter particle density of the Universe drops to a value below what is required for the production and annihilation processes to occur, the equilibrium dark matter density at that point is "frozen out". If the production process is too slow to have reached equilibrium yet, the density is "frozen in".

- **Electrically neutral**: Dark matter cannot be electrically charged, otherwise it would not be "dark" and already been detected through its electromagnetic interaction, i.e., light. Furthermore, there are limits on other non-gravitational interactions with ordinary matter as well as self-interaction.
- **Non-relativistic**: Dark matter has to be predominantly "cold", i.e., non-relativistic, to allow for the observed structure formation. Relativistic dark matter would have washed out much of the finer structure of the matter distribution observed today.
- **Stable**: Dark matter has to be stable on cosmological time scales in the sense that it was present in the early Universe and is still present today.
- **Non-baryonic**: Dark matter cannot be of baryonic origin, e.g., undetected gas clouds or black holes, as those would be visible in the acoustic oscillations of the CMB, compare section 1.1.4.

1.2.2 WIMPs and the WIMP Miracle

A particle with a mass in the $10\,\mathrm{GeV}/c^2$ - TeV/c^2 range with a dark matter - baryon interaction cross section in the range of the weak interaction would naturally produce the right abundance of dark matter in a freeze-out process. This has historically been referred to as the "WIMP-Miracle", where WIMP stands for **W**eakly **I**nteractive **M**assive **P**article [27].

Apart from being excellent dark matter candidates, WIMPs are theoretically well motivated. They are predicted by several theories developed independently of the dark matter problem, most notably from supersymmetry as the lightest neutralino. WIMPs are also readily accessible by various experimental approaches, e.g., via dark matter - nucleus scattering. Consequently, considerable experimental efforts have been directed at the detection of WIMPs. Strong experimental limits exist from these efforts, mostly excluding the WIMP in its standard, weakly interacting form and mass range.

1.2.3 Hidden Sector Dark Matter

Given the absence of a conclusive detection of a WIMP candidate so far, the idea of the WIMP can be extended to encompass massive particles with interaction channels with a strength very different from the weak force. Notably, with a weaker interaction with baryonic matter also many experimental and cosmological constrains are weakened. This allows to extend the possible mass range down to keV/c^2s [27].

Candidates are for example dark photons, different solutions/particles from supersymmetry, particles based on asymmetric dark matter theories and strongly interacting massive particles. Experimentally, hidden dark matter behaves similar to the classic WIMP if there is an interaction channel with baryonic matter.

1.2.4 Axion

The axion is a well established candidate for very light dark matter in the $\mathcal{O}(\mu\mathrm{eV}/c^2)$ range. It is motivated by the strong CP problem, where the strong interaction contains a phase that would allow violation of charge-parity symmetry. However, experiments show no such violations, implying a phase close to or at zero. To explain this fine tuning, the phase is linked to a dynamic, pseudo-scalar field, that relaxes to a minimum. Such a field comes with a new particle, the Axion. Axions are not produced in a thermal freeze in/out, but during the phase transition, when the axion field relaxes to its minimum value.

The detection of axions requires different kinds of experiment than those that will be presented for WIMP-like particles in the next section. Those experiments exploit the expected coupling of axions to (strong) magnetic fields [28].

1.3 The Search for Dark Matter

This section presents the most prevalent approaches taken to detect a potential dark matter candidate. It will focus on the detection of WIMP-like particles, i.e., particles in the keV/c^2 to TeV/c^2 scale that have an interaction channel with baryonic matter that allows for a Feynmann interaction diagram as shown in figure 1.4. From this diagram, three main approaches for the non-gravitational detection of dark matter can be classified:

- Dark matter can be experimentally produced in the interaction of standard model particles in collider experiments, see section 1.3.1.
- Standard model particles produced in the annihilation (or decay) of dark matter can be detected, mainly in satellite based experiments. This is referred to as indirect detection, see section 1.3.2.
- Finally, dark matter particles can scatter on standard model particles, transferring a measurable amount of energy. This is called direct detection, see section 1.3.3.

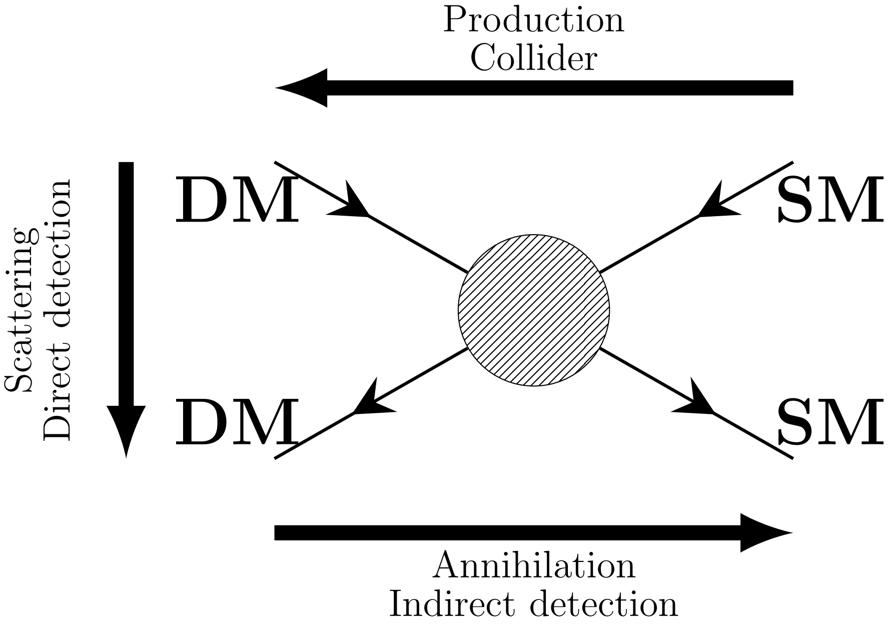

Figure 1.4: Schematic Feynman diagram for the possible detection channels of dark matter. Detection of dark matter particles (DM) requires a form of interaction with standard model particles (SM). This interaction can be exploited for detection either through production in colliders, scattering on SM particles or annihilation of dark matter into SM particles.

1.3.1 Collider Production

Collider experiments aim for the production of dark matter. Alternatively, they can also measure the effect of a dark matter interaction on known production and decay channels. The content of this section is compiled from [29], [30] and [31].

1.3.1.1 Detection Mechanism

Colliding standard model particles may produce a pair of WIMP-like dark matter particles. This requires a mediator coupled to the standard model as well as to the dark matter sector. In the special case that the mediator is a standard model particle, this is called a “portal interaction”. Viable candidates are, e.g., the Z or the Higgs boson. Given the general lack of interaction with baryonic matter and their required stability over the age of the Universe, the produced dark matter particles will escape any detector. Therefore, a pure dark matter production as indicated in figure 1.4 will not be detectable. For detection, interactions where only part of the total energy ends up in the dark matter channel are required.

In this case, knowing the kinematics enforced by the collider setup, the missing mass and momentum associated with the invisible particles can be calculated from the observed standard model products. In collider experiments, collisions usually are head on. This implies that the total momentum transverse to the beam direction has to be zero. The observable quantity to search for deviations from the standard model expectation is the missing transverse momentum.

Colliders can also search for new potential mediators between the standard model and the dark sector in interactions that do not have dark matter directly in the final state. As an example, the mediator could be produced in the SM-SM particle collision but then decay back into two standard model particles instead of dark matter. This would lead to a resonance, i.e., increased rate of interactions around the mass of the mediator. While not necessarily related to dark matter, such a new mediator would indicate where to look for physics beyond the standard model.

1.3.1.2 Experimental Approaches and Experiments

Collider results currently stem predominately from the Atlas and CMS detector at the Large Hadron Collider (LHC) at CERN. At the LHC, protons are accelerated in a 26.7 km long ring and then collided at a 13-TeV center-of-mass energy. Each collision produces a host of particles which are detected and classified in the multi-layer particle detectors Atlas [32] and CMS [33]. Those experiments require extensive simulation and data analysis efforts. The E_T^{miss} parameter has to be reconstructed and possible dark matter signal entangled from the dominating standard model backgrounds. A schematic view of the Atlas detector is shown in figure 1.5.

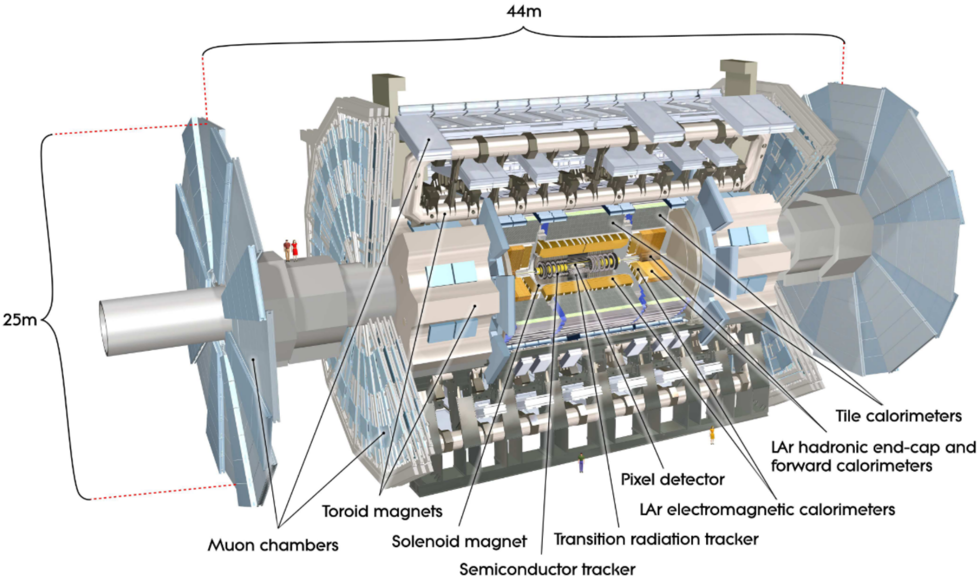

Figure 1.5: Schematic view of the Atlas detector at the LHC. Picture taken from [32].

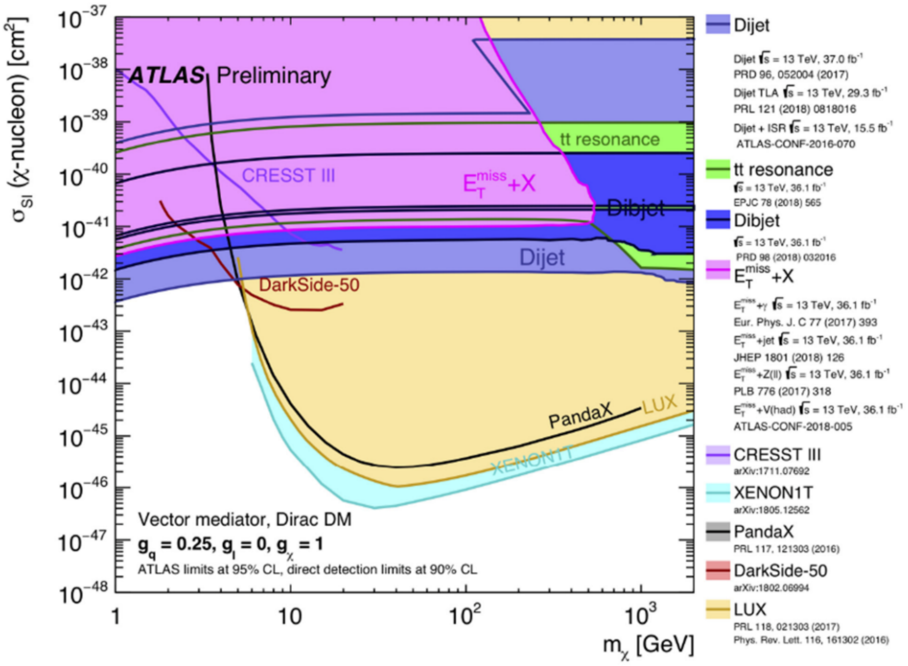

Figure 1.6: Limits from the Atlas detector for spin independent dark matter compared to limits from direct detection experiments. Figure taken from [31], references for displayed data see legend. The limits assume a specific dark matter model.

1.3.1.3 Current Results

So far, dark matter search at colliders has not found any dark matter candidate. Therefore, it can only set limits on dark matter masses and mediator masses/interaction cross sections. Comparison between collider and (in)direct detection limits require dark matter physics model assumptions on the side of the colliders and astrophysical assumptions on the side of the (in)direct detection experiments. They are therefore only possible for a given model.

Nonetheless, for a qualitative impression of how those limits compare, an example for direct detection is shown in figure 1.6. The analyses of collider experiments usually focuses on a very specific channel due to the complexity, e.g., mono-jet + E_T^{miss}. Therefore, for one experiment, several limits corresponding to the different channels can exist.

1.3.2 Indirect Searches

Indirect searches aim for the detection of secondary particles from dark matter interactions or decays in the cosmic radiation. The content in this section is mostly compiled from references [34], [35] and [36].

1.3.2.1 Detection Mechanism

Thermal production in the early Universe implies that dark matter can also annihilate into standard model particles. With the thermal freeze out, dark matter particle densities dropped to a value where this process becomes irrelevant on large scales. However, it is still expected to appear, mostly where dark matter is concentrated in a gravitational potential. This includes galactic centers but also potentially the core of Sun or Earth. Depending on the annihilation channel, an excess cosmic radiation in the form of γs, protons/antiprotons, electrons/positrons or neutrinos is expected. There are a few conceivable decay channels which would produce γ lines that would be a strong hint for a dark matter origin.

Alternatively, if the dark matter sector is more complex, dark matter decays ultimately emitting standard model particles could be possible. This would also lead to a signal in the cosmic radiation spectrum.

1.3.2.2 Experimental Approaches and Experiments

Depending on the energies and messenger particles, different approaches are required for indirect searches. At lower energies and higher rates up to $\mathcal{O}(100\,\mathrm{GeV}/c^2)$, satellite based experiments like Fermi-LAT [37] avoid the background and undesired shielding of Earth's atmosphere. Imaging atmospheric Cherenkov telescopes (IACTs) like Magic [38] and Hess-II [39] are used for higher energies and lower rates from GeV/c^2 to more than $100\,\mathrm{TeV}/c^2$. They exploit the effect of the atmosphere where particle showers induced by the cosmic rays produce Cherenkov light that can be detected by ground based telescopes. For very high energies to the EeV/c^2

range, coinciding with very low rates (1 /km^2/y and less), water-Cherenkov detectors like HAWC [40] and Auger [41] are required. They detect charged particles from the showers via the Cherenkov light they produce in ground based water tanks.

When it comes to neutrinos as messengers, their small interaction cross section requires very large detector masses. This can be realized with huge water tanks equipped with photo-multipliers as in the Super-Kamiokande experiment [42]. Another approach is equipping a naturally available target mass with a read-out as done by the IceCube experiment [43]. Ice cube installed a photo-multiplier array into 1 km^3 of the antarctic ice shelf.

1.3.2.3 Current Results

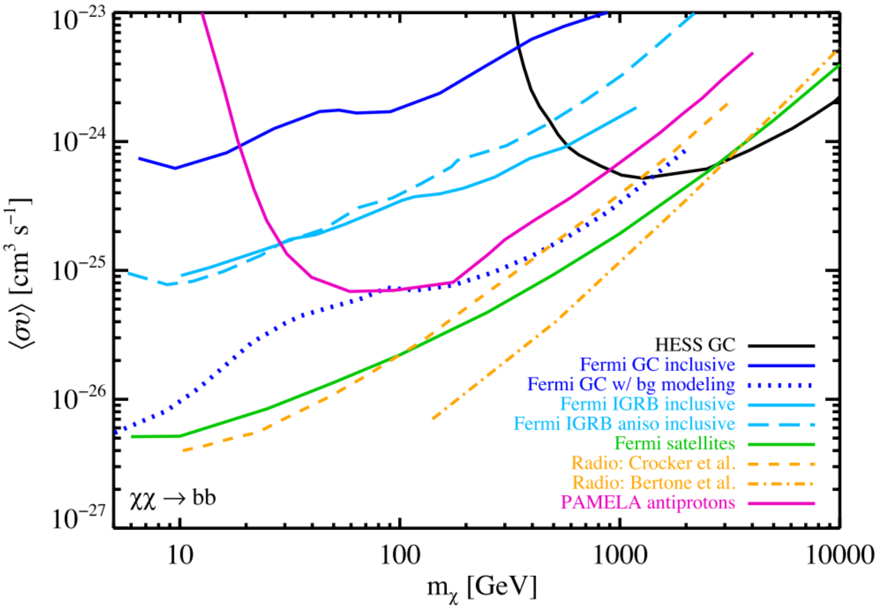

Figure 1.7: Example exclusion limits plot from indirect detection, taken from [34](2016). The investigated channel is an annihilation to $b\bar{b}$, the limits are for this specific decay only.

Assuming a WIMP-like dark matter particle and dark matter annihilation, the annihilation cross section $< v \cdot \sigma >$ is the quantity most relevant for indirect dark matter search. Here σ is the pair annihilation cross section, v the dark matter velocity and $<>$ marks an average over the velocity distribution. As in collider experiments, indirect searches have to look at different annihilation/decay channels separately. Constraints on $< v \cdot \sigma >$ vs dark matter particle mass are then given for one specific channel. An example for dark matter annihilation into $b\bar{b}$ is shown in figure 1.7.

An ongoing discussion in indirect dark matter search concerns an observed γ ray excess from the galactic center at a few GeV/c^2, e.g., see [44],[45] and [46]. If it were confirmed as a dark matter signal it would point to a mass $\mathcal{O}(10\,\mathrm{GeV}/c^2)$. However, observations at the galactic center require extensive modeling due to the high number of objects and processes involved, leading to high uncertainties.

1.3.3 Direct Searches

Direct detection aims to identify galactic dark matter candidates by their interaction with Earth bound detectors. As before this section focuses on the detection of WIMP-like dark matter candidates. It neglects direct searches for, e.g., Axion dark matter [28] or very heavy dark matter particles via gravitation [47] as those require entirely different detector concepts than presented in this work.

1.3.3.1 Detection Mechanism

In the standard scenario for direct detection, elastic, coherent scattering of a dark matter particle on a nucleus or an electron in a target is assumed. In the following all the formulas are for the nuclear recoils case relevant for this work. The detected differential rate is then governed by three factors [48]:

- Astrophysical quantities, namely the dark matter particle density $n_{DM} = \frac{\rho_{DM}}{m_{DM}}$ where ρ_{DM} is the local dark matter density and m_{DM} the dark matter particle mass, the velocity distribution $f(\vec{v})$ and the galactic escape velocity v_{esc}. They govern how much dark matter is available for an interaction within the detector.
- A particle physics factor, namely the differential interaction cross section

  $$\frac{d\sigma}{dE_R}(v, E_R) \approx \frac{\sigma_0}{E_R^{max}} \cdot F^2(q) \tag{1.2}$$

  between the dark matter particle and the nucleus. Here σ_0 is the zero momentum transfer cross section and E_R is the nuclear recoil energy. $F(q)$ is the nuclear form-factor, containing all of the dependency on the transferred momentum $q = \sqrt{2m_T E_R}$, where m_T is the mass of a target nucleus. $E_R^{max} = \frac{2\mu^2 v^2}{m_T}$ is the maximum recoil energy with μ the reduced dark matter - nucleus mass.
- The number of target atoms in the detector. The formula given in the following calculates the rate per unit target mass. Therefore, the number of target atoms is taken into account by a factor $\frac{1}{m_T}$.

For a real detector, also energy resolution and threshold have to be taken into account. In the following an ideal detector with infinite resolution and zero energy threshold is assumed. The differential rate per unit target mass for such an ideal detector is then given by [48]:

$$\frac{dR}{dE_R} = \frac{1}{m_T} \cdot \frac{\rho_{DM}}{m_{DM}} \cdot \int f(\vec{v}) \cdot v \cdot \frac{d\sigma}{dE_R}(v, E_R) d^3v \tag{1.3}$$

Inserting equation 1.2, the cross section can be removed from the integral:

$$\frac{dR}{dE_R} = \frac{\rho_{DM}}{m_{DM}} \cdot \frac{1}{2\mu^2} \cdot \sigma_0 \cdot F^2(q) \int_{v_{min}}^{v_{esc}} \frac{f(\vec{v})}{v} d^3v \tag{1.4}$$

Here, v_{min} is the minimal dark matter particle velocity required for a nuclear recoil of energy E_R and v_{esc} is the galactic escape velocity. Some more details concerning the cross-section, form-factor and velocity distribution are given in the following.

Cross-section In the standard framework, the zero momentum transfer can be split in a cross-section for coherent, spin independent scattering and one for spin dependent scattering. Both have their own σ_0 and $F^2(q)$. The coherent, spin independent scattering assumes that the energy transfer is small enough that the dark matter particle effectively interacts with the whole nucleus. The rate therefore scales with A^2, the square of the number of nucleons. The spin dependent scattering amplitude scales with the total spin of the nucleus, which is governed by the number of unpaired nucleons. Here the focus lies on the spin independent interaction.

To be able to compare direct detection experiments with different target materials, the zero momentum transfer cross section is usually given per nucleon. The normalization is chosen as $\sigma_0 = A^2 \frac{\mu^2}{\mu^2_{DM,proton}} \sigma_0^{nucleon}$, where $\mu_{DM,proton}$ is the reduced dark matter - proton mass. Equation 1.4 can then be rewritten for spin-independent scattering as:

$$\frac{dR}{dE_R} = \frac{\rho_{DM}}{m_{DM}} \cdot \frac{1}{2\mu^2_{DM,proton}} \cdot A^2 \cdot \sigma_0^{nucleon} \cdot F^2(q) \int_{v_{min}}^{v_{esc}} \frac{f(\vec{v})}{v} d^3v \tag{1.5}$$

Form Factors In case the transferred momentum is big enough, the interaction will start to resolve the nucleus and its structure. It is hence not fully coherent anymore. This effect is taken into account by the square of the nuclear form factor $F^2(Q)$. In first approximation, it consists of a Fourier transform of the scattering centers [49]. For some elements measured data from electron scattering are available [50]. For other elements, approximate formulas as for example given by Helm [51] can be applied. In figure 1.8 the squared form factors for the elements relevant to this work, Ca, W and O are shown. Data are available for Ca and O, while the form factor for W is calculated from Helm with the parametrization chosen by [49].

For the $\mathcal{O}(10\,\mathrm{eV}) - \mathcal{O}(1\,\mathrm{keV})$ nuclear recoils of interest in this work, the form factor is mainly relevant for tungsten.

Velocity Distribution The expected dark matter density at the position of the solar system can be estimated with reasonable precision of about a factor of 2 [52]. The local velocity distribution is much less certain [53]. In the low mass side of their detection range, direct detection experiments commonly only probe the high

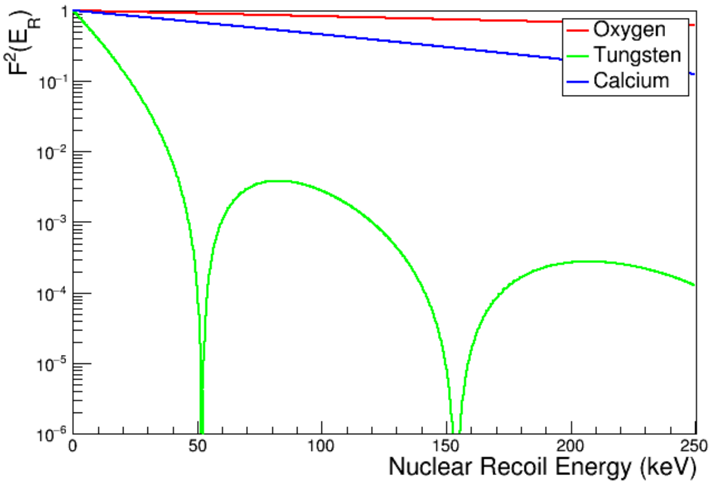

Figure 1.8: Squared form factors for nuclear scattering and the elements relevant for this work: oxygen, calcium and tungsten.

velocity tail of the distribution. They are therefore strongly affected by its exact shape.

Commonly, a Maxwell-Boltzmann $f(v) \propto e^{-\frac{3v^2}{2v_0^2}}$ velocity distribution and a stationary, non-rotating dark matter halo is assumed [48]. Here $v_0 = \sqrt{\frac{3}{2}} v_\infty$ is the root mean square velocity and v_∞ the asymptotic velocity. In order to get the expected velocity distribution on an earth-bound detector, the velocity of the solar system of about $v_\odot$ =231 km/s around the galaxy has to be taken into account. An analytical expression for the velocity integral can be found in the appendix of [48].

Furthermore, due to the rotation of the Earth around the Sun with a velocity of about 30 km/s, an annual modulation on the values of the velocity distribution is expected. If observed, it would be a strong hint for a dark matter origin of a possible dark matter observation.

Expected Signal under Standard Assumptions Direct detection limits are commonly calculated with a set of standard values for the required parameters. This allows to easily compare results between different experiments. A set of commonly used values is summarized in table 1.1.

Under these assumptions, the expected interaction rates for a $CaWO_4$ detector are shown in figure 1.9. The example dark matter masses and cross sections are chosen at the edges of the current limits of direct detection (compare figure 1.11). Visible are the very different energy scales. For the 100 GeV/c^2 dark matter candidate recoil energies extend above 250 keV. At the low mass frontier of direct detection at 0.2 GeV/c^2, nuclear recoil energies are around 30 eV even for the comparably light element oxygen. There, a low detector threshold becomes

Parameter	Variable	Value
Local dark matter density	ρ_0	$0.3\,\mathrm{GeV/cm^3}$
Solar velocity	$v_\odot$	$231\,\mathrm{km/s}$
Asymptotic velocity	v_∞	$220\,\mathrm{km/s}$
Galactic escape velocity	v_esc	$544\,\mathrm{km/s}$

Table 1.1: Current standard values of the astrophysics parameters for limit and discovery calculation of direct dark matter detection experiment as described in [48].

essential.

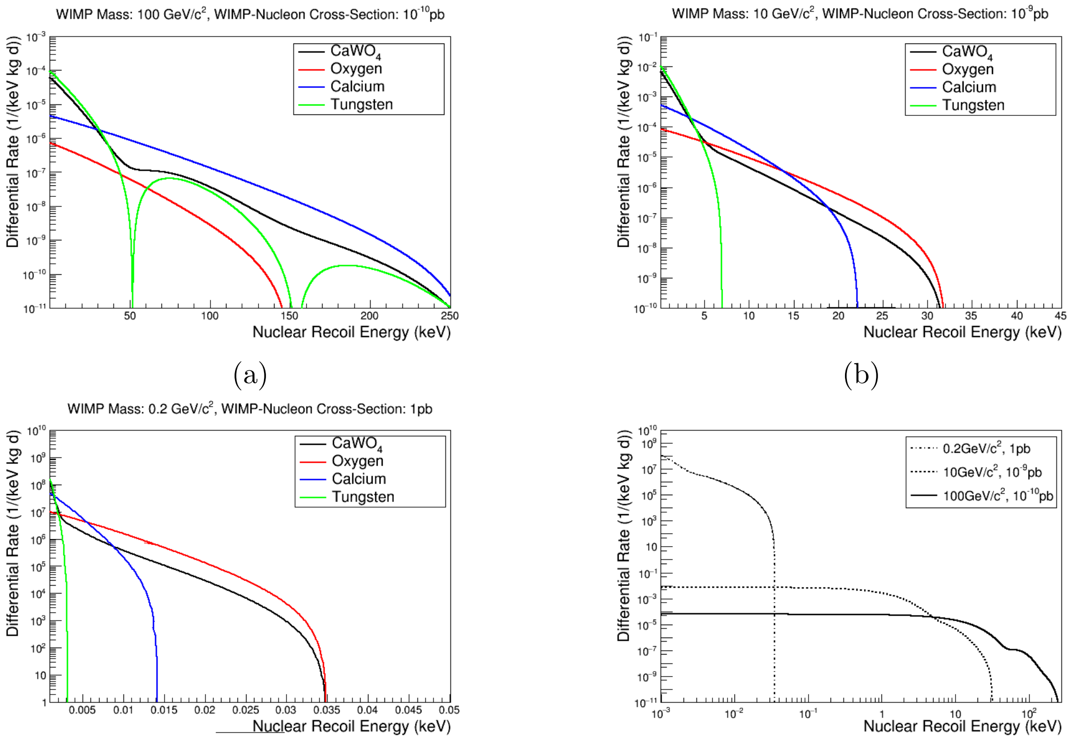

(a) (b)

(c) (d)

Figure 1.9: Expected differential interaction rates for a CaWO4 based, ideal direct detection experiment at current limits of mass and cross section, compare figure 1.11. In figures (a) to (c) expected rates on the pure elements and on a $\mathrm{CaWO_4}$ target are given for dark matter masses of $100\,\mathrm{GeV}/c^2$, $10\,\mathrm{GeV}/c^2$ and $0.2\,\mathrm{GeV}/c^2$ with dark matter - nucleon cross-sections of $1{\times}10^{-10}\,\mathrm{pb}$, $1{\times}10^{-9}\,\mathrm{pb}$ and $1\,\mathrm{pb}$ respectively. All rates are given per kg of pure material, hence the dominating element for each mass and energy range shows a higher expected rate than $\mathrm{CaWO_4}$. In figure (d) the three expected spectral rates for $\mathrm{CaWO_4}$ can be compared directly.

Furthermore, the changing signal composition is visible. The maximum possible energy transfer of elastic scattering is given when the target nucleus mass equals the dark matter particle mass. Hence, for higher masses, calcium and tungsten are dominating, although tungsten suffers from a strong suppression by the form factor. For lower masses, oxygen becomes the dominating component in terms of nuclear recoil energies. Here, having even lighter target elements like lithium or hydrogen would be preferable.

Finally, the different absolute expected rates are visible. The rate scales linearly with the cross-section which is already much more constrained by experiments at higher energies. Assuming the same cross section, expected rates for lower masses are still higher due to their higher number density for a fixed dark matter mass density ρ_0. At very low recoil energies, tungsten dominates in all cases due to its higher value of A^2 in the cross section. However, real detectors might not be able to make use of this high rate due to a finite, higher detector threshold.

In summary, a mostly featureless, exponentially decaying spectrum is expected for a single target element. Having multiple elements in a target leads to edges in the expected spectrum.

1.3.3.2 Experimental Approaches and Experiments

Observing the low expected event rates and energies discussed in the previous section is not trivial. It requires extremely sensitive detectors with very low backgrounds. Several successful detector techniques have been developed over the last decades [54]. The majority is designed to measure one or two of the signal channels heat (phonons), ionization or scintillation light induced by a nuclear recoil. Measuring two of the signal channels often has the advantage of enabling a discrimination between background electron recoils, βs, αs and the sought after nuclear recoils. The most relevant techniques are presented in the following.

Liquid Noble Gas TPCs Liquid noble gas **T**ime **P**rojection **C**hambers (TPCs) read out the scintillation and the ionization signal from interactions in a liquid noble gas target. A schematic view of the setup and signal production in a TPC with the example of the LUX experiment [55] is shown in figure 1.10. The top and bottom of the detector are covered with photo sensors (circles). When a particle interacts with the liquid noble gas filling most of the detector, scintillation light is produced. This light is detected in the photo sensors as the “prompt” or “S1” signal. In addition, any electron from ionization is drifted by a strong electric field towards the top of the detector. At the top, some space is reserved for the noble gas in its gaseous phase. When the electrons reach the gas phase, they are extracted and accelerated, producing another flash of scintillation light, also detected by the photo sensors. This is the “delayed” or “S2” signal.

The time difference between the S1 and S2 signal allows to reconstruct the vertical (z) position of the interaction. Together with the x-y information of the PMTs, the 3D interaction location can be recovered. This information allows for a fiducialization, where events close to the radioactively less clean walls are rejected. The relative strength of the S1 and S2 signal allows for further particle discrimination.

Liquid noble gas TPCs are dominating the high mass region of the direct dark matter search due to their high achievable target masses ($\mathcal{O}(tonnes)$) and low backgrounds. Their higher nuclear recoil thresholds compared to some other detection techniques have so far limited their sensitivity at low dark matter masses. However, analyses based on Bremsstrahlung and the Migdal Effect [56] have the potential to significantly extend their reach [57][58].

The leading liquid noble gas TPC experiments based on Xenon currently are Xenon [59][60], LUX [55]/LUX-ZEPLIN [61] and PandaX [62]. The DarkSide experiment uses liquid Argon instead of Xenon [63][64].

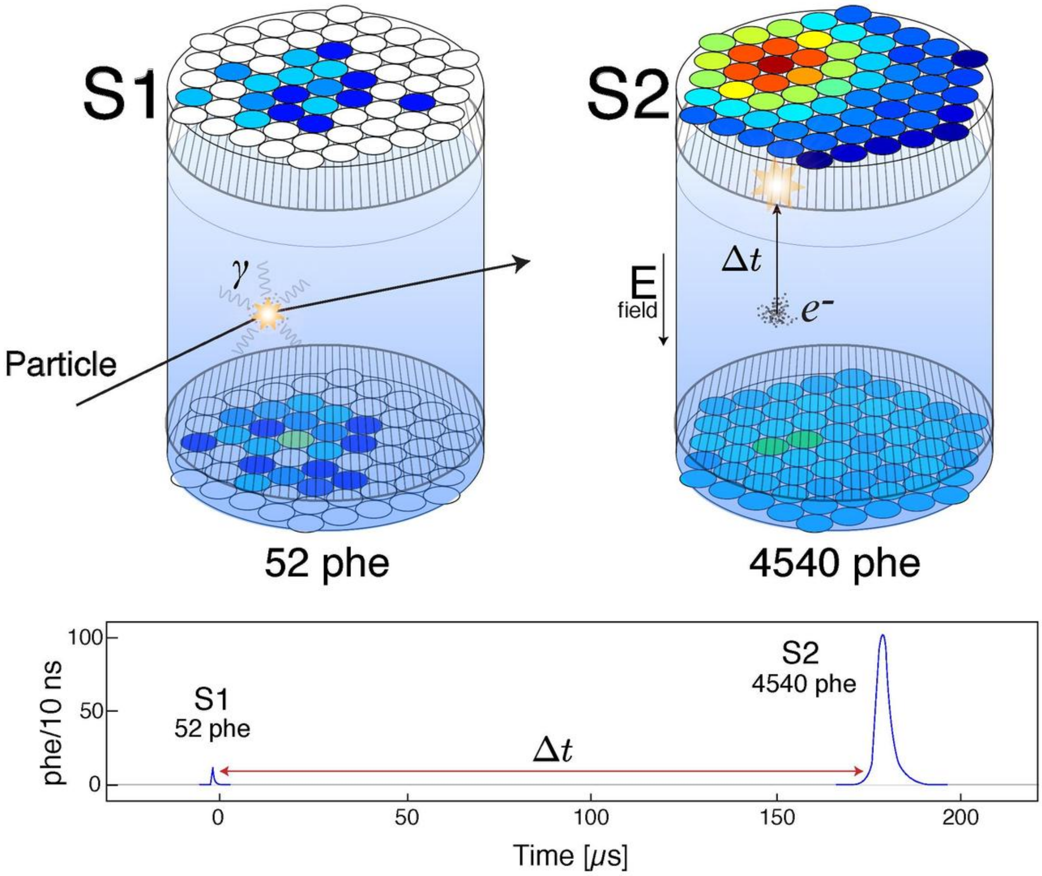

Figure 1.10: Schematic view of a liquid noble gas TPC with the example of LUX. Picture taken without further changes from [65]. Particle interactions in the liquid noble gas (light blue) produce scintillation light and ionization. The scintillation light is registered in the photo multipliers (small circles, top and bottom) as the fast S1 signal. The electrons from ionization are drifted to a gas phase on top of the detector, producing another flash of light, the S2 signal.

CCDs At lower dark matter masses, the field of relevant detection techniques is more diverse. The DAMIC experiment, for example, uses modified, scientific grade versions of CCDs (Charge-Coupled Devices). They detect the ionization signal of a possible dark matter induced nuclear recoil in the doped bulk silicon of the CCD [66][67]. An advantage of this technique are low thresholds of a few hundred eV nuclear recoils and a good spacial resolution similar to a CCD camera. Particle discrimination can be done based on the track through the detector array.

Spherical Proportional Counter (SPC) Another approach is taken, e.g., by the News-G experiment [68]. It aims to detect dark matter nuclear recoils in a **S**pherical **P**roporitonality **C**ounter (SPC) [69] filled with noble gas, operating similarly to a classic Geiger-Mueller counter. Ionization electrons induced by a recoil are drifted in an electric field. This causes secondary ionization in an avalanche process which is then measured. While sensitivity for nuclear recoils is again in the hundred eV range, TPCs have the advantage of being able to employ various different target elements. This way, they can optimize the energy transfer for a given dark matter mass. This especially includes the lightest element, hydrogen.

Bubble Chambers The Pico experiment [70][71] uses super-heated fluids in bubble chambers read out by cameras and acoustic sensors. Among others, it has the advantage that γs are very unlikely to nucleate a bubble in the bubble chamber. Thereby, the main background to the sought for nuclear recoils is strongly suppressed.

Cryo-Detectors Cryogenic particle detectors are taking a leading role in direct detection of low dark matter masses ($< 3 - 4\mathrm{GeV}/c^2$). Operation at extremely low temperatures, often in the mK range, greatly reduces any thermal related noise and heat capacities. This allows to detect the tiny phonon signal induced by potential dark matter interactions.

Cryo-detectors make use of different combinations of the three available readout channels. Germanium and silicon semiconductor detectors as for example employed by the (Super)CDMS/CDMSlite experiment [72, 73, 74, 75] as well as Edelweiss [76] can read out the phonon and the ionization signal. In general, ionization signals can also be converted to a strongly amplified phonon signal by applying a strong electric field (Neganov Trofimov Luke effect [77][78]). This has the drawback of losing the particle discrimination power from measuring two distinct signals.

By contrast, the CRESST experiment[79][80] uses scintillating crystals, predominantly $CaWO_4$, and reads out the scintillation signal in addition to the phonon signal. A more detailed description of the operating principle of CRESST detectors will be given in section 2.2.

1.3.3.3 Current Results

Results from direct dark matter search experiments are given in the dark matter particle-nucleon cross section ($\sigma_0^{nucleon}$) vs dark matter particle mass plane, compare equation 1.5 and figure 1.11. So far, no undisputed dark matter signal has been detected. Therefore, results are given in the form of exclusion limits in figure 1.11. All cross sections above the drawn lines are excluded.

At high dark matter masses liquid noble gas TPCs dominate the exclusion limits. The cryogenic ionization and scintillation detectors are mostly relevant at lower dark matter particle masses.

The grey area on the lower part of the plot marks the experimental sensitivity where one or more events are expected from coherent neutrino nucleus scattering, the so called "neutrino floor". Neutrino nucleus scattering poses an irreducible background to direct dark matter searches. Displayed is the neutrino floor for $CaWO_4$ as calculated in [92]. To extend the range of direct searches significantly below this limit novel techniques, e.g., with directional detection will be required.

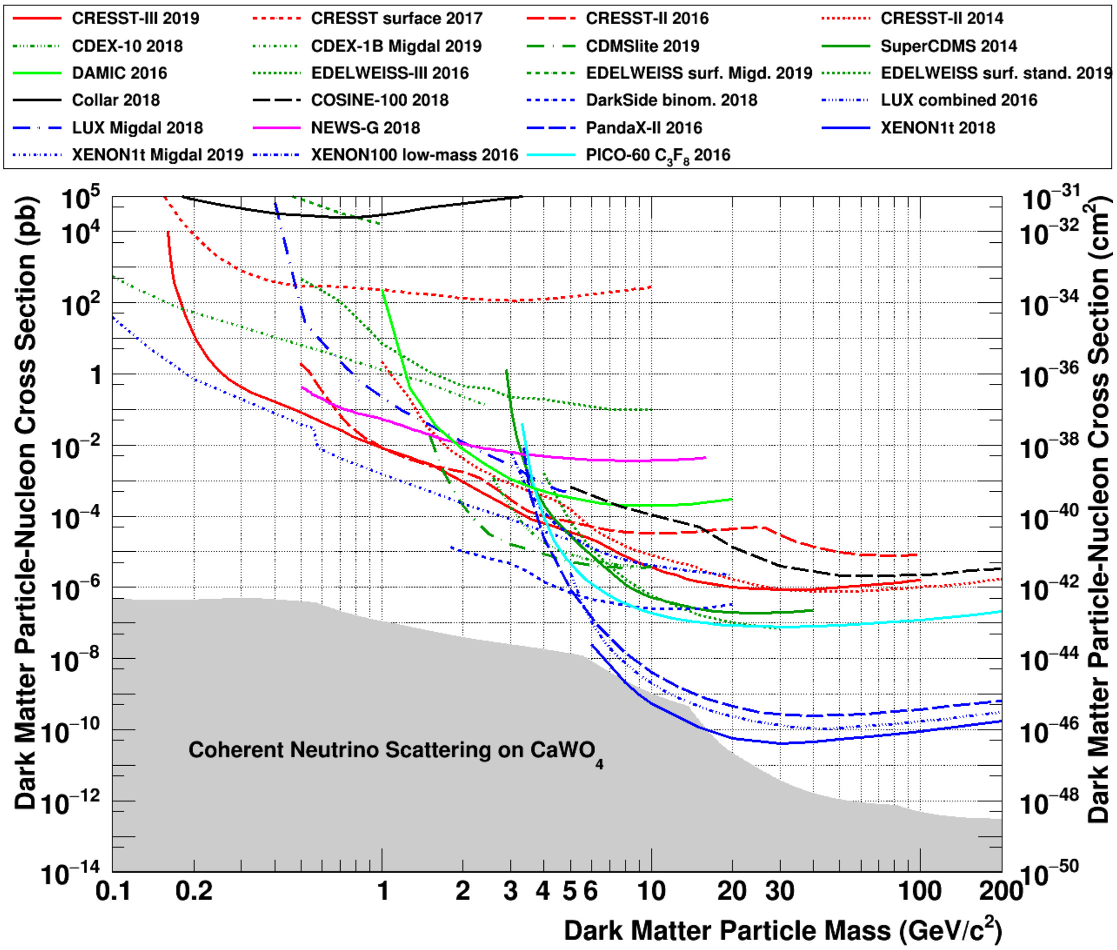

Figure 1.11: Current dark matter exclusion limits from direct detection experiments. Plot contains limits published after the results of this work. The limits assume standard values as discussed in section 1.3.3.1 regarding dark matter abundance and velocity. The shown limits are: CRESST-III 2019 [80], CRESST surface 2017 [81], CRESST-II 2016 [82], CRESST-II 2014 [83], CDEX-10 2018 [84], CDEX-1B Migdal 2019 [85], CDMSlite 2019 [75], SuperCDMS 2014 [86], DAMIC 2016 [67], EDELWEISS-III 2016 [87], EDELWEISS surf. Migd. 2019 and EDELWEISS surf. stand. 2019 [88], Collar (H) [89], COSINE-100 2018 (NaI) [90], DarkSide binom. 2018 [64], LUX combined 2016 [55], LUX Migdal 2018 [58], NEWS-G 2018 (Ne + CH_4) [68], PandaX-II 2016 [62], XENON1t 2018 [59]), XENON1t Migdal 2019 [57], XENON100 low-mass 2016 [91], PICO-60 C_3F_8 2016 [70]. Grey area: experimental sensitivity at which one or more events from coherent neutrino scattering are expected for a dark matter search with $CaWO_4$ [92]. Coherent neutrino scattering forms an irreducible background for most direct dark matter search experiments.

Chapter 2

The CRESST Experiment

The CRESST (**C**ryogenic **R**are **E**vent **S**earch with **S**uperconducting **T**hermometers) experiment is a direct dark matter search. In the following, a detailed description of the experiment is given. The chosen experimental environment including the location is described in section 2.1. In section 2.2 the CRESST detector design is introduced. This is followed in section 2.3 by information on the thermometers and electronics necessary for the detector read out. Data acquisition and triggering are discussed in section 2.4.

2.1 Experimental Environment

Expected rates of dark matter interactions on earth-bound detectors are in the order of a few counts/(kg keV y) with deposited energies on the eV to keV scale (compare section 1.3.3). To be able to identify such rare events, direct detection experiments like CRESST require high sensitivity and very low rates of background interactions. The location and major parts of the experimental setup are hence dictated by the requirement to minimize exposure to natural radioactivity and external disturbances. The setup is schematically shown in figure 2.1.

To shield the experiment from cosmic radiation, predominantly muons, the main installation is located in the Laboratori Nazionali del Gran Sasso (LNGS) underground laboratory in Italy. LNGS has a rock overburden of about 1400 m [93, 94], corresponding to 3600 mwe to 3800 mwe (meter water equivalent). The muon flux is reduced by about six orders of magnitude compared to the surface down to a rate of 1 muon/m^2/h [94, 95, 96].

Within the laboratory, the sensitive parts of the experiment are enclosed in a Faraday cage that protects from electromagnetic interference [97]. Electromagnetic interference can either mimic signals or increase the noise in the electronic system, reducing the sensitivity.

Inside the faraday cage, a 40 cm thick polyethylene shielding is installed to protect from environmental neutrons. Polyethylene is especially well suited to moderate neutrons down to energies below the ones of the sought after signal due to its high abundance of hydrogen. Shielding against neutrons is important for CRESST, as neutron interactions cannot be distinguished from dark matter interactions as they both produce predominantly nuclear recoils. Therefore, neutrons pose a serious background threat for CRESST. The neutron flux at LNGS has been measured and simulated to be about $4{\times}10^{-6}/(\mathrm{cm\,s^2})$ [98, 99].

Despite the underground installation, a few muons reach the experimental site.

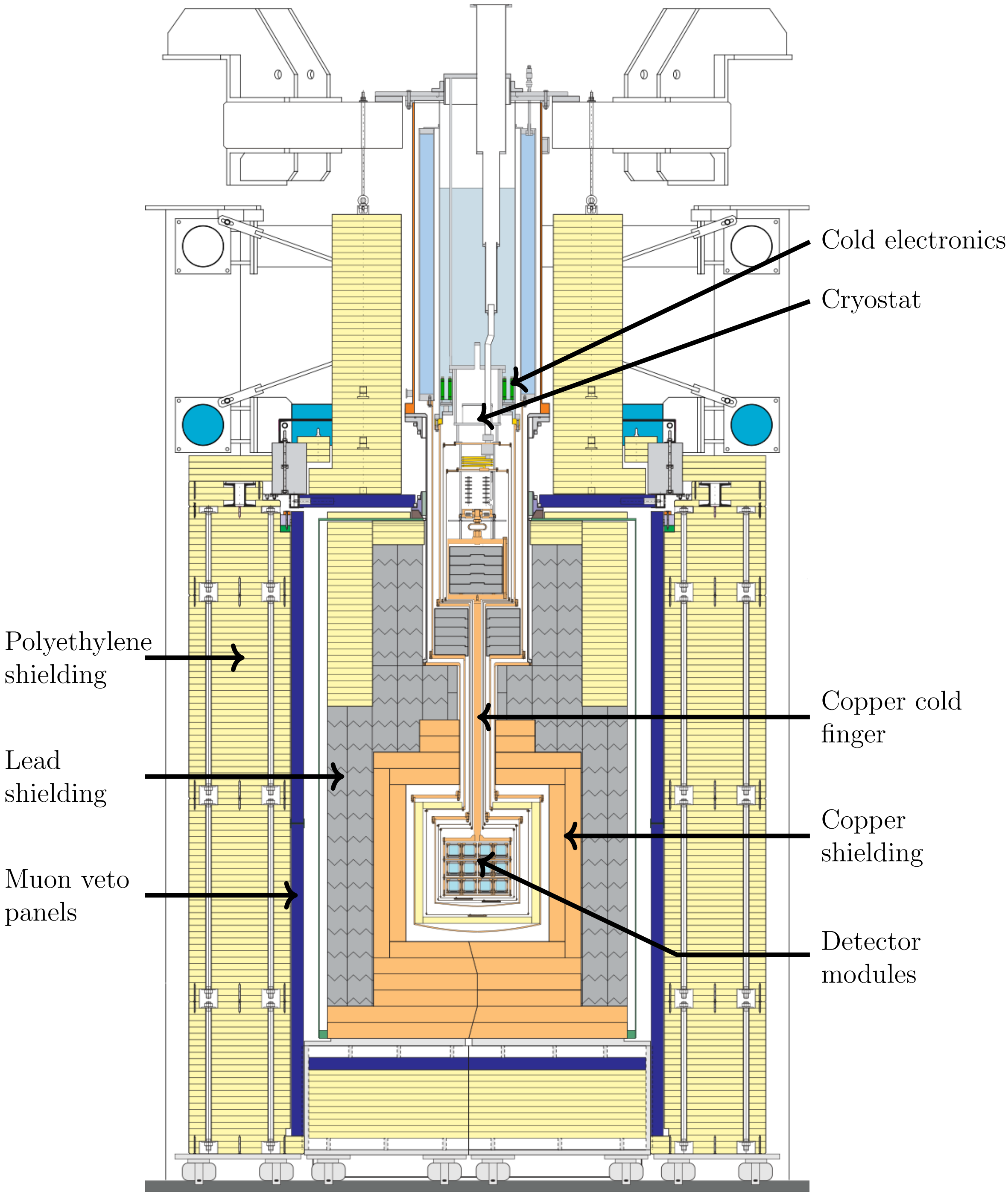

Figure 2.1: Schematic view of the CRESST shielding and cryostat. Yellow: Polyethylene shielding; Blue: Muon veto panels; Grey: Lead shielding; Orange: Copper shielding and cryostat copper parts. The cryostat on top is connected by a copper cold finger to the experimental volume in the center with the detector modules inside.

A muon veto is installed between the polyethylene and the inner shieldings to veto muons not shielded by the underground location. It consists of plastic scintillator panels equipped with photo multipliers and a 98.7% coverage of solid angle with only a small hole on top for the cryostat.

Inside the muon veto, a layer of 20 cm of ultra pure lead constitutes the main shielding against γ backgrounds. Lead has the advantage of a high stopping power due to its high density and atomic mass and is easily available.

The lead has a radioactive contamination of ^{210}Pb from the ^{238}U chain. Therefore, another 14 cm layer of ultra pure copper is added inside of the lead shielding.

The CRESST detectors require cryogenic temperatures for operation. Such an environment is provided by a commercial He3/He4 dilution refrigerator positioned on top of the described layers of shielding. The thermal coupling to the detectors is achieved by a 1.3 m copper cold finger, see figure 2.1. In this way, any direct line of sight from the main body of the cryostat to the detectors is avoided and the cryostat can be kept outside of the shielding.[1]

An additional polyethylene shielding is installed within the inner vacuum chamber of the cryostat. It is intended to protect from neutrons emitted in the copper and lead shielding. A picture of the inner shielding can be found in [100].

---

[1] The experimental volume with the detectors is made out of selected materials with a very low intrinsic radioactivity. The cryostat is a commercial product that has been produced without corresponding considerations.

2.2 CRESST Detector Modules

In this section the CRESST detector modules and their mode of operation are described. First, in section 2.2.1 technique for particle discrimination is introduced. It dictates many of the design choices for the CRESST detector modules. Over the years several designs have been developed. In section 2.2.2 the components common to all current CRESST detector modules are described. Section 2.2.3 summarizes an analytical model for the signal generation in such a detector. Section 2.2.4 introduces different actual designs relevant for this work.

2.2.1 Phonon-Light Particle Discrimination

As already mentioned in section 1.3.3.2, many direct dark matter detection experiments combine two detection channels to allow for particle discrimination and remove undesired backgrounds. In CRESST the two channels are a phonons and scintillation light from interactions in a scintillating target crystal. The phonon signal serves to determine the energy deposited in the interaction while the scintillation light serves for discrimination.

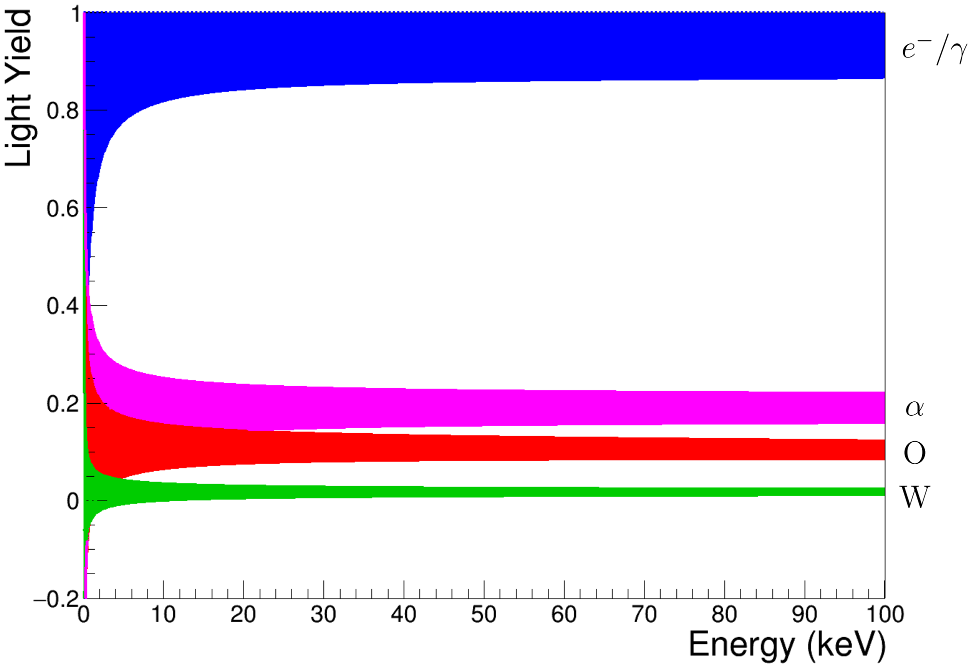

Figure 2.2: Schematic representation of a light yield plot for particle identification in CRESST. The areas within the 90 % upper and lower limits of the e^-/γ (blue), α (purple), oxygen (red) and tungsten (green) event distributions are colored, i.e., 80 % of the respective interactions fall into the colored parameter space.. The e^-/γ band is centered around one by choice of energy calibration, compare section 3.5.5.

This is possible as the amount of scintillation light depends on the stopping power of the crystal for the particle releasing the energy in the crystal. The stronger the stopping power, the less scintillation light is produced. This effect is called **(light) quenching**. A theoretical model describing this behavior is discussed in detail in [101]. In general, the stopping power is greater, the heavier the particle. For both, β and keV γ radiation, the energy is released in the crystal by an electron, hence they have the same amount of scintillation light. WIMP dark matter is expected to only appear in CRESST as scattering on atomic nuclei. The same is true for neutrons. The atomic nuclei are much heavier and therefore produce less scintillation light than electrons. α radiation falls in-between the two.

The discrimination capability is best exploited with the help of the light yield parameter defined as the ratio of energy detected in the light and the phonon channel:

$$LY = \frac{E_{Light}}{E_{Phonon}} \tag{2.1}$$

In CRESST, the energy calibration is commonly done such that the light yield of γ events is centered around unity by definition. Plotting the light yield vs the energy deposited in the phonon channel results in a number of horizontal bands as schematically shown in figure 2.2. The exact relative positions of the β/γ and nuclear recoil bands have been measured in [102].

With the light yield and energy information available, most of the β/γ backgrounds can be avoided by focusing the analysis on a **region of interest (ROI)** in the light yield plot, where dominantly nuclear recoils are expected.

2.2.2 Generic Components

A schematic drawing of a generic CRESST detector module is shown in figure 2.3. It consists of the following components:

- a **main absorber crystal** equipped with a thermometer. This is the heart of the detector module and the place where energy depositions from incoming particles are expected. The main absorber crystal can be made of different materials. In CRESST-I it was made of sapphire (Al_2O_3). Since CRESST-II, $CaWO_4$ is used due to its stronger scintillation and the presence of th heavy element tungsten [103]. The high A^2 of tungsten results in a higher cross-section for spin independent scattering, compare section 1.3.3.1. Different materials like Si or other crystals are also currently under investigation, e.g., see [104]. However, if the material is non-scintillating, the particle discrimination from the phonon-light technique is lost. The energy of a particle interaction in the main absorber is detected in the form of phonons. Therefore, the main absorber crystal together with its thermometer is also called **phonon detector**.

- a **light absorber** also equipped with a thermometer. It absorbs and detects potential scintillation light from the main absorber crystal. The light

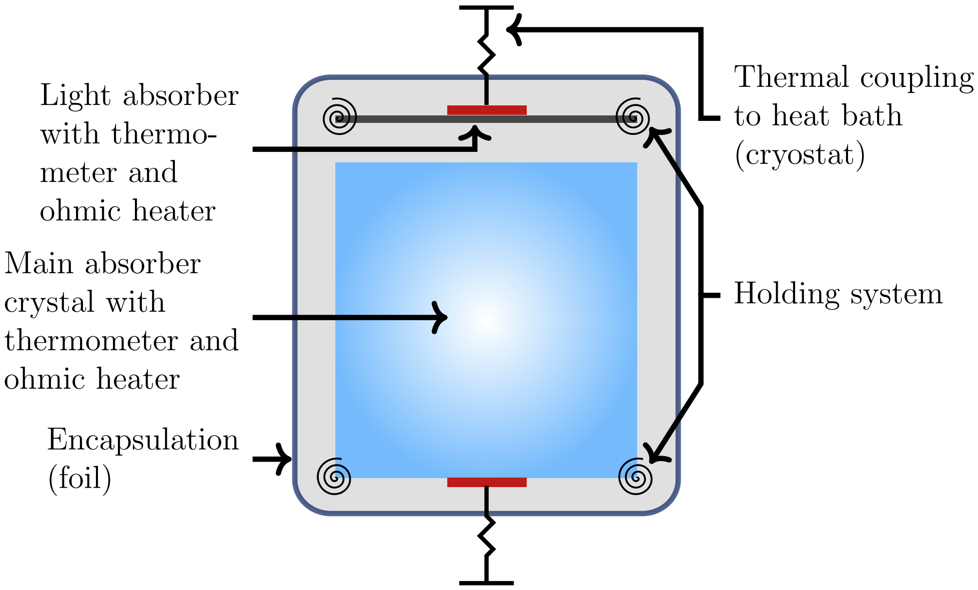

Figure 2.3: Schematic view of a generic CRESST detector module. Compare text for details.

absorber together with its thermometer is therefore also called **light detector**.

- **ohmic heaters** for each thermometer. The heaters allow to induce a constant heating power as well as heat pulses. Those are required for temperature stabilization of the detector and thermometers as well as a method of energy calibration, both discussed later. Heater pulses induced for temperature stabilization are also referred to as **control pulses** and heater pulses for the energy calibration as **testpulses**.
- **thermal couplings** of the thermometers to the cryostat. They are required to cool down the detector and remove the energy deposited by an interaction after it has been detected.
- an **encapsulation** of the detector which can serve multiple purposes. An important feature is a high reflectivity of the surface to collect as much scintillation light as possible in the light detector.
- a **holding system** that holds the detector components in place. Different options are shown in section 2.2.4, when the practical realizations of the modules are presented.

Detector components are called **instrumented** if they are directly equipped with a thermometer for read-out. Components that can produce a signal but are not instrumented themselves are called **active**. An example for an active component is the scintillating foil, where the scintillation light can be detected by the light channel.

2.2.3 Detector Response Model

An analytical model describing the response of a standard CRESST detector module to an energy deposition in the main absorber is summarized in a simplified form in the following. The model has been developed in [105] and applied to detector development e.g. in [106].

The relevant quantity for the temperature measurement is the temperature T_e of the electron system in the thermometer. At the $\mathcal{O}(10mk)$ temperatures of detector operation, the electron system is only weakly coupled to the (thermal) phonon system of thermometer and absorber. The two systems can hence be modeled as thermally separated with a thermal coupling G_{et} in-between, see figure 2.4. Both systems are also thermally coupled to the heat bath via G_{eb} and G_{tb} respectively.

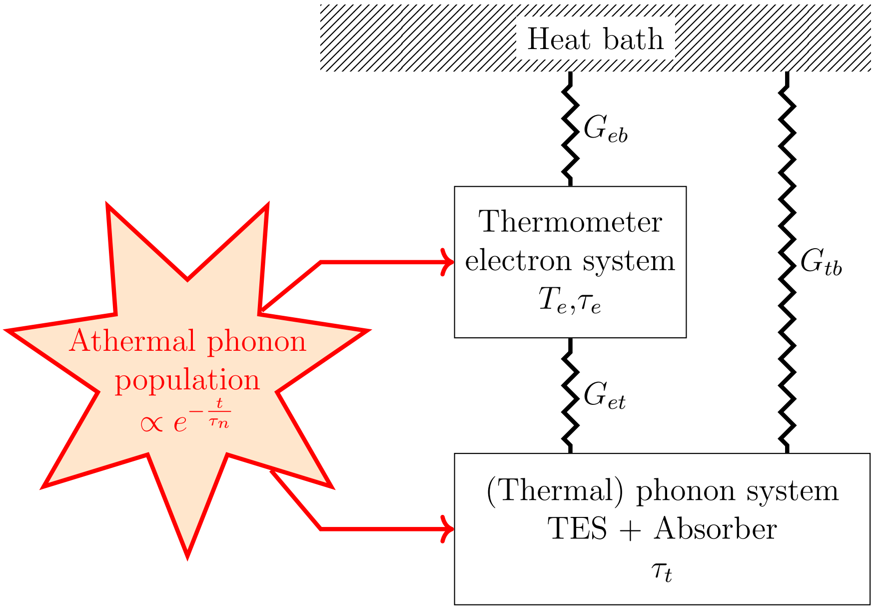

Figure 2.4: Simplified thermal model for a readout channel of a generic CRESST detector. Adapted from [105], for details see text.

Energy deposition from a particle in the main absorber crystal excite a high-frequency phonon population in the interaction site. This population is not in thermal equilibrium with the resident thermal phonon system in the crystal and, hence, does not contribute to its temperature. It is therefore named **non-thermal or athermal**. The athermal phonons decay quickly in frequency but stay athermal over the time scales relevant for the detector response. They quickly fill the volume of the crystal uniformly.

The energy from the athermal phonons can reach the electron system of the thermometer in two ways:

First, their high frequency translates in a strong coupling directly to the electron system of the thermometer compared to thermal phonons. Within the electron system, they thermalize quickly, adding to T_e. This can be modeled as a direct power input from the athermal phonons into the thermometer electron system (upper red arrow in figure 2.4). It is called the **athermal component** or athermal contribution to the measured temperature increase.

Second, athermal phonons can decay into thermal phonons in the absorber and subsequently reach the electron system via the thermal coupling G_{et}. This contribution is usually slower than the athermal component and is called the **thermal component**. In CRESST detectors, the athermal component is dominating the sensitivity to energy depositions in the main absorber crystal.

This two component structure is also reflected in the analytical solution for the detector response as derived in [105]:

$$\mathit{\Delta} T_e(t) = \quad \pm A_n \cdot (e^{-t/\tau_n} - e^{-t/\tau_e}) \quad + \quad A_t \cdot (e^{-t/\tau_t} - e^{-t/\tau_n})) \tag{2.2}$$

with $t \geq 0$, the energy deposition occuring at $t = 0$, amplitudes A_n and A_t and time constants τ_n, τ_e and τ_t. A_n is the amplitude of the non-thermal component and A_t the amplitude of the thermal component. Furthermore, the solution has three time constants, τ_n, τ_e and τ_t. τ_n is the decay time of the non-thermal population caused by the parallel thermalization into the electron and thermal phonon systems. τ_e is the relaxation time constant of the thermometer electron system. It is usually dominated by the coupling to the heat bath G_{eb}. τ_t is the thermal relaxation time of the absorber, given by G_{tb} and the combination of G_{et} and G_{eb}.

In general, for CRESST detector geometries, $\tau_t \gg \tau_n, \tau_e$. In this case, τ_n acts as the time constant for the rise of the thermal component. Energy accumulates in the thermal phonon system while the much shorter-lived non-thermal population is still present and then slowly dissipates to the heat bath with time constant τ_t.

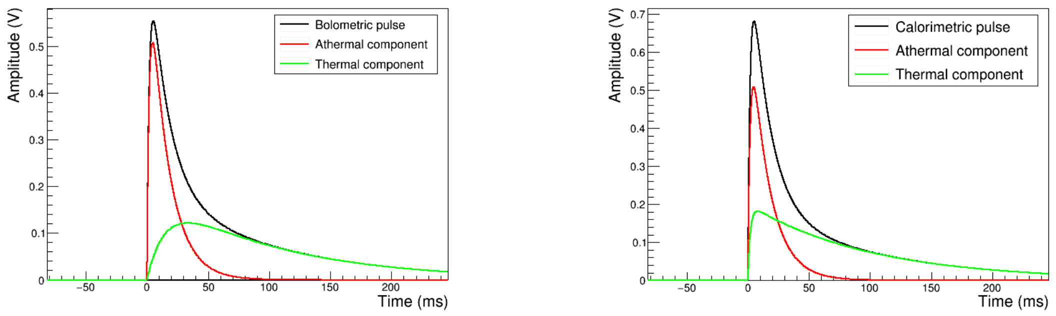

(a) (b)

Figure 2.5: Example pulses from the analytical pulse model with parameter values around what is observed in the data presented in this work. For details see text. a) Bolometric pulse: the decay time of the non-thermal component is the rise time of the thermal component. Parameters: $A_n = 0.8$, $A_t = 0.2$, $\tau_e = 2\,\mathrm{ms}$, $\tau_n = 15\,\mathrm{ms}$, $\tau_t = 100\,\mathrm{ms}$. b) Calorimetric pulse: both components share the same rise time τ_n and integrate over the energy input from the athermal phonons. Parameters: $A_n = 0.8$, $A_t = 0.2$, $\tau_e = 15\,\mathrm{ms}$, $\tau_n = 2\,\mathrm{ms}$, $\tau_t = 100\,\mathrm{ms}$.

For the athermal component the cases $\tau_n \gg \tau_e$ and $\tau_n \ll \tau_e$ have to be distinguished. In the first case, the non-thermal energy input is quickly dissipated into the heat bath. The thermometer reaches an equilibrium between energy inflow and energy outflow within a time constant of τ_e. The resulting equilibrium temperature is directly proportional to the energy inflow. As the energy inflow decays with the athermal population, i.e., with τ_n, so does the non-thermal temperature component. This is called the **bolometric operation mode** as it measures the non-thermal phonon induced energy flux through the thermometer to the heat bath. It corresponds to a plus sign in front of A_n in equation 2.2.

In the second case, the thermometer integrates the energy input over the live time of the non-thermal phonon population, slowly dissipating it into the heat bath. Consequently, τ_n is the time constant governing the rise and τ_e the time constant governing the decay of the non-thermal component. This corresponds to a minus in front of A_n in equation 2.2. The amplitude of the non-thermal component is proportional to the integrated energy input into the electron system. Therefore, this is referred to as the **calorimetric operation mode**.

Examples of $\Delta T_e(t)$ for both cases and with realistic values for the constants are shown in figure 2.5.

2.2.4 Realized Detector Designs

In this section the module designs relevant for the work at hand are presented. They mainly differ in their housing concept. Examples for more module designs not relevant for this work can be found in, [107, 108].

2.2.4.1 Conventional Module

In the conventional design, both the main absorber crystal and the light detector are held by bronze clamps. Those clamps can be covered with a reflective, scintillating coating to reduce scintillation light losses and allow vetoing of events caused by surface contaminations [109]. For the same reason, the reflective foil encapsulating the module is also made of a scintillating material. The light detector consists of a silicon-on-sapphire disc with a TES, matched to the flat top side of the usually cylindrical main absorber crystal. The detectors are encapsulated in a reflecting and scintillating foil. A schematic drawing can be seen in figure 2.6

2.2.4.2 Stick Holder Module

A new holding scheme has been developed for CRESST-II phase 2 [110]. It tackles some issues related to possible non-active surfaces surrounding the main absorber crystal. The clamps are replaced by scintillating $CaWO_4$ sticks as can be seen in figure 2.7. Results from such a module have been published in [83].

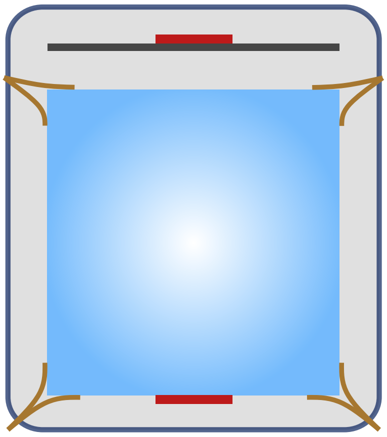

Figure 2.6: Schematic view of a conventional CRESST detector module. The main absorber crystal (blue) is held by bronze clamps (brown), paired with a light detector (black) and surrounded by a scintillating, reflective foil.

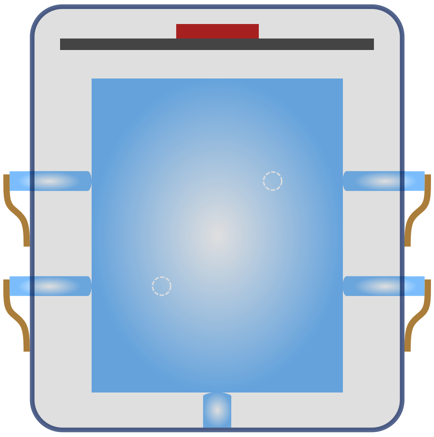

Figure 2.7: Stick holder module; Compared to figure 2.6, the bronze clamps inside the detector housing have been replaced by $CaWO_4$ sticks. This way, there are only at least active materials in line of sight of the main absorber crystal.

2.2.4.3 Instrumented Stick Module

The **i**nstrumented **Stick** (**iStick**) module is an adaptation of the stick module where the sticks holding the main absorber crystal are also instrumented. This serves as an additional veto channel for energy depositions within the iSticks. Furthermore, for the iStick modules relevant for this thesis, the size of the absorber crystal is reduced by about a factor of ten compared to previous modules (24 g vs 300 g). Everything is encapsulated in a box made of copper plates. A schematic drawing and a picture of an opened iStick module are shown figure 2.8.

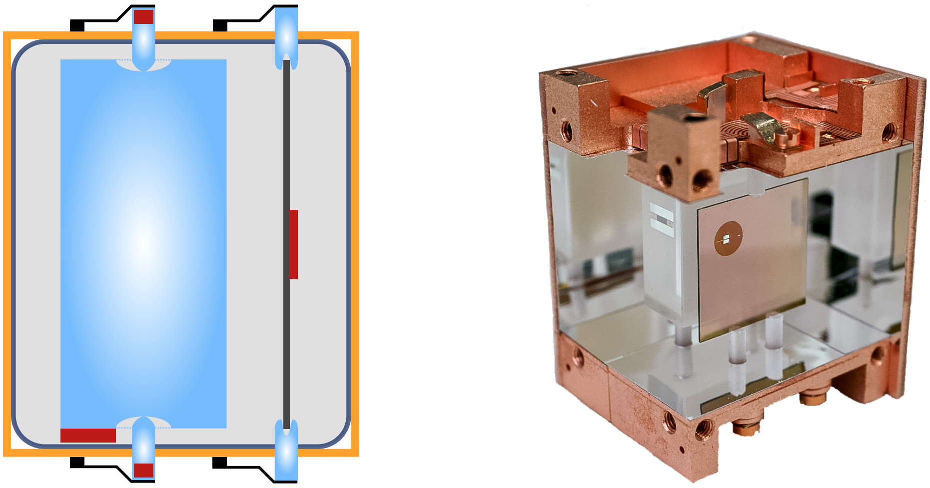

(a) (b)

Figure 2.8: iStick detector module, schematic view and picture. The front copper plates with the scintillating foil are removed to view the inside. Compared to figure 2.7, the sticks holding the main absorber crystal are now instrumented and the module is fully covered with copper plates.

2.3 Thermometers and Read-out Electronics

Sophisticated thermometry and read-out electronics are required to achieve the required keV to eV sensitivity of the detectors. The working principle and practical operation of the employed thermometers is presented in section 2.3.1. Thermometer read-out is described in section 2.3.2 and section 2.3.3 covers the remaining electronics up to the data acquisition system.

2.3.1 Transition Edge Sensors

2.3.1.1 Working Principle

The thermometers in CRESST are so called **transition edge sensors**. They consist of a superconducting thin film with its temperature stabilized within the transition from the normal to the superconducting phase. In this regime the resistance changes rapidly with temperature and measurable resistance differences are observed for tiny temperature changes. For typical CRESST thermometers investigated in this work, changes in the mΩ range for µK temperature increases are achieved.

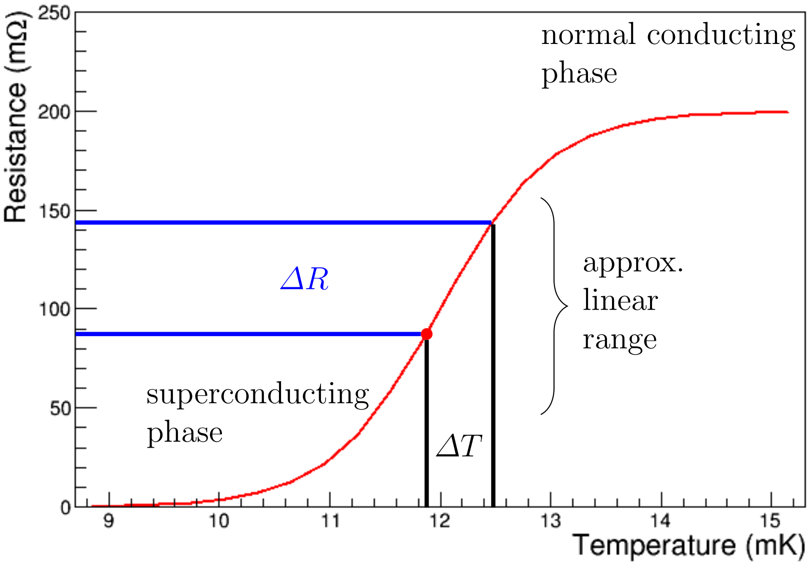

Figure 2.9: Schematic view of a TES transition and working principle. The red curve shows the resistance of the superconductor thin film in the range between the normal and the superconducting phase. For operation as a thermometer, the superconductor is stabilized at an operating point (red dot) within the transition. Small changes of temperature ΔT lead to measurable changes in the resistance ΔR. An approximately linear relation between ΔT and ΔR is only given in the vicinity of the operating point.

The phase transition of a TES and the effect of a temperature increasing heat deposition are schematically shown in figure 2.9. The investigated CRESST thermometers are made out of tungsten with transition temperatures in the 10 mK to 20 mK range. The width of the transition is $\mathcal{O}(1\,\mathrm{mK})$ which corresponds to deposited energies in $\mathcal{O}(1\,\mathrm{keV})$ for the detector modules relevant for this work. This restricts their dynamic range. Outside this range, the TES is either normal or superconducting and the resistance does not change significantly with temperature anymore. Higher or lower slopes are achievable by adjusting production settings. However, there is always a trade-off between higher sensitivity (high slope) and bigger dynamic range (low slope). Furthermore, approximate linearity of the TES response is usually limited to the central part of the transition.

These limitations can be partially overcome in analysis as discussed later (compare section 3.2.2.4).

2.3.1.2 Temperature Stabilization and Heaters

Due to the small width of the TES transition and the problem of non-linearity, a very precise temperature stabilization at the desired operating point of the TES is required. To serve this purpose, in CRESST an ohmic heater is added close to, or on top of each TES. The current temperature/operating point can be measured by injecting a short heat spike via the heater. The spike has to be intense enough to drive the TES from its current operating point into the normal conducting phase where the resistance is approximately constant. This is called a **control pulse**. The thus induced change in resistance from the operating point to the normal conducting state is measured. As the resistance of the normal conducting state is a fixed quantity, this resistance difference is a measure of the current operating point.[2] If the value deviates from the set point the heater power is adjusted accordingly. The concept is schematically shown in figure 2.10.

Stabilizing directly on the measured TES resistance, i.e., the baseline of the detector output, is not easily feasible due to limitations of the further read-out, see section 2.3.2. Therefore, the described "differential" approach is taken.

The desired operating point is determined at the start of a measurement. It is optimized with respect to several parameters, most prominently the signal to noise ratio.

2.3.2 SQUID Resistance Measurement

A very precise measurement of the resistance changes induced in the TES has to be achieved. To that end, a very sensitive magnetometer in the form of a DC **SQUID** (**S**uperconducting **Qu**antum **I**nterference **D**evice) is magnetically coupled to the TES as schematically shown in figure 2.11. The TES is placed in parallel with a shunt resistor and a coil. A TES bias current is applied that splits between the shunt and the TES branch depending on the TES resistance. Changes in

---

[2] The dependence of the resistance on the temperature in the normal conducting state is negligible in comparison to the resistance change from the transition.

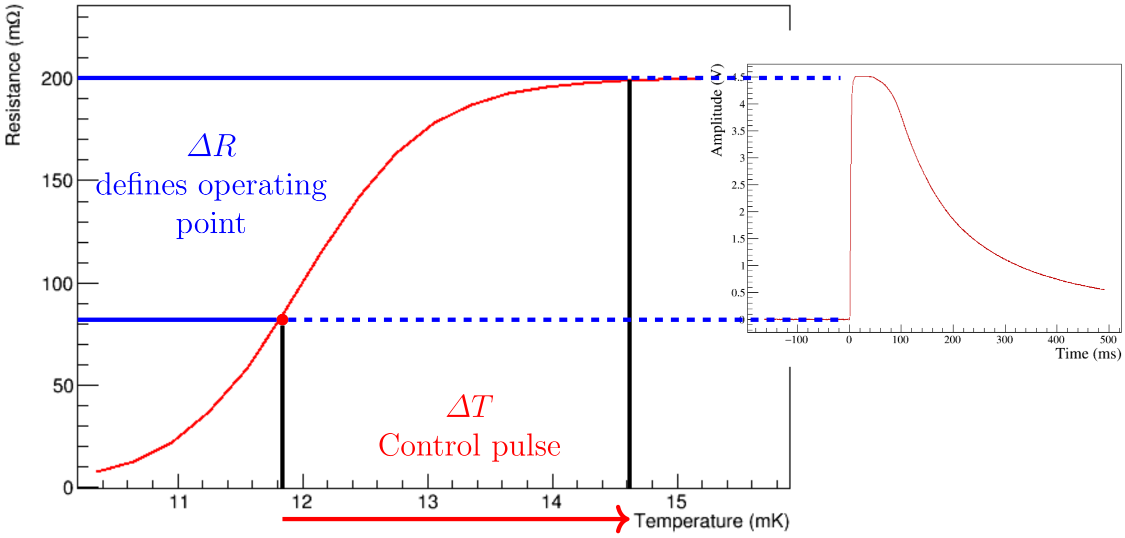

Figure 2.10: Heater and control pulse based stabilization scheme for a TES in CRESST. A control pulse (red arrow) is injected with a high enough ΔT to drive the TES from the operating point (red dot) into the normal conducting phase. As the resistance is approximately constant in the normal conducting phase, the measured resistance difference ΔR gives the position of the operating point in the transition. It corresponds to the pulse height of a saturated pulse (right).

the branching lead to changes in the magnetic field of the coil. This change is picked-up by a SQUID resulting in a measured voltage drop. SQUIDs in CRESST are operated in the so called “flux locked loop mode”. In this mode, the SQUID electronics actually compensate the change in magnetic field with a compensation coil, trying to keep the magnetic field through the SQUID constant. The signal finally transmitted to the DAQ is then the required compensation current.

In this operation mode, a certain type of artifacts can appear when the change in magnetic field is too fast: **flux quantum losses (FQLs)** and **SQUID resets**. The voltage drop over the SQUID is not a monotonous function of the magnetic field but actually oscillating with a periodicity corresponding to an internal unit of one flux quantum. The voltage drop is also the input for the compensation electronics, compare figure 2.11. When the magnetic field from the input coil changes too fast for the compensation electronics to follow, the information about the starting magnetic field can get lost to the electronics. It then settles at the closest number of flux quanta with the correct set point for the SQUID voltage as soon as the change slows down enough to re-establish control. When the magnetic field from the input coil slowly returns to its initial value, the compensation electronics sticks to the new number of flux quanta and thereby a different compensation current. This is an FQL. A schematic representation is shown in figure 2.12. If, after several FQLs, the compensation electronics reach the end of its dynamic range, it

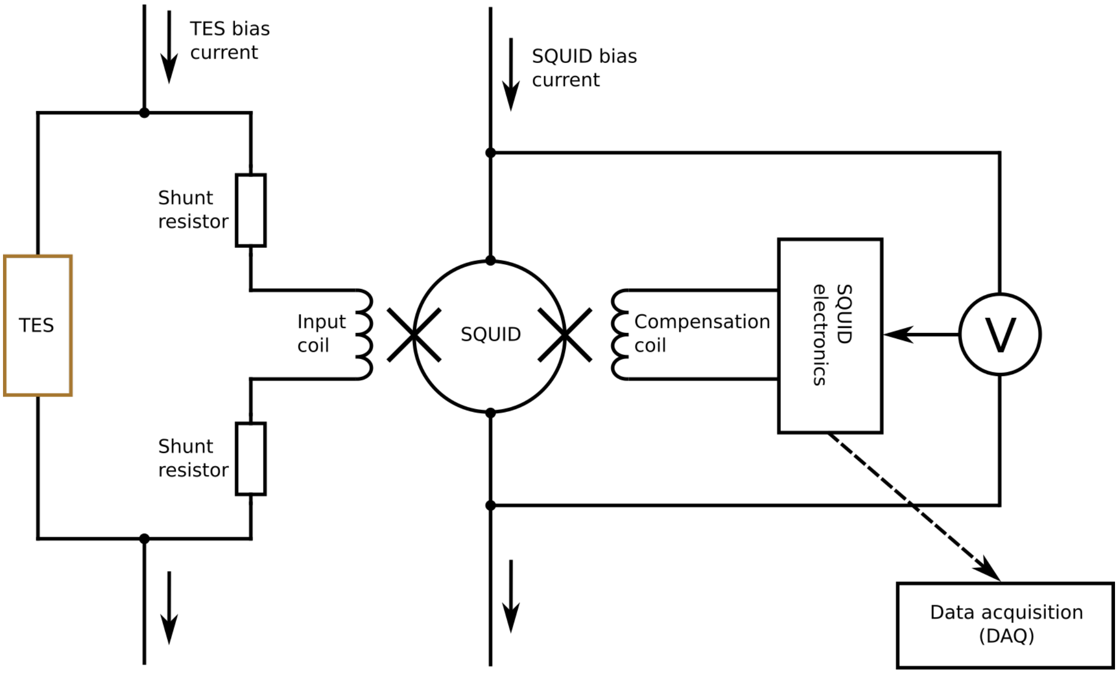

Figure 2.11: Schematic representation of the SQUID readout circuit for a CRESST TES. For details see text.

”resets” back to its starting value. This is a SQUID reset. Both effects lead to artifacts problematic for the data analysis.

2.3.3 Electronics

The total electronic setup per detector channel is summarized in figure 2.13, taken from [111]. There are several branches and components:

- The heater electronics (red) allows to apply a variable current to the ohmic heater coupled to the TES. This usually includes a constant current via the DAC for stabilization in the operating point as well as short pulses via a waveform generator to measure the response of the TES. A square rooter is applied in the line to linearize the heating power with respect to the input voltage. An electronic low pass filter is added at the 4 K stage to reduce noise contributions. The heater electronics is controlled by the DAQ.

- The TES bias electronics (black) provides the bias current through the TES/shunt circuit. This current creates the TES resistance dependent magnetic field picked up by the SQUID, compare figure 2.11. The TES bias electronics also have a low pass filter at the 4 K stage and are controlled by the DAQ.

- The SQUID read-out branch is shown in blue. The output from the SQUID electronics is filtered, digitized and fed to the DAQ (purple). The continuous

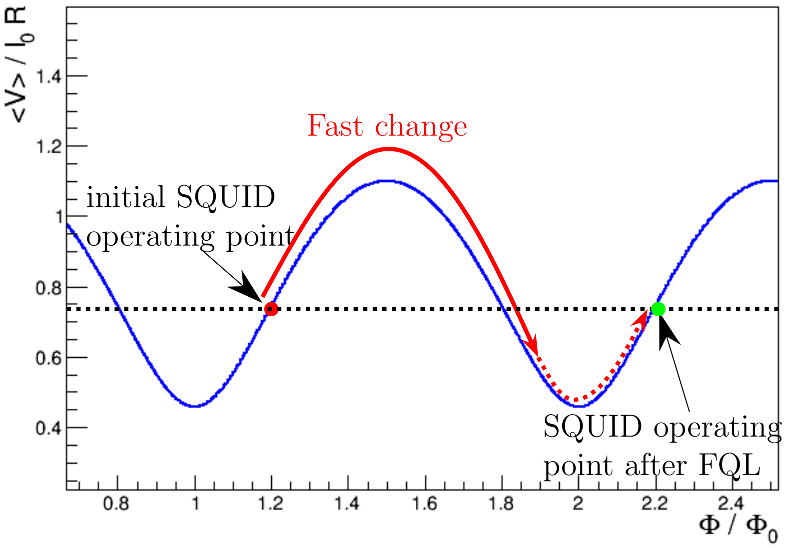

Figure 2.12: Flux quantum loss mechanism in a SQUID. The periodic SQUID response to an external magnetic field in units of one flux quantum is plotted in blue. It is stabilized at a set point indicated by the dotted black line. If a disturbance of the external field happens too fast for the electronics to compensate, the squid is pushed over the maximum and a flux quantum is added or removed (red arrow). The compensation, having no information concerning the total number of flux quanta, will stabilize the SQUID to the next operating point (dashed red arrow, green dot). When the external disturbance vanishes, the compensation now has to keep up the magnetic field corresponding to the new number of flux quanta. This causes a change in the baseline value of the SQUID output corresponding to one flux quantum .

sampling for the DAQ has been added in CRESST-III phase 1 as discussed in detail in [111] as well as section 2.4. The SQUID output can also be fed through a triggering unit that fires a trigger signal every time the output exceeds a certain threshold.

- The muon veto panels, compare section 2.1, are shown in green.
- A common time stamping unit (top left) synchronizes all components.

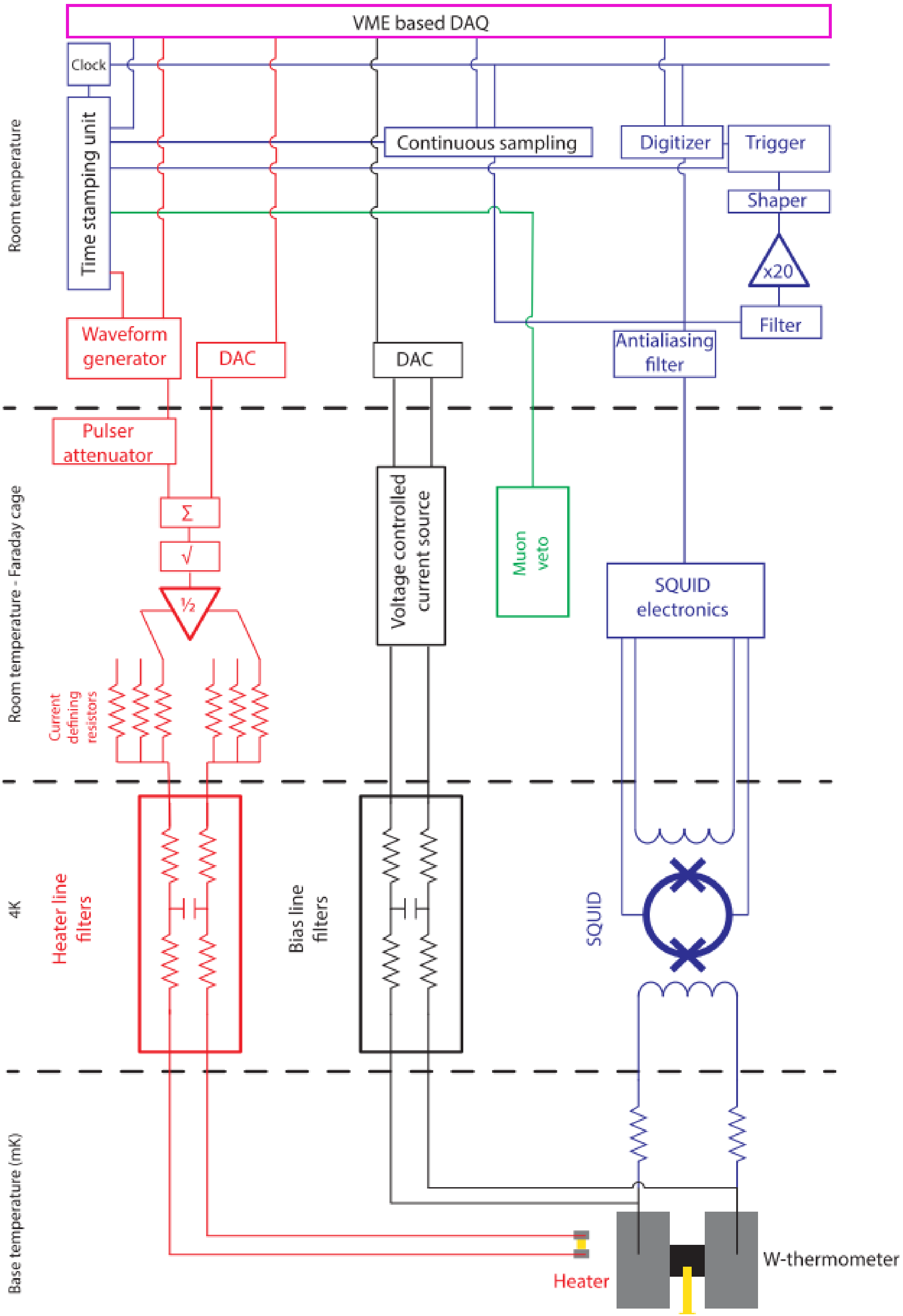

Figure 2.13: CRESST electronics. Red: Heater electronics; Black: TES bias; Blue: SQUID electronics; Purple: Data acquisition; Continuous sampling newly added by [111]. Figure taken from [111].

2.4 Data Acquisition and Triggering

The analogue voltage signals coming from the detector electronics are digitized and, depending on the triggering scheme, partially or fully written to disk. No further processing is applied at this stage, i.e., the raw detector output is available for later analysis. For the measurements presented in the work at hand the sampling rate for the digitization is 25 kHz ($\hat{=}$0.04 ms). The precision is 16 bits over [−10 V,10 V], i.e., 0.3 mV.

Triggering is used to identify interesting signals in the data. This is usually done by searching for times where the detector output exceeds a certain threshold value. There are two approaches for triggering currently implemented, which also determine which part of the data is actually saved. Historically, CRESST has used a hardware triggered acquisition that only records a short period of data whenever the detector output exceeds a certain threshold. This is described in section 2.4.1. In CRESST-III phase 1, a continuous acquisition of the full detector output over the whole measurement was implemented. Triggering is then performed in software on the recorded stream. This is described in section 2.4.2.

2.4.1 Hardware Trigger based Acquisition

The classical read-out splits the detector signal into two branches. One is directly sent to a transient digitizer with a ring buffer. The other one is sent to the trigger electronics. This includes additional filters, an amplifier and a comparator unit. The comparator compares the signal to a given, programmable threshold and outputs a logical signal as soon as the input exceeds that threshold [111].

When the logical signal reaches the digitizer, further data is recorded for a set **post-trigger** length. Then, the data in the digitizer's buffer is written to disc. This includes some of the data still stored in the ring buffer from before the trigger signal, the so called **pre-trigger** region. During the read-out, the digitizer cannot record data leading to a dead time. After the read-out is finished, the trigger is disarmed until at least one pre-trigger length is again available in the buffer. This dead time applies to all eight detector channels sharing a digitizer module, even if they did not trigger. For detector modules with multiple channels, e.g., light and phonon, all channels are read-out if at least one has triggered. Pre- and post-trigger lengths have to be fixed at the beginning of the measurement.

For the control pulses, only the observed pulse height and time stamps are stored in a separate file. For other heater pulses, an additional parameter corresponding to the heating power is written. The muon veto is read-out separately and only synchronized time stamps and pulse heights are recorded.

2.4.2 Continuous Acquisition and Optimum Triggering

For the continuous acquisition, the output of the detector over the whole measurement time is digitized and saved to disc. This is possible by running two digitizers in parallel in switching mode. While one is read out, the other is recording and vice versa, avoiding any dead times. A detailed description can be found in [111].

Triggering is performed in software as part of the data analysis. Having the full data stream available for triggering has several advantages. Most prominently, trigger settings can be changed and iteratively optimized. This also allows to apply filters to the stream that take into account the known noise and pulse shape properties. The resulting improved signal to noise ratio then enables lower trigger thresholds. Furthermore, a well defined amplitude reconstruction algorithm for the triggering removes inconsistencies between the trigger and the later energy reconstruction of events in the analysis.

For the data obtained with the continuous acquisition, triggering is based on the same algorithm as the amplitude reconstruction in the analysis, the so called optimum filter. This is described in more detail in section 3.2.2.3 in the analysis chapter. After reconstructing amplitudes on the stream with the optimum filter, a simple threshold trigger is applied. Further details concerning the subtleties about the triggering can be found in [111].

Chapter 3

Analysis Basics

Two different analyses plus a third one in the appendix are presented in this work. They all follow the same underlying structure that is common for all CRESST analyses. This standard structure is presented in the following. The specific analyses adhere to the introduced structure and only the specific details are presented in the respective chapters.

The standard analysis consists of the following steps:

1. Parameter gathering, section 3.2
2. Data selection, section 3.3
3. Calculation of survival probabilities, section 3.4
4. Energy calibration, section 3.5
5. Light Yield calculation, band fit, particle identification and definition of the region of interest, section 3.6
6. Dark matter limit calculation, section 3.7

Some general information, important settings and naming conventions relevant for the analysis are first summarized in section 3.1.

3.1 General Information, Important Settings and Naming Conventions

The general CRESST detector design has been presented in section 2.2. Specific information concerning the relevant detectors will be given in the respective analysis chapters. There are two features of the TES based read-out discussed in section 2.3 that play an important role in the analysis, namely the non-linearity and saturation of the TES response and the possibility of flux quantum losses (FQLs).

Concerning the naming, an energy deposition in an ideal detector causes a **pulse signal** of the **pulse shape** presented in section 2.2.3. This ideal pulse signal has a **signal amplitude** that is directly proportional to the deposited energy. When measured, the pulse signal is not obtained in its pure form. Instead, the detector read-out distorts the pulse shape, e.g., due to the non-linearity of the TES transition, and adds some **baseline noise**. This is schematically shown in figure 3.1.

To record the data from the detectors, each instrumented part is assigned a **read-out channel** where its signal is recorded (compare section 2.3.3). Together

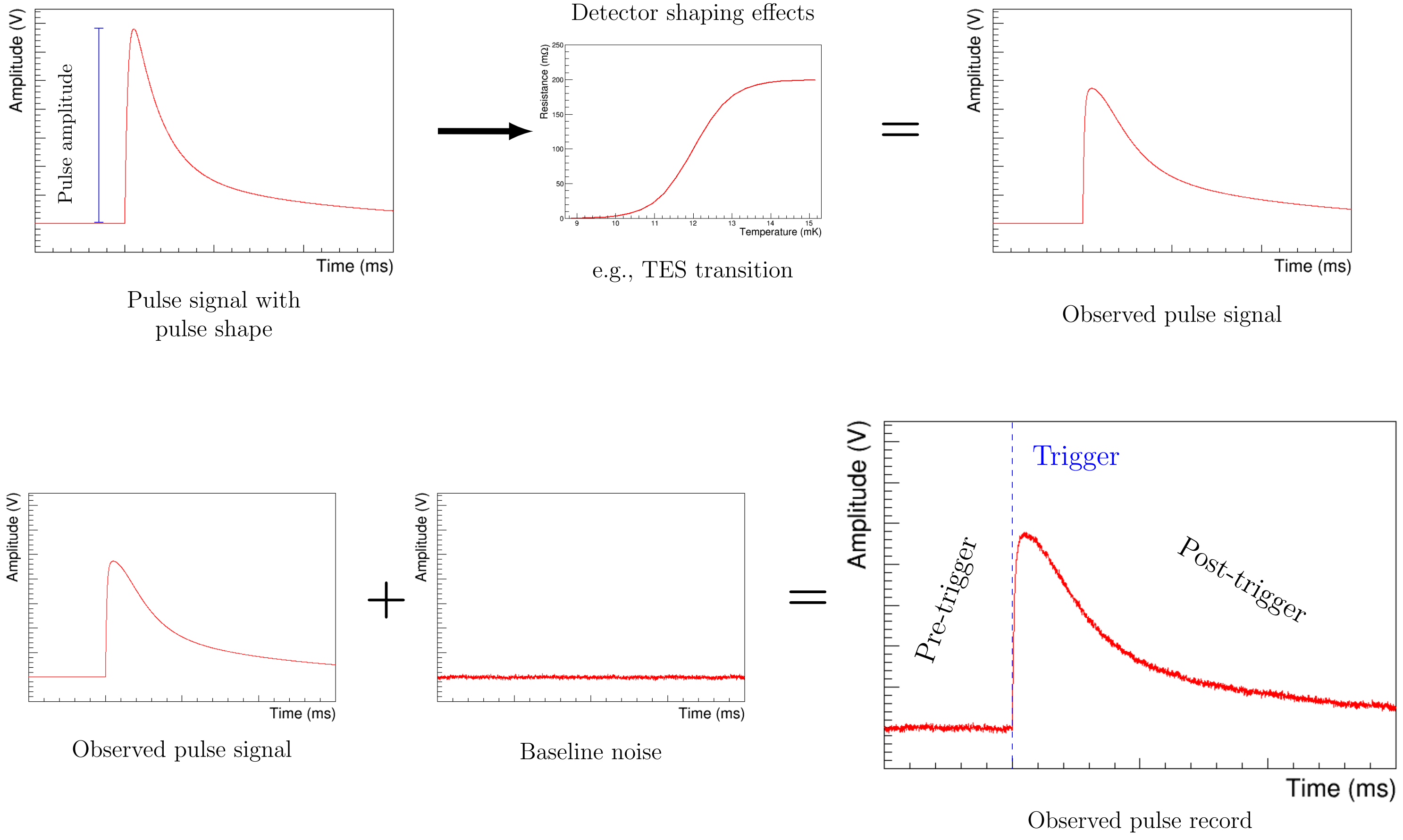

Figure 3.1: Composition of an observed pulse record with a pulse signal. The pulse signal represents the underlying response of the ideal detector to an energy deposition in the detector. Its pulse amplitude is directly proportional to the deposited energy (top left). Detector effects like the finite width of the TES transition distort this ideal pulse shape into the observed pulse signal (top right). Additionally, detector and electronics add noise to the recorded samples leading to the finally observed pulse record (bottom left). The pulse record splits up in a part before and a part after the trigger algorithm fired.

they form a **detector channel**, e.g., the main absorber crystal the "phonon channel" and the light detector the "light channel".

Pulse signals in the data stream coming from the different channels are identified either online or offline by a trigger algorithm. When a pulse signal is identified, the recorded trace around the trigger time is stored as a **pulse record**. An associated quantity is the **record window (length)** which defines the length of the stored pulse record. The pulse record consists of a **pre-trigger** region and a **post trigger** region, compare figure 3.1. The pulse signal is recorded in the post-trigger. The chosen number of samples for the pre- and post-trigger can vary and will be summarized at the beginning of each specific analysis. The pulse record together with the parameters like pulse height, baseline offset, etc. listed in section 3.2.1, is called a **pulse**.

Sometimes random record windows are stored for various purposes without a trigger firing. Those are called **empty baselines**. Contrary to their name, they may include a pulse signal, if one happens to appear at that time. However, in most cases, the record window only contains baseline noise.

CRESST detectors usually have two or more read-out channels per detector module. When one channel of a detector module triggers, a pulse is stored for all of the channels in the same module. These pulses are then grouped and some additional parameters added to form an **event**.

The measurement has to be interrupted every two to three days for cryogenic maintenance. This leads to a natural splitting of the data into **data files** containing 40 h to 60 h of measurement data. Shorter files can also appear for various reasons.

3.2 Parameter Gathering

This section introduces the different parameters the analysis relies on. Parameters are discussed as they appear in the analysis software "OxRop" [112, 113] used in this thesis. Other software may have different naming conventions and slight differences in parameter calculation. However, most of the presented parameters will appear in any CRESST analysis.

3.2.1 Basic Parameters

Some simple parameters are available or can be calculated for each pulse or event without much further knowledge. These basic parameters are:

- Trigger Delay
- Pulse Number
- Baseline Offset
- Pulse Height and Peak Position
- (Plain) FWHM of Baseline
- Peak Onset
- Peak Position - Onset
- Risetime
- Decaytime
- Right - Left Baseline
- Integral over PH
- Baseline Gradient

- Pile-up Voltage/RMS and Pile-up Time Width
- Delta Voltage (-)/RMS
- Testpulse Amplitude
- Heater Demand
- Deadtime and Live Time
- Event Number
- Time since Start
- Trigger Amplitude (Continuous Acquisition only)

A detailed description of the basic pulse parameters can be found in appendix B. A simplified version of the C++ code used for their calculation is included where applicable.

Furthermore, there are the energies reconstructed for the pulse signals in the different channels and the "light yield". The energy calibration required for the energy parameters is discussed in section 3.5. The light yield is the ratio between energy detected in the light and in the phonon channel and discussed in more detail in section 3.6.

3.2.2 Template Event Fit and Optimum Filtering Parameters

A crucial part of the analysis is the precise reconstruction of the signal amplitude required for the later energy reconstruction. A good energy reconstruction in turn is an important aspect when it comes to background rejection, thresholds and reliability of results of CRESST detectors.

In a first approximation, the signal amplitude is described by the pulse height parameter (compare appendix B.8). However, there are other parameters which can be calculated which produce much better results. They are based on the knowledge of the expected pulse shape and allow to partially disentangle the noise contribution from the pulse signal.

In section 3.2.2.1 two approaches to obtain the expected pulse shape are introduced. Sections 3.2.2.2 and 3.2.2.3 describe two of the methods that allow to benefit from that knowledge. Section 3.2.2.4 presents how those methods can deal with the issue of non-linearity and saturation in the detector response.

3.2.2.1 Pulse Shape Determination

In the linear region of the thermometer, the pulse shape is fixed by three time constants and the splitting between the thermal and the athermal component (compare section 2.2.3). Those in turn are fixed by detector geometry and thermal couplings, being constant during a measurement campaign. In first approximation, different deposited energies only scale the size of the pulse signal.

The ideal pulse shape that is obtained with the following methods is also referred to as a **standard pulse** for a single channel. The standard pulses of the different channels for one event type together are a **standard event**.

Analytical Model The analytical solution for the pulse shape presented in equation 2.2 can be fitted to recorded pulses to extract the model parameters. Figure 3.2 shows a fit of the calorimetric model to a pulse record from a CRESST-III phonon channel.

The parameters from the analytical models should always be extracted from fits to several pulses, e.g., by averaging the values of each parameter. A plot of the parameter values vs energy/pulse height is a possible way to check if the assumption of an energy independent pulse shape is justified by the data. When the parameters are fixed, the standard event is commonly normalized to a signal amplitude of one.

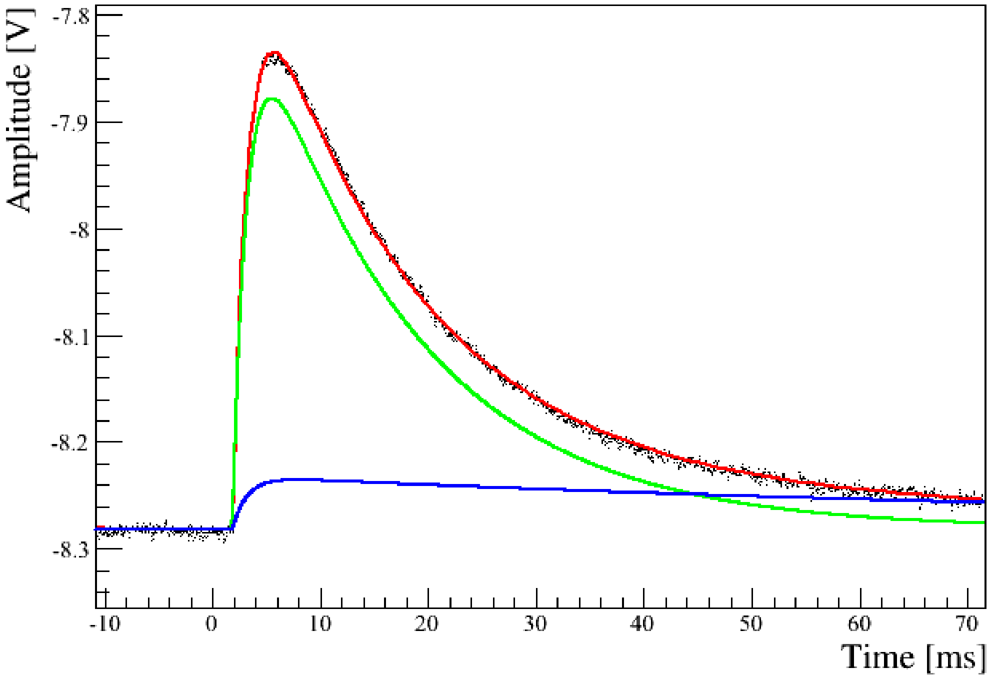

Figure 3.2: Fit (red) of the calorimetric pulse model as given in section 2.2.3 to a phonon channel pulse record of a CRESST-III detector (black dots). The non-thermal component is displayed in green, the thermal component in blue.

Averaging Another method of extracting the pulse shape is averaging over a large number of pulse records. It requires less prior understanding of the expected pulse shape. Assuming the pulse signal in all pulse records is always at the same position, the uncorrelated noise will average towards zero while the pulse signal remains. The standard pulse in this case is not an analytical function but the resulting averaged pulse record, usually normalized to a pulse height of one.

The calculation requires a selected set of artifact free pulses from within the strictly linear region of the detector. Obtaining this list can be ensured by iteratively fitting the pulses in the set with the obtained standard pulse. Those which are badly fitted are then discarded, the standard pulse rebuild and the process repeated.

A brief discussion of the minimum number of events required to build a good standard event by averaging can be found in [114].

Depending on the trigger algorithm, the assumption of a constant position in the record is only justified for events of a single energy. This is due to the so called "trigger walk effect" of threshold triggers. Trigger walk refers to the problem, that pulses of the same shape but different height will reach the trigger threshold at different times relative to their onset, see figure 3.3. In case of the hardware trigger, this leads to a different placement of the pulse in the recorded data. For the software trigger, the position is set in a way that prevents this effect (see [111] for details).

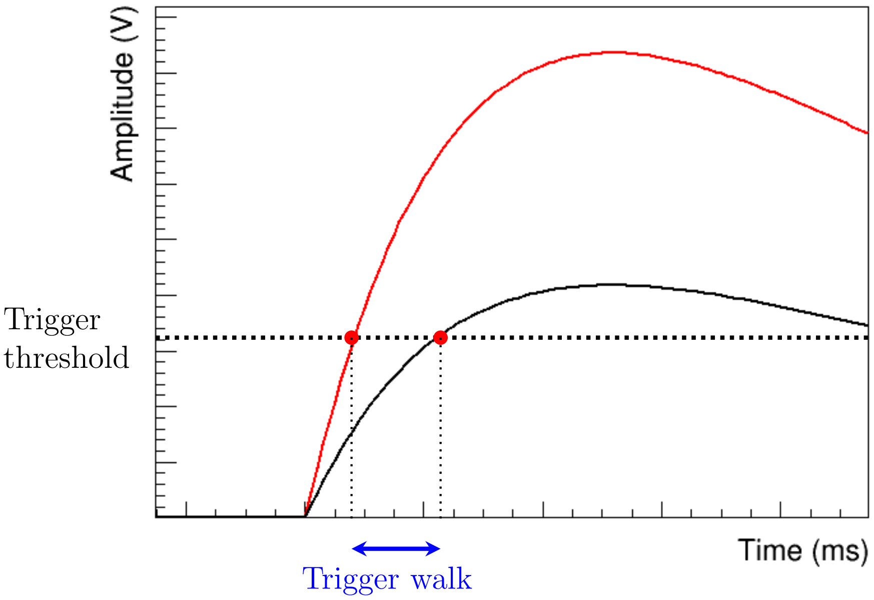

Figure 3.3: A simple threshold trigger suffers from the effect of trigger walk. For pulses with the same shape but different amplitudes the trigger fires earlier for higher pulses. This leads to a systematic error on the position of the pulse if derived from the moment of triggering.

If the hardware triggered data is used and no population of mono-energetic pulses is available in the linear region of the detector, it is possible to try and correct for the trigger walk. To this end, the pulse records are time-aligned by the pulses' onset or peak position parameter before averaging.

In figure 3.4a, an example of the effect of the trigger walk on the standard event is displayed. Figure 3.4b shows a normal pulse record with noise. Figure 3.4c shows a standard pulse extracted from summing over pulses with signal amplitudes similar to the one shown in 3.4b.

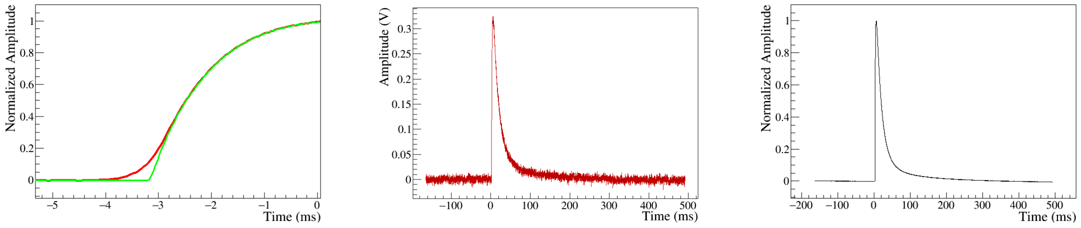

(a) (b) (c)

Figure 3.4: a) Standard pulses build by averaging from a wide energy range with trigger walk effects (red) show a smearing of the onset compared to a good standard event (green). b) An example of a recorded pulse; 3.4c) Standard event build by averaging from pulses of amplitudes comparable to the pulse shown in b.

3.2.2.2 Standard Event Fit

With the standard event at hand the signal amplitude can be extracted by a **standard event fit**. In its most simple form it is a three variables fit of the standard pulse to a pulse record as shown in figure 3.5. The extracted parameters are:

Time shift The time shift is the number of milliseconds the standard pulse has to be moved on the time-axis to align with the fitted pulse signal. Without trigger walk or similar effects, the pulse signal should always be at the same position in the pulse record by definition. This parameter therefore takes a value of zero plus minus the time corresponding to one sample. With trigger walk effects, the position of the pulse signals in the pulse records shifts with pulse amplitude.

(Fitted) offset is the baseline offset that has to be added to the standard pulse.

Fitted amplitude The fitted signal amplitude is, for a unit-normalized standard pulse, the required scaling factor to match the height of the recorded pulse.

(Fit) RMS The fit RMS is the mean squared difference between pulse record and standard event fit. It is a measure for the goodness of the fit.

Baseline model parameters Different baseline models can be included in the fit. They account for deviations from the flat baseline assumption and can improve the resolution of the standard event fit. The baseline model applied in this work is a simple polynomial of third degree. The fitted parameters are the four polynomial coefficients.

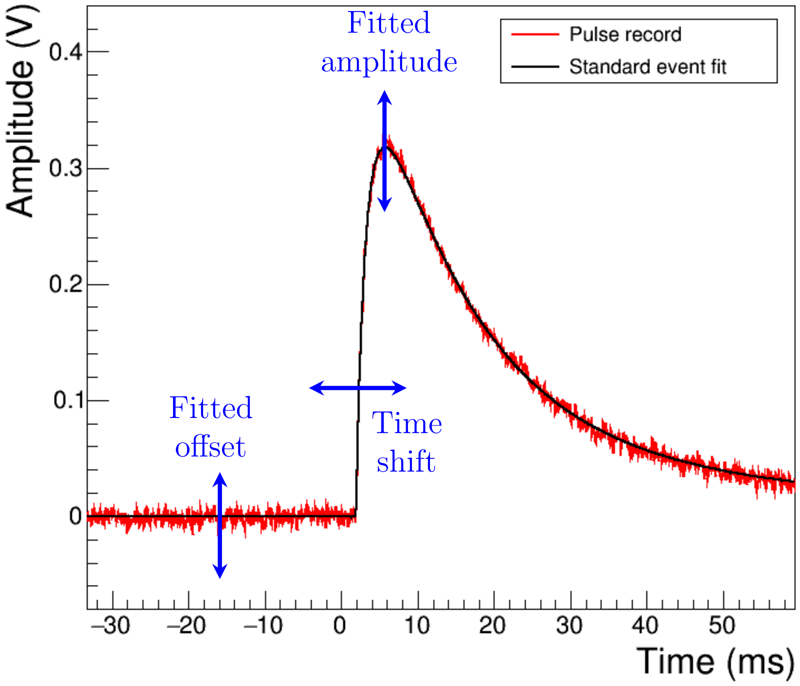

Figure 3.5: Standard event fit, the standard pulse (black) is fitted to the pulse record (red). In total, the fit encompasses three parameters indicated by the blue arrows: The position in time (time shift), the offset of the baseline (fitted baseline offset) and the scaling of the standard event to match the height of the recorded pulse signal (fitted amplitude). An additional model for the baseline can be added, increasing the number of parameters (not shown).

Technically, this fit is implemented in OxRop as a grid search along the time axis. A minimization is performed at different, fixed time shifts and the RMS calculated:

$$RMS_j = \sqrt{\frac{1}{n} \cdot \sum_i [y_i - A_j \cdot s_{i-j} - b(i,j)]^2} \tag{3.1}$$

where j is the time shift in units of samples, n the number of samples, y_i the value of the i-th sample in the pulse record, A_j the fitted amplitude for the given shift j, s_{i-j} the sample value of the normalized standard event at position $i - j$ and $b(i,j)$ the baseline model including the baseline offset. RMS_j is then minimized with respect to j.

If a detector has several channels, the pulses of an event can either be fitted separately or correlated. The separate fitting is done as described above. In case of a correlated fit, the sum of the RMSs of all channels is minimized with respect to a shared time shift:

$$RMS_j^{Co} = RMS_j^1 + RMS_j^2 \quad (+RMS_j^3 + ...) \tag{3.2}$$

where RMS_j^{Co} is the combined RMS and RMS_j^X is the RMS of the X-th channel with fixed, shared time shift j. The fit parameters are then extracted for all channels at the time shift j_{min} where RMS_j^{Co} is minimal. This approach guarantees that pulse signals from the same energy deposition are fitted in all correlated channels. It is especially important in case the pulse signal in one channel is below the noise fluctuations.[1]

3.2.2.3 Optimum Filtering

Another possibility is the use of an optimum filter algorithm as introduced in section 2.4.2. The optimum filter is constructed to optimize the signal to noise ratio on a data stream or data record. It operates in frequency space and re-weights frequencies such that pulse signal like frequencies are amplified and noise like frequencies are suppressed.

Assuming ergodic noise of value $n(t)$ and a pulse signal with a known, normalized pulse shape $s(t)$ and amplitude A, the total recorded detector output $y(t)$ is:

$$y(t) = A \cdot s(t) + n(t) \tag{3.3}$$

The noise power spectrum $N(\omega)$ measures the prevalence of different frequencies in the detector noise:

$$N(\omega) =< \hat{n}(\omega)\hat{n}^*(\omega) > \tag{3.4}$$

where $\hat{n}(\omega)$ is the Fourier transform of $n(t)$, * marks the complex conjugate and $<>$ indicates averaging over a large number of noise samples.

Then, the transfer function $H(\omega)$ of an optimum filter in frequency space is

$$H(\omega) = K\frac{\hat{s}^*(\omega)}{N(\omega)}e^{-i\omega\tau_M} \tag{3.5}$$

with $\hat{s}^*(\omega)$ the complex conjugate of the Fourier transform of the pulse shape, a normalization constant K and a phase τ_M that corresponds to a time shift. $H(\omega)$ basically re-weights frequencies by their signal to noise ratio.

For convenience, the normalization constant K can be adjusted such that in time space the amplitude of the pulse is preserved. Similarly, τ_M can be chosen such that the filtered pulse is in a specific position relative to the original pulse in time space. The optimum filter does not conserve the pulse shape. The filtered pulse is symmetrical in time, extending to before the actual start of the signal. For the white noise case, it forms a somewhat triangular cusp or spike, for the non-white noise the exact shape depends on the noise power spectrum. An example of a standard pulse from this work in normal and filtered form is shown in figure 3.6.

The optimum filter excels in the case of non-white noise compared to other methods of amplitude reconstruction. In the case of white noise, other methods

---

[1] This method requires the standard pulses of the standard event to have the correct relative alignment to each other. This is usually guaranteed by building the standard pulses of all channels from the same set of events.

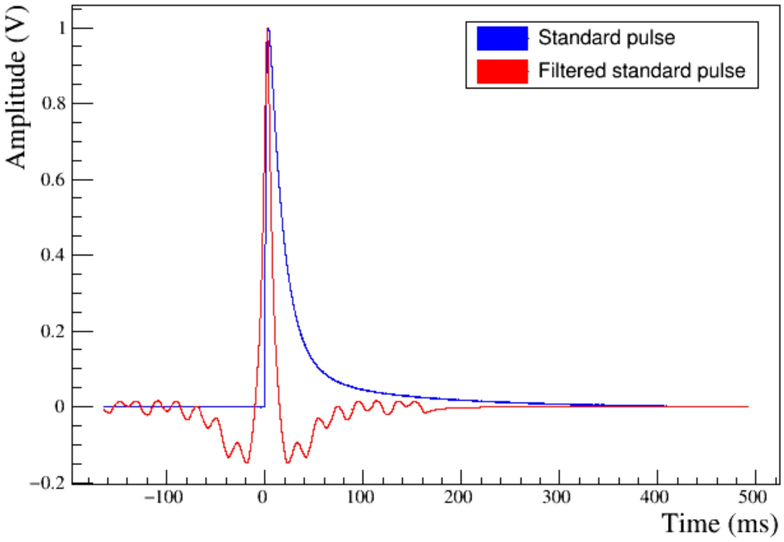

Figure 3.6: Example of an optimally filtered standard pulse. The wiggles are a result of the non-white noise. If the filter was calculated from perfect white noise it would only show one symmetric cusp.

like the standard event fit are equivalent or mathematically identical. More details concerning the derivation of the optimum filter can be found in [115][116], more technical details and performance studies for its application in CRESST in [111].

Calculating the optimum filter for a detector channel requires knowledge of the pulse shape and the noise power spectrum. The pulse shape is known from the standard pulses. The Fourier transform of an ideal pulse can even be analytically derived from equation 2.2 and the Fourier transform of a one sided exponential $\mathcal{F}(e^{-ax}|_{x>0}) = \frac{1}{\sqrt{2\pi}(a+i\omega)}$. The corresponding power spectrum numerically calculated from a real standard pulse is displayed in blue in figure 3.7.

The required noise power spectrum can be obtained by averaging over the noise power spectra of a selected[2], large set of empty baselines. A typical power spectrum of the noise can be seen in figure 3.7. Dominating components are a $\frac{1}{f}$ noise at low energies, a flat spectral contribution at medium energies with peaks for example at the 50 Hz of the electric power grid, and a cut off due to the installed low pass filters at higher frequencies.

The parameters in this work that are calculated from applying the optimum filter to the pulse records are:

(Filtered) amplitude For a correctly normalized optimum filter, the filtered amplitude is just the maximum sample value in the record after filtering. This

---

[2] Empty baselines are commonly recorded at random in CRESST, hence, they can contain pulse signals. Therefore, a careful selection is required to remove those.

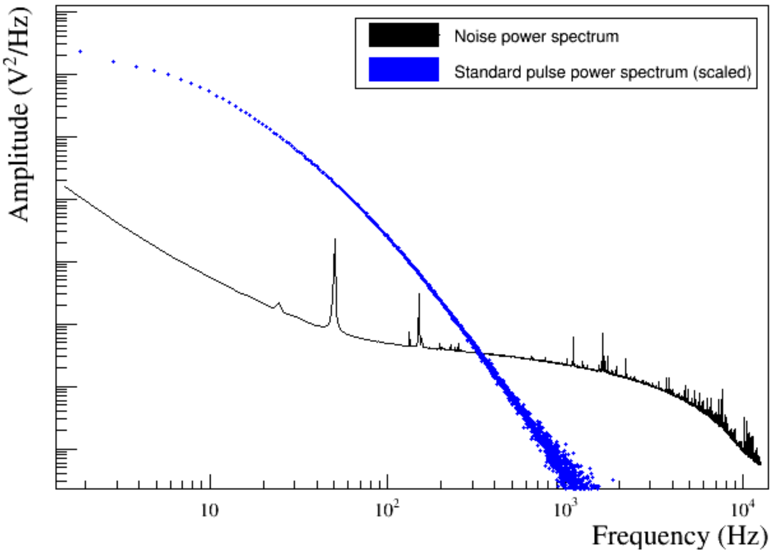

Figure 3.7: Example for a noise power spectrum (black) and a pulse power spectrum from a CRESST-III phonon channel. Spectra are arbitrarily scaled to fit in one plot.

parameter is taken as the estimator of the signal amplitude for the later energy reconstruction as well as for the software triggering when applying the filter to the data stream.

Filter RMS The filter RMS is the root mean squared difference between the filtered pulse record and the filtered and scaled standard event. The effects of the noise are suppressed compared to the standard event fit RMS. Therefore, the filter RMS is more sensitive to pulse shape differences.

(Filter) local RMS Changing noise conditions were observed in CRESST-III. Therefore, the RMS based on the whole pulse record loses some of its discrimination power for pulse shape deviations. This affects both, the standard event fit and the optimum filter. The pulse shape information for the filter is concentrated around the sharp peak. Hence, a less noise-sensitive local RMS can be calculated from just the samples around this peak.

Filtered minimum (MinOF) The filtered minimum is the minimum in the filtered pulse record. The first and last samples in the pulse record are excluded (500 samples in this work). This exclusion is required to prevent artifacts from the discontinuity caused by the filter assuming the pulse record is a periodically repeating signal (see [111]). There are two effects that can lead to an increased MinOF value. First, deviations from the expected pulse shape that lead to a distorted filter output. Second, any features in the pulse record with a fast, negative flank.

3.2.2.4 Linearity Limitations

The described methods only work in the linear range of the detector where the pulse shape is constant. Practically, this condition is often only fulfilled for small energies up to a few keV or less. Above, the slope of the TES transition decreases, reducing the sensitivity. For high enough energies, it reaches the normal conducting phase where the resistance remains about constant (compare section 2.3.1). Pulses of one detector but from different energy ranges are shown in figure 3.8 fitted by naively applying the standard event fit. Figure 3.9 shows the behavior of the optimum filter that reproduces the saturation amplitude instead of the true signal amplitude.

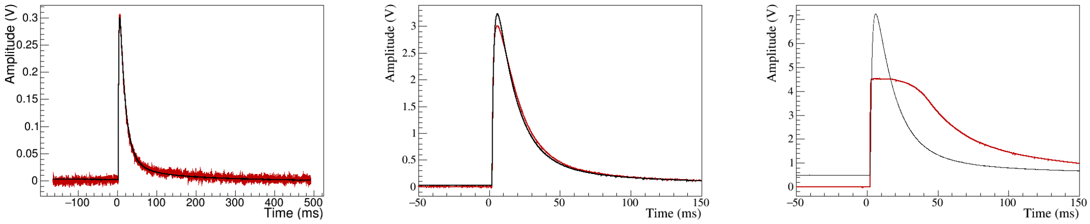

(a) (b) (c)

Figure 3.8: Standard event fit and saturation. a) Standard event fit (black) to a pulse (red) in the linear range. b) Standard event fit to a pulse in the non-linear range. The pulse shape no longer matches. c) Standard event fit to a saturated pulse. The standard event fit fails to reproduce the signal amplitude.

Several approaches are possible to nonetheless extract the true signal amplitude. Methods applied in this work are based on truncating the fitted event above the linear range which is described in the following. Another method, based on analytically including the saturation in the fit, has been successfully applied in [117].

Truncation The standard event fit in its most simple form has only three parameters. It can therefore already be fixed with three points. Conceptually one in the baseline for the offset, one in the rising flank for the position/onset and one in the falling flank to fix the scaling/amplitude of the standard pulse. Hence, it is possible to perform the fit only on the part of the pulse record that stems from the linear part of the transition. This is called a **truncated standard event fit**. Figure 3.10 shows an example of the truncated fit for a pulse in the non-linear range. To find the truncation limit, a standard event is build from the clearly linear regime. Then, a standard event fit is performed without truncation. A good choice for the truncation limit is slightly below the amplitude at which the fit RMS of this fit starts to increase (see also [100]).

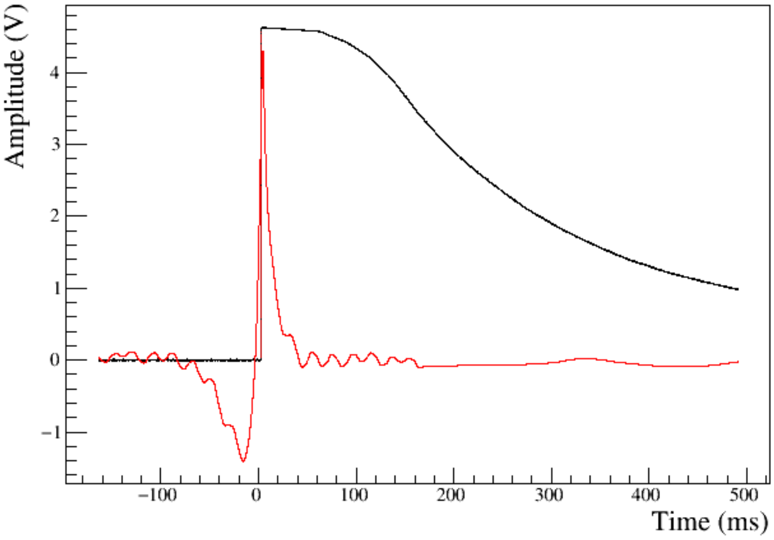

Figure 3.9: Saturated pulse raw (black) and optimum filtered (red). The optimum filter reproduces the saturation amplitude, not the signal amplitude. Furthermore, the filtered pulse is strongly asymmetric.

Optimum Filter and Saturation The optimum filter works in frequency domain. Hence, it is not possible to remove the samples during the time the detector is outside of the linear region. It is possible to combine the truncated fit and the optimum filter as will be discussed in the dark matter analysis in chapter 5. However no reliable standard method has been established for the CRESST analysis yet.

Electro-thermal Feedback Problem The bias current going through the TES as part of the SQUID based read-out results in an ohmic heating power due to the TES' resistance. This heating power increases with increasing resistance, e.g., when the TES heats up because of a particle induced pulse. This effect acts similar to a fixed change of the thermal couplings and thereby the signal pulse shape and is automatically included in the standard pulse. It is extensively discussed in [118]. However, for pulses that reach the strongly non-linear or saturated region, the electro-thermal feedback is capped as the resistance does not change anymore. This implies, that the effective thermal couplings and thereby also the underlying signal pulse shape is different while the pulse is in the saturated regime. The truncated standard event fit described above is not capable of compensating this effect as it assumes a constant underlying signal pulse shape.

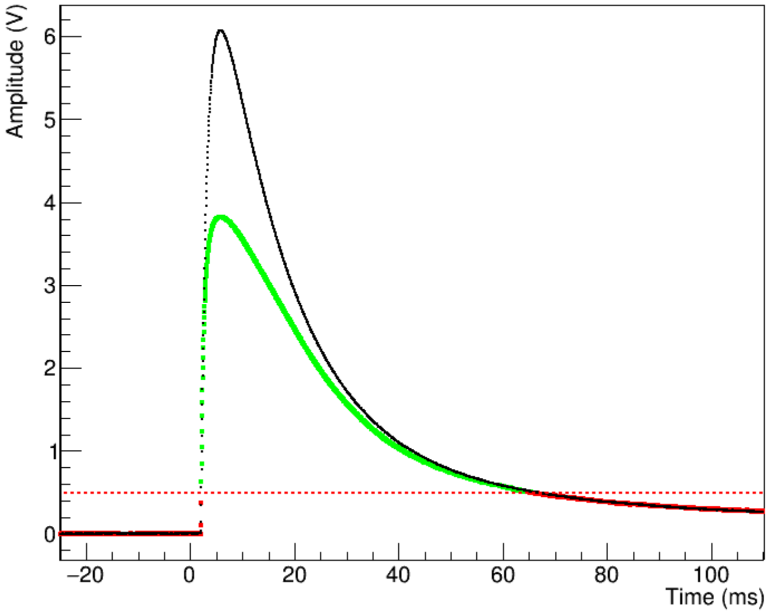

Figure 3.10: Truncated standard event fit. The fit (black) only takes into account the data points from the linear region of the detector (red) and ignores those above (green). It can thereby recover the underlying signal amplitude. The truncation limit at 0.5 V is marked by the red dashed line.

3.2.3 Simulation related Parameters

The data simulation techniques are discussed in section 3.4. For completeness, the associated parameters are listed in the following. In general, the simulation is done by adding a scaled standard pulse to empty baselines or the data stream.

Simulated amplitude The simulated amplitude is the signal amplitude that the standard pulse is scaled to. This is usually directly proportional to the simulated energy.

Simulated energy The simulation can take the time dependence of the detector's response function into account. In that case, converting simulated amplitude to simulated energy is not straight forward anymore. Therefore, the simulated energy is saved as an additional parameter.

Simulated timestamp The absolute time stamp in Unix time of the simulated event.

Time difference to simulation (continuous acquisition only) Time difference between the trigger and the actual position of the simulated event for the continuous simulation. If the trigger fired on the simulated signal pulse, this usually corresponds to $0 \pm 1 sample$. A difference above a few milliseconds means that the trigger triggered on something else, but the simulated event is still within the time window of the record.

3.3 Data Selection

In this section a number of selection criteria are discussed that remove part of the data that is irrelevant or harmful to the analysis. In subsection 3.3.1 selection criteria that operate on time periods or whole data files are presented. Subsection 3.3.2 introduces a number of selection criteria that operate on an event by event basis and targeting artifacts, e.g., introduced by the read out electronics. Finally, in subsection 3.3.3 selection criteria are presented that are capable of removing background events caused by a particle or particle-like energy depositions.

3.3.1 Preselection on Files and Time Periods

3.3.1.1 Bad Files

For each data file, information about earthquakes and other possible disturbances as well as problems with the data acquisition is stored. All files with recorded problems are discarded. Furthermore, files that are less than a few hours long are removed as the number of recorded heater pulses of different amplitudes is too low for a reliable energy calibration (compare 3.5.3).

3.3.1.2 Training and Blind Set

To avoid subjective bias in the analysis, CRESST data is usually split into a **training set** and a **blind set**. The training set contains a smaller, but representative fraction of the full data set. The blind set contains the remaining data. The analysis with all the steps described in this chapter is then defined looking at the training set only. Afterwards it is applied "blindly", i.e., without further changes, to the blind set. The final analysis results are then only based on the blind set.

The motivation for defining the data analysis on a subset of real data is that CRESST detectors tend to show a very individual behavior, depending strongly on small differences in manufacturing and working conditions. Hence, defining the analysis steps in a more generalized, automated way or based on simulated data would largely produce inferior or unreliable results compared to the method described above.

3.3.1.3 Rate Cut

Radioactive backgrounds and dark matter are expected to produce a constant rate of events in the detector. Time periods where the detected event rate is significantly above the average rate can be caused by e.g. electrical or mechanical disturbances. The safest approach in this case is to discard those periods. To that end, the data is binned in time and all bins that exceed a certain number of events are removed. Furthermore, the bins adjacent to removed bins are discarded as well. An example is shown in figure 3.11a.

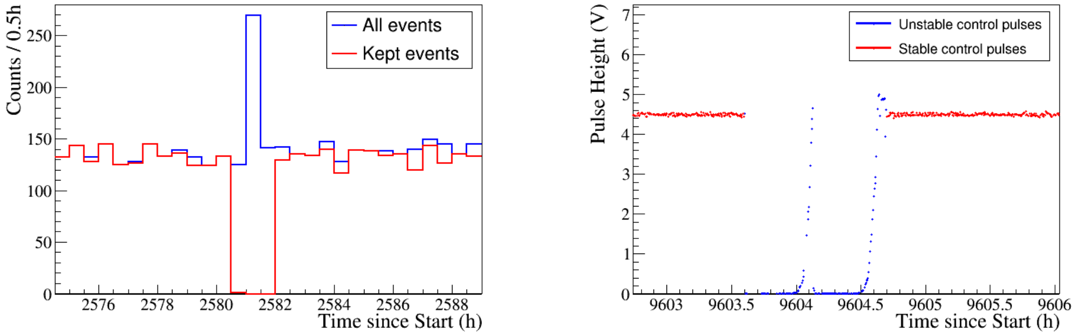

(a) (b)

Figure 3.11: a) Event rate over time before (blue) and after (red) application of the rate cut and the stability cut. The rate cut removes the time period with increased rate in the center as well as the events in the 0.5 h bins before and after. b) Pulse height of control pulses vs time. Periods where the pulse height deviates too far from the set-point get removed (blue).

3.3.1.4 Stability Cut

The resistance value of the TES in their transitions is periodically monitored and stabilized (compare section 2.3.1.2). If a TES is not actively stabilized with the help of control pulses, the baseline position or noise can be monitored instead.

In any case, stable operation and a constant detector response cannot be guaranteed in periods where the monitoring variable deviates from its set point or is not available. Therefore, those periods are removed by the stability cut, see figure 3.11b for an example.

3.3.2 Selection Criteria for removing corrupted Pulses

There are several classes of pulses and events that cannot be analyzed properly. Those can, e.g., be electronic artifacts, suffer from distortion related to the readout, or, in general, not be produced by a particle interaction. Those are called **corrupted events** in the following. The ones relevant for this work and the data selection criteria to remove them are presented in this section. Similar compilations can be found in, e.g., [114], [100] and [107].

3.3.2.1 Decaying Baselines

Decaying baselines are caused from very high energy pulse signals. Those pulse signals have a decay much longer than one or two record windows. A common cause for decaying baselines in the presented measurement campaign are the control pulses for the stabilization (compare section 2.3.1.2). For the hardware trigger this means that the detector output is still above threshold when the trigger is rearmed after recording a pulse record. Therefore, it will trigger again immediately, recording the decaying tail of the pulse. For the software trigger on the continuous data something similar happens with the moving search window [111].

Decaying baselines can be removed by a selection on the peak position. Their highest samples will be around the start of the pulse record while real pulses have their highest sample close to the start of the post-trigger region. Another option is a selection on the right - left baseline parameter. Decaying baselines have a strongly negative right - left baseline values while pulses with a good pulse signal can be found around zero. An example is shown in figure 3.12.

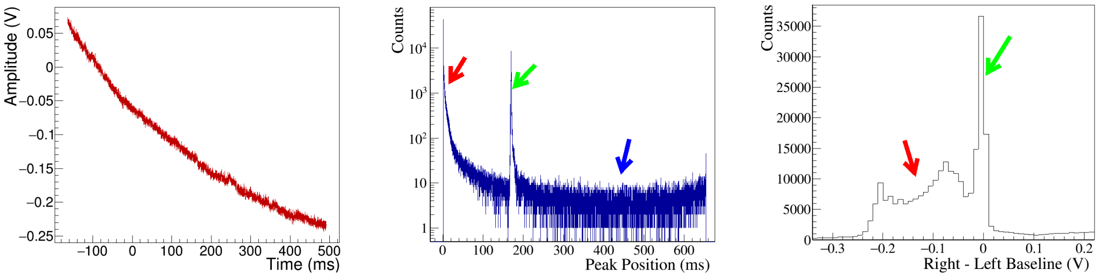

(a) (b) (c)

Figure 3.12: Decaying baselines and possible identification by peak position and right - left baseline. a) Example of a decaying baseline in the phonon channel. b) Peak position spectrum of a software triggered neutron calibration campaign. Decaying baseline have their highest sample at the start of the record (red arrow) and good pulses around the trigger position (green arrows). Pulse records without a significant pulse signal in the investigated channel have a random peak position from the baseline noise (blue arrow). c) Right - left baseline spectrum of the same measurement. Decaying baselines appear at negative values (red arrow) while good pulses and records without a pulse signal form the peak around zero (green arrow).

3.3.2.2 Flux Quantum Losses and SQUID Resets

The flux quantum losses (FQLs) of the SQUID introduced in section 2.3.2 appear as a drop in the baseline value by a fixed voltage per flux quantum. The related SQUID resets show up in the output as a sharp jump of the baseline by around 10 V.

Pulses with an FQL in the pulse record cannot be reconstructed without significant additional effort. Therefore, they are usually discarded. SQUID resets will trigger but are pure artifact events that have to be removed. Both can be identified with the right - left baseline parameter as they do not return to the original baseline. Hence, their right - left baseline value deviates substantially from zero.

Example events and a right - left baseline spectrum are shown in figure 3.13. A loose selection on the peak position against decaying baselines has been applied beforehand to improve the visibility of the relevant event populations.

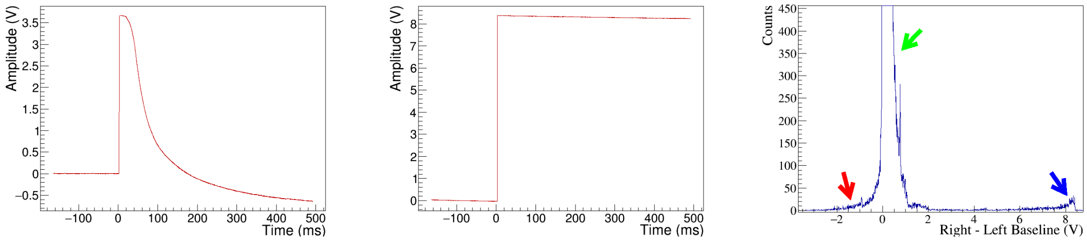

(a) (b) (c)

Figure 3.13: a) Pulse record with a flux quantum loss. The pulse returns to a lower baseline value. b) A SQUID reset, appearing as a 8 V to 10 V jump in the baseline value. c) Right - left baseline spectrum with decaying baselines already removed by a peak position cut. FQLs appear at values below zero (red arrow), good pulses around zero (green arrow) and SQUID resets as a peak at a high value usually around 8 V and 10 V.

3.3.2.3 Delta Spikes

Presumably some switching process in the data acquisition electronics can cause negative “spikes” in the detector output. Those spikes are a few samples long with negative amplitudes clearly outside the detector noise. Due to their timescale and negative excursion, they cannot be related to any physical effects in the detector module. The delta voltage / RMS parameter (compare appendix B.18) was specifically designed to remove those events. This is shown in figure 3.14.

3.3.2.4 Early Pulses and Pile-up

The hardware trigger has a certain dead time after recording a pulse where the transient recorder has to get enough samples for a new pre-trigger region. A pulse signal starting within this window triggers as soon as the trigger is rearmed. In this case, the trigger position does not match the onset of the pulse. As a result, the pulse will not be centered in the pulse record, but appear in the pre-trigger region. This leads to a wrong calculation of several parameters. A related effect is pile up, where two or more pulse signals appear within one record window. This also leads to wrong parameter calculations.

There is no single selection criterion to remove all of these pulses. Parameters that are sensitive to them are peak position, right - left baseline and the pile-up

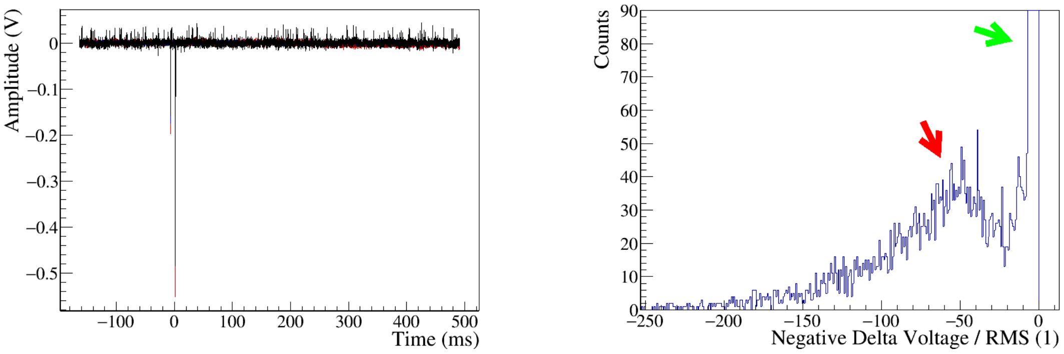

(a) (b)

Figure 3.14: Removal of negative, electronic delta spikes. a) Example of a spike. b) The negative delta voltage / RMS parameter allows to identify the spikes. Pulses without spikes form the peak close to zero (green arrow) while spikes appear at strongly negative values (red arrow).

voltage. Furthermore, they can be partially identified in a 2D plot of fitted or filtered RMS vs fitted amplitude or pulse height. Figure 3.15 shows examples of those events.

3.3.3 Background and Veto cuts

There are a number of events induced by particle or particle-like energy depositions that can be identified as not being caused by a nuclear recoil of dark matter in the main absorber crystal. Removing these events simplifies the analysis and can improve the sensitivity to a possible dark matter signal. Some of these events are related to the detector design, e.g., the carrier events of CRESST-II that are extensively discussed in [100]. They often show a different pulse shape than the sought for recoils in the main absorber. Another option arises from dark matter not being expected to deposit energy at multiple sites of the setup at once due to its small interaction probability. In combination with the overall low event rate of CRESST detectors, this allows to reject some backgrounds that do deposit energy at multiple sites. It can be implemented as an anti-coincidence or veto selection.

3.3.3.1 RMS

Events with a pulse shape that differs from the pulse shape of the standard event have higher RMS values. They can be targeted by a 2D selection in the RMS vs fitted/filtered amplitude plane. The 2D information is required, as the RMS also depends on the amplitude. If the pulse shape deviations are pronounced enough, the standard event fit may fail. In this case, however, discrimination by other parameters is typically possible.

Depending on the available amount of events in the training set, the RMS selec-

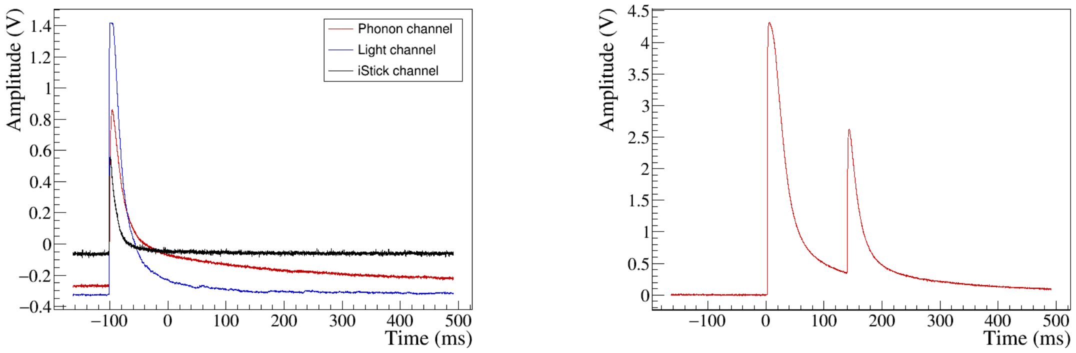

(a) (b)

Figure 3.15: a) Early pulse, the pulse onset is not around zero but in the pre-trigger region. The baseline offset for the automatic offset subtraction in the plot is therefore calculated incorrectly. b) Pile-up event, several pulse signals appear in one pulse record.

tion can be automated to produce more reliable and uniform results than a manual selection, see [107].

Pulse shape deviations of background events are mainly expected if the primary energy deposition was not by a particle in the main absorber crystal.

3.3.3.2 Muon Veto

Plastic scintillator muon veto panels are installed around the shielding of the CRESST setup, see section 2.1. Events which appear in coincidence with a signal in the muon veto are discarded. The size of the required time coincidence window mainly depends on the time resolution of the cryodetector as discussed in [107] and [100]. In general, the rate of events in the muon veto is dominated by radioactive backgrounds from within the panels and the surrounding materials.

3.3.3.3 Coincidence with other Detector Modules

Events occurring in coincidence between multiple detector modules can be discarded. The chance of a dark matter particle scattering in more than one detector is completely negligible. For CRESST-III, the solid angle around a detector covered by the other detectors is small. Hence, this selection is not very relevant. Different configurations, as, e.g., proposed for the CRESST derived $\nu-$cleus detector [119] can veto surface events and neutrons in that way.

3.3.3.4 Instrumented Holder Parts

It is possible to instrument different parts around the target crystal. This way, events that deposit energy in there can be discarded. An example in CRESST-III are the instrumented holding sticks.

3.4 Survival Probabilities

The data selection criteria will also remove some of the events of interest. Additionally, some artifact types are correlated to a certain event type. E.g., FQLs appear only for high energy depositions, which has to be taken into account when they are analyzed. Furthermore, also the trigger algorithm will introduce a selection and deadtimes. This happens independently of whether it is realized in hardware or software.

All data selection effects have to be considered for a quantitative statement about measured event rates and spectra. The effects are combined in the survival probability which states the chance that an occurring event of the type of interest appears in the final data set after triggering and application of all data selection criteria. The main approaches to estimate the survival probability are summarized in the following.

3.4.1 Life and Dead Time Estimate

The classical approach for the hardware triggered data was to split the whole measurement time into an effective live time and dead time. Dead time in a first step are the time intervals the DAQ was not ready to record a new, incoming pulse signal, e.g., because the trigger was still disarmed from a previous one. This is what is recorded in the live time and dead time pulse parameters (see appendix B.20). Furthermore, selection criteria that remove time periods, e.g. the rate and stability cut, remove live time and introduce dead time accordingly. The exact calculation of the live time is discussed in [120].

3.4.2 Event Simulation - Hardware Trigger Data

The live and dead time calculation described above is not capable of measuring the effect of data selection criteria that do not remove time periods but events of interest on an event by event basis. Therefore, the **event simulation** method was developed and applied in [107].

During the data taking, the trigger is periodically fired by the DAQ. The data acquisition then records an empty baseline.

The shape of a pulse signal is known from the standard event. A scaled version can be added to the pulse records of the empty baselines to create simulated pulses with an ideal shape and realistic noise (see figure 3.16). The scaling has to be done according to the desired simulated energy.

The set of simulated events is then subjected to the same selection criteria as the measured events. The survival probability is calculated as the ratio of the number of events after selection criteria and the total number of simulated events. It is then assumed to be the same for real events of the simulated event type.

If the survival probability is energy dependent, the simulation is performed for various discrete energies and the survival probability interpolated in-between with an appropriate function.

This empty baseline based survival probability has to be taken into account in addition to the live time reductions considered in the previous section.

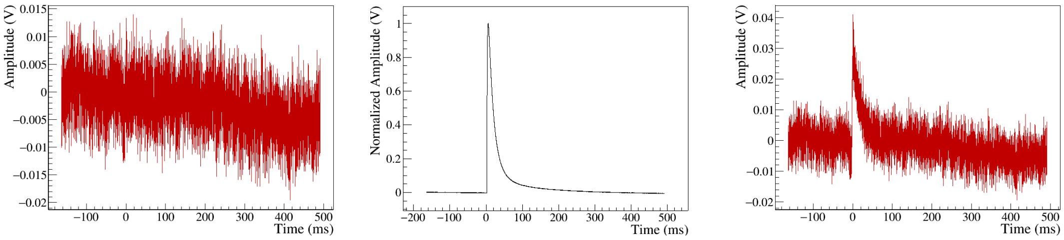

(a) (b) (c)

Figure 3.16: Simulation of pulses. An empty baseline or a random position in the continuous data stream is chosen (a). A standard event (b) is scaled to the amplitude matching the simulated energy. The standard event is added to the empty baseline or stream to create an artificial pulse record (c).

3.4.3 Continuous Simulation - Continuous Data

The combination of dead time calculations and event simulation is a rather complex way to estimate the different selection effects. The availability of the complete stream from the continuous acquisition offers a more simple approach that can cover all relevant aspects at once.

In the **continuous simulation**, the scaled standard pulses are superimposed at random positions on the data stream before it is fed to the trigger algorithm. Care is taken that the simulated events cannot pile up with each other. The triggered simulated events then undergo the complete data analysis pipeline. That way all possible selection effects except for correlated artifacts like FQLs are included.

This method has several advantages:

- The trigger efficiency is automatically included
- Random positioning on the full stream means that any dead times are automatically included and don't have to be calculated separately
- The number of simulated events is not limited by the number of available empty baselines
- All time-varying conditions are naturally included as they are present in the data stream.

3.5 Energy Calibration

Several parameters that estimate the signal amplitude are available. To convert them to energy, a calibration measurement with one or more radioactive sources is performed

The energy calibration could be done linearly if the signal amplitude was perfectly reproduced by the parameters, within the limitations of the energy resolution. The reconstructed signal amplitude would just be multiplied by the the calibration factor obtained from one of the radioactive lines. In practice this is often not the case and and more robust approaches are described in sections 3.5.2 and 3.5.3, while section 3.5.4 tackles the issue of a time dependent detector response.

3.5.1 Energy Calibration Sources

Two radioactive sources are commonly used for calibrations in CRESST, $^{57}_{27}$Co and $^{55}_{26}$Fe. The presence of copper all around the detector modules means that also copper X-rays are potentially available. Furthermore, internal radioactive lines can serve as fix points for the energy calibration, e.g., in this work, the cosmogenic activation lines of tungsten:

$^{57}_{27}$Co decays via electron capture to an excited state of $^{57}_{26}$Fe. It subsequently relaxes to ground state by emitting γ radiation of 136.5 keV or 122 keV and 14.4 keV. The 14.4 keV γs are not capable of penetrating the cryostat's walls. The 136.5 keV and 122 keV will produce photo-peaks and a contribution from Compton scattering towards lower energies [114]. Additionally several X-ray escape peaks from tungsten are expected for a $CaWO_4$ target between 50 keV and 90 keV. In this case the X-ray leaves the detector without being detected and the remaining energy is the 136.5 keV or 122 keV minus the characteristic X-ray energy.

The decay scheme is shown in figure 3.17. A detailed measured and labeled spectrum for a $^{57}_{27}$Co calibration in $CaWO_4$ can be found in [114]. A copy of it has been added in appendix C for convenience.

$^{55}_{26}$Fe decays to $^{55}_{25}$Mn via electron capture. During the subsequent relaxation to ground state, X-rays of mainly 5.9 keV and 6.49 keV are emitted [122]. These are too low in energy to penetrate the walls of a cryostat. Therefore, the source has to be installed on the inside, close to the detectors.

Copper Fluorescence In most designs, the detector is surrounded by copper surfaces either of the cryostat or of the detector module itself. Photoelectron excitation by high energy γs close to the surface leads to X-rays being emitted by the copper. The dominant characteristic copper lines are at 8.048 keV ($K_\alpha 1$) and 8.028 keV ($K_\alpha 2$) [123, 124], appearing as a single peak due to the resolution of the detector.

Cosmogenic Activation Lines of Tungsten The ^{182}W in the $CaWO_4$ target crystals can be activated by proton capture from cosmic radiation followed by an α decay. The resulting ^{179}Ta has a half life of about two years [122] and decays via electron capture to ^{179}Hf. The decay energy is carried away by the ν_e. What is

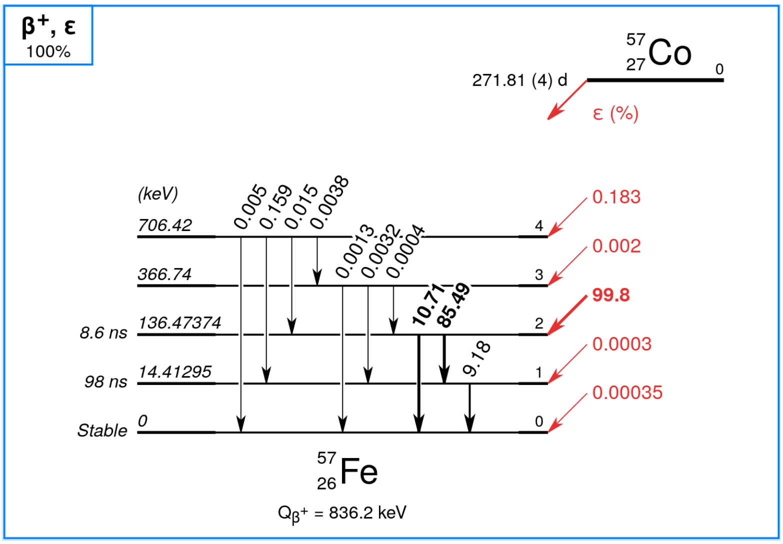

Figure 3.17: Decay scheme of $^{57}_{27}$Co. The $^{57}_{27}$Co decays into an excited state of $^{57}_{26}$Fe with subsequent deexcitation emitting 136.5 keV or 122 keV gammas. Decay scheme taken from [121].

visible in the detector is the full binding energy in ^{179}Hf of the captured electron. Depending on the captured electrons, this can be 2.6 keV (M_1), 10.74 keV (L_2), 11.27 keV (L_1) or 65.35 keV (K) [125].

The signature of the Ta decay has been clearly identified in a previous CRESST measurement [126]. Further details concerning cosmogenic activation backgrounds can be found in [127].

3.5.2 Peak Based Calibration

A peak based calibrations is possible if there are enough calibration lines available. In this case, an appropriate function can be fitted to energy vs reconstructed signal amplitude of the calibration lines. Standard choices are a polynomial or a spline. This method has the advantage that the events from the calibration lines are of the same type and undergo the same treatment as the events of interest. This way, systematic errors are the same for calibration and physics data.

3.5.3 Heater Pulse Based Calibration

The calibration can also be based on injected heater pulses. To this end, heater pulses of different energies are injected via the ohmic heaters installed with the TES. They map out the detectors response. With the heater pulses available, the heater pulse based calibration consists of two steps. First, the detector response is linearized against the heater generated pulses. Second, the proportionality factor between the linearized response and the deposited energy is determined from a calibration measurement for particle induced events.

For the linearisation a constant resistance is assumed for the ohmic heaters. The injected heater power is then given by

$$P(t) = U(t)\dot{I}(t) = R \cdot I(t)^2 \tag{3.6}$$

and the injected energy by the corresponding integral over time. The square in equation 3.6 is compensated by a square root in the electronics as shown in section 2.3.3. That way, a simple, linear scale is obtained between the chosen control voltage and injected energy. The DAC amplitude in V of the injected heater pulse is saved in the testpulse amplitude (TPA) parameter. The TPA is then directly proportional to the injected energy.

The TES transition is then mapped out and fitted in terms of TPA vs (reconstructed) signal amplitude of the heater pulses, see figure 3.18. To get the energy of a particle energy deposition, first, its reconstructed amplitude is plugged into this response function (green arrows). That way, a TPA value is calculated, that would produce the same signal amplitude. Thus, for each particle pulse, a parameter directly proportional to energy, the **equivalent TPA** is obtained.

The factor converting equivalent TPA to deposited energy of a particle interaction (orange arrow) is called the **CPE factor** [107, 114]. It is directly available from applying this procedure once to events of a known energy from a calibration source. [3]

3.5.4 Dealing with Time Dependencies

Despite the detector stabilization presented in section 2.3.1.2 and the application of a stability cut to the data as presented in section 3.3.1.4, the detector response varies with time. Figure 3.19a shows an example of the reconstructed signal amplitude of injected heater pulses vs time for a detector that is analyzed in chapter 5. Similar plots can be found e.g. in [114] and [107].

These variations are of systematic nature, i.e., they shift the mean signal amplitude. Therefore, the mean response to a calibration source or the heater pulses over the course of a full measurement is not a good basis for applying the calibration methods discussed above.

Instead, the signal amplitude of the calibration lines or heater pulses is evaluated at the time of each particle interaction. This can be done with an interpolation in measured signal amplitude vs time as shown in figure 3.19b. This interpolation is done for each calibration line or heater amplitude. It contains a locally averaging component to take the resolution into account, as well as a removal system for unphysical outliers. With the time-interpolated amplitudes available, the response function as described in section 3.5.2 can be obtained for each event separately at

---

[3] Heater and particle pulses have very different pulse shapes. The same energy deposition from event types with different pulse shapes may not yield the same signal amplitude. Hence, the CPE factor is only valid for events with the same pulse shape as the employed calibration events.

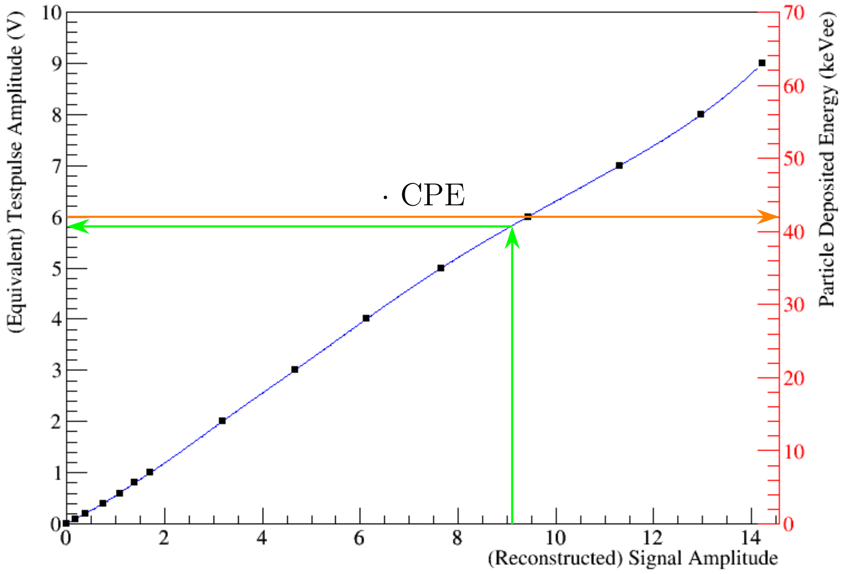

Figure 3.18: Heater pulse based energy calibration. The detectors response to a temperature change in the TES is mapped with the help of heater pulses (black squares) and interpolated by a spline (blue line). The testpulse amplitude is directly proportional to the injected energy. For each particle event, the corresponding heater input that would cause the same signal amplitude is calculated by the spline (green arrows). The thus obtained equivalent testpulse amplitude is directly proportional to deposited energy and the proportionality factor (CPE factor, orange arrow) can be determined from a calibration measurement with known energy.

the correct time. This way, time dependencies can be compensated and the energy resolution is improved.

The interpolation function applied in this work is a spline with its smoothing optimized as described in [107].

3.5.5 Energy Calibrating in the Presence of Scintillation Light and a Light Detector

3.5.5.1 Phonon Anti-quenching

As introduced in section 2.2.1, CRESST uses scintillating crystals as the main target for its particle detectors. The relative amount of scintillation light depends on the type of interacting particle.

For $CaWO_4$ around 5 % to 10 % of the deposited energy of electron or γ interactions is converted to scintillation light [128, 83]. Only about a tenth of that value is reached for nuclear recoils. Nuclear recoils, hence, have slightly more energy detected in the phonon channel than β/γ events for the same initial energy

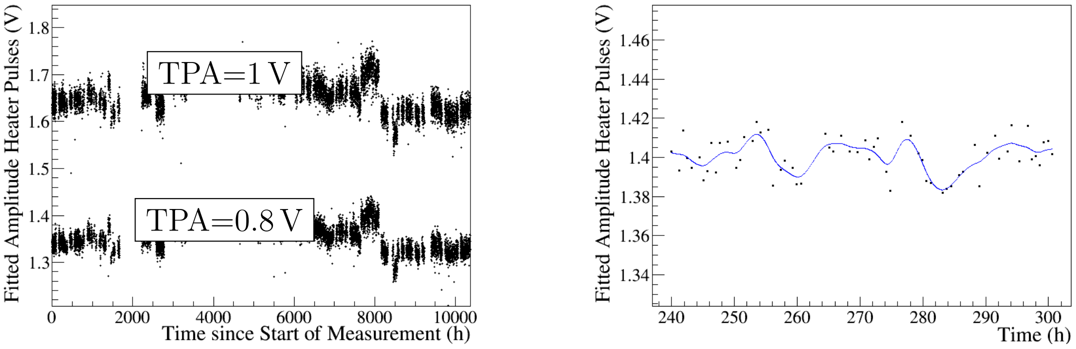

(a) (b)

Figure 3.19: a) Fitted amplitude for injected heater pulses with a testpulse amplitude of 0.8 V and 1 V for a detector analysed in chapter 5. Despite the detector stabilization, the detector response shows systematic changes with time that have to be compensated in an energy calibration. b) The detector response to a given heater pulse power or calibration line is interpolated by a spline. In this way, the detector response can be evaluated at the time of each particle interaction separately.

deposition.

The energy calibration for particle events described above is based on γ calibration peaks, i.e., includes the 5 % to 10 % reduced signal due to scintillation losses. The energy of nuclear recoils is accordingly overestimated by the calibration.

This effect can be corrected to obtain a scintillation light independent energy with the help of the information from the light detector. The energy compensation for the different amounts of energy lost in scintillation light can be calculated as described in [129] and discussed for the application in CRESST among others in [83]. This is referred to as **phonon anti-quenching**.

3.5.5.2 Calibration of the Light Detector

The light detector can be calibrated in either of two ways. First, in terms of keVee, i.e., energy deposition in the main absorber crystal that leads to the observed signal in the light detector. The actual deposited energy in the light detector is much smaller, $\mathcal{O}(1\,\%)$ of the keVee value. It is given by the combination scintillation and detection efficiency for the scintillation light [128]. This method has the advantage that the same events can be used for calibration of the light and the phonon channel. It centers the light yield of the β/γ events at one by definition.

Second, the light detector can be calibrated in terms of absolute deposited energy, analogous to the phonon detector. This requires a suitable calibration source. The light detector is optimized to detect the few percent scintillation light from an interaction occurring in the main absorber crystal. Therefore, a low energy calibration source like $^{55}_{26}$Fe is required in order to be at least close to the linear energy range.

The choice of calibration units only affects the CPE/proportionality factors of the calibration methods described before. All other steps applied are the same as for the phonon channel.

3.6 Light Yield, Band Fit, Particle Identification and Region of Interest

A core feature of the CRESST detectors since the introduction of $CaWO_4$ crystals as target material is the particle identification based on the relative amount of scintillation light. It was introduced in section 2.2.1. With the energy calibration for both phonon and light detector available, the light yield can be calculated and the data displayed in the form of a light yield plot as introduced in figure 2.2.

A phenomenological model for the description of the bands can be fitted to the data as for example introduced in [120, 130] based on the relative position of bands measured in [102]. With the position of the bands available, the region of interest (ROI) for the dark matter limit calculation can be defined. The exact choice of ROI depends on the analysis and the applied limit calculation method. An optimization strategy for the ROI in combination with the so called “Yellin method” for the limit calculation is for example presented in [120]

3.7 Limit Calculation

For CRESST, limits on the dark matter nucleon interaction cross-section have been calculated with two different methods in the past. The first one is the maximum gap/interval method developed by S. Yellin [131] for the calculation of limits in the presence of unknown backgrounds. The other one is the maximum likelihood method that relies on a precise knowledge of the observed backgrounds. The general ideas will be briefly presented in the next sections.

3.7.1 Expected Dark Matter Spectrum

Both the Yellin and the maximum likelihood method require knowledge of the expected observable spectrum of dark matter. The parameters classifying dark matter in the scope of the standard assumptions of direct detection is the mass m_χ and the WIMP-nucleon interaction cross section σ_0 (compare section 1.3.3). The mass influences the expected spectral shape, the cross section scales the number of expected events. From the detector side, the different types of nuclei as well as survival probabilities from data taking and analysis influence the shape of the expected spectrum. In general one can write

$$\frac{dN}{dE}(m_\chi, \sigma, det, E) = \sigma_0 \cdot \frac{d\mathit{\Gamma}}{dE}(m_\chi, det, E) \tag{3.7}$$

where $\frac{dN}{dE}$ is the expected event spectrum, det summarizes the influence of detector and analysis and $\frac{d\Gamma}{dE}$ is the expected spectral shape for a given dark matter mass and detector.

3.7.2 Accounting for Analysis Systematics

To calculate $\frac{d\Gamma}{dE}(m_\chi, det, E)$ the first information required is the expected spectral shape of a dark matter signal in an ideal detector with infinite resolution and zero threshold $\frac{dR}{dE_{True}}(E_{True})$ which can be calculated from theory (compare section 1.3.3.1). Here, E_{True} is the energy actually deposited in the detector by the interaction. For a real experiment, E_{True} is not available and can only be reconstructed within the experimental resolution. This reconstructed energy is labeled E_R in the following.

To compare the expected spectrum and the measured spectrum, the expected spectrum in terms of E_{True} has to be transformed to E_R by including the detector resolution. This is commonly done by a convolution with a normalized Gaussian $G_\sigma(E_R - E_{True})$ with width σ equaling the detector resolution:

$$\frac{dR}{dE_R}(E_R) = \int \frac{dR}{dE_{True}}(E_{True}) \cdot G_\sigma(E_R - E_{True})\, dE_{True} \tag{3.8}$$

However, the final spectrum is also influenced by the analysis, mainly in the form of the triggering and data selection criteria. Therefore, the survival probability $s(E_{True}, E_R)$ of a dark matter event in the analysis is required which depends on both, E_{True} and E_R. This has to be included in the convolution to obtain the spectrum expected from dark matter for the given setup and analysis:

$$\frac{dR}{dE_R}(E_R) = \int s(E_{True}, E_R) \cdot \frac{dR}{dE_{True}}(E_{True})) \cdot G_\sigma(E_R - E_{True})\, dE_{True} \tag{3.9}$$

The most straight forward way to obtain $\frac{dR}{dE_R}(E_R)$ is by simulating the dark matter spectrum $\frac{dR}{dE_{True}}(E_{True}))$ with a sufficient number of events, then applying the full analysis to those events. With correct normalization, the resulting spectrum of reconstructed energies E_R of the simulated events is directly the expected dark matter spectrum. This way no analytical or approximate expressions for $s(E_{True}, E_R)$ or the resolution $G_\sigma(E_R - E_{True})$ is required as it is naturally included. This method is applied with the help of the continuous simulation in the dark matter analysis in this work (compare section 3.4.3 and chapter 5).

Previously, with the hardware triggered data acquisition, not enough events could be simulated to apply this method due to a lack of empty baselines. Therefore, only the E_{True} dependency of $s(E_{True}, E_R)$ was extracted with the help of the event simulation (compare 3.4.2) and $\frac{dR}{dE_R}(E_R)$ calculated numerically from equation 3.9. This method is a good approximation as long as the survival probability only weakly depends on E_R. However, it breaks down when there is a strong dependency on E_R, e.g., at the trigger threshold that removes all events with a reconstructed energy below the set threshold.

This issue is summarized and visualized in figure 3.20 with the example of a normalized dark matter spectrum depositing only a single true energy, i.e., $\frac{dR}{dE_{True}}(E_{True}) = \delta(E_{True} - E^0_{True})$.

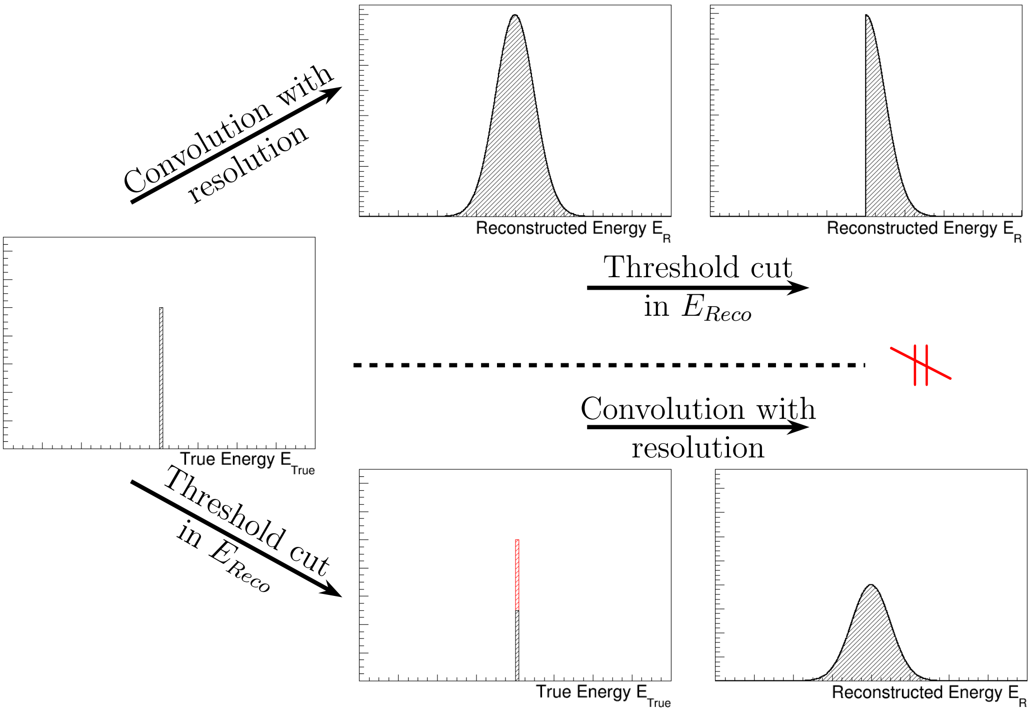

Figure 3.20: Issue with the previously used determination of survival probabilities in CRESST with the example of applying a threshold selection in reconstructed energy E_R to a mono-energetic set of events in true deposited energy E^0_{True}. The threshold is set as $E_R^{Thresh} = E^0_{True}$ for simplicity, hence, 50 % of events are removed. Switching from E_{True} to E_R is done via convolution with a Gaussian of a given resolution σ. If the selection is applied after switching from E_{True} to E_R, the correct final spectrum is obtained (upper half). If the selection is applied first, the information of the dependency on E_R is lost and the final spectrum is not correctly reproduced after the convolution (lower half).

What was previously done is simulating sets of events with discrete values of E_{True}, similar to what is shown for one value in figure 3.20. Those events do have the correct Gaussian distribution in their reconstructed energy and are correctly affected by the analysis which is applied to them. However, what is finally extracted are only the average survival probabilities $\bar{s}(E_{True})$ at the simulated energies E_{True}, integrating over, and losing the information on the E_R dependency. When the dependency is later required when introducing s in equation 3.9 it is not available and leads to wrong results.

This can be mathematically shown with the example of a mono-energetic event set at E^0_{True} combined with a threshold cut in E_R at -for the sake of simplicity- $E^{Thresh}_R = E^0_{True}$. In this case, $s(E_{True}, E_R)$ can be written explicitly as $s(E_{True}, E_R) = s_1(E_{True}) \cdot s_2(E_R) = 1 \cdot H(E_R - E^{Thresh}_R)$ where $H(E_R - E^{Thresh}_R)$ is the Heaviside step function.

Introducing this information correctly into equation 3.9 yields

$$\frac{dR}{dE_R}(E_R) = \int 1 \cdot H(E_R - E^{Thresh}_R) \cdot \delta(E_{True} - E^0_{True}) \cdot G_\sigma(E_R - E_{True})\, dE_{True} = H(E_R - E^{Thresh}_R) \cdot G_\sigma(E_R - E^0_{True}) \tag{3.10}$$

which is a Gaussian vertically cut in half as displayed in the upper branch of figure 3.20.

The approach of first integrating out the E_R dependency yields, keeping in mind that G_σ is normalized and $E^0_{True} = E^{Thresh}_R$:

$$\bar{s}(E^0_{True}) = \int 1 \cdot H(E_R - E^{Thresh}_R) \cdot G_\sigma(E_R - E^0_{True})\, dE_R = 0.5 \tag{3.11}$$

The way it is done in this example, the survival probability is only defined at E^0_{True} as no information is available anywhere else. Inserting the result into equation 3.9 yields:

$$\frac{dR}{dE_R}(E_R) = \int \bar{s}(E^0_{True}) \cdot \delta(E_{True} - E^0_{True}) \cdot G_\sigma(E_R - E_{True})\, dE_{True} = 0.5 \cdot G_\sigma(E_R - E^0_{True}) \tag{3.12}$$

which is a Gaussian of half the original amplitude which, problematically, extends below the threshold E^{Thresh}_R. This is displayed in the lower branch of figure 3.20 and is clearly different from the correct result in the upper branch. Expecting events below threshold is problematic for a limit calculation, as it leads to a fake sensitivity expectation at those energies.

This example can also be calculated based on a flat spectrum, e.g., $\frac{dR}{dE_{True}}(E_{True}) = 1$ and a sharp threshold in E_R which will also lead to a fake sensitivity below threshold for the old method. This had already been realized in previous analysis, therefore energies below the nominal threshold were not taken into account in the limit calculation.

3.7.3 Yellin Method

Particle detectors with an energy measurement have an additional dimension of information available compared to a pure counting experiment. They can compare expected spectral shapes in addition to expected rates. The **maximum gap** and **maximum interval** methods developed by S. Yellin [131] allow to exploit the spectral information even when the shape of the background components is not known. They look for the maximum deviation of the observed spectrum from the expected (dark matter) spectrum. The idea is briefly summarized in the following:

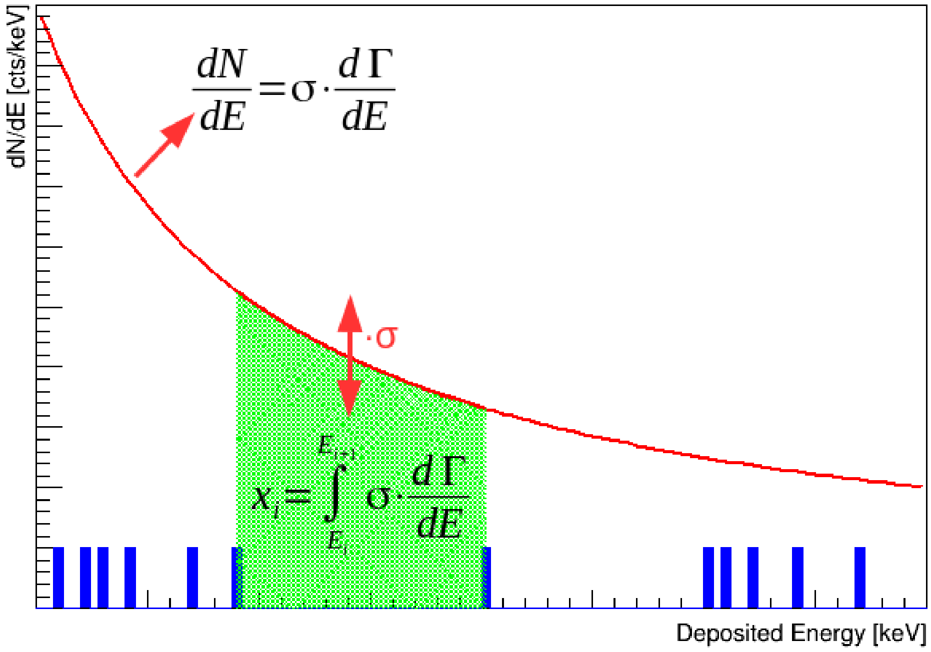

Figure 3.21: Schematic presentation of the maximum gap method for the calculation of limits in the presence of an unknown background. For details see text and [131].

For the maximum gap method, the intervals between adjacent observed events in energy are compared, see figure 3.21. The number of observed events in such an interval is zero by definition. The number x_i of expected events is the integral of the expected spectrum over the interval:

$$x_i = \int_{E_i}^{E_{i+1}} \sigma \cdot \frac{d\Gamma}{dE} \tag{3.13}$$

where E_i is the energy of the i-th event. The x_i of the interval where the discrepancy between the expected number x_i of events and the non-observation of an event is biggest is the **maximum gap**. In his paper S. Yellin derived a formula for the probability of observing a certain maximum gap for a given spectral shape and σ. With the help of this formula, a frequentist limit can be calculated on σ, where, e.g., 90 % of the time the maximum gap would be smaller.

The optimum interval method is a generalization of the optimum gap method where N events are allowed in the integration window of x_i. If N is chosen to get the most stringent limit, a statistical penalty for the search has to be taken into account. This method is explored in more detail in [132] and tabulated values and software implementation can be found in [133].

3.7.4 Likelihood Fit

When a reliable, parameterized model for the signal and the backgrounds of a measurement exists, methods that exploit this information become favorable. One such approach is a likelihood analysis. The likelihood is the chance of observing the measured experimental outcome depending on the model parameters describing the experiment. Maximizing the likelihood yields the model parameters that are most likely to produce the measured outcome with the given model. A detailed description of the likelihood analysis and how to apply it to CRESST data can be found in [79, 107]. In those cases, the likelihood was defined for the 2D representation of CRESST data in the light yield vs phonon energy plane. In particular, it took into account the band structure described in section 3.6. This approach has not been applied in the present work.

In the following, the application of a likelihood analysis on a 1D, binned energy spectrum with a simplified model is described. It focuses on estimating the parameters space for a possible dark matter signal in a frequentist framework and is applied in chapter 5.

The likelihood analysis requires a model of the data. For the 1D energy spectrum this model contains the expected event densities $\rho_x(E, \theta)$ per energy for different contributions x and model parameters θ. In the simplest case this includes a possible dark matter signal $\rho_{DM}(E, m_{DM}, \sigma_{DM})$ and a background model $\rho_b(E, \theta_b)$:

$$\rho_{total}(E, \theta) = \rho_{DM}(E, m_{DM}, \sigma_{DM}) + \rho_b(E, \theta_b)(+...) \tag{3.14}$$

In this example, detector effects and measurement parameters like the exposure and survival probabilities are fixed by the setup and taken as already included in the ρ_x.

In a binned energy spectrum produced by independent events, each bin represents an independent counting experiment. The probability $P(n, \lambda)$ of observing n events in a given bin follows a Poisson distribution $P(n, \lambda) = \frac{\lambda^n e^{-\lambda}}{n!}$ around a given expectation value λ. The expectation value $\lambda(\theta)$ is the integral of $\rho_{total}(E, \theta)$ over the size of the bin. The Likelihood $\mathcal{L}(\theta|Spectrum)$ of observing the measured binned energy spectrum as a function of θ then is the product of the single bin i probabilities:

$$\mathcal{L}(\theta|Spectrum) = P(Spectrum, \theta) = \prod_i P(n_i, \lambda_i) \tag{3.15}$$

Maximizing $\mathcal{L}(\theta|Spectrum)$ gives the best fit of the parameters to the observed spectrum. θ here includes the dark matter parameters of interest, m_χ and σ_χ.

For reasons of simplicity, commonly $-ln\,\mathcal{L}(\theta|Spectrum)$ is minimized instead of maximizing $\mathcal{L}(\theta|Spectrum)$ which yields the same result.

The best fit parameters θ for a likelihood function including a dark matter component and without a dark matter component can be compared to obtain a significance for the presence of a dark matter like component in the spectrum. Furthermore, a confidence interval for the dark matter model parameters can be calculated. In both cases, the negative logarithm of the likelihood ratio can serve as a χ^2 distributed test statistic [134, 135]:

$$q = -2ln\frac{\mathcal{L}(\theta_0|Spectrum)}{\mathcal{L}(\hat{\theta}|Spectrum)} = 2[l(\hat{\theta}|Spectrum) - l(\theta_0|Spectrum)] \tag{3.16}$$

where $\hat{\theta}$ marks the best fit parameters, θ_0 marks the true parameter values and $l(\theta|Spectrum)$ the logarithm of the likelihood. As the analysis is only interested in the dark matter parameters, the background parameters are actually fitted to the data for both, $\mathcal{L}(\theta_0|Spectrum)$ and $\mathcal{L}(\hat{\theta}|Spectrum)$. Their effect is thereby "profiled-out".

The more unlikely the experimental result for the true parameters, the bigger is q. For the significance of the best fit, it is assumed that the true parameters contain no dark matter signal, i.e., $\sigma_{DM} = 0$, corresponding to a q value $q0$. The background only hypothesis can then be rejected at a certain confidence level cf if the chance of producing the observed or a bigger $q0$ is smaller than $1 - cf$. This chance can be readily calculated by integrating the χ^2 distribution from the calculated $q0$ to infinity. It gives the probability of observing the measured or a more unlikely spectrum if the background only hypothesis were true.

The confidence interval in terms of m_{DM} and σ_{DM} is supposed to include all combinations of m_{DM} and σ_{DM} that, if they were the true values, would not be rejected at the desired confidence level by the observed spectrum. Accordingly, the likelihood ratio is now built comparing the tested m_{DM}, σ_{DM} as "true" values to the best fit. Pairs that produce a q value above the desired confidence level are rejected. In this case, the integral of the tail of the χ^2 distribution with two degrees of freedom is required [79]. For a confidence level of 90 % this puts the border at $q = 4.6$:

$$q(m_{DM}, \sigma_{DM}) = -2ln\frac{\mathcal{L}(m_{DM}, \sigma_{DM}, \hat{\theta}_b|Spectrum)}{\mathcal{L}(\hat{\theta}|Spectrum)} = \begin{cases} \leqq 4.6 \text{ accept} \\ > 4.6 \text{ reject} \end{cases} \tag{3.17}$$

where $\hat{\theta}_b$ corresponds to the background parameters maximizing the likelihood with m_{DM}, σ_{DM} fixed. The accepted combinations of m_{DM} and σ_{DM} then form the 90 % confidence islands of a positive analysis of a dark matter signal.

Chapter 4

CRESST-II Phase 2 Alpha Analysis

A detailed α analysis on the data of the CRESST-II phase 2 measurement campaign, called **MCII-2** in the following, has been performed. The limits on the dark matter particle-nucleon interaction cross-section below $2\,\mathrm{GeV/c^2}$ presented in [82] and [83] were based on MCII-2.

Section 4.1 introduces the motivation for an α analysis in CRESST, the expected α signature of the natural decay chains and a few selected, additional sources of MeV energy depositions. Section 4.2 largely follows the analysis steps outlined in chapter 3 with focus on the special requirements for α events. Results and a comparison to related work within the CRESST collaboration are presented in sections 4.3 and 4.4 respectively, with a summary in section 4.5.

4.1 Introduction

4.1.1 Relevance of Alpha Analyses for CRESST

Internal radioactivity is a major source of background for CRESST. "Internal" refers to radioactive isotopes embedded in the main absorber crystals. In [136, 127] it has been concluded that about one third of the β and γ background in the investigated main absorber crystal was caused by internal decays from the natural decay chains. This main absorber crystal was produced within the CRESST collaboration and already has a significantly improved radio-purity compared to previously used commercial crystals [126]. Similar work as presented in this chapter has been performed in [126], [137] and [138]. Some of the α rates in [136, 127] are based on the analysis discussed in this chapter, see also section 4.4.2. However, there have been several improvements to the analysis since then which are included in the present work.

CRESST detectors search for dark matter nuclear recoils in the eV to keV range. Internal α decays deposit energies between $\sim$3 MeV and 15 MeV. Hence, they are not a dangerous background for the dark matter search. However, many α decays are in secular equilibrium with internal β decays that do fall into the relevant energy range. Disentangling them from other background contributions is important for a thorough understanding of backgrounds [126, 127]. Having the α events as a reference region allows to calculate the number of expected internal β decays and simulate the resulting energy spectrum [126, 136, 127].

Knowing the internal α contamination also allows to compare the radio-purity of different target crystals. This helps to identify and evaluate promising steps for improvement as, e.g., discussed in [138].

4.1.2 Radioactive Decay Chains and their Alpha Signature

4.1.2.1 Decay Chains and Secular Equilibrium

There are three main naturally occurring decay chains on earth, Uranium-238, Uranium-235 and Thorium-232. They are summarized with their decay energies (**Q-values**) in table 4.1. The β decays are grayed out as they are not relevant for the α analysis itself.

In case of an internal α decay, neither the decaying nucleus nor the α particle can escape the target crystal. Therefore, the full Q-value is detected in a CRESST detector. As a result, each decay chain leaves a defined pattern of mono-energetic peaks in the α region of the data. These patterns are shown in appendix D. They allow to identify the different decays in the data when no ad-hoc energy calibration is possible.

Decays that are in **secular equilibrium** with each other have peaks with the same rate. Secular equilibrium occurs when a parent isotope has a much longer half-life than its daughter isotopes. After sufficient time, any initial contamination of the daughter isotopes has decayed away. At this point they are only produced by the decay of the long-lived parent. The resulting equilibrium between production and decay requires decay rates of all involved isotopes to be the same. The internal β background can then be extracted from the observed number of equilibrium α decays.

Crystal production can reduce or enrich certain elements compared to others. As a consequence, secular equilibrium can be broken at any isotope in a decay chain with a half-life around the age of the employed target crystal. For the following analysis it is assumed that secular equilibrium can be broken by any element with a half-life of more than one year as crystals are typically a few years old. The relevant isotopes are marked in red in table 4.1. In [136] a more quantitatively motivated criterion was applied.

$^{238}_{92}$U			$^{235}_{92}$U			$^{232}_{90}$Th		
Isotope	Energy	Half-life	Isotope	Energy	Half-life	Isotope	Energy	Half-life
$^{238}_{92}$U	4.27 MeV	4.47×10^{9} y	$^{235}_{92}$U	4.678 MeV	7.04×10^{8} y	$^{232}_{90}$Th	4.082 MeV	1.4×10^{10} y
$^{234}_{90}$Th	0.272 MeV	24.1 d	$^{231}_{90}$Th	0.39 MeV	25.52 h	$^{228}_{88}$Ra	45.8 keV	5.75 y
$^{234m}_{91}$Pa	2.269 MeV^{*1}	1.16 min	$^{231}_{91}$Pa	5.15 MeV	3.27×10^{4} y	$^{228}_{89}$Ac	2.124 MeV	6.15 h
$^{234}_{92}$U	4.858 MeV	2.45×10^{5} y	$^{227}_{89}$Ac*	44.8 keV	21.8 y	$^{228}_{90}$Th	5.52 MeV	1.91 y
$^{230}_{90}$Th	4.77 MeV	7.54×10^{4} y	$^{227}_{90}$Th	6.146 MeV	18.7 d	$^{224}_{88}$Ra	5.789 MeV	3.63 d
$^{226}_{88}$Ra	4.871 MeV	1600 y	$^{223}_{88}$Ra	5.979 MeV	11.4 d	$^{220}_{86}$Rn	6.405 MeV	55.8 s
$^{222}_{86}$Rn	5.59 MeV	3.82 d	$^{219}_{86}$Rn	6.946 MeV	3.98 s	$^{216}_{84}$Po	6.906 MeV	0.148 s
$^{218}_{84}$Po	6.115 MeV	3.1 min	$^{215}_{84}$Po	+7.526 MeV	1.78 ms	$^{212}_{82}$Pb	0.570 MeV	10.64 h
$^{214}_{82}$Pb	1.019 MeV	26.9 min		=14.5 MeV		$^{212}_{83}$Bi	branching	60.5 min
$^{214}_{83}$Bi	3270 MeV	19.8 min	$^{211}_{82}$Pb	1.367 MeV	36.1 min	36%	6.207 MeV	
$^{214}_{84}$Po	+7.833 MeV	0.162 ms	$^{211}_{83}$Bi	6.750 MeV	2.15 min	$^{208}_{81}$Tl	4.999 MeV	3.06 min
	=11.1 MeV		$^{207}_{81}$Tl	1.418 MeV	4.77 min	$^{208}_{82}$Pb	stable	
$^{210}_{82}$Pb	63.5 keV	22.2 y	$^{207}_{82}$Pb	stable		64%	2.252 MeV	
$^{210}_{83}$Bi	1.161 MeV	5.01 d		5.04 MeV		$^{212}_{84}$Po	+8.954 MeV	300 ns
$^{210}_{84}$Po	5.407 MeV	138 d					=11.2 MeV	
$^{206}_{82}$Pb	stable					$^{208}_{82}$Pb	stable	

Table 4.1: Nuclear decay chains with Q-values and half-lifes. β decays are grayed out as they are not relevant for the α analysis. Isotopes that can break secular equilibrium with the isotopes above due to their long half-life are marked in red. For subsequent fast decays that cannot be resolved by a CRESST-II detector also the summed energy of the involved decays is given. Values are taken from [121]. *: $^{227}_{89}$Ac has a 1.38% branching ratio into an α decay to $^{223}_{87}$Fr with a Q-value of 5.04 MeV that can be observed with enough exposure. After a subsequent β decay to $^{223}_{88}$Ra at again follows the main decay chain.

4.1.2.2 Alpha Cascades and Pile up

There are three decays with a half-life below two milliseconds. In those cases, the parent and the daughter decay are not resolved by the intrinsically slow investigated detectors, see figure 4.3. They appear as an energy deposition of the summed energy and are referred to as **α-β-** and **α-α-cascades** in the following. In the $^{238}_{92}$U chain, $^{214}_{84}$Po with a half-life of 0.162 ms piles up with the beta decay of its parent nucleus $^{214}_{83}$Bi. β particles do not necessarily deposit their whole energy in the crystal but produce a Compton continuum. Therefore, these events will appear between 7.883 MeV, the energy of the α decay, and 11.2 MeV, the summed energy of both decays. The same is true for the decay of $^{212}_{84}$Po following $^{212}_{83}$Bi in the $^{232}_{90}$Th chain. In the $^{235}_{92}$U chain $^{215}_{84}$Po and $^{219}_{86}$Rn form an α-α-cascade with a mono-energetic peak at 14.5 MeV.

Additionally, $^{216}_{84}$Po has a decay time of 145 ms. As the post-trigger length is 245.76 ms (compare section 4.2.1.2), it can produce pile-up events with the preceding $^{220}_{86}$Rn α decay. Those pile up events cannot be properly analyzed.

4.1.2.3 Gamma Escape Lines

For the α decays of the $^{235}_{92}$U chain there is a high (>10 %) chance that part of the energy is released in the form of γs [121]. Those are either absorbed in the crystal or can escape. In the last case only a reduced energy will be observed for the decay. Observation of this effect is also discussed in [139], where the escaping γs are detected in a neighboring detector. The relevant decays with a γ whose emission probability is $> 5\%$ and that have an energy >100 keV are summarized in table 4.2.

The mean free path of γ particles in $CaWO_4$ can be estimated to be around ~1 mm for the relevant ~200 keV γ energies [140]. The escape process can therefore only happen close to the surface. For the detector geometries analyzed in this chapter the 1 mm surface layer takes up about 10 % of the volume. The summed probability for γs is about 20 % per decay. Therefore, about 2 % of the relevant α decays are expected to end up in the γ escape peaks.

The γ escapes are also visible in the simulation of α decays performed in [136, 127]. The simulation allows for a more precise estimate of the number of escape events. The decays were placed at random positions within the absorber crystal. The total probability for the γ escape lines as taken from the simulation is given in table 4.2.

The γ escape lines of $^{223}_{88}$Ra and $^{227}_{90}$Th appear in the densely populated region of the α spectrum. Their precise energy is therefore of primary interest for the identification. The simulated energy spectrum for internal alpha decays for $^{223}_{88}$Ra and $^{227}_{90}$Th in a TUM40 like detector geometry is shown in figure 4.1. There are some dominating peaks between about 5880 keV and 5930 keV that overlap in the measured data. As they are not separable in the measured data, the total probability of an event to occur in this energy interval is given for $^{223}_{88}$Ra and $^{227}_{90}$Th in table 4.2. Since $^{223}_{88}$Ra and $^{227}_{90}$Th are in secular equilibrium with each other, their relative contribution to the mixed escape peak around 5900 keV is fixed. The simulation yields a 37 % contribution from $^{223}_{88}$Ra and 63 % from $^{227}_{90}$Th.

It is not possible to identify less dominant escapes than the ones given in table 4.2 due to the limited number of events in the data and the overlapping in energy of more intense lines. Therefore, only the listed escape peaks are taken into account in the analysis.

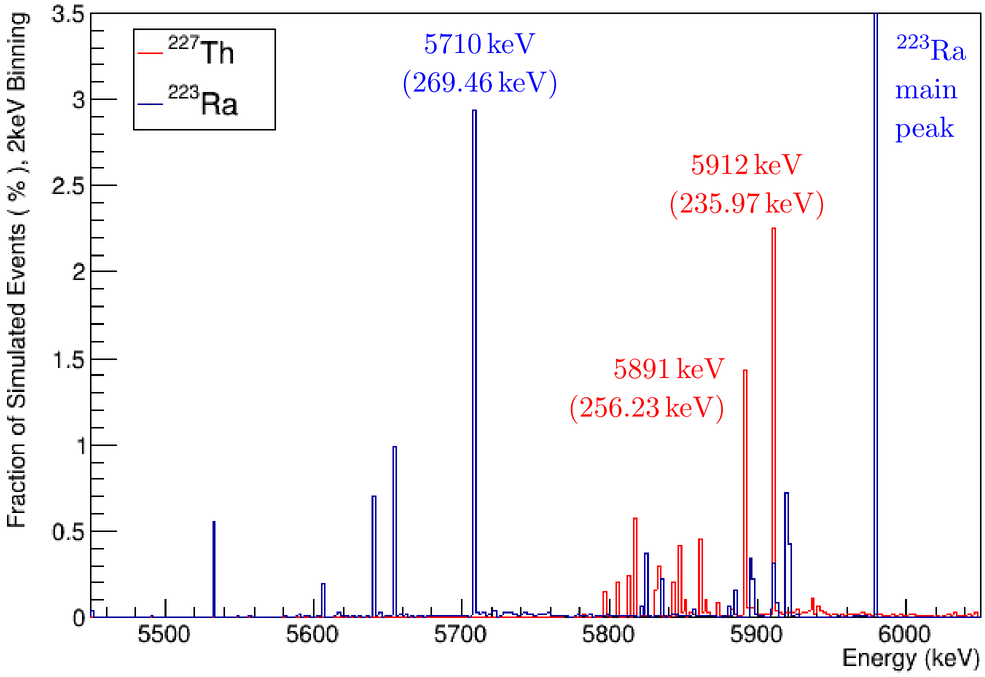

Figure 4.1: Simulated energy spectrum for internal α decays of $^{223}_{88}$Ra and $^{227}_{90}$Th in a TUM40 like detector [136, 127]. The main peak of $^{223}_{88}$Ra can be seen at 5979 keV. The main peak of $^{227}_{90}$Th is not shown. The energies of the main escape peaks and the energies of the escaping γs are indicated.

4.1.3 Other Sources of MeV Energy Depositions

There are three more lines in the MeV energy range commonly visible in CRESST detectors:

$^{147}_{62}$Sm is a radioactive isotope of the rare earth metal samarium with an α line at 2311.2 keV and a half-life of 1.08×10^{11} y [121]. It decays into the stable $^{143}_{60}$Nd.

$^{180}_{74}$W is a radioactive isotope of tungsten with a natural abundance of about 0.12% [141]. It α decays to $^{176}_{72}$Hf with a half life of $(1.8 \pm 0.2) \cdot 10^{18}$y and a Q

Isotope	γ energy (keV)	Chance of emittance (%)	Chance of escape (simulation [136, 127]) (%)	Escape line energy (keV)
$^{235}_{92}$U	185.7	57		4492
	143.76	10.96		4534
	163.4	5.08		4515
	205.3	5.02		4473
total			10.7	
$^{227}_{90}$Th	235.97	12.3	2.26	5912
	256.23	6.8	1.44	5891
			4.33	5880-5930
total			9.8	
$^{223}_{88}$Ra	269.46	14.23	2.93	5710
	154.2	5.84	0.37	5825
			2.5	5880-5930
total			10.4	
$^{219}_{86}$Rn	271.2	11.07		α cascade
	401.8	6.75		α cascade
$^{211}_{83}$Bi	351	13	4.0	6400
total			5.9	

Table 4.2: Dominant γ quanta emitted with α decays in the $^{235}_{92}$U chain. The α decay is detected with a reduced energy if the γ escapes the crystal. Data taken from [121]. The $^{211}_{83}$Bi escape peak overlaps with the $^{220}_{86}$Rn α decay at 6405 keV. There are several overlapping γ escape lines from $^{223}_{88}$Ra and $^{227}_{90}$Th between 5880 keV and 5930 keV. Therefore, the total percentage of simulated events in this region is also given. The number listed under "total" is the percentage of simulated events that do not appear in the main peak of the decay.

value of $(2516.4 \pm 1.1(\text{stat.}) \pm 1.2(\text{sys.}))$keV. This decay was first unambiguously measured by the CRESST experiment [141].

$^{208}_{81}$Tl γ line Thallium-208 is a β emitter from the $^{232}_{90}$Th chain which can produce 2.6 MeV γ quanta. Those can show up as a line in case of an external contamination [121, 126]. It can be distinguished in CRESST detectors from α decays based on the light yield, compare section 3.6.

4.2 Analysis

4.2.1 Measurement Setup

4.2.1.1 Detectors

In the following, a total of three detector modules from MCII-2 are investigated, “TUM40”, “Lise” and “VK28”. The main published results from MCII-2 are based on TUM40 and Lise [83, 82]. VK28 is analyzed mainly for demonstration purposes. Schematic drawings of all three detectors can be seen in figure 4.2.

TUM40 is of the fully scintillating type that was introduced in MCII-2. It is designed to ensure a vetoing of all surface backgrounds. The main absorber crystal is held by $CaWO_4$ sticks and is surrounded by a scintillating foil. For a detailed description see [110]. The target crystal was produced at the TU München within the CRESST collaboration. It has already been shown in [126], [138] and [137] that TUM40 has a lower intrinsic radioactive contamination than commercially available crystals. The TES is evaporated onto a small carrier crystal that is then glued onto the main absorber.

Lise is a conventional CRESST detector module, compare [142], with the main absorber crystal and light detector held by bronze clamps. As for TUM40, the TES is not directly evaporated on the main absorber, but on a small, glued carrier crystal. The module has a light detector showing an exceptionally bad performance [82]. Therefore, only the phonon channel is relevant for the analysis.

VK28 is of the ”beaker” design [108]. The main absorber crystal is glued to a big carrier crystal and suspended into a silicon beaker. The TES for the main absorber read-out is on the carrier crystal. The silicon beaker serves as light detector. With this design the target crystal is completely surrounded by instrumented components. This allows to identify surface events with great accuracy.

More details on the modules can be found in the in-depth descriptions of the MCII-2 dark matter analyses in [107] and [100].

4.2.1.2 Data Acquisition Settings

In MCII-2 only the hardware trigger based read-out was available. The data is therefore recorded with a fixed trigger threshold and fixed number of samples in pre- and post-trigger (compare section 3.1). The relevant settings are summarized in table 4.3.

The trigger is blocked for the time of the pre-trigger each time after an event is recorded. This can be specifically relevant here as it introduces a systematic loss of α events with a half life of the order of the pulse record length.

MCII-2 took about two years including calibration measurements. For the α analysis only data without a calibration source present is analyzed. The total measurement time, raw live time and exposure are summarized for all three detectors in table 4.4.

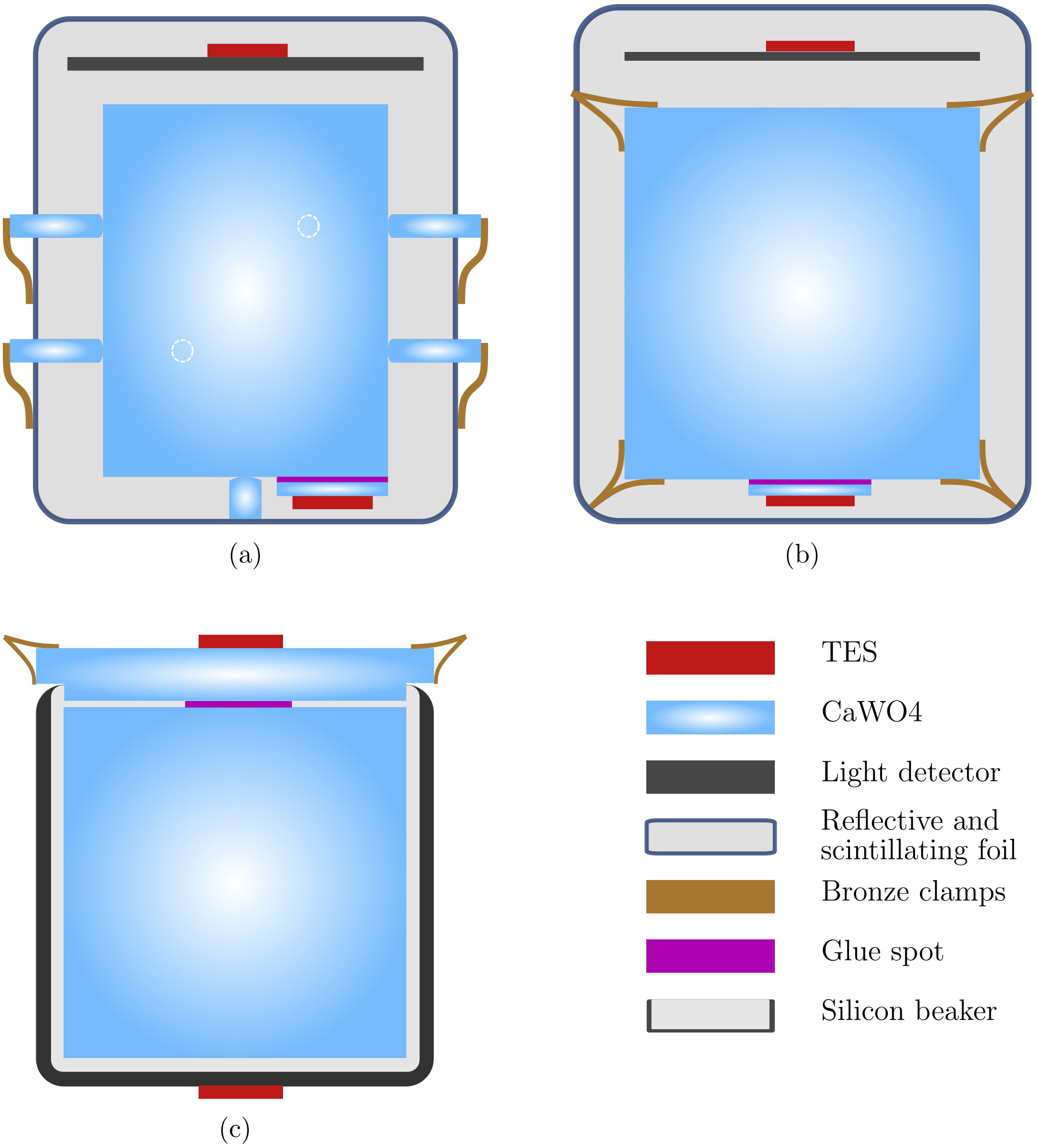

Figure 4.2: a) Schematic view of the detector design of "TUM40". The main absorber crystal is held by $CaWO_4$ sticks resulting in a fully scintillating housing to veto surface events [110]. The main absorber TES is placed on a small carrier. b) Schematic view of the detector design of "Lise". It is a standard CRESST detector with a TES carrier and bronze clamps holding the main absorber crystal. c) Schematic view of the detector design of "VK28". It is of the beaker type [108]. The main absorber crystal is hanging from a carrier crystal into a silicon beaker, which serves as light detector. With this design, the main absorber crystal is fully surrounded by instrumented parts.

Parameter	Value
Sampling rate	25 kHz $\hat{=}$ 40 µs/sample
Record length	8192 samples $\hat{=}$ 327.68 ms
Pre-trigger	2048 samples $\hat{=}$ 81.92 ms
Post-trigger	6144 samples $\hat{=}$ 245.76 ms

Table 4.3: Settings chosen for the pulse records in CRESST-II phase 2. Values taken from [107].

Parameter	Lise	TUM40	VK28
Module type	Conventional [142]	Stick module [110]	Beaker type [108]
Absorber mass	306 g	248 g	194 g
Measurement time	13 610.2 h	13 610.2 h	13 610.2 h
Live time (raw)	12 511 h	12 572.1 h	12 452.6 h
Exposure	159.5 kg d	129.9 kg d	100.7 kg d

Table 4.4: Mass and exposure of the modules investigated in the present chapter. Values taken from internal documentation and the measurement data. The exposure is the product of mass and raw live time.

4.2.1.3 Specific Limitations related to Alphas

The MCII-2 detectors were optimized for energies between a few hundred eV and hundred keV [82, 83]. At the MeV energies of the α decays, problems of non-linearity, saturation and flux quantum losses as introduced in sections 2.3.1, 2.3.2 and 3.3.2 become the dominating challenge for the analysis. Furthermore, the fixed record length is significantly too small to record the full pulse signal of an MeV energy deposition. An example of an α event in TUM40 is shown in figure 4.3. It can be seen that both the phonon (red) and the light channel (blue) are fully saturated. Additionally, the phonon channel does not return to the baseline level within the record window.

4.2.2 Parameter Gathering

4.2.2.1 Important Basic Parameters

The following basic pulse and event parameters (see appendix B for details) are of major importance for the α analysis: right - left baseline for the α identification, peak position for data selection and baseline offset as well as pulse height for further data treatment.

4.2.2.2 Template Fit with high Truncation Limit

The template fit for the α analysis is performed with the standard events produced within the framework of the dark matter analysis of the MCII-2 data presented

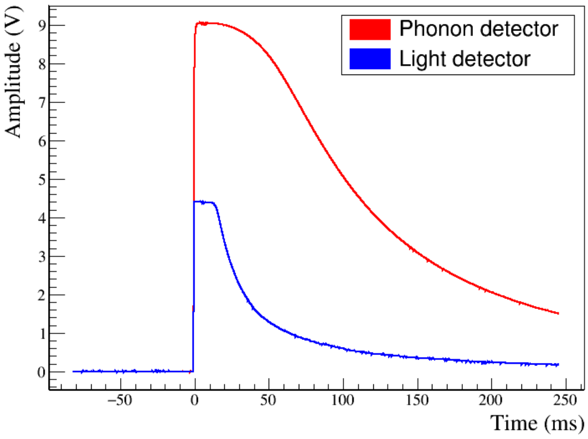

Figure 4.3: Pulse records of a typical α event in the detector module TUM40. Both the phonon (red) and the light pulse signal (blue) are completely saturated around their peak. The record window is too short for the phonon pulse signal to fully return to the baseline level.

in [100]. To extend the fit into the non-linear and saturated region of the detector, the truncated standard event fit as discussed in section 3.2.2.4 is applied. Phonon and light detector are fitted correlatedly for TUM40 and VK28. For Lise, only the phonon detector is analyzed due to the bad performance of the light detector.

The truncation limit for the α analysis has to be chosen in the already non-linear region of the detector response. This is because of two reasons: First, the rising flank of the pulse is very steep. Without a high truncation limit, not enough samples are left for the fit to determine the onset of the pulse. Second, the pulse signal in the phonon channel does not return to the baseline within the record window. If no samples in the falling flank are below the truncation limit, a fit is not possible. This is shown in figure 4.4.

The final truncation limits for the fit are summarized in table 4.5. They are significantly higher than the truncation limits chosen for a dark matter analysis, e.g., in [100]. Figure 4.4 shows a corresponding fit applied to an α event of TUM40. The truncation limit of the dark matter analysis of [100] is also marked (dashed red line). Several combination of truncation limits and baseline models for the fit have been tried. The settings giving the best resolution for the final result are presented here.

With the higher truncation limit the standard event fit no longer describes the observed pulse record correctly, although the effect is not strongly visible in figure 4.4. A linear relation between fitted amplitude and deposited energy can no longer be assumed. Furthermore, the high truncation limit degrades the resolution of the signal amplitude evaluation compared to the ideal case of being able to only fit the linear part.

The underlying effect for the decrease in resolution is mostly small changes in the operating point of the detector. When only investigating the linear range,

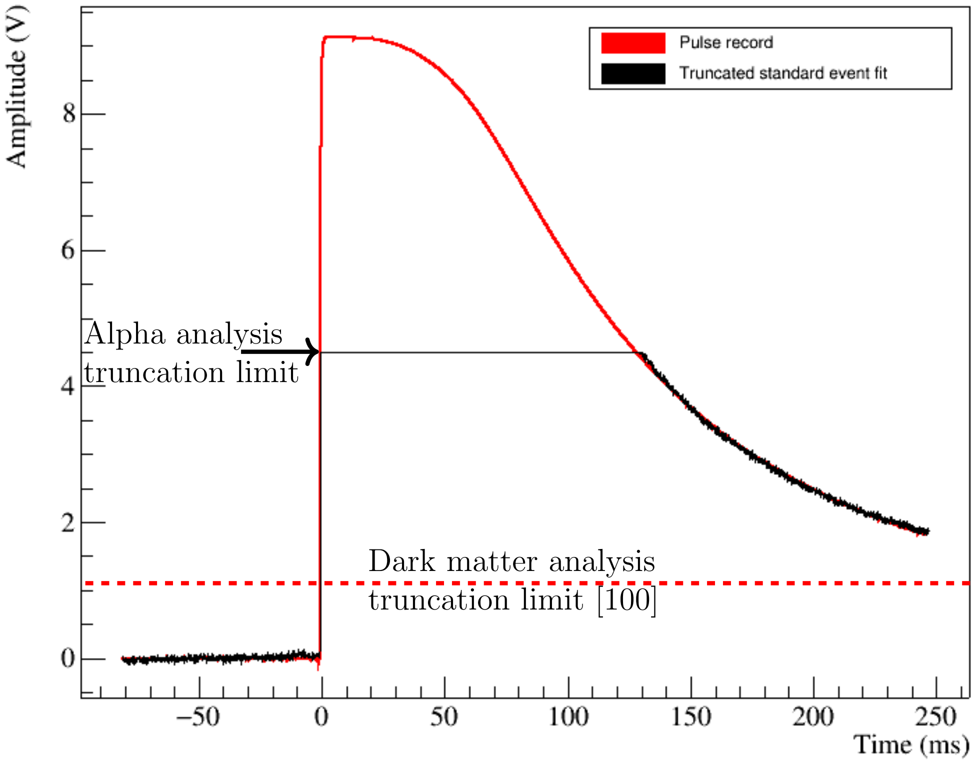

Figure 4.4: Typical α pulse record (red) of TUM40, phonon, fitted with a truncated standard event fit (black), a high truncation limit of 4.5 V and a linear baseline model. The truncation limit for the linear region of the pulse was set to 1.1 V in the dark matter analysis of [100] (red dashed line). For the α events, no samples would remain in the falling flank and the fit would therefore fail. Furthermore, the fit would not be able to find the pulse onset due to the low number of samples remaining in the rising flank.

Parameter	TUM40	Lise	VK28
Truncation limit phonon	4.5 V	3 V	4.5 V
Truncation limit light	0.6 V	–	0.4 V
Baseline model	Linear	Linear	Linear

Table 4.5: Standard event fit settings for the three detectors of the MCII-2 α analysis performed in this chapter.

small changes do not affect the amplitude evaluation. However, when the non-linear region is included, changes in the operating point change the onset of the non-linearity and thereby do affect the evaluation. In this case, there are several parameters that show a correlation with the operating point and fitted amplitudes of the α events, most notably the baseline offset. The correlation can be exploited to compensate these changes and improve the resolution of the amplitude/energy reconstruction. This is described in detail in appendix F and yields the **operating point corrected fitted (signal) amplitude**.

From the fit mainly this operating point corrected fitted amplitude is relevant for the α analysis.

4.2.3 Data Selection

The data selection criteria are described in the following and summarized in appendix E.

4.2.3.1 Pre-selection on Files and Time Periods

The α analysis is done in a non-blind manner. The full data set of MCII-2 except for calibration data is directly analyzed. No rate cut is applied as no period with significantly increased rate is observed. During analysis it was recognized that, in its current form, the stability cut systematically removes certain α events. This is due to the long time required to recover the operating point after the large energy input of an α decay. Therefore, no stability cut is applied.

4.2.3.2 Corrupted Pulses

A selection on the peak position allows to remove decaying baselines and events in the pre-trigger region. No strict selection can be applied on a late peak position as it is not *a priori* clear where the maximum sample of a saturated α pulse record appears.

4.2.3.3 Veto Cuts

No muon veto cut is applied. Only α events in the main absorber crystal are of interest for the analysis. All events that only triggered the light detector are removed via the trigger delay parameter.

4.2.3.4 Alpha Analysis specific Data Selection

The data selection criteria presented in this section achieve two goals: First, a minimal set of events that still contains all possibly α induced events is identified. This set of possible α events is called the **α-basis** in the following. Second, the α-basis is separated into events which can be properly analyzed and problematic events with artifacts, predominantly FQLs. The problematic events are either treated separately, where possible, or considered in the error estimation. Knowing the total number of potentially α induced events is necessary to estimate the survival probability of α events for the calculation of α activities.

As a first step, the too short record window allows to use the right - left parameter as a proxy for the signal amplitude for the α identification. Different features of the right - left baseline spectrum can be seen in figure 4.5. The α induced events without artifacts show up in black between 0.5 V and 3 V. The decaying baselines that are already removed by the selection on the peak position are displayed in red. As visible in figure 4.5, they mirror the α spectrum as with the MCII-2 settings energy depositions in the MeV range trigger a second time as a decaying baseline. In green there are events that have a right - left baseline value too small to be caused by an α . They are removed by an α identification selection on this parameter. For Lise, e.g., events between $[-0.5\,\mathrm{V}, 0.6\,\mathrm{V}]$ are discarded.

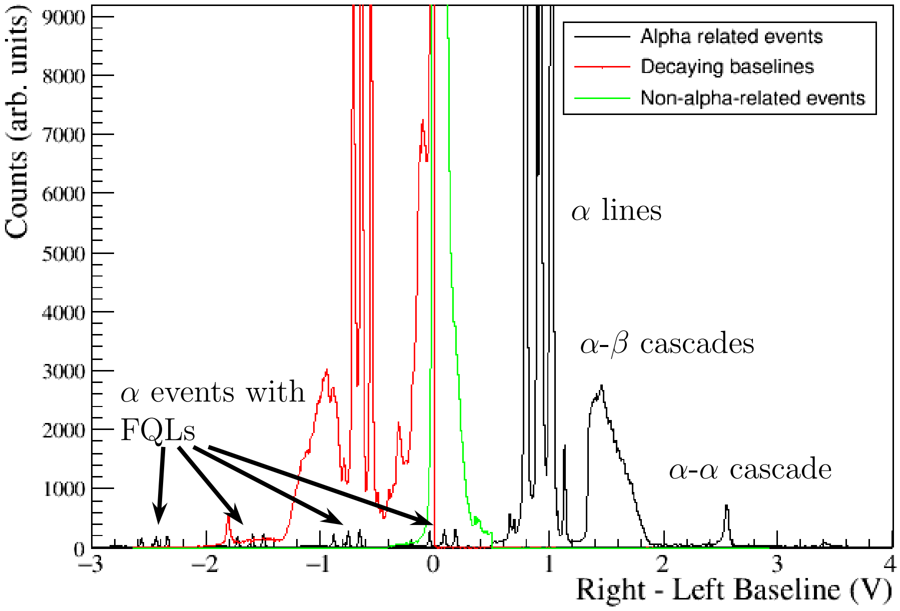

Figure 4.5: Right - left baseline spectrum of Lise. Events in red get removed by the peak position selection, i.e., they are mainly decaying baselines which result in a "mirrored" spectrum in the RL parameter. Events in green get removed by the RL α identification, i.e., they are mainly e^-/γ events. Events in black are the potentially α induced events. The shifted α spectra due to flux quantum losses can be clearly identified.

For the analysed measurement, a flux quantum loss changes the value of the right - left baseline parameter by $\approx$1 V per lost flux quantum. This leads to shifted α spectra as marked between −3 V and 0.5 V in figure 4.5. A SQUID reset adds about 10 V (not shown). It can be seen that some α events with one or two losses of flux quanta fall into the removed low right - left baseline parameter region. Those can be recovered into the α basis by a 2D selection in the right - left baseline parameter vs fitted amplitude plane as shown in figure 4.6.

With these basic selection criteria, the main α population can already be identified and separated from other events. Several additional data selection criteria targeting some remaining, smaller non-α event populations are summarized in appendix E. Great care was taken not to remove any potential α induced events. The resulting number of events in the α basis is an upper limit on the total number of recorded α interactions.

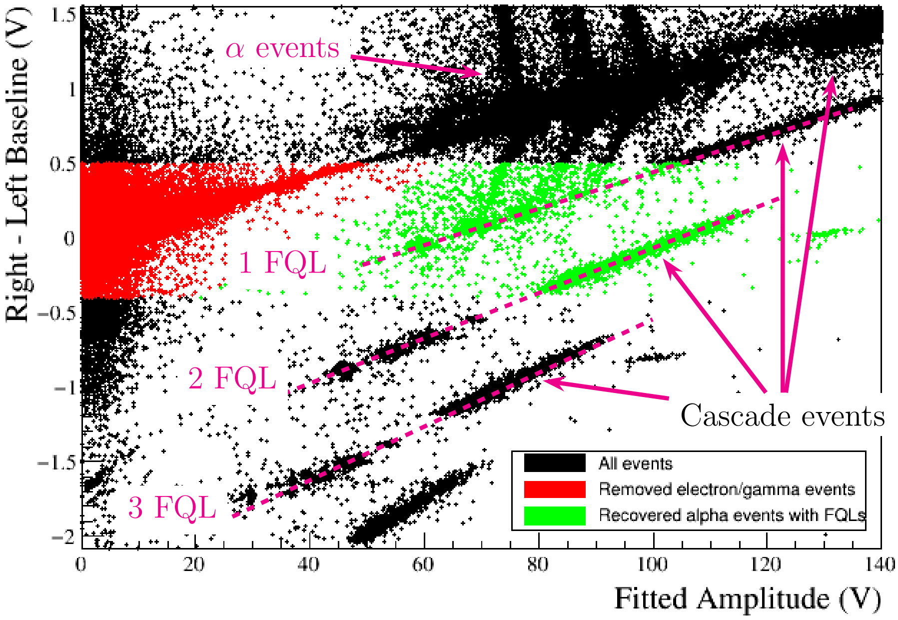

Figure 4.6: Right - left baseline vs fitted amplitude of Lise-phonon. The events in red and green get removed by the α identification selection on the right - left baseline parameter. The events in green, which correspond mainly to αs with one or two FQLs, are recovered based on a 2D selection in the shown parameter plane. Events lying on the dotted purple lines labeled "1/2/3 FQL" have a respective number of FQLs in the phonon channel.

To get to the properly analyzable α events a selection on the right - left baseline parameter, peak position and an RMS have to be applied. Furthermore, events where the standard event failed are removed.

The α-β and α-α cascades have an increased chance of an unsuccessful or wrong standard event fit. This is due to their even higher energies compared to the single α events. The resulting higher rate of problematic events complicates and worsens the estimated error on the activities of the other lines. Therefore, if possible, the cascades are identified and treated separately. Similarly, the $^{147}_{62}$Sm and $^{180}_{74}$W peaks at lower α energies have a higher survival probability and are excluded from the analysis where possible.

4.2.4 Survival Probabilities and Rate Calculation

A simulation of α events as presented in section 3.4.2 is currently not available. Such a simulation would have to include four not implemented or not implementable effects: First the non-linearity and saturation of the events as the truncated standard event fit has a truncation limit above the linear range. Second, electro-thermal feedback (compare [118]) which is limited by the full saturation and, hence, is reduced compared to what is expected from an ideal pulse signal. Third, flux quantum losses and SQUID resets, that, as yet, cannot be precisely simulated. Fourth, the time structure of decays with a small half-life, that would require simulating pile up and dead time effects. Those effects are not relevant for the dark matter analysis of CRESST, hence, their implementation in simulation is not pursued.

Instead of the simulation, a minimum/maximum estimation is applied to obtain upper and lower limits on the α activities. The lower limit is based on the number of events clearly identified in an α line after data selection. The upper limit is based on adding to that number all removed events that could possibly belong to the line. If no further information is available, this is the total number of events removed as problematic from the α basis. The rate is calculated by dividing the number of events by the raw live time in both cases.

In addition, the activity assuming an average survival probability is calculated. The average survival probability is taken to be the ratio between the number of analyzable α s and the number of events in the α basis:

$$\overline{\text{survProb}} = \frac{|analyzable\ \alpha s|}{|\alpha\ basis|} \tag{4.1}$$

4.2.5 Energy Calibration

The peak based approach described in section 3.5.2 is taken for the energy calibration. Two dominant peaks are identified at the start and the end of the α spectrum, usually ${}^{232}_{90}\mathrm{Th}$ or ${}^{238}_{92}\mathrm{U}$ and ${}^{211}_{83}\mathrm{Bi}$. A simple, time independent calibration can be performed by linearly interpolating between the means of the two peaks.

All three detectors have a time-dependent detector response visible in the reconstructed signal amplitudes of the α lines. The energy resolution can be improved by a time dependent evaluation of the position of the calibration peaks. The improvement from the time independent to the time dependent calibration is visualized for Lise for the ${}^{210}_{84}\mathrm{Po}_{\mathrm{ext}}$ to ${}^{222}_{86}\mathrm{Rn}$ α lines in figure 4.7. Figure 4.7a shows the energy assigned to the events vs time in case of a linear, time independent energy calibration. There is a clear time dependency leading to an overlap in energy of seemingly well separated lines if different time periods are compared. Figure 4.7b shows the same data, this time with the time dependent approach. Now the lines at about 5520 keV and 5590 keV are clearly separated for all times. Figure 4.7c compares the achieved energy resolutions.

Due to the comparably small event rate of the calibration lines, the time dependent calibration is susceptible to outliers or misidentified events. This can be mitigated by an appropriate smoothing of the amplitude vs time interpolation. The events in the calibration peaks are chosen by a selection on the fitted amplitude. Therefore, far outliers are already excluded. The linear interpolation in energy vs amplitude is not forced through zero.

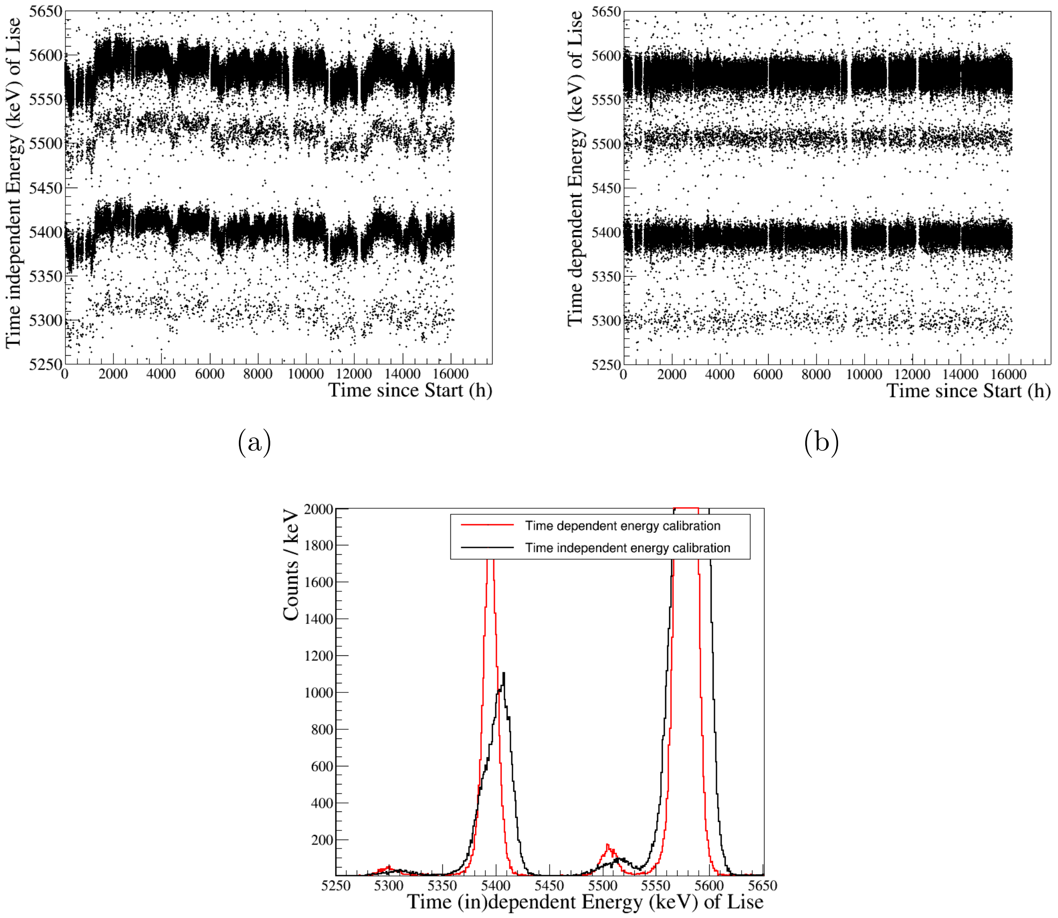

(a) (b)

(c)

Figure 4.7: Time independent and time dependent energy calibration of α events for Lise. a) Time independent calibration result, the time dependence of the detector response is clearly visible. b) Time dependent calibration result, α lines are clearly separated, even when comparing different time periods. c) Visual comparison of energy resolution obtained with the two methods. The shown α lines are from high to low energies: $^{222}_{86}$Rn (5590 keV), $^{228}_{90}$Th (5520 keV), $^{210}_{84}$Po (5407 keV) and $^{210}_{84}$Po$_{\mathrm{ext}}$ (about 5300 keV). The calibration is based on the already operating point corrected amplitudes as discussed in appendix F.

4.3 Results

4.3.1 TUM40

The data selection criteria for TUM40 are listed in table E.1 in appendix E. The detector module TUM40 has the advantage of having almost no FQLs. After initial cuts the α basis of TUM40 comprises 35775 events corresponding to an upper limit of the total α rate of 3.2 mBq/kg. To improve the error estimate, cascade and true pile-up events are separated. In total 2381 events (6.6 %) can be safely assigned to those.

Of the remaining 33394 events a total of 1769 events (~5 %) are not analyzable mainly because of FQLs. Of the separated 2381 cascade/pile-up events almost 50 % (1007 events) are not analyzable which is the motivation for treating them separately. Another 167 events are removed because their SQUID flux quantum level cannot be assigned correctly for the operating point correction (see appendix F for details).

The energy calibration is based on the $^{238}_{92}$U and $^{211}_{83}$Bi peaks. The final spectrum is shown in figure 4.8. All observed lines can be assigned to known origins except of one at (5640±20)keV. The literature values for the energies of the α peaks are indicated by the colored lines. The energy calibration does show a deviation from literature values of around 10 keV. Nonetheless, the unambiguous identification of the lines is possible so no further corrections were applied. A total of 251 events could not be assigned to any line. This can be, e.g., due to errors in the energy reconstruction, unidentified escape lines with low probabilities, or unstable time periods as no stability cut is applied.

In table 4.6 the observed activities are summarized. The rates with upper and lower limits are calculated as described in section 4.2.4. The quoted rates are calculated with an estimated average survival probability of $\frac{\#(\alpha basisNoCascades)-\#(problematic)-\#(operatingPointCorrectionLoss)}{\#(\alpha basisNoCascades)} = \frac{33394-1769-167}{33394} = 0.94.$

Most of the lines are well separated and no further error from assigning events from overlapping lines has to be considered. For some lines, overlap with other lines cannot be disentangled and rates have to be derived from equilibrium considerations of well separated lines. Furthermore, the γ escape lines discussed in section 4.1.2.3 have to be taken into account. The exact treatment of both cases is described in the following.

For the decays with γ escape lines in the $^{235}_{92}$U chain, the number of events is given for the main peak, the total identified escape peaks and the sum of both. Furthermore, the percentage of escape events relative to the sum of both is noted. The overlapping $^{223}_{88}$Ra and $^{227}_{90}$Th escape peaks have a total of 178 events which are assigned according to the 37 %:63 % ratio from simulation (compare section 4.1.2.3). The amount of escape events thus assigned to $^{227}_{90}$Th is higher (8 %) than expected from simulations (4 %). $^{223}_{88}$Ra has an observed 8 % with an expectation of 5 %-6 %. For $^{235}_{92}$U and $^{211}_{83}$Bi about 10 % and 4 % γ escapes are observed.

Concerning the separation of overlapping α lines there are three double peaks of interest. Their constituents' rates are given in brackets in table 4.6 and marked with the corresponding indices $^{(x)}$:

- **$^{234}_{92}$U and $^{226}_{88}$Ra** $^{(1)}$**:** $^{226}_{88}$Ra is in equilibrium with the clearly identifiable $^{222}_{86}$Rn line. Therefore, it is assumed to contribute the same number of events to the combined peak. The remaining number of events is assigned to $^{234}_{92}$U.
- **$^{218}_{84}$Po and $^{227}_{90}$Th** $^{(2)}$**:** The partially separable double peak has a total of 1938 events with roughly one third on $^{218}_{84}$Po and two thirds on $^{227}_{90}$Th. Both, $^{218}_{84}$Po and $^{227}_{90}$Th are in secular equilibrium with other decays in their respective decay chains. In table 4.6 two values for the number of events are given for each. One is derived from the equilibrium condition inside the respective decay chain. The other value is calculated by fixing the number of events of one decay to the value derived from equilibrium conditions and assigning the remaining number of events in the peak to the other decay.

  From the $^{218}_{84}$Po containing decay chain, the equilibrium with $^{222}_{86}$Rn yields 605 events for $^{218}_{84}$Po and 1333 events for $^{227}_{90}$Th.

  From the $^{227}_{90}$Th containing decay chain, there is a secular equilibrium with the measurable $^{223}_{88}$Ra and $^{211}_{83}$Bi peaks. Belonging to the $^{235}_{92}$U chain they all have γ escape lines which complicates the equilibrium estimation (compare section 4.1.2). Taking the average number of events, including escape lines, from $^{223}_{88}$Ra and $^{211}_{83}$Bi and subtracting the 112 $^{227}_{90}$Th escape events yields an expected 1326 events in the peak for $^{227}_{90}$Th. The remaining 612 events are then assigned to $^{218}_{84}$Po. Both results are given in table 4.6.
- **$^{220}_{86}$Rn and $^{211}_{83}$Bi γ escape peak** $^{(3)}$: $^{220}_{86}$Rn is in equilibrium with $^{228}_{90}$Th and $^{224}_{88}$Ra. The number of $^{211}_{83}$Bi γ escape events can, hence, again be calculated by subtracting the expected amount of $^{220}_{86}$Rn events from the total number of events in the peak.

  However, $^{220}_{86}$Rn has a subsequent $^{216}_{84}$Po decay with a half-life of 145 ms. In about $1-\left(\frac{1}{2}\right)^{\frac{245.76\text{ms}}{145\text{ms}}} = 69\%$ of cases the $^{216}_{84}$Po decay happens in the 245.76 ms post-trigger. In this case the event is labeled as problematic due to pile-up. Therefore, the expected number of visible $^{220}_{86}$Rn events is only 31% of the average number of events of $^{228}_{90}$Th and $^{224}_{88}$Ra expected from secular equilibrium.

  This yields 71 events in the peak for $^{220}_{86}$Rn, leaving 55 events for the $^{211}_{83}$Bi escape line.

Finally, the **$\boldsymbol{\alpha}$ cascades** have to be considered. In total there are 2381 events identified as potential cascade and/or α pile-up events by the data selection. Of those 242 can be removed with a selection on the pile-up voltage parameter (compare appendix B.17). Since the cascades should not show visible pile up behavior due to their short half-lifes, the removed events are most likely $^{220}_{86}$Rn/$^{216}_{84}$Po pile-ups, some random pile-up and some carrier events with FQLs. This number of removed events is in agreement with the expectation of having at least 160 events already from $^{220}_{86}\mathrm{Rn}/^{216}_{84}\mathrm{Po}$ pile-up, derived from equilibrium and decay time considerations.

The two α-β cascades overlap in phonon energy. Therefore, the additional energy information from the light channel is required. An additional light only standard event fit with a truncation limit of 1 V was performed for this purpose. The result is shown in figure 4.9. Taking the right - left baseline value for the phonon channel, the FQLs of the 14.5MeV α-α cascades can be clearly identified. Due to their different treatment, no errors are estimated for the α cascades. Only the raw rates are given in table 4.6, i.e. number of observed events divided by raw live time.

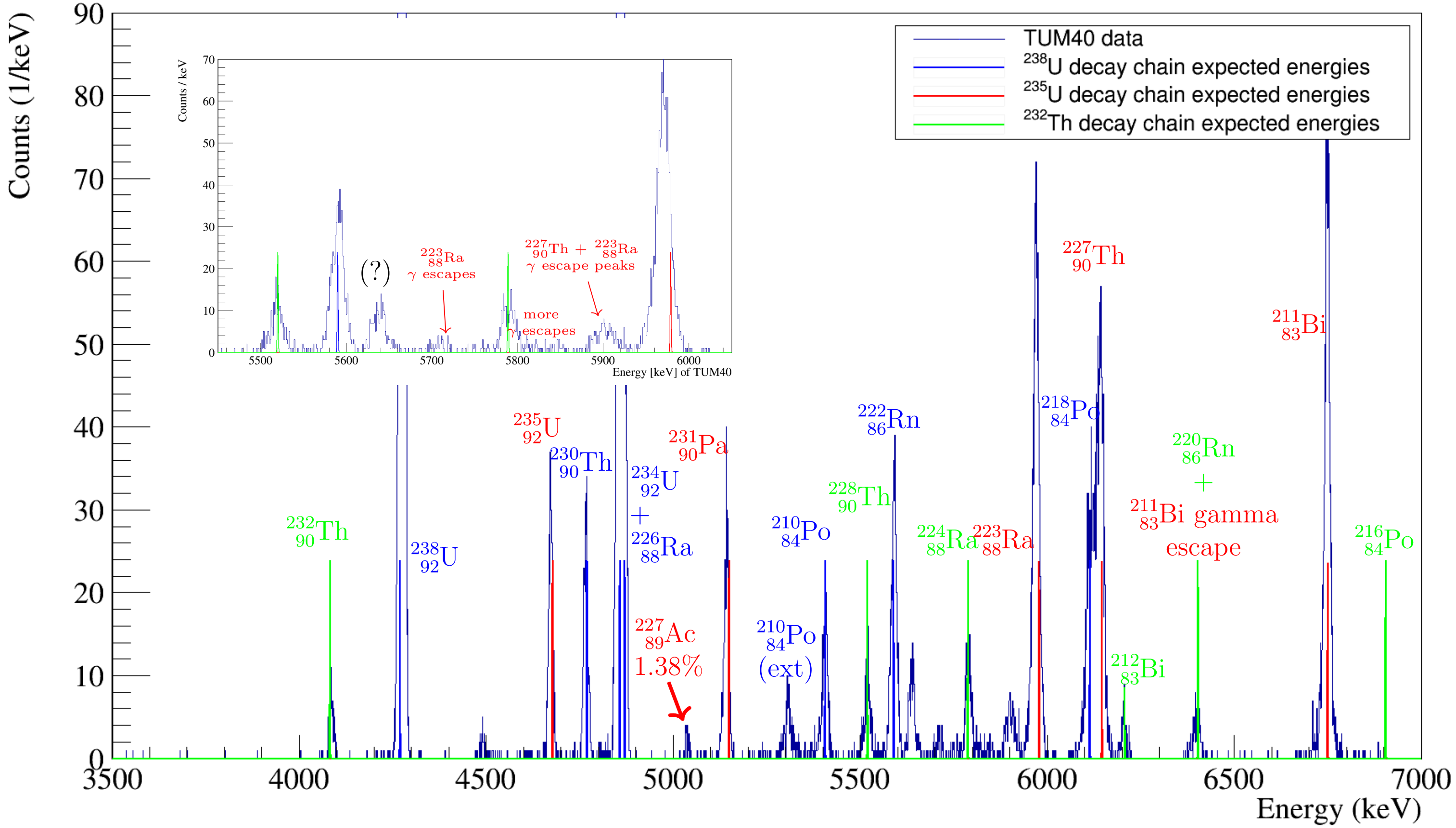

Figure 4.8: Energy spectrum for the α events of TUM40 with the expected energies produced by the different decay chain isotopes indicated. The inset shows a zoom into the energy region between 5450 keV and 6050 keV. Here, most of the γ escape lines from the $^{235}_{92}$U decay chain are located (compare table 4.2). While three of them can be identified the origin of the one marked with a question mark is not clear.

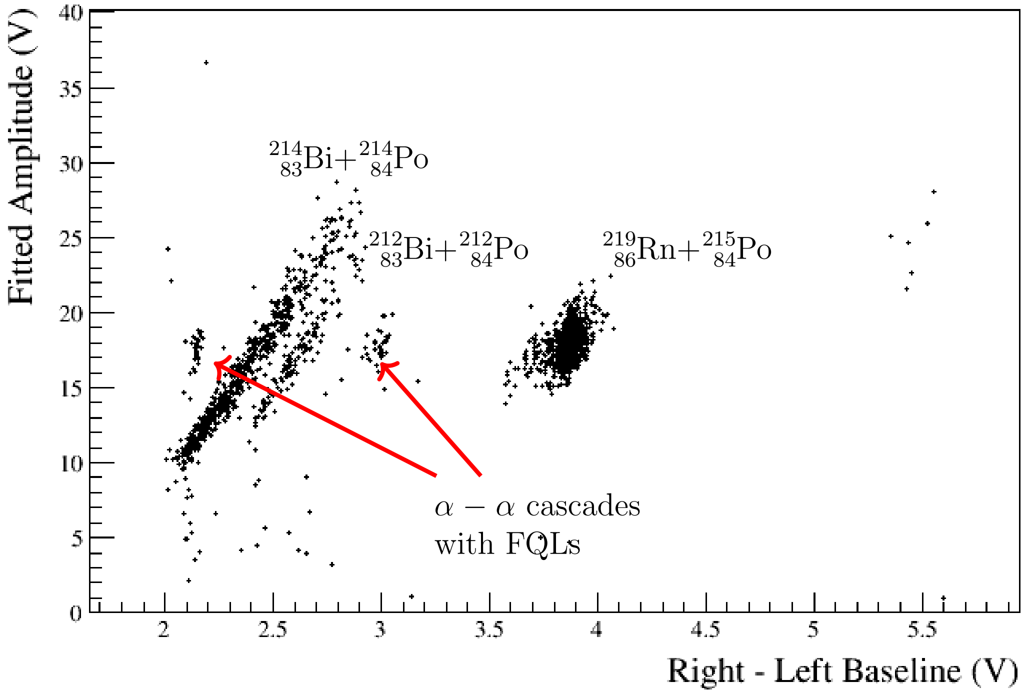

Figure 4.9: The α cascades in TUM40 can be clearly identified with the phonon channel right - left baseline parameter and a fitted amplitude of the light channel. The right - left baseline parameter is used for the phonon channel as the standard event fit with the applied truncation limit becomes unreliable at the energies of the cascades. Furthermore, the right - left baseline parameter is available for the FQLs in the phonon channel for the α-α cascades where the standard event fit would not produce a sensible amplitude parameter.

$^{238}_{92}U$			$^{235}_{92}U$			$^{232}_{90}Th$		
Isotope	Events	Rate [µBq/kg]	Isotope	Events	Rate [µBq/kg]	Isotope	Events	Rate [µBq/kg]
$^{238}_{92}U$	10676	1010^{+114}_{-59}	$^{235}_{92}U$	435		$^{232}_{90}Th$	105	10^{+172}_{-1}
$^{234}_{92}U$	$[10777]^{(1)}$	$[1019]^{+113.4}_{-59}$	Escape	48 (9.9 %)		$^{228}_{90}Th$	214	20^{+171}_{-1}
$^{230}_{90}Th$	406	38^{+170}_{-2}	total $^{235}_{92}U$	483	46^{+170}_{-3}	$^{224}_{88}Ra$	241	23^{+171}_{-2}
$^{226}_{88}Ra$	$[605]^1$	57^{+169}_{-3}	$^{231}_{91}Pa$	445	42^{+170}_{-2}	$^{220}_{86}Rn$	$71^{(3)}$	$6.7^{+172}_{-0.4}$
$^{222}_{86}Rn$	605	57^{+169}_{3}	$^{227}_{90}Th$	$[1326{,}1333]^{(2)}$		$^{212}_{83}Bi$ 36%	93	9^{+172}_{-1}
$^{218}_{84}Po$	$[605{,}612]^2$	$[57^{+169}_{-3}, 58^{+169}_{-3}]$	escape	$112^{(2)}$ (8 %)		$^{212}_{83}Bi$ 64% + $^{212}_{84}Po$	136	12
$^{214}_{83}Bi$+$^{214}_{84}Po$	613	55	total $^{227}_{90}Th$	[1438,1445]	$[136^{+165}_{-8}, 137^{+164}_{-8}]$			
$^{210}_{82}Pb$	β decay		$^{223}_{88}Ra$	1297				
$^{210}_{84}Po$	311	29^{+171}_{-2}	escape $^{223}_{88}Ra$	112 (8 %)				
$^{210}_{84}$PoExt	163	15^{+171}_{-1}	total	1408	133^{+165}_{-8}			
			$^{215}_{86}Rn$ + $^{215}_{84}Po$	1330	118.5			
			$^{211}_{83}Bi$	1412				
			escape	55 (3.7 %)		≈5.64 MeV	212	20^{+171}_{-1}
			total $^{211}_{83}Bi$	1467	139^{+164}_{-8}			

Table 4.6: Rates of α events observed for TUM40. Isotopes marked in red can break secular equilibrium. The column labeled “events” gives the number of events measured in an α peak among the analyzable αs. For an explanation of the error intervals see text. There is an unidentified line observed at around 5.64 MeV.

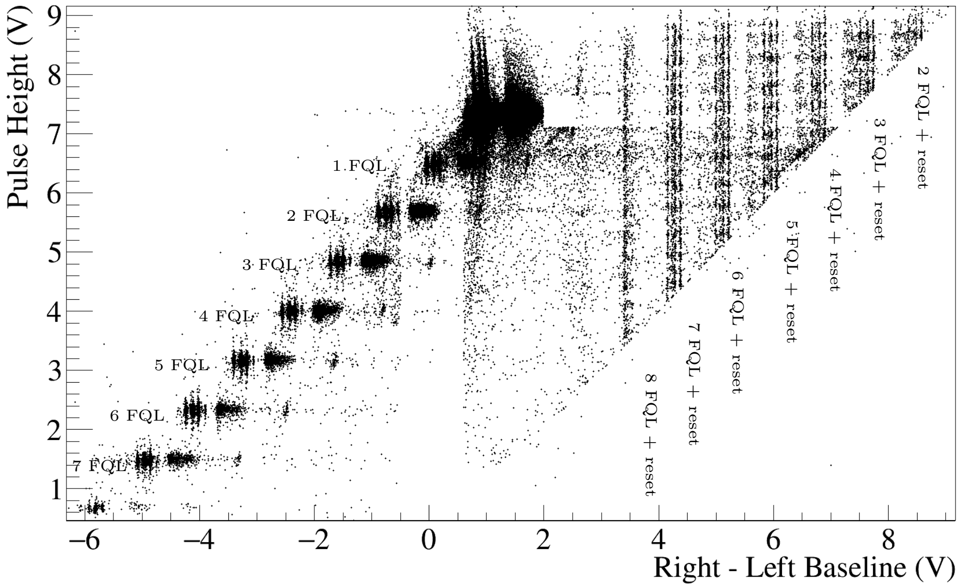

Figure 4.10: The different FQLs and SQUID resets for Lise can be clearly identified in the pulse height vs right - left baseline plane. FQLs reduce the pulse height and the right - left baseline parameter by about 0.83 V. SQUID resets add about 9.23 V to the right - left baseline parameter and randomize the pulse height depending on the timing of the reset in the pulse record.

4.3.2 Lise

The data selection criteria for Lise are listed in table E.2 in the appendix. The α basis of Lise includes 694681 events, corresponding to an upper limit on the total α rate of 50.4 mBq/kg. Out of those, a total of 631326 are analyzable. The estimate of the average survival probability yields $\frac{631326}{694681} = 0.91$. Most problematic events are FQLs which are much more abundant in Lise than in TUM40.

The plot of pulse height vs right - left baseline parameter shown in figure 4.10 can be used to identify and partially assign the FQLs to their original α line.

Taking the SQUID resets into account, each of the eight visible FQL levels appears to have about the same amount of events (3000-3500 events). The clearly identifiable FQLs make up 60-70 % of the deemingly problematic events. The exact number of FQLs for a given α line depends on its energy. The $^{230}_{90}$Th + $^{234}_{92}$U + $^{226}_{88}$Ra peak has about 0.6 % single FQLs, the $^{218}_{84}$Po+$^{227}_{90}$Th peak about 0.85 %.

The error estimation is adapted to that knowledge. The lower limit is again the number of events directly observed in a peak divided by the raw live time. The quoted value is based on the observed number N_0 of events in the peak corrected by the maximum expected FQL loss for the α lines: $N = N_0 \cdot (1 + 8 \cdot 0.0085) = N_0 \cdot 1.068$. Here 8 is the number of observed FQL levels and 0.0085 the estimated ratio between 1 FQL and 0 FQL events of the $^{218}_{84}$Po+$^{227}_{90}$Th peak. The first upper limit is the observed number of events corrected by the estimated average survival probability of 0.91. The second upper limit is the value obtained from correcting for identifiable FQL losses and then assigning the total number of still unexplained lost events ($\sim$ 20000 events) to the peak in question.

The energy calibration of the phonon channel of Lise is based on the $^{238}_{92}$U and $^{211}_{83}$Bi peaks. The final spectrum is shown in figure 4.11. All observed lines can be assigned to known origins except for two small lines marked with a (?). One of those is again in the $\approx$5640 keV range, where an unexpected line is also observed in TUM40. The energy calibration shows a deviation from literature values especially between 4500 keV and 5400 keV. The unambiguous identification of α lines is still possible, so no further corrections were applied. In Table 4.7 the observed activities are summarized. The γ escape events are treated as for TUM40.

Again, there are three double peaks that cannot be separated. Their activities are given in brackets in table 4.7 and marked with the corresponding indices $^{(x)}$:

- **$^{234}_{92}$U and $^{226}_{88}$Ra $^{(1)}$:** $^{226}_{88}$Ra is in equilibrium with the clearly identified $^{222}_{86}$Rn line. Therefore, it is assumed to contribute the same number of events to the combined peak and the remaining number is assigned to $^{234}_{92}$U.
- **$^{218}_{84}$Po and $^{227}_{90}$Th $^{(2)}$:** similar to TUM40, the activities are estimated via the equilibrium with $^{222}_{86}$Rn on the $^{218}_{84}$Po side. On the $^{227}_{90}$Th side, the equilibrium with the average of $^{211}_{83}$Bi and $^{223}_{88}$Ra is exploited, including escape peaks.
- **$^{220}_{86}$Rn and $^{211}_{83}$Bi escape peak $^{(3)}$:** as described for TUM40, it is estimated that $^{220}_{86}$Rn contributes 31% of the average number of events of $^{228}_{90}$Th and $^{224}_{88}$Ra to the peak.

The analysis of the **α cascades** is complicated by the bad performance of the light detector. The two α-β cascades cannot be distinguished. Therefore, only the total number of observed events is given. The estimated rate for the α-α cascade of the $^{235}_{92}$U chain fits to the observed rates for $^{211}_{83}$Bi and $^{223}_{88}$Ra. FQLs are much more prevalent for this cascade, estimated to $\approx 8 * 0.024 = 19\%$ with eight FQL levels and an average loss of 2.4 % per level, analogously to the estimate discussed for the normal α events. Furthermore, mixing with other pile-up sources and similar artifacts is expected. Due to these complications no error is determined. The two quoted rates are based on the number of events in the α-α peak and the events in the α-α peak plus the identified FQLs.

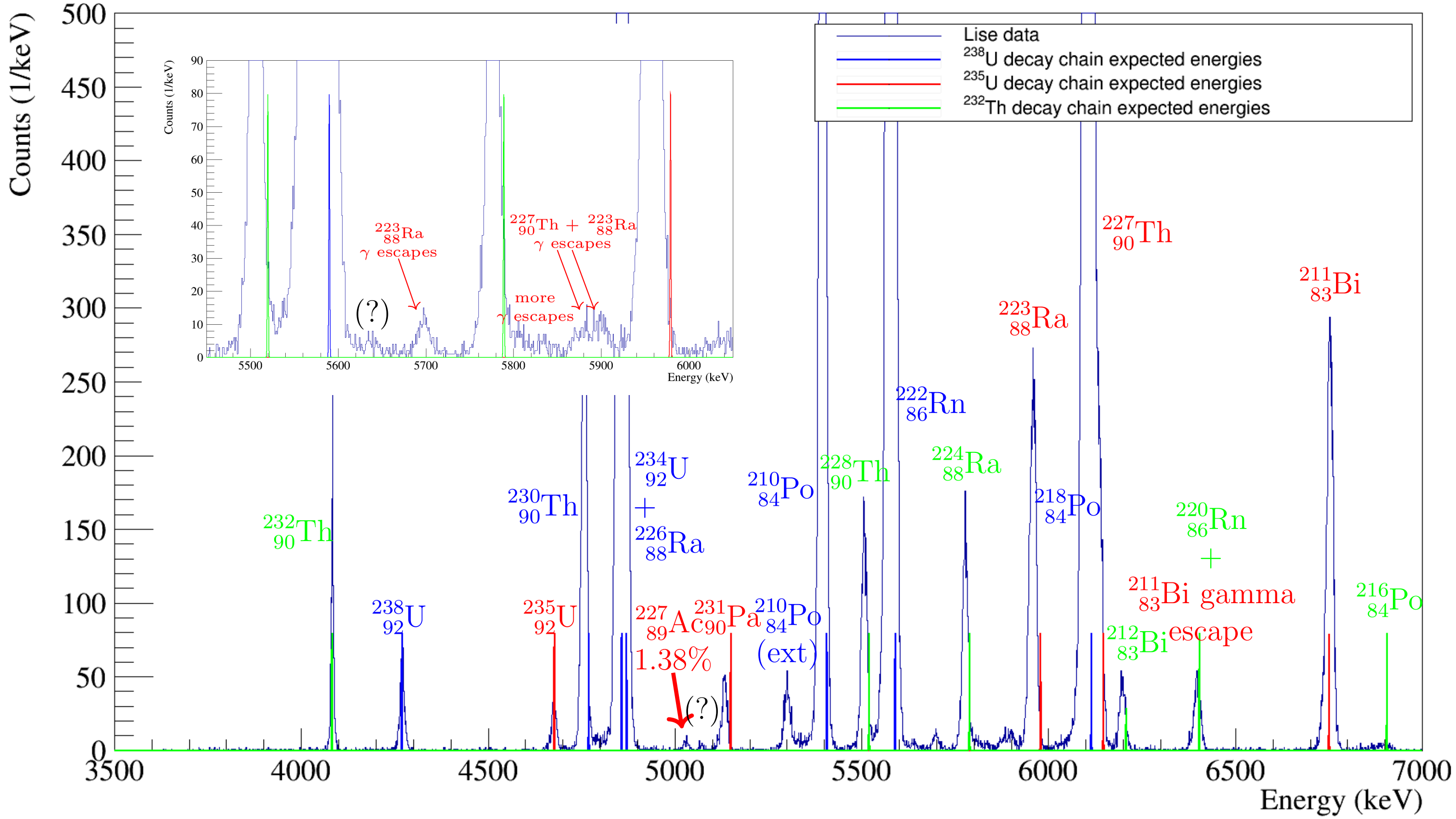

Figure 4.11: Energy spectrum of the α events of Lise with the expected energies produced by the different decay chains indicated. The $^{238}_{92}$U chain is dominating. The inset shows a zoom into the energy region between 5450 keV and 6050 keV where most of the γ escape lines from the $^{235}_{92}$U decay chain are located, compare table 4.2. While three of them could be identified, the origin of the lines marked with a question mark is not clear. As described in the text the energy calibration is slightly off with respect to literature values.

$^{238}_{92}$U			$^{235}_{92}$U			$^{232}_{90}$Th		
Isotope	Events	Rate [µBq/kg]	Isotope	Events	Rate [µBq/kg]	Isotope	Events	Rate [µBq/kg]
$^{238}_{92}$U	883	$68^{+2+1445}_{-4}$	$^{235}_{92}$U	545	$42^{+1+1447}_{-4}$	$^{232}_{90}$Th	1370	$106^{+3+1441}_{-7}$
$^{234}_{92}$U	$[2073]^1$	$[161]^{5+1436}_{-10}$	Escape	26 (4.6 %)		-$^{228}_{90}$Th-	2912	$226^{+7+1430}_{-14}$
$^{230}_{90}$Th	6240	$484^{15+1406}_{-30}$	Sum	571	$44^{+1+1447}_{-3}$	$^{224}_{88}$Ra	2850	$221^{+7+1430}_{-14}$
$^{226}_{88}$Ra	$[139021]^1$	$[10773]^{326+439}_{-686}$	$^{231}_{91}$Pa	889	$69^{+2+1444}_{-4}$	$^{220}_{86}$Rn	903^3	$70^{+2+1445}_{-4}$
$^{222}_{86}$Rn	139021^1	$[10772]^{326+439}_{-686}$	$^{227}_{90}$Th	$[5179,5904]^2$		$^{212}_{83}$Bi 36%	984	$76^{+2+1444}_{-5}$
$^{218}_{84}$Po	$[138296,139021]^2$	$[10716^{325+444}_{-682}, 10772^{326+439}_{-686}]$	Escape	267 ^{2} (4 %-5 %)		$^{212}_{83}$Bi 64% + $^{212}_{84}$Po	??	
$^{214}_{83}$Bi+$^{214}_{84}$Po	total 136988		Sum	[5447,6171]	$[422^{+13+1410}_{-27}, 478^{+14+1407}_{-30}]$			
$^{210}_{82}$Pb	β		$^{223}_{88}$Ra	5606				
$^{210}_{84}$Po	31268	$2423^{+73+1223}_{-154}$	Escape	377 (6.3 %)				
$^{210}_{84}$PoExt	1007	$78^{+2+1443}_{-5}$	Sum	5983	$463^{+14+1407}_{-30}$			
			$^{215}_{86}$Rn + $^{215}_{84}$Po	[5616,6000]	407-465			
			$^{211}_{83}$Bi	6152				
			Escape	208^3 (3.4 %)		≈5.64 MeV	78	$6.0^{+0.2+1451}_{-0.6}$
			Sum	6360	$493^{+15+1405}_{-31}$			

Table 4.7: Rates of α events observed for Lise. Isotopes marked in red can break secular equilibrium. The column labeled “events” gives the number of events measured in an α peak among the analyzable αs. For an explanation of the error intervals see text. The number of events in the unidentified line observed at around 5.64 MeV is also listed.

4.3.3 VK28

VK28 does not play a major role in the main analysis of CRESST-II. Therefore, no quantitative, detailed analysis of the α lines has been performed. Nonetheless, VK28 is of interest for the qualitative understanding of the α behavior. The beaker design has a high coverage of the detector surface by the light detector. This is especially important for surface α decays where only the α but not the recoiling nucleus deposits its energy in the main absorber crystal. Due to the high surface coverage by the light detector, most of the recoiling nuclei are stopped by the light detector, leading to a clear "light" signal. The surface decays can happen on both, the light detector and the main absorber crystal surfaces.

Unfortunately γs of the γ escape lines cannot be detected in the beaker for further characterization. This is due to the fact that the beaker is made of silicon and has a thickness of only 0.5 mm while the attenuation length of 200 keV γs in silicon is in the order of cm [143].

The analysis follows the same steps as described for TUM40 and Lise. Data selection criteria are chosen very strict to have a clean spectrum of events. A pulse height based amplitude correction and a time dependent, peak based calibration are applied to the phonon channel. A peak based calibration in terms of keVαe (keV α equivalent) is applied to the light channel, analogously to the keVee calibration described in section 3.5.5.2.

The resulting light vs phonon energy plot is shown in figure 4.12. The surface α events can be clearly identified. They have a high "light" signal and a slightly lower phonon signal compared to the same, completely contained decay. It can be seen that such surface events appear for most of the α lines. Furthermore, the cascades can be clearly identified and separated. The tilt of the α lines in the light vs phonon energy plane corresponds to the splitting of energy between beaker and phonon detector with some losses due to the detection efficiency for the light in the beaker.

Some lines, predominantly of the $^{235}_{92}$U decay chain, have a population with a higher fraction of energy in the light channel, compare figure 4.12, bottom. A possible explanation is the reabsorption in the absorber crystal of the γs discussed for the γ escape lines, compare section 4.1.2. γs have a higher light yield and will therefore slightly increase the total light yield of the α decay. The increased light yield can also be seen in TUM40 to a certain extent. However, the difference between the α only and $\alpha + \gamma$ lines are not resolved by the TUM40 light detector. The performance of the Lise light detector does not allow for an analogous observation.

The line tilt due to the energy splitting can be corrected similarly to what is discussed in appendix F. This improves the resolution in the phonon channel. The final energy spectrum with all corrections applied can be seen in figure 4.13. The two $^{227}_{90}$Th + $^{223}_{88}$Ra escape lines can be separated. It is clearly visible that the line at around 5640 keV also seen in TUM40 and Lise actually consists of two lines. It is still not possible to resolve the escape lines between the $^{223}_{88}$Ra and $^{224}_{88}$Ra peaks. The correction assigns slightly too high energies to the surface events. This is most likely due to the fact that a recoiling nucleus from an α decay deposits all of its energy in the beaker while the scintillation light has some losses. As the correction is based on the line tilt due to scintillation light it overestimates the energy lost to the phonon channel for the surface events.

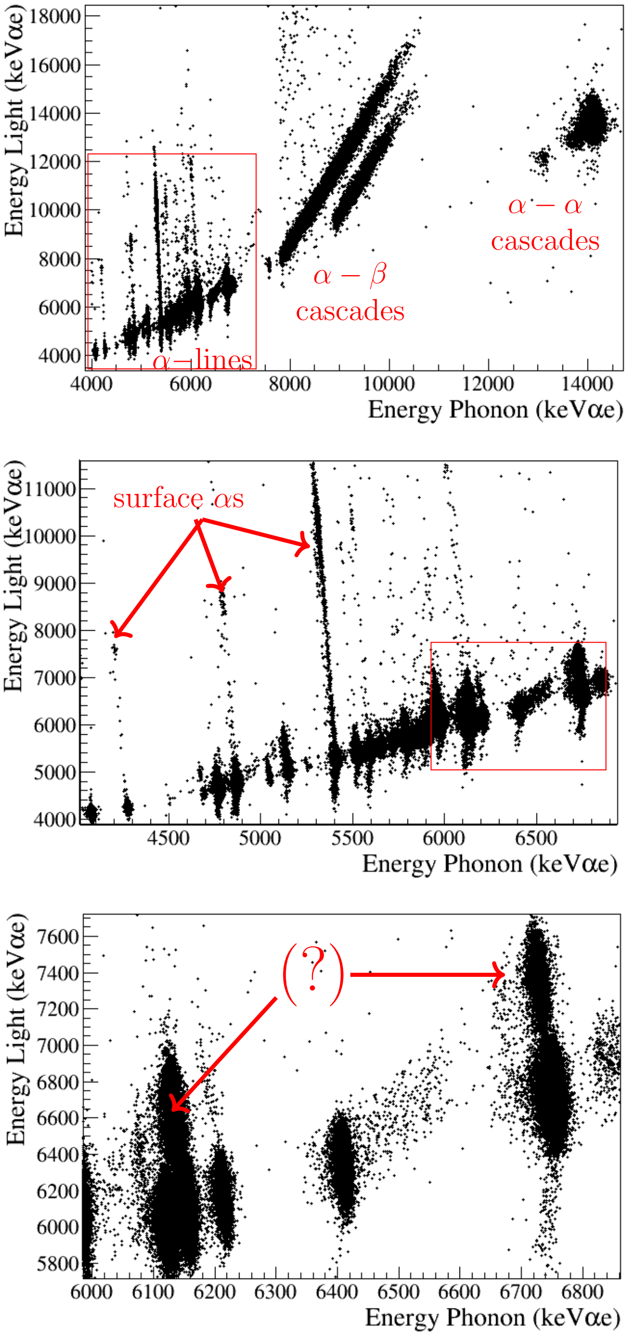

Figure 4.12: Light vs phonon energy plot in terms of keVαe of the VK28 data. Energies are not yet corrected for the splitting of energy between light and phonon channel, hence, a tilt in the lines can be observed. The events extending from the main populations between 4000keVαe and 7500keVαe to higher light energies are surface decays. The red squares mark the zoom area of the subsequent picture. A possible origin of the populations with only a slightly increased light output, marked with an (?), is the re-absorption of γs emitted in the α decays.

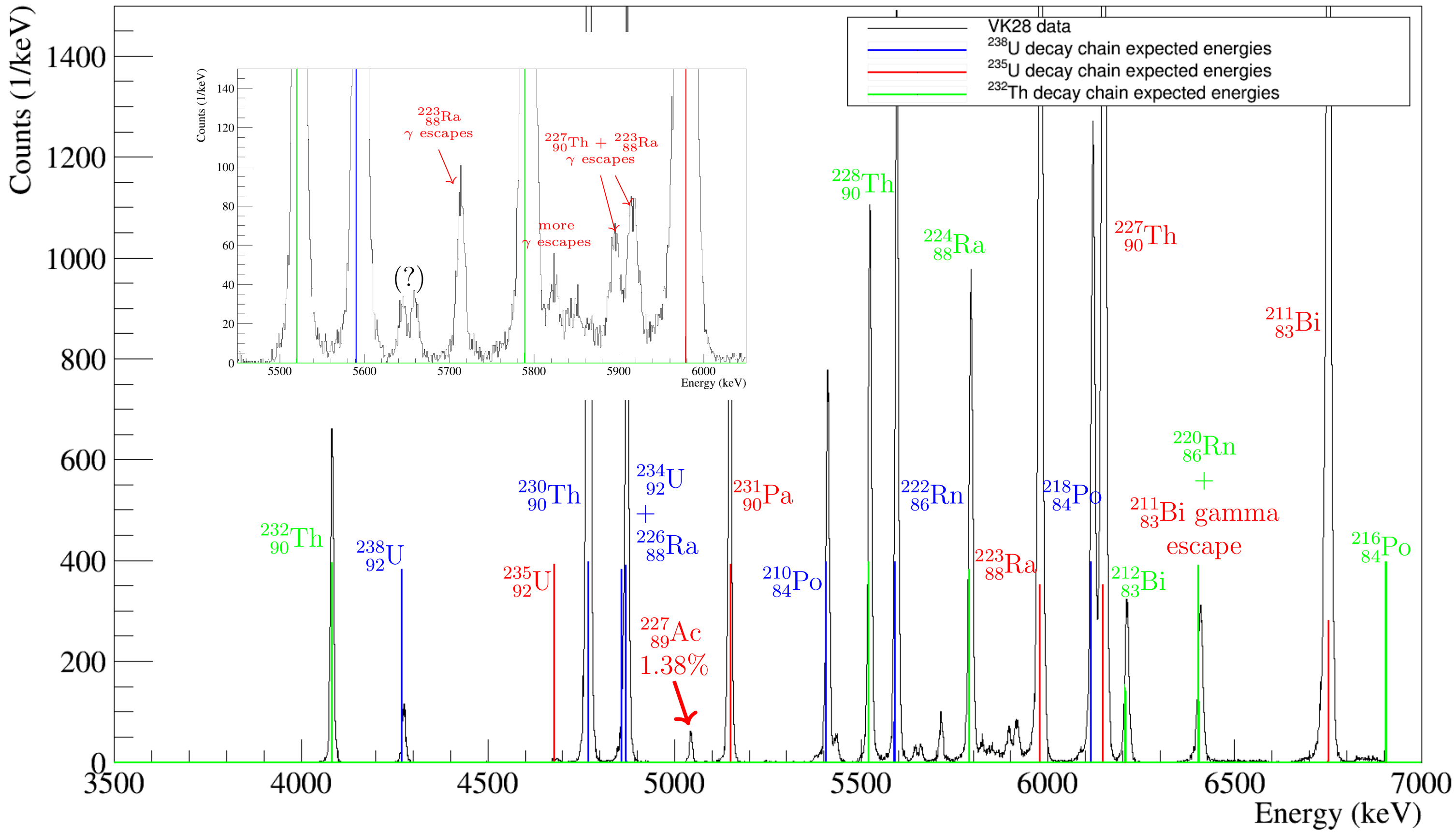

Figure 4.13: Energy spectrum of the α events of VK28 with the expected energies produced by the different decay chain isotopes indicated. The energy is corrected for the loss of scintillation light, see text for details. The inset shows a zoom into the energy region between 5450 keV and 6050 keV where most of the γ escape lines from the $^{235}_{92}$U decay chain are located, compare table 4.2. While three of them could be identified, the origin of those marked with a question mark is not clear.

4.4 Comparison with related Works

4.4.1 Beta/Gamma and Alpha Backgrounds in CRESST-II Phase 2 [126]

In [126] an α analysis has already been performed for TUM40 with the first 29 kgd of the total 130 kgd exposure of MCII-2. Additionally, an analysis of the β/γ background and a background simulation based on that data is presented.

In general, the resolution of the α lines could be improved in the present work compared to [126]. Furthermore, the presence of the γ escape peaks was not taken into account in [126].

The observed rates are compared in table 4.8 in the columns marked with "TUM40 MCII-2 [126]". The values for the comparison from this work are the lower limit and the given value as presented in table 4.6. Where relevant, only the rate obtained for the main peaks without γ escape lines is considered for better comparability.

In general, the limits determined in this work are higher than the rates observed in [126]. Differences can be the result of the different size of the data sets and different analysis approaches. It should be noted that the errors in [126] have a different meaning compared to the limits on the observed rate given in this work. There are a few α decays that should be noted explicitly:

- For $^{231}_{91}$Pa, [126] indicates a rate of 23.2 ± 4.4µBq/kg while this work finds limits for the observed rate of 40 µBq/kg to 42 µBq/kg. No explanation for the difference can be given in this work.
- In general, there is a good agreement of rates for the $^{232}_{90}$Th chain. The comparably high difference for the $^{228}_{90}$Th peak of 15.2 ± 4.2µBq/kg in [126] compared to between 19 µBq/kg and 20 µBq/kg in the present work can be explained by a better separation from the $^{222}_{86}$Rn peak. The same holds for $^{230}_{90}$Th and the $^{234}_{92}$U/$^{226}_{88}$Ra peak.
- The low value of 38.1 ± 4.9µBq/kg for $^{222}_{86}$Rn in [126] compared to 54 µBq/kg to 57 µBq/kg in this work is somewhat surprising. The overlap with the unexplained line at around 5640 keV is not resolved in [126], hence a higher rate should be expected.

$^{238}_{92}$U				$^{235}_{92}$U				$^{232}_{90}$Th			
Isotope	Rate [µBq/kg] from TUM40 MCII-2 [126]	Rate [µBq/kg] from C.Turkoglu [136]	Rate [µBq/kg] this work	Isotope	Rate [µBq/kg] from TUM40 MCII-2 [126]	Rate [µBq/kg] from C.Turkoglu [136]	Rate [µBq/kg] this work	Isotope	Rate [µBq/kg] from TUM40 MCII-2 [126]	Rate [µBq/kg] from C.Turkoglu [136]	Rate [µBq/kg] this work
$^{238}_{92}$U	$1.01 \pm 0.02) \cdot 10^3$	1073.2 ± 15.4	[951,1010]	$^{235}_{92}$U	39 ± 4.4	45.5 ± 3.2	[39,41]	$^{232}_{90}$Th	9.2 ± 2.3	10.9 ± 1.5	[9.4,9.9]
$^{234}_{92}$U	$(1.08 \pm 0.03) \cdot 10^3$	1085.5 ± 16.5	[960,1020]	$^{231}_{91}$Pa	23.2 ± 4.4	45.0 ± 3.1	[40,42]	$^{228}_{90}$Th	15.2 ± 4.2	25.4 ± 3.4	[19,20]
$^{230}_{90}$Th	55.8 ± 5.4	51.2 ± 4.4	[36,38]	$^{227}_{90}$Th	105 ± 19	141.7 ± 8.5	[109,126]	$^{224}_{88}$Ra	19.8 ± 8.1	31.1 ± 2.8	[21,23]
$^{226}_{88}$Ra	43 ± 9.9	66.1 ± 5	[54,57]	$^{223}_{88}$Ra	104 ± 7	134.8 ± 5.6	[116,123]	$^{220}_{86}$Rn	8.4 ± 3.4	13.2 ± 1.8	[6.3,6.7]
$^{222}_{86}$Rn	38.1 ± 4.9	66.1 ± 5.0	[54,57]	$^{219}_{86}$Rn + $^{215}_{84}$Po	107 ± 7		[118]	$^{212}_{83}$Bi 36%	$7.7^{+8.9}_{-7.7}$		[8.3,8.8]
$^{218}_{84}$Po	43.1 ± 9.9	66.1 ± 5.0	[54,67]	$^{211}_{83}$Bi	105 ± 7	147.1 ± 5.5	[126,134]	$^{212}_{83}$Bi 64% + $^{212}_{84}$Po	15.8 ± 2.8		[12]
$^{214}_{83}$Bi + $^{214}_{84}$Po	47.4 ± 4.9		[55,58]								
$^{210}_{84}$Po	17.8 ± 4.0	33.1 ± 2.8	[28,29]								

Table 4.8: Comparison of activities obtained in different analyses for α decays of TUM40 in MCII-2. Isotopes marked in red can break secular equilibrium. For details see text.

4.4.2 Development of a Geant4 Based Electromagnetic Background Model for the CRESST Experiment [136]

The data presented in [136] for the α lines is based on a previous version of the analysis presented in this chapter. It uses the average survival probability calculated from the α basis and the number of analyzable events, as described in section 4.2.4.

The estimate for the survival probability in [136] yielded 86 %. With the optimized version in this work about 94 % is achieved by safely removing more of the non-α artifacts. Therefore, the values given in [136] are systematically higher than the ones reported in section 4.3.1. They are summarized in the columns marked with ”C.Turkoglu [136]” in table 4.8.

4.4.3 High-Purity CaWO 4 Single Crystals for Direct Dark Matter Search with the CRESST Experiment [138]

In [138] an α analysis has been performed on a number of CRESST-III phase one detectors. The target crystals of the investigated detectors where produced within the CRESST collaboration, analogously to the target crystal of the TUM40 detector. The results for TUM40 presented in this work are compared to the results found in [138] for the CRESST-III phase one detector modules A and E in table 4.9. These two detector modules are relevant for the dark matter analysis presented in chapter 5 of this work. The same comparison to TUM40 has been performed in [138] with the α background rates extracted in [126].

Due to technical limitations the α analysis presented in [138] does not achieve the required resolution to resolve a number of lines and only quotes a summed activity. For the values of TUM40, the limits of the summed activity for those lines is calculated following the same procedure as for a single line, i.e., by summing the number of events and then following the steps outlined in section 4.2.4.

In total, the results of this work do not show a drastically different picture compared to the original comparison with the activities for TUM40 taken from [126]. Hence, detailed conclusions on the comparison can be found in [138] and are not repeated here.

4.5 Summary and Conclusions

A detailed α analysis of the most relevant detectors TUM40 and Lise of MCII-2 has been presented in this chapter. Furthermore, the detector module VK28 has been qualitatively analyzed. Dedicated methods for analyzing highly saturated, high energy (MeV) events have been presented. Those methods might be of relevance for future, similar analyses.

As an immediate result this chapter provides the observed internal α activities with different assumptions for the uncertainties. Compared to [126] and [136] an

	Activities [mBq/kg]			
α line(s)	TUM40 (this work)	TUM40 as quoted in [138] from [126]	Module A [138]	Module E [138]
single α lines	$2.98^{+0}_{-0.17}$	3.08 ± 0.04	2.020 ± 0.098	3.319 ± 0.122
α cascades	$0.19^{+0.02}_{-0}$	-	0.353 ± 0.041	0.682 ± 0.055
$^{232}_{90}$Th	$0.01^{+0.172}_{-0.001}$	0.009 ± 0.002	0.052 ± 0.023	0.185 ± 0.044
$^{238}_{92}$U	$1.01^{+0.11}_{-0.06}$	1.01 ± 0.02	0.293 ± 0.054	
$^{235}_{92}$U	$1.09^{+0.11}_{-0.07}$	0.04 ± 0.004	0.409 ± 0.068	0.616 ± 0.087
$^{230}_{90}$Th		0.06 ± 0.01		
$^{234}_{92}$U		1.08 ± 0.03		
$^{226}_{88}$Ra		0.04 ± 0.01		
$^{211}_{83}$Bi	$0.14^{+0.16}_{-0.01}$	0.11 ± 0.01	0.077 ± 0.030	-

Table 4.9: Comparison of α activities obtained for TUM40 in this work and α activities obtained for two detector modules of CRESST-III phase one in [138].

improved resolution and a more detailed understanding of possible γ escape lines is achieved.

However, there is some discrepancy between the estimated rate of escape events and the observed rate. Furthermore, there are two well visible lines at about 5.64 MeV that could not be identified. There are two γ escape lines from $^{223}_{88}$Ra expected at this position, but with a much smaller expected activity, compare figure 4.1.

The primary purpose of determining the α rates is to understand the low energy β background through equilibrium conditions and simulations as presented in [126] and [136]. The lower limits given in this work can thereby serve for a conservative background subtraction. The quoted values help to simulate how much of the background can be reliably understood. The upper limit, which presents a limit on the worst case sensitivity of the analysis, can give very conservative limits for sensitivity studies. Some of those considerations have already been applied in [136] based on a previous version of the presented analysis.

Furthermore, the results serve as benchmarks for future improvements in crystal radio-purity.

Chapter 5

CRESST-III Phase 1 Dark Matter Analysis

This chapter presents the dark matter analysis of the CRESST-III phase 1 measurement campaign, called MCIII-1 in the following. The main focus lies on the best performing detector module, labeled "detector A". Detector A reaches the lowest nuclear recoil threshold in the phonon channel of the employed detectors: $30.0^{+4.8}_{-6.5}(sys.) \pm 0.2(stat.)$eV.

This chapter is split into two main sections. In the first main section, section 5.1, the primary analysis of detector A is described, leading to limits on dark matter particle-nucleon interaction cross-sections presented in section 5.1.8.5. One of the results of the analysis of detector A is the presence of an exponentially rising background at low energies, severely limiting its sensitivity. Therefore, in the second main section, section 5.2, the origin of this excess is investigated in detail including additional analysis, e.g., of other detector modules. Finally, a summary is given in section5.3.

5.1 Primary Analysis

This section contains the primary dark matter analysis of MCIII-1, detector module A. General information concerning the measurement campaign is summarized in section 5.1.1. Sections 5.1.2 to 5.1.7 largely follow the analysis steps outlined in chapter 3. Section 5.1.8 introduces some error considerations. The results are presented in section 5.1.8.5.

5.1.1 Measurement Setup

5.1.1.1 Detectors

A total of ten identical detector modules of the instrumented stick design were installed in MCIII-1, compare section 2.2. A schematic view of the detector module design is shown in figure 5.1. The modules are alphabetically labeled as detector module A to J. The relevant features for the analysis are the presence of a phonon and a light detector as well as three instrumented holding sticks. The phonon and light detector have their own read-out channel each. The instrumented sticks are read out with a single read-out channel but have separated heater channels. The phonon channels are denoted X-PH, the light channels X-L and the instrumented holding sticks channels X-I.

Three of the ten detector modules (A,E,J) had a satisfactory performance and all channels fully operational. Another three detector modules (B,C,D) had satisfactory performance but not all of the instrumented sticks were operational. The remaining four detector modules were not considered for the analysis due to bad performance or problems with the phonon and/or light channel.

The masses of the main absorber crystals of the relevant detector modules are summarized in the first row of table 5.1.

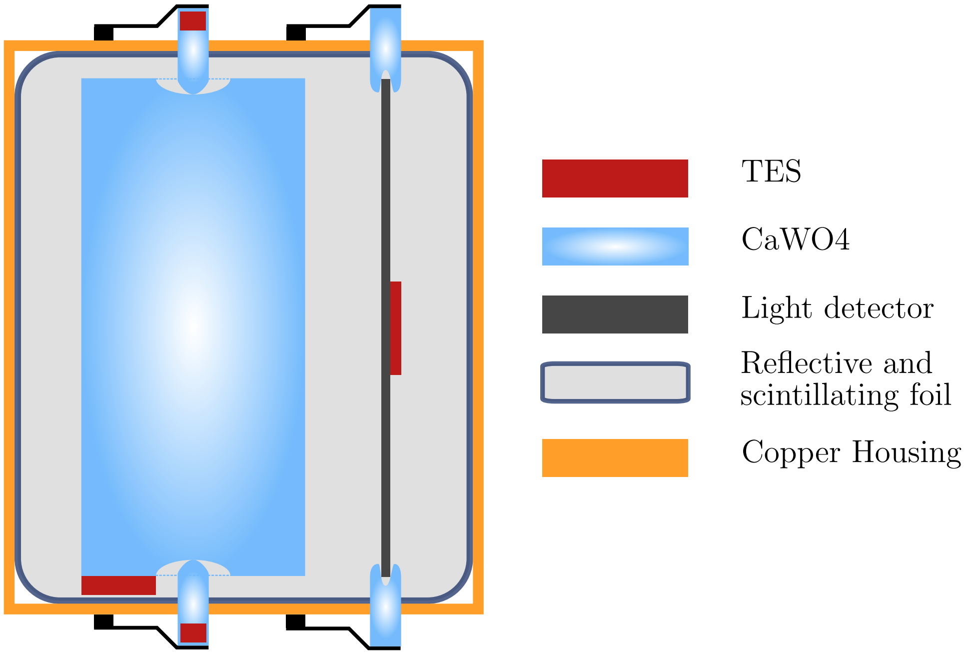

Figure 5.1: Schematic view of the MCIII-1 detector design. The main absorber crystal is surrounded by a scintillating foil and held in place by instrumented $CaWO_4$ sticks (compare section 2.2).

5.1.1.2 Data Acquisition Settings

DAQ type and record window: The hardware triggered and the continuous data acquisition were operated in parallel in MCIII-1, compare section 2.4. The data analyzed in this chapter is solely based on the continuous acquisition and optimum filter based triggering. Details on building the required filter are presented in section 5.1.2.2. The settings concerning record length, thresholds and pre-/post-trigger lengths are summarized in table 5.2.

The record windows of an event are aligned to the phonon detector. This means that the phonon trigger timestamp overwrites the light trigger timestamp. Accordingly, the trigger delay of the phonon channel is always 0 or 491.52 ms where 491.52 ms indicates that the channel did not trigger.

Trigger settings The trigger thresholds were set as described in [144] based on the expected noise trigger rate. The chosen noise trigger expectancy after data selection is 1 count/kg d. A cross-check on the number of observed noise triggers is presented in section 5.2.2.

The channels of the instrumented holding sticks are not triggered.

Heater pulse settings Heater pulses of different energies were injected every few seconds. This is required for the energy calibration (compare section 3.5.3). Heater pulses injected in one of the instrumented holding sticks are also visible in the phonon channel as heat can be transferred via the contact point between the main absorber and the holding sticks. Therefore, the heater pulses could no longer be injected to all channels simultaneously as done for previous CRESST measurements. Because of limitations in the hardware, a sophisticated heater pulsing scheme is required. Furthermore, control pulses for stability control are injected with a similar rate (compare sections 2.3.1.2 and 3.3.1.4).

	Module name	A,D	B,C,E	J
	Absorber mass	23.6 g	24.5 g	23.9 g
Measurement	Raw measurement time (h)	Raw exposure (kg d)		
$^{57}_{27}$Co Calibration	391.828	0.385	0.40	0.39
Neutron calibration	806.121	0.793	0.823	0.803
Dark matter search data (blind)	5689.23	5.594	5.808	5.666
Dark matter search data (training)	865.368	0.851	0.883	0.862
Total dark matter search data	6554.598	6.445	6.691	6.528

Table 5.1: Main absorber mass and exposure of the detector modules suited for analysis of MCIII-1. Information taken from internal documentation and recorded measurement data.

Parameter	Value	Software trigger thresholds			
		A-PH	6.8 mV	B-PH	15 mV
Sampling rate	25 kHz$\widehat{=}$40 µs/sample	A-L	7.5 mV	B-L	6 mV
Record length	16 384 samples$\widehat{=}$655.36 ms	C-PH	21 mV	D-PH	15 mV
Pre-trigger	4096 samples$\widehat{=}$163.84 ms	C-L	60 mV	D-L	30 mV
Post-trigger	12 288 samples$\widehat{=}$491.52 ms	E-PH	10.7 mV	J-PH	6.6 mV
		E-L	2 mV	J-L	13 mV

Table 5.2: Settings for the pulse records and triggering of MCIII-1.

5.1.1.3 Data Sets

The data sets are summarized in table 5.1. Relevant data taking for MCIII-1 started in October 2016 with a two weeks ${}^{57}_{27}$Co calibration measurement. More than one month of neutron calibration data with an AmBe neutron source has been recorded in 2017, corresponding to a total analyzable raw measurement time of 806.12 h.

About 240 days of data suitable for dark matter search have been collected. The measurement campaign was stopped in February 2018 due to technical problems. All stated measurement times already include the pre-selection of analyzable files (compare section 5.1.3.2).

5.1.2 Parameter Gathering

5.1.2.1 Basic Parameters

Basic parameters relevant for the analysis are the peak position, right minus left baseline, delta voltage, pulse height and trigger delay. Furthermore, the testpulse amplitude identifies heater pulses as well as the heater channel used to inject each specific heater pulse.

5.1.2.2 Standard Event Fit and Optimum Filter

For the analysis of MCIII-1, both, the standard event fit and the optimum filter are employed (compare section 3.2.2). The specific choices and challenges for MCIII-1 related to the standard event fit and optimum filter are summarized in the following.

Linear Range of the Detectors The standard event fit as well as the optimum filter require knowledge of the pulse signal shape in the strictly linear region of the detector (compare section 3.2.2). MCIII-1 has a very low number of observed events. Hence, building a first standard pulse from a for sure linear range is impractical. Therefore, the approach described in section 3.2.2.4 is applied to the heater pulses instead. Heater pulses have a different pulse shape than particle events. However, saturation effects, being a feature of the underlying transition of the TES, show up the same way. The required heater standard standard event is build from the lowest heater pulses with a clear pulse signal in the record. The worsening of the fit RMS with increasing amplitude is displayed in figure 5.2. The thus determined linear ranges of the relevant detectors are summarized with the fit settings in appendix G. They determine the truncation limit for the standard event fit.

Building the Standard Event The continuous optimum filter based triggering does not suffer from trigger walk. Therefore, it is not necessary to build the standard pulses from a mono-energetic event population. Furthermore, it is possible to

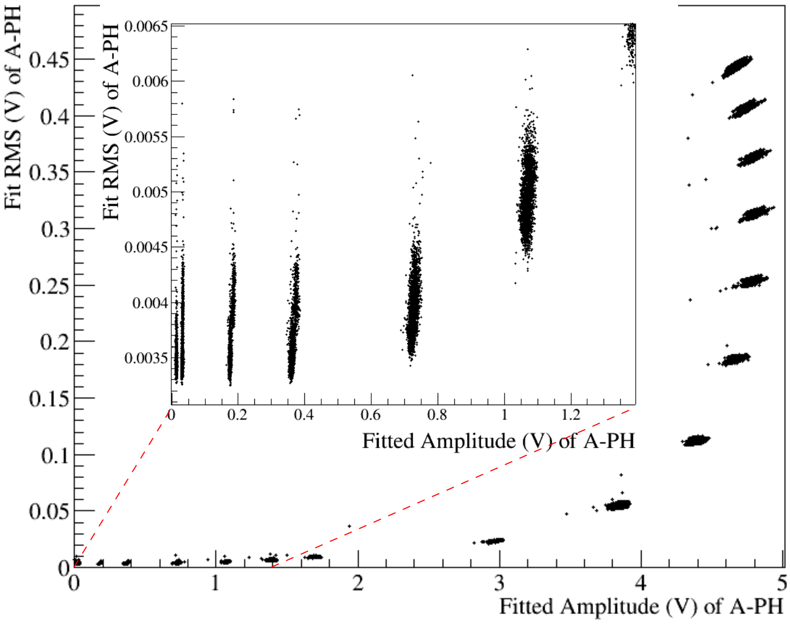

Figure 5.2: Determination of truncation limit and linear range based on heater pulses. Non-linearities lead to an increase in the fit RMS for the displayed untruncated standard event fit. The different event clusters correspond to the different injected heater pulse energies. In case of the displayed detector channel A-PH, the truncation limit is finally set to 0.6 V.

build phonon, light and instrumented stick standard pulses from different events as the standard event will have the correct relative alignment of pulse signals nonetheless.

The standard pulses are build from neutron calibration data as this contains the highest number of events at low energies.

The finally chosen events for building the standard pulses for detector module A are shown in figure 5.3. The chosen events for the phonon channel are displayed in red, the ones for the light channel in green. The truncation limits are marked with accordingly colored lines. Neutron and γ events have the same pulse shape to a very good approximation (compare also appendix A.8.2). Therefore, using them both for the standard event creation does not lead to inconsistencies.

The standard event is built iteratively. The first standard event was taken from the hardware triggered data, including the problem of trigger walk. Then, the data was triggered with the optimum filter build from that standard event. From the triggered data, a new standard event and filter were built and the process repeated.

Building the Optimum Filter Apart from the standard event, the optimum filter requires the noise power spectrum. The noise power spectrum is extracted from

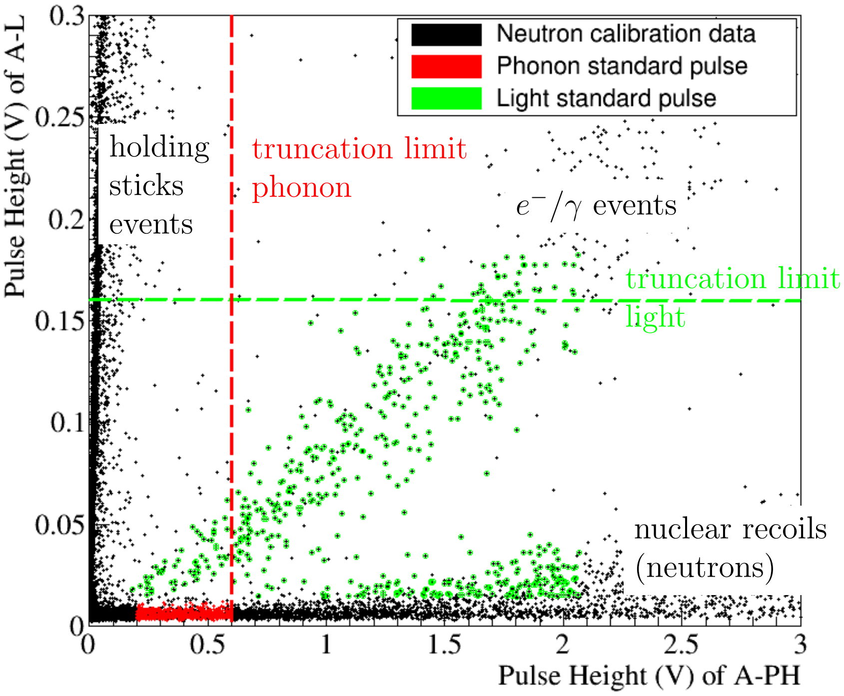

Figure 5.3: Choice of events for building the standard pulses of phonon and light detector with the example of detector module A. Red marks the events from which the phonon standard pulse is build. They are dominantly nuclear recoils. Green marks events with enough light to be used in the light standard pulse. They are found mainly in the β/γ band. Red and green lines mark the truncation limits of the channels which are set with a safety margin below the onset of the non-linearities.

empty baselines of the training set. The set of baselines has to be cleaned from pulse records containing pulse signals or artifacts. This is done by adding a 1 keV pulse signal to the empty baselines, analogous to the event simulation described in section 3.4.2, and applying the data selection criteria of the analysis to the resulting simulated events (compare section 5.1.3 for the selection criteria). If the simulated event passes the data selection, the corresponding empty baseline is kept for the calculation of the noise power spectrum.

For detector modules B,C and D, performance issues were already known from the training set of the hardware triggered data. Therefore, only brief selection on the pulse height and the baseline RMS of the empty baselines is applied.

Applying the Standard Event Fit and Optimum Filter The standard event fit is applied in the correlated, truncated form as described in section 3.2.2. The fit settings are summarized in table G.1 in the appendix. The continuous triggering is very reliable in correctly placing the pulse signal always at the same position in the record. Therefore, the start value for the fitted shift is always taken as zero, avoiding the sophisticated search for the correct position of the pulse signal in the record introduced in [107].

The heater pulses do show a trigger walk effect. This is due to their different pulse shape compared to the particle events the optimum filter of the trigger is build from. The different pulse shape leads to a wrong, energy dependent placing of the pulse onset by the trigger. Therefore, the standard event fit has to be set to cover a broader range of possible time shifts in order to find the pulse signal, reflected in the settings given in table G.1 in the appendix.

The same optimum filter as in the trigger is applied again to the pulse records to obtain the optimum filter parameters.

The optimum filter is not capable of dealing with the saturation of the pulses (compare section 3.2.2.4). This limits its validity to below the truncation limit. To extend the validity, the filtered amplitude parameter is compared against the fitted amplitude of the standard event fit, see figure 5.4. A polynomial of 9th degree is fitted in the non-fully-saturated range. With this polynomial the filtered amplitude can be linearized to a **fitted amplitude equivalent** value. A polynomial is not the optimal choice for this purpose however, as it tends to deviate strongly at the end of the data range. This can be highly problematic as the low energy end is of major interest. Special care was taken in the presented analysis to avoid this effect. However, for future analysis a different fitted function or general approach is required.

5.1.3 Data Selection

The following sections focus on the data selection criteria for detector A. In general, each detector module behaves differently. Therefore, not all described data selection criteria and considerations are directly applicable to the other detectors. The specific choices for the detectors are summarized in appendix G. A special artifact type that poses the dominant background contribution in some of the detector modules of MCIII-1 in terms of rate is introduced in section 5.1.3.1.

5.1.3.1 Special Artifact Class - Baseline Jumps

A previously unobserved type of artifact appears in several detector modules of MCIII-1, compare figure 5.5. They consist of a sudden, temporary jump in the baseline level to a higher or lower value and back. Usually, the jumps last around 10 ms to 100 ms with a height typically between 0 mV to 100 mV. Separation of those events from particle interaction becomes challenging at very low energies as for small amplitudes not much shape information is available. Unfortunately, the low energy range is of major interest for the MCIII-1 dark matter analysis. Therefore, the jump events pose a dangerous background.

The baseline jumps show a strong time dependency. Figure 5.6a shows the trigger rate over the whole of MCIII-1. Time periods with increased rate are dominated by jump events. There are practically no jump events in the other time

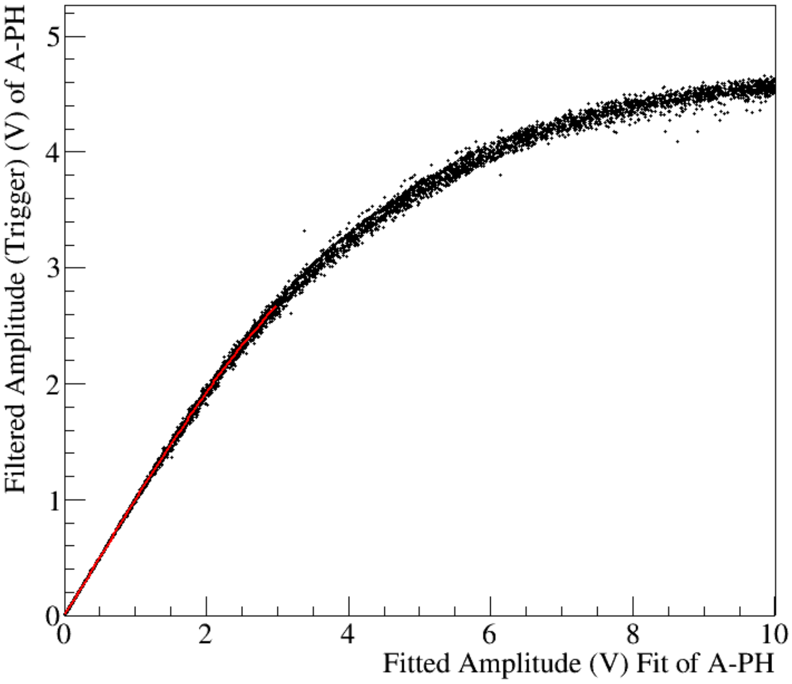

Figure 5.4: Polynomial fit (red) to the relation between the signal amplitudes derived by the optimum filter and the truncated standard event fit. The shown data is from the neutron calibration of detector A. Unlike the truncated standard event fit, the filtered amplitude cannot compensate for the saturation of the observed pulse signals.

periods, at least in detector module A. The rate induced by the baseline jump events follows a 24 hours pattern. This can be seen with the example of detector J in figure 5.6b. It indicates human electronic activity in the experimental hall as a likely origin. However, for most of MCIII-1 and for the other detector modules the correlation is less pronounced. On a smaller time scale, the baseline jump events in detector module A appear mainly in short $\mathcal{O}(\mathrm{min})$ bursts, see figure 5.6c.

The origin of these events and whether they are induced at the level of the TES or the SQUID electronics could not be clarified. In section 5.2.3 the contribution of those events to the final observed spectrum in detector A is discussed in more detail.

5.1.3.2 Preselection on Files and Time periods

Unusable Files Data files with a measurement time below five hours are excluded from the analysis as they often indicate unstable running conditions and complicate the energy calibration. Similarly, data files with known issues are discarded. This includes files with technical issues as well as with earthquakes during the time of recording. All measurement times presented in this chapter refer to the time

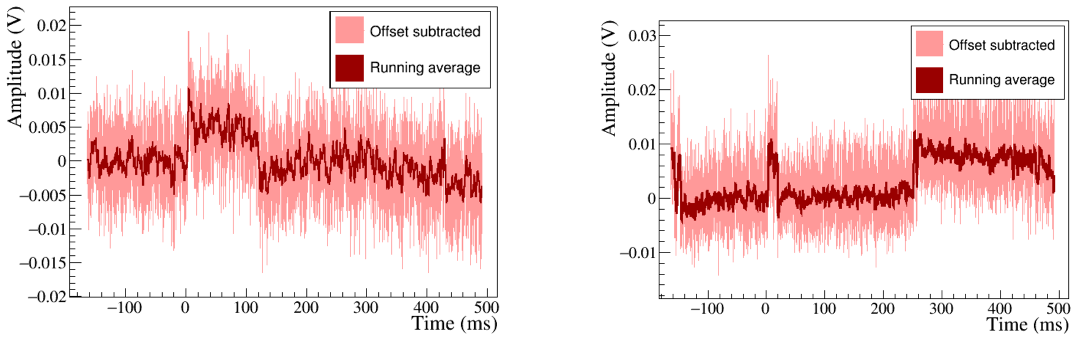

(a) (b)

Figure 5.5: Examples for the baseline jump artifacts observed in several detectors of MCIII-1. The pulse records are shown in light red with only the offset subtracted. In dark red additionally a 50 samples running average is applied. a) Detector module A-phonon b) Detector module J, phonon

remaining after this selection.

Trainings and Blind Set The training set (compare section 3.3.1.2) is chosen as about 20 % of the dark matter search data. The 20 % are equally distributed over the complete measurement time of MCIII-1. The remaining 80 % form the blind set.

Rate Cut The jump events introduced in section 5.1.3.1 show a strong clustering in time. Accordingly, a rate cut is applied that removes those high rate periods. Any emerging separated time period of less than 5 h is also removed. The settings are summarized in appendix G. The events removed by stability and rate cut are indicated in red in figure 5.6a .

Stability Cut A stability cut is applied as described in section 3.3.1.4. The settings are summarized in appendix G. While the control pulse based stabilization does not show any indication of unexpected instability, the baseline noise is far from stable. This is discussed in more detail in section 5.2.1

5.1.3.3 Corrupted Pulses

Data selection criteria against corrupted pulses are applied based on the peak position parameter, the right minus left baseline parameter of both phonon and light channel, the delta voltage parameter, the RMS of the standard event fit of both the phonon and light channel and the local RMS of the optimum filter in the phonon channel. They target the usual types of artifacts as described in section 3.3.2. The settings are summarized in appendix G. Decaying baselines as targeted by the selection on the peak position are much more abundant in the continuous

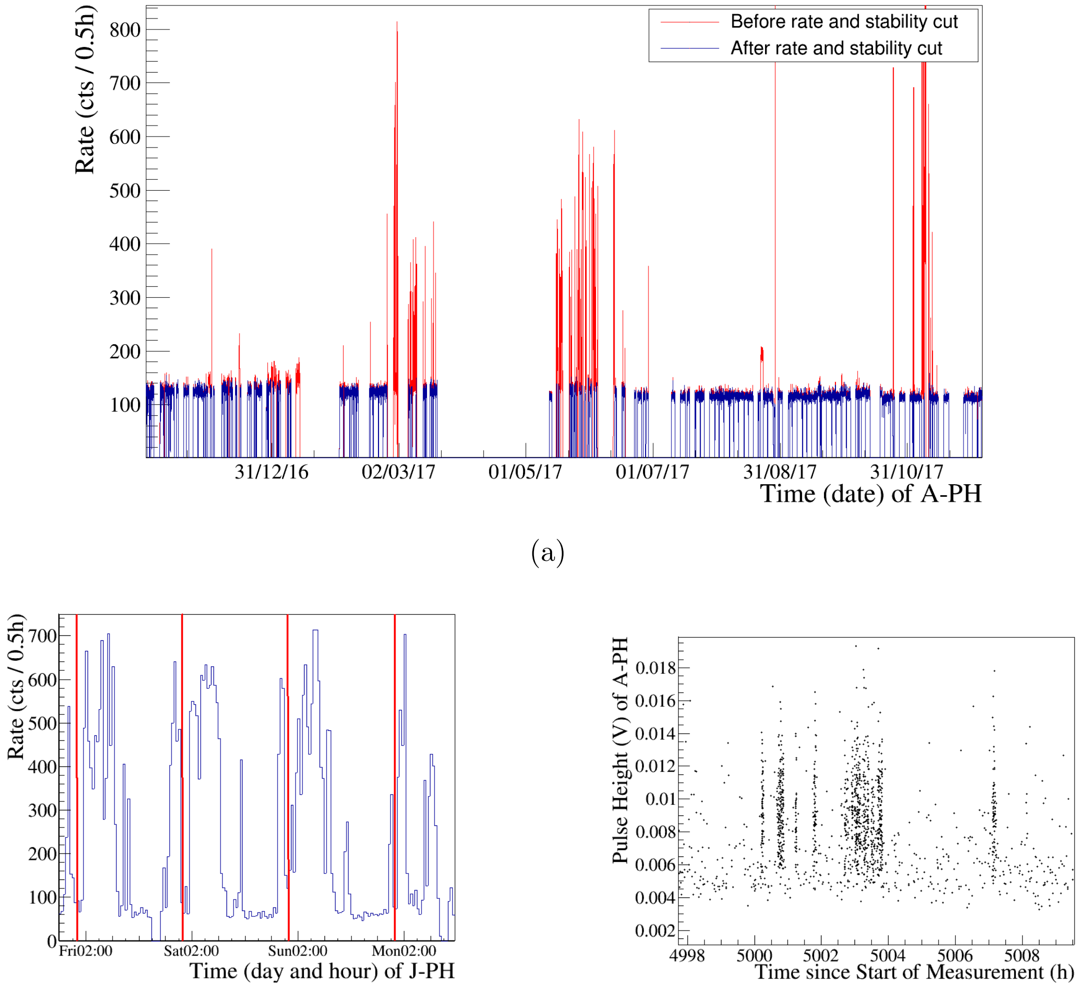

(a)

(b)

(c)

Figure 5.6: Detector trigger rate, rate cut and time distribution of baseline jumps. a) Trigger rate of the blind data set of the whole of MCIII-1, detector module A. The trigger rate before (red) and after rate and stability cut (blue) is shown. The high rate periods are caused by the baseline jump artifacts. b) Four day interval of the rate of detector J during a time with high baseline jump activity. 24 h periods are marked by the red lines. A 24 h pattern is clearly visible. c) On an even shorter period of a few hours, it can be seen that the artifacts appear in $\mathcal{O}(\text{min})$ bursts.

data than in the hardware triggered data as the hardware trigger is disarmed for some time after a heater pulse which the software trigger is not.

The continuous trigger produces a few wrongly constructed events with a trigger amplitude well above the trigger threshold and the noise that appear to be empty baselines when manually investigated. Those are removed by comparing the amplitude assigned to the record by the trigger to the filtered amplitude from running the optimum filter on the pulse records. In the case of these events, the trigger assigned an amplitude above threshold, while the evaluation of the record yields a value close to zero. Normally, very similar or identical values are expected, as both, the trigger and the evaluation of the pulse record apply the same optimum filter.

A new selection criterion was introduced for the jump events of some detector modules. The jumps have a fast upward and downward flank. A fast downward flank does not appear for particle or heater events. Those can only decay with the thermal relaxation time defined by the thermal coupling of the detector components. The optimum filter ”interprets” the fast falling flanks of the baseline jumps as a negative pulse. This leads to a negative spike in the filtered output, see figure 5.7c. Due to this effect, the minimum filter (MinOF) parameter allows for a partial separation of jump and particle events down to lowest energies, see figure 5.7a. The data shown is from detector A and has some custom data selection applied to remove other artifacts beforehand.

5.1.3.4 Background and Veto Cuts

Only events where the phonon channel did trigger (trigger delay=0) are considered for the dark matter analysis. Events within a $[-10\,\text{ms}, 5\,\text{ms}]$ time window around an energy deposition in the muon veto are discarded. Events within a $\pm 10\,\text{ms}$ window around a triggered energy deposition in any of the other detector modules are discarded. Events exceeding a certain pulse height in the instrumented holding stick veto are discarded.

The selection on the RMS has little influence on the background reduction in MCIII-1.

“Light stick events” are not specifically targeted for removal as they only appear at light yields far outside the region of interest. Light stick events are caused by an energy deposition in one of the $CaWO_4$ sticks holding the light detector and are discussed in more detail in appendix A.8.4.

5.1.3.5 Analysis Limitation Cuts

The conversion from filtered to fitted amplitude equivalent described in section 5.1.2.2 is limited to not fully saturated pulses. Similarly, there are issues with the standard event fit for too high light energies. Therefore, events that exceed one of those limits as summarized in appendix G are not considered in the dark matter analysis. For detector A-phonon this limits the analysis to up to 20 keV.

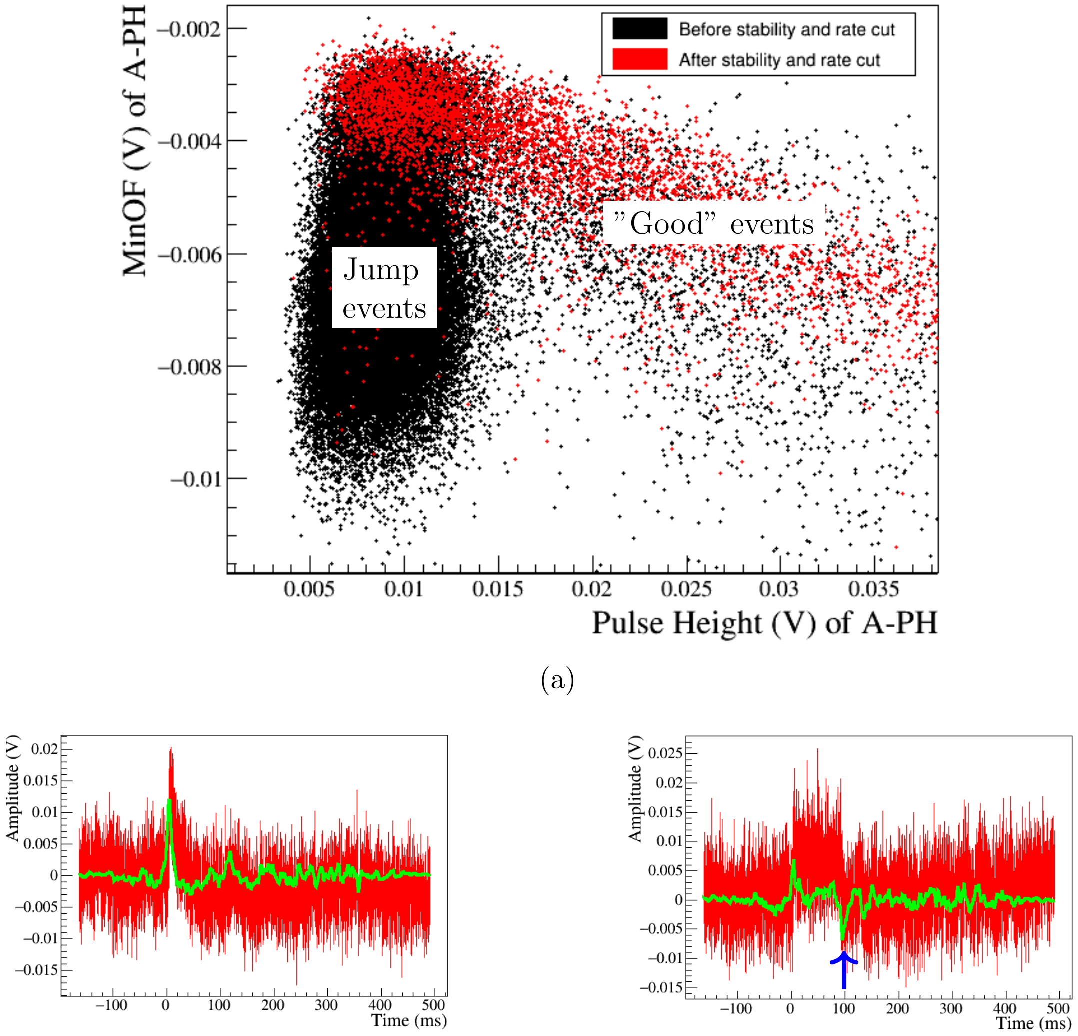

(a)

(b)

(c)

Figure 5.7: Minimum optimum filter (MinOF) based data selection to remove baseline jump events. a) MinOF parameter vs pulse height before and after the rate cut. The rate cut mainly removes baseline jumps based on their temporal distribution. The MinOF value allows a further, partial discrimination. For clarity, some other known artifact types were removed beforehand. The reason for the possible discrimination is shown in figures b) and c). Figure b shows a simulated, i.e., ideal pulse in raw (red) and optimum filtered (green) form where no significant minimum appears. The baseline jump displayed in figure c shows a minimum corresponding to the downward flank, highlighted with the blue arrow.

5.1.4 Survival Probability

The survival probability for nuclear recoils in detector A is determined with the help of the continuous simulation as described in section 3.4.3. The following choices are applied for detector A:

- A flat spectrum in real energy is simulated from 0 keV to 20 keV
- The time dependent detector response function determined for the energy calibration in section 5.1.5 is taken into account. This is evaluated for each simulated event to obtain the time dependent amplitude required for the given simulated energy. That way, the full energy reconstruction algorithm can be applied to the simulation in the end.
- Events with more than 1 ms time difference between trigger position and position of the simulated event are discarded. This removes the majority of cases where a pile-up event instead of the simulated dark matter event is reconstructed. In that case the dark matter event does not actually survive the analysis even though it is contained in a pulse record of a surviving event. Not removing those events results in a wrongly evaluated sensitivity down to zero energy.
- As a further protection from outliers, simulated events with a reconstructed energy deviating from the simulated energy by more than two standard deviations are discarded.

The survival probability that will be presented is not directly used in the final limit calculation. Instead, the spectrum is re-weighted event by event to create the expected dark matter spectrum for the limit calculation (compare section 3.7.2).

This time and resource intensive approach is only applied to detector module A in this work. The performance of the other modules does not allow to produce results competitive with detector A. Therefore, those modules are only relevant for comparison and verification of results, where the precision of the less time consuming event simulation presented in section 3.4.2 is sufficient.

5.1.5 Energy Calibration

The energy calibration for all detector modules is based on the injected heater pulses. They sample the time dependent detector response over the entire measurement time (compare section 3.5.3).

The amplitude of the heater pulses is reconstructed with a standard event fit. The relevant parameter for particle pulses in the phonon channels of modules A, E, J is the fitted amplitude equivalent (compare section 5.1.2.2). All other modules and the light channels base the calibration fully on the fitted amplitude, also for the particle pulses.

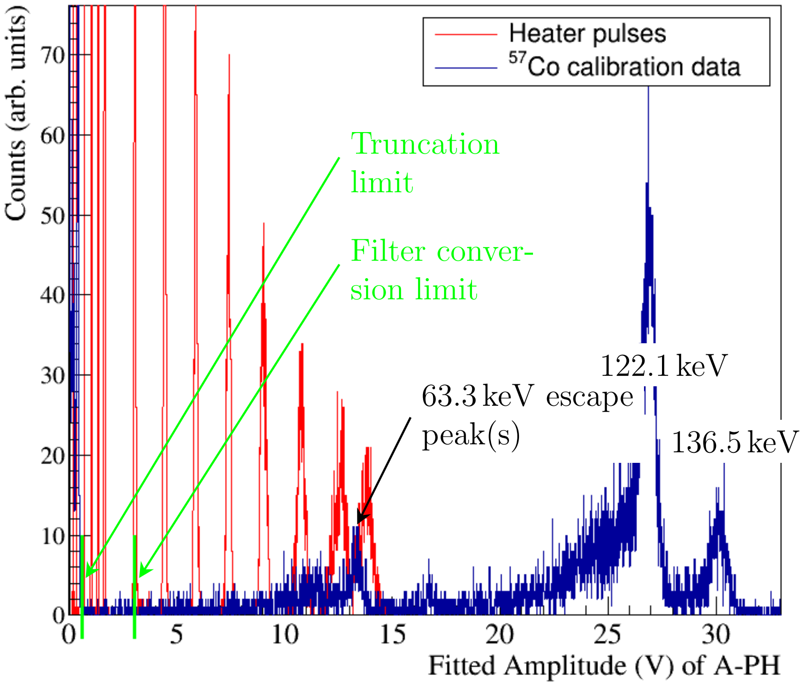

Figure 5.8: ${}^{57}_{27}$Co calibration spectrum of detector A-phonon. Heater pulses (red) are required for the calibration. However, they only extend up to the 63.3 keV $K_{\alpha 1/2}$ escape peak and show a significant degradation in resolution with increasing energies. The degradation is due to the truncation limit for the standard event fit being far below, at 0.6 V. The limit of the conversion from filtered to fitted amplitude equivalent is also indicated.

No correction for different scintillation light losses as discussed in section 3.5.5 is applied since none of the detector modules has a β/γ line with sufficient statistics to obtain the necessary correction factors. The effect is considered in the error estimation.

There were two major complications observed in MCIII-1 with the default calibration method:

Problem 1: Lack of a low Energy Calibration Source Figure 5.8 shows the ${}^{57}_{27}$Co calibration spectrum in fitted amplitude for detector module A. Additionally, the fitted amplitudes of the heater pulses, the truncation limit and the limit of the conversion to fitted amplitude equivalent are indicated.

It can be seen that the commonly used 122.1 keV peak is far outside the range of the heater pulses. Sending heater pulses at an energy comparable to the 122.1 keV does not improve the situation as their bad resolution in reconstructed amplitude would render them unusable. At the position of the 63.3 keV peak, the resolution has already significantly degraded as can be seen from the width of the mono-energetic heater pulse lines. One of the reasons is the lack of samples below the truncation limit, especially in the rising flank of the pulse signal. This can be seen in figure 5.9a. Therefore, the energy calibration is performed in two steps. A first CPE factor is determined from the 63.3 keV line. Then, the cosmogenic activation line of $^{179}_{73}$Ta at 11.27 keV is identified and the CPE factor adjusted to its position. The resulting calibration is cross-checked with the 2.6 keV line also produced by the $^{179}_{73}$Ta decay (compare section 3.5.1). The correction was calculated from the training set where the lines are hardly visible due to the low exposure. In figure 5.9b the lines are shown for the blind data set of detector module A, confirming the consistent calibration.

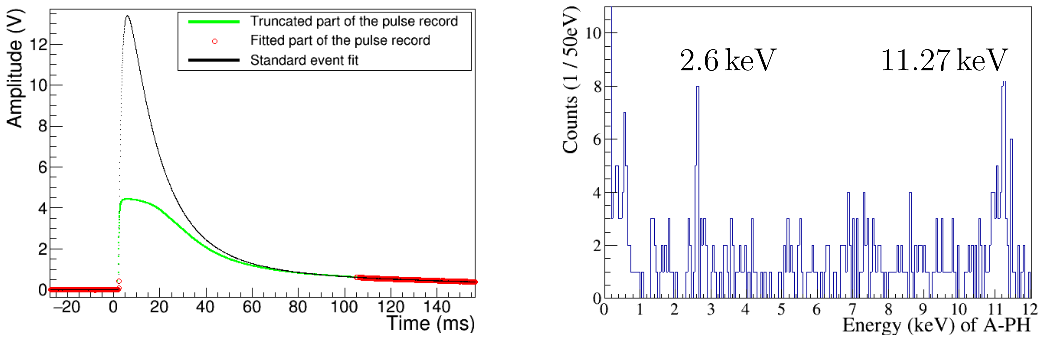

(a) (b)

Figure 5.9: a) Truncated standard event fit to a 63.3 keV pulse of detector A-phonon. Only one or two samples in the rising flank fall below the truncation limit. b) Energy spectrum of detector A-phonon, blind data set. Shown are the activation lines at 11.27 keV and 2.6 keV relevant for the energy calibration.

2: Offset at low Energies Injected heater pulses have a negative offset in fitted amplitude, i.e., the fitted amplitude reaches zero already for a non-zero heater control voltage. Data from a threshold measurement of detector A-phonon is shown in figure 5.10. This measurement was originally performed to map the hardware trigger response. It includes injected heater pulses at various low energies which are not present under normal operation. A linear fit in heater control voltage vs fitted amplitude is performed, once with an offset, once forced through (0|0). The heater control voltage is expected to be directly proportional to the injected energy (compare section 3.5.3). However, the fit with an offset (red) describes the data much better. The offset in the mV range is not compatible with the resolution obtained from fitting empty baselines that gives an average fitted amplitude for detector A-phonon in the 0.01 mV to 0.1 mV range. Simulated data also does not show this effect. This implies that it is not caused by an issue with the standard event fit in the presence of noise and is likely caused by a problem with the heater electronics.

An offset is subtracted from the heater control voltage to compensate the effect.

This is chosen such that the heater control voltage to fitted amplitude relation passes through (0|0) when linearly extrapolating from the two or three lowest heater pulses. The offsets are summarized in appendix G. They are around 2 mV for the phonon channels of all six investigated modules. The correction is not applied to the light channels.

It is assumed that particle energy depositions do not have this offset effect. Unfortunately, there are not enough lines from radioactive contamination or calibration sources available at low energies to thoroughly verify this assumption.

The offset is taken into account in the continuous simulation.

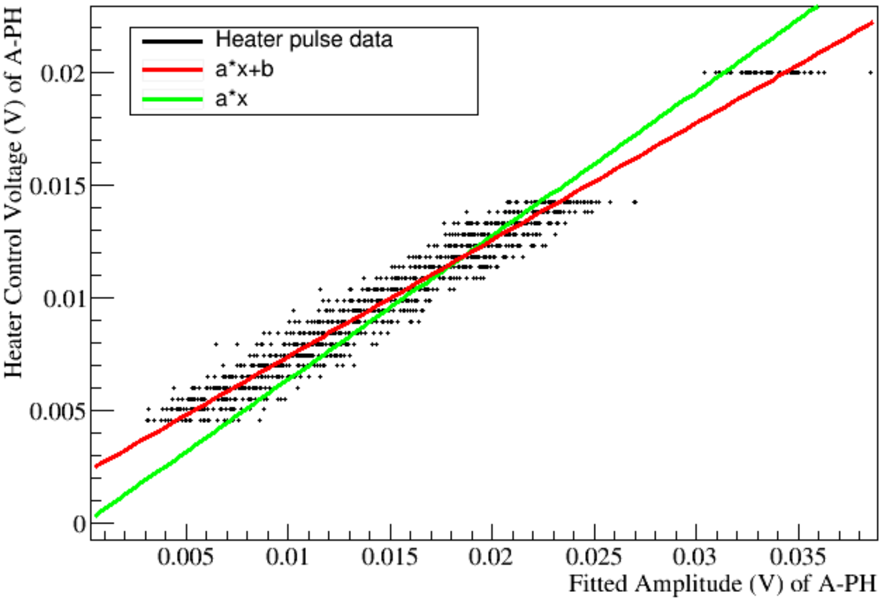

Figure 5.10: Offset determination for the energy calibration. Injected heater pulses at discrete low energies are available from a dedicated measurement of the hardware threshold. Fitting a polynomial of degree one reveals that there is an offset of about 2 mV in heater control voltage (red). For comparison also a polynomial forced through zero is displayed in green. The actual determination is performed with inverted axes compared to the plot at hand due to technical reasons.

5.1.6 Light Yield and Band Fit

The light yield is calculated as described in section 2.2.1. The position of the β/γ and nuclear recoil bands is fitted on the neutron calibration data analyzed in this work with a maximum likelihood approach by [130, 145] as also presented in [80].

5.1.7 Limit Calculation

The final limit calculation for detector module A was performed in [146, 130, 145]. The expected dark matter spectrum follows the standard assumptions as presented in section 3.7.1. It includes survival probabilities and resolution based on re-weighting the simulated flat spectrum from the continuous simulation analyzed in this work (compare section 3.7.2 for the general method and section 5.1.4 for the specific choices for the simulation). The limit calculation was limited to energies above the nominal trigger threshold, i.e., to above the position of 50 % trigger survival probability.

The Yellin optimal interval method was chosen to calculate the final exclusion limit (compare section 3.7.3).

5.1.8 Uncertainty Considerations

5.1.8.1 Scintillation Light Losses

Due to the small exposure, good radio purity and limited dynamic range, no well populated γ lines are available. Therefore, the required correction factor for the phonon anti-quenching cannot be extracted, compare section 3.5.5. Consequently, the energy of nuclear recoils is overestimated by up to 10% as the calibration is based on the 11.27 keV gamma line.

5.1.8.2 Position of the 11.27 keV Calibration Line

The 11.27 keV line has very limited statistics both in the training and the blind data set. Nonetheless, the position could be determined. A cross-check can be performed with the 2.6 keV line. Observed errors range from below 1% for most modules including detector A to up to 10% for detector E, phonon.

5.1.8.3 Time Dependency of the Threshold

The energy calibration and the trigger are based on the same amplitude evaluation. Nominally, a sharp trigger cut off in measured energy is expected. However, the sensitivity of a detector shows slight variations in time. Those are corrected by the time dependent testpulse based energy calibration while the trigger threshold does not have a time dependent adjustment. The constant trigger threshold in filtered amplitude therefore corresponds to a slightly varying threshold in terms of energy.

This is a systematic effect and should not be confused with the effect of a sharp threshold folded with a resolution as seen in figure 5.11 at low energies. This effect is correctly covered by the simulation (compare section 5.1.4).

5.1.8.4 Choice of the Heater Control Voltage Offset

The origin of the offset introduced for the injected heater pulses is unknown. It should therefore be considered a potential error source. Furthermore, determining the correct offset is challenging. It requires interpolation from the few heater pulses between zero and the non-linear range of the detector. The error induced in the result is estimated by varying the offset by ±50%.

5.1.8.5 Final Results of Detector A

Detector module A shows an exceptionally good performance in the phonon channel with a baseline resolution of 4.6 ± 0.1eV. The threshold chosen for the continuous triggering of 6.6 mV corresponds to an energy of $30.0^{+4.8}_{-6.5}(sys.) \pm 0.2(stat.)$eV as determined from the simulated data shown in figure 5.11. The high number of simulated events makes the statistical error as determined by the fit comparably small. As presented in section 5.1.4, the simulation also includes the time and energy dependent detector response. The much more significant uncertainty stems from the systematic errors considered in section 5.1.8 that shift the whole energy scale at threshold. The derived minimal dark matter mass that can still produce a nuclear recoil energy deposition at the value of the threshold is $188^{+15}_{-23}\mathrm{MeV}/c^2$.

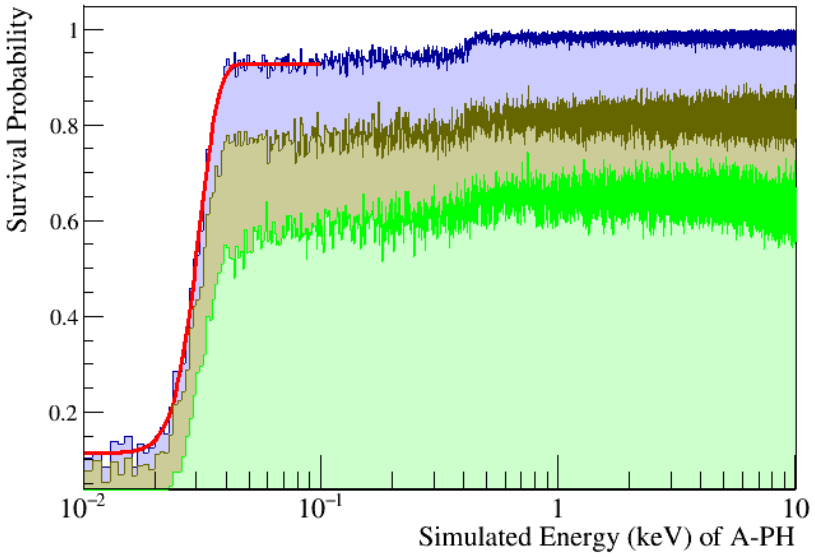

Figure 5.11: Event survival probability as determined from data simulated on the continuous stream. Blue: after triggering with the optimum filter based software trigger; Brown: after rate and stability cut; Green: after all data selection criteria have been applied. The red line shows a fit of a sigmoidal function with an offset. It is used to determine the trigger threshold to 30.0±0.2 eV (statistical error only).

The MinOF parameter cut was not applied since the jump like artifacts discussed in section 5.1.3.1 are restricted to well defined time periods removed by the rate cut.

The final results in terms of band fit and energy spectra are shown in figure 5.22. The final limit obtained for the dark matter - nucleon interaction cross section is presented in figure 5.13.

The background rate between 3 keV and 10 keV without identified decay lines amounts to $6.4 \pm 0.5(stat)$counts/(kg keV d). This value is already corrected for the survival probability. No β/γ leakage or other events are observed in the nuclear recoil bands above 1 keV.

Nuclear and β/γ recoil bands can no longer be separated clearly in terms of light yield below 1 keV. Accordingly, some events from the β/γ band leak into the region of interest. Less than four such events are expected if a flat spectrum with the same rate as above 1 keV is assumed.

What is seen however, is an exponential rise in rate, starting at 100 eV to 200 eV and extending down to threshold. In total, 804 events are observed between 30 eV to 100 eV. About half of them are in the region of interest, as expected for events with no light signal.

This unexpected excess of events severely limits the sensitivity of the detector at lowest energies. No obvious time dependency is observed. The spectral shape closely follows an exponential with a small pedestal at around 160 eV (compare figure 5.12d) mimicking a potential dark matter signal. The survival probability is flat, also at low energies. The threshold in terms of reconstructed energy is sharp by definition.

The following sections are dedicated to investigating the possible origins of the observed excess.

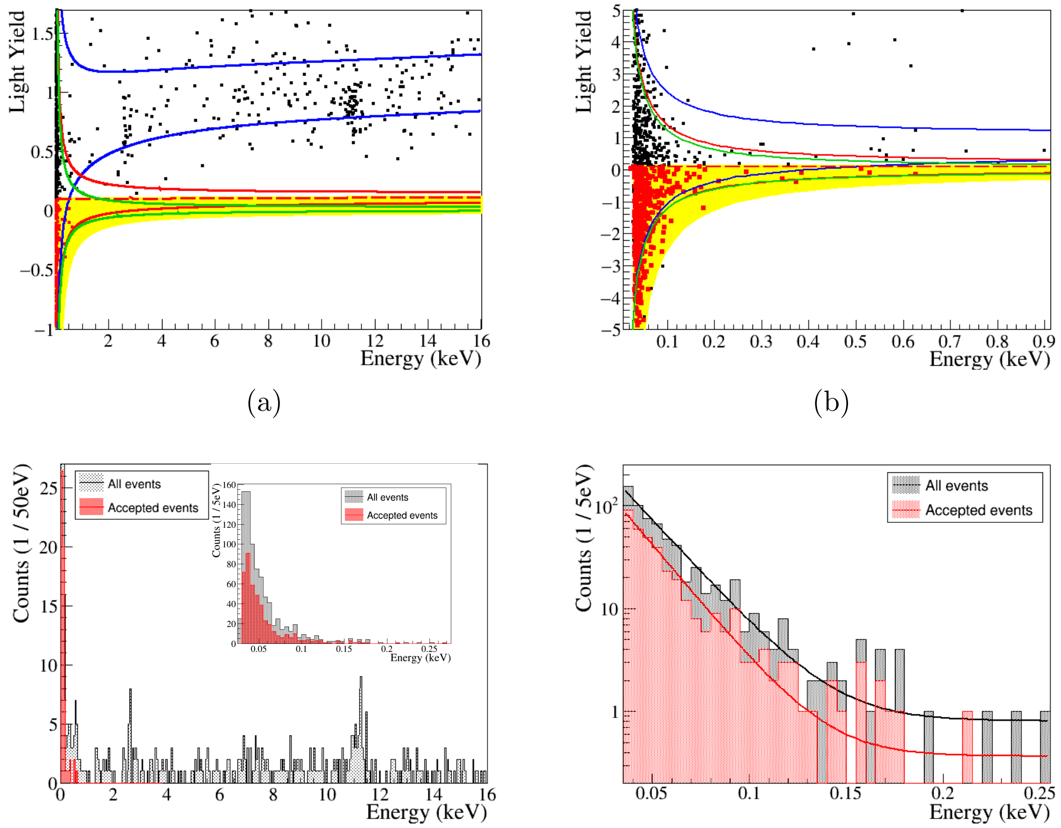

(a) (b)

(c) (d)

Figure 5.12: Summary of results of the dark matter analysis of detector module A. a) Band description from the neutron calibration superimposed onto the blind data set after data selection. Shown are the 90 % borders, i.e., 80 % of events are expected within their respective drawn bands. Blue: β/γ band; Red: oxygen recoil band; Green: tungsten recoil band; calcium band not shown for clarity. The region of interest is marked in yellow. b) Zoom into the low energy region. The bands overlap and full discrimination is no longer possible. The excess below 200 eV is clearly visible. c) Final energy spectrum of detector A-phonon after data selection and within a light yield of ±10. Black: all events; Red: events in the region of interest. An exponential rise of events is observed starting at around 200 eV. The inset shows a zoom into the low energy region. d) Zoom into the low energy region and logarithmic scale for better visibility of the exponential rise of the excess events. An exponential decay plus offset has been fitted, yielding a decay constant of about 50 keV^{-1}

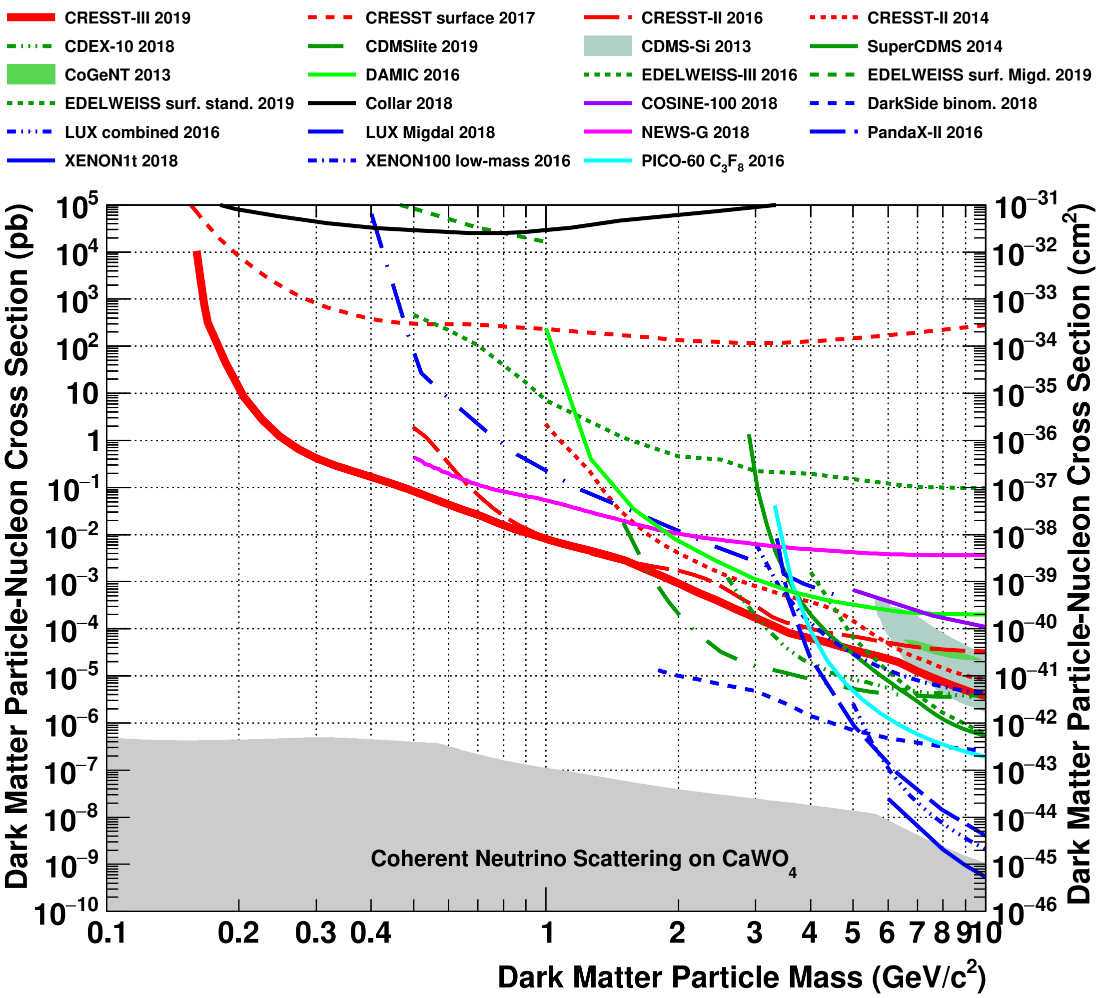

Figure 5.13: Final results of the dark matter analysis as published in [80]. Shown are the exclusion limits from different experiments on the dark matter - nucleon interaction cross-section as a function of dark matter mass. The limits assume standard values as discussed in section 1.3.3.1 regarding dark matter abundance and velocity. The solid red line marks the limit derived from the analysis presented in this work. The other limits are: CRESST-II 2016 [82], CRESST surface 2017 [81], CDEX-10 [84], CDMSlite [75], DAMIC [67], EDELWEISS [87, 88], SuperCDMS [86], CDMS-Si (90 %C.L.) [86], CoGeNT (90 %C.L.)[147], DarkSide [64], LUX [55, 58], Panda-X [62], Xenon100[91], Xenon1t [59]), COSINE-100 (NaI) [90], Collar (H) [89], NEWS-G (Ne + CH_4) [68], PICO (C_3F_8) [70]. Grey area: experimental sensitivity at which one or more events from coherent neutrino scattering are expected for a dark matter search with $CaWO_4$ [92]. Coherent neutrino scattering forms an irreducible background for most direct dark matter search experiments.

5.2 Investigation of the observed Excess Events

This section is focused on the investigation of the excess observed in the dark matter analysis of MCIII-1, detector A. Sections 5.2.1, 5.2.2 and 5.2.3, take a closer look at detector and analysis related effects, namely time stability, noise triggers and baseline jumps. Sections 5.2.4 to 5.2.7 focus on the comparison of different measurements and detectors. In section 5.2.8, a number of event types stemming from the detector geometry are discussed.

5.2.1 Time Stability

Figure 5.14 shows the baseline RMS of empty baselines over time. The baseline RMS is obtained by fitting a polynomial of third degree to a set of empty baselines and computing the RMS difference of such an analytical model to the data samples. The same polynomial is used for the baseline model in the standard event fits. A time variation over the whole of MCIII-1 is observed. In [107] similar considerations were made regarding the relevant detectors of MCII-2. There, a comparable instability is only observed for the light detector of the TUM40 module.

A drift in noise can indicate a change in sensitivity. Therefore, in figure 5.14 also the fitted amplitude of the 1.5 keV heater pulse is shown. Indeed, the fitted amplitude shows a pattern similar to the empty baseline noise. This is taken into account by the time dependent energy calibration.

Great care should be taken in future measurement campaigns to obtain more stable running conditions, simplifying the analysis. However, a direct link from the unstable running conditions to the excess could not be found. The excess does not show a similar, clear time dependency.

5.2.2 Crosscheck of the expected Number of Noise Triggers

The trigger threshold is set with the goal of a maximum of one noise trigger per kg d after data selection (compare section 5.1.1.3). This section presents a data based verification of this goal.

In a first step the samples of the data stream of the training set are sign inverted, i.e., multiplied by -1. True energy deposition in the detector can only produce positive pulses. Different noise types by contrary are expected to produce fluctuations in both directions, compare figure 5.15. Triggering on the inverted stream therefore only produces noise triggers, at least at low energies. With this method the influence of any sub-threshold real particle energy depositions can be avoided.

The normal data selection criteria are applied to the inverted stream. The delta voltage parameter against electronic spikes (compare section 3.3.2.3) has to be inverted, too. The spikes now point in positive direction, see figure 5.15a. For the rate cut the same time periods as in the normal training set were removed.

The training set has a total exposure of 0.851 kg d. With the chosen threshold

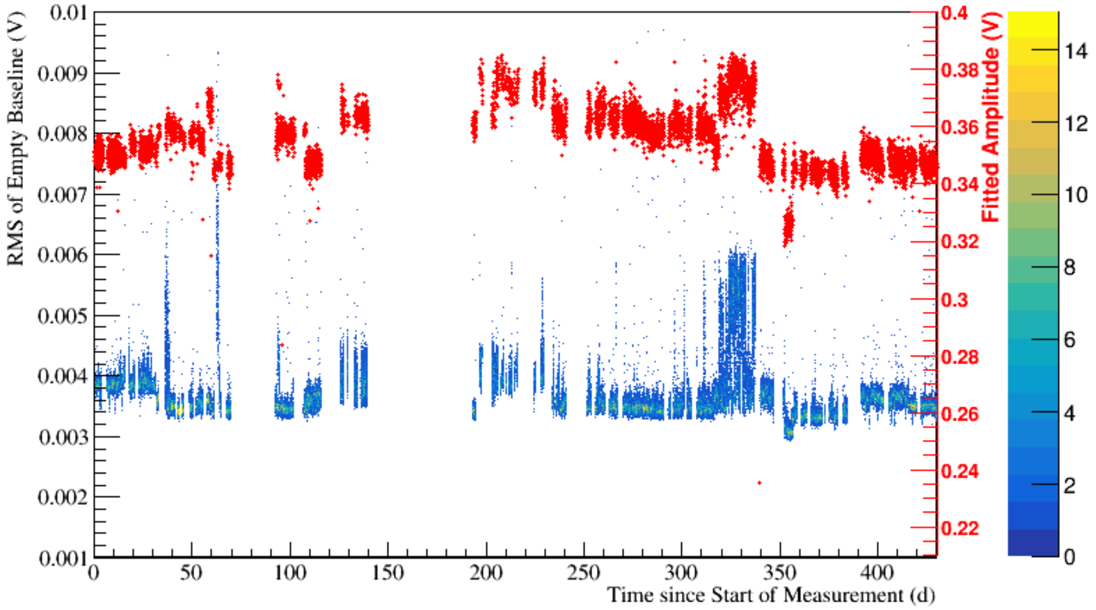

Figure 5.14: Time stability of noise (blue/colorcoded) and fitted amplitude of the 1.5 keV heater pulse (red) of detector A-phonon over the whole of MCIII-1. Rate and stability cut have already been applied. For a satisfying stability a normal distribution around a constant value would be expected. The gap around 160 d is caused by the neutron calibration which is not displayed in the plot.

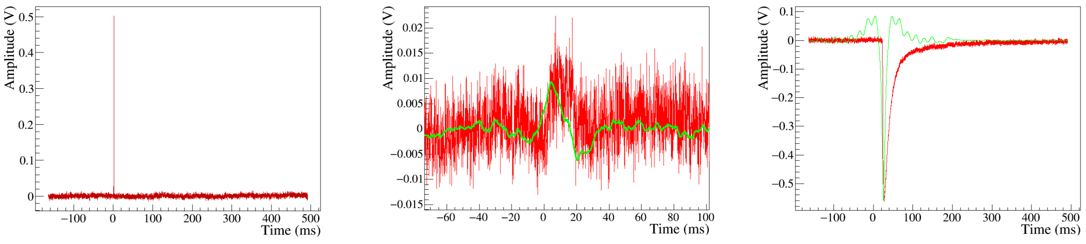

(a) (b) (c)

Figure 5.15: Examples of events triggering with the inverted data stream. a) Electronic spike artifacts, extending in the positive direction after the inversion. b) Baseline jump artifacts which have a rising and a falling flank and therefore trigger in both, the normal and the inverted stream. c) Larger normal events still trigger with the optimum filter based triggering.

accordingly less than one noise event is expected. No events remain after applying all data selection criteria. This is in accordance with the expectation.

A special case are the jump like electronic disturbances. They have a sharp rising and falling flank and occur in positive and negative direction. Hence, they will trigger as before in the inverted stream. This enables further study of their effect and is presented in section 5.2.3. Without the rate cut over a hundred baseline jump events would survive. This underlines its importance and the potential threat posed by the jump events.

The results of this cross-check exclude noise triggers as the origin of the excess events.

5.2.3 Baseline Jumps as Candidates for the observed Excess

An obvious candidate for the excess at low energies are the already discussed baseline jumps. The blind data was analyzed without the rate cut to investigate their influence. The final energy spectrum is shown in figure 5.16 in red. The final spectrum with rate cut is shown in green. This analysis does not apply a region of interest but takes all events with a light yield in the range [-10,10]. The contribution from the jump events neither reaches up to the necessary energies, nor does it have the correct spectral distribution. The excess follows very well an exponential function. The jumps produce a Gaussian distribution in energy centered around the threshold. A combination of a Gaussian distribution for the jump like noise, an exponential for the excess and a constant for the approximately flat β/γ background fits the final spectrum very well.

The spectral shape of the baseline jumps is verified with the inverted stream. There, only the contribution from the jumps remains, shown in figure 5.16 in purple. The amount of events from the inverted measurement is scaled such that the shapes can be easily compared.

In summary the electronic jumps do not appear to be a viable explanation for the excess in detector A-phonon due to the different shape and reach in energy.

5.2.4 Comparison to the Light Detector

The light detectors in MCIII-1 have a comparable surface to the main absorber crystal and can therefore be used to test the hypothesis that the excess is caused by a surface contamination or by surface absorbed backgrounds, e.g., electrons or low energy photons. In case of a surface related effect, a similar excess spectrum as observed in the phonon detector would be expected in the light detector. However, if the excess is caused by penetrating particles and thus scales with the mass, the thin light detector should only see a much reduced rate if any. To obtain this additional information, an analysis of the light only events is performed. A similar analysis for previous measurement campaigns has already been done e.g. in [114] and found an exponential rise in events in the light detector albeit starting at around 1 keV.

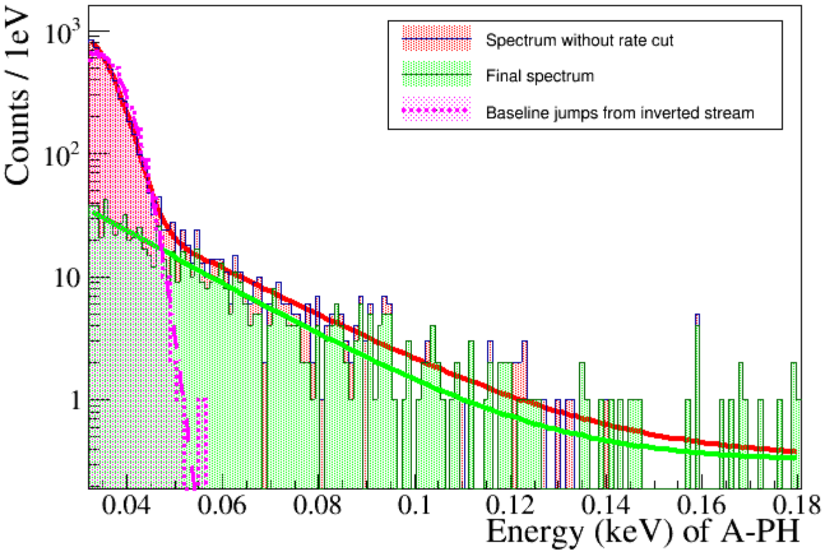

Figure 5.16: Potential influence of the baseline jumps on the energy spectrum of detector A-phonon. In green the spectrum with full data selection and restricted to the β/γ + nuclear recoil bands by a selection on the light yield is shown. In red the same data selection, except for the rate cut, is applied with the baseline jumps dominating below 50 eV. The baseline jump spectrum as obtained from the inverted stream is superimposed in purple. It is scaled for better comparability of the shape. Fits contain a flat background and an exponential decay for the green spectrum, an additional Gaussian for the red spectrum and only a Gaussian for the purple spectrum.

5.2.4.1 Analysis Steps

Data Selection For the light only analysis only events that did not trigger the phonon detector are investigated.

The data selection criteria are obtained by exchanging the role of light and phonon detector in the steps presented in section 5.1.3.3. The values are summarized in appendix G. The rate and stability cuts are applied as before, i.e., remove the same time periods as for the main analysis. No RMS or other shape cuts are applied.

Events with a fitted amplitude above zero in the phonon channel are removed. This is done to exclude the influence of events caused by scintillation light from the scintillating foil. Those events show a small signal also in the phonon channel due to absorption of light in the main absorber crystal. A detailed discussion of these “foil events” can be found in appendix A.8.5. This selection is expected to reduce the survival probability of light only events by 50 %.

Amplitude Reconstruction Triggering and energy calibration of the light detector is based on the optimum filter for the light detector obtained from the main absorber β/γ standard event. Only very low energies well in the linear region of the light detector are of interest. Therefore, no conversion polynomial between the filtered and fitted amplitude equivalent was applied.

The light only events without phonon trigger have a slightly different position of the pulse signal in the record window. Furthermore, direct energy deposition in the light detector lead to a slightly faster rise time of the observed pulse signal compared to scintillation light. This is discussed in more detail in appendix A. This difference does not significantly affect the amplitude reconstruction.

Energy Calibration The energy calibration of the light detector is based on the heater pulses and the amplitude reconstructed by the optimum trigger. An offset in heater control voltage could not be determined, therefore it was set to zero.

The main challenge concerning the analysis of direct hits on the light detector lies in the lack of a calibration line. Direct hits of γs of the calibration sources will either not deposit their full energy in the thin light detector or be too far beyond its linear range. The calibration discussed in 5.1.5 only calibrates the light detector in terms of keVee, i. e., energy deposition in the main absorber. A conversion into deposited energy in the light detector requires the fraction of energy converted to scintillation light (scintillation efficiency) and the fraction of scintillation light absorbed in the light detector (detection efficiency).

The scintillation and detection efficiencies have been determined for a previous measurement in [128]. In [110] the amount of energy lost from the phonon channel due to scintillation for a detector of MCII-2 is given as about 6.6%. In [128] scintillation efficiencies were determined to be around 8.5% and detection efficiencies in the 20 to 30% range. Detection efficiencies in the MCIII-1 modules are expected to be higher due to smaller modules with a relatively large light detector. In total a conversion factor from $\mathrm{keV_{ee}}$ to keV energy deposition in the light detector between 1% to 5% appears realistic. In the following, all plots are drawn with a factor of 5%. This choice increases clarity in the plots and the resulting spectra are close to what is observed in the phonon channel.

5.2.4.2 Results of the Light Detector Analysis

The obtained light detector spectra for γ and neutron calibration as well as the blind data set are shown in log and linear scale in figure 5.17. They are normalized to a raw measurement time after rate and stability cut of 1h. Similar survival probabilities after rate and stability cut are expected as the same selection criteria are applied. Therefore, the spectra can be directly compared.

The spectrum of the blind data set is compared to the excess in the phonon channel in figure 5.18. Again, both spectra are normalized to 1 h. The survival probabilities are expected to be lower up to a factor of two for the light detector events. The data selection choices are similar, but for the light events there is the additional selection on the phonon channel amplitude below zero.

A rise in the number of events starting at about 100 eV is observed in the

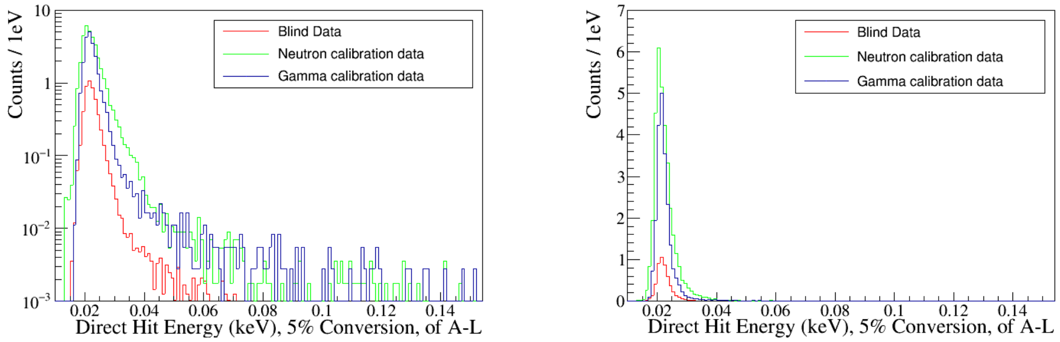

(a) (b)

Figure 5.17: Comparison of energy spectra for light only events in detector module A of the γ calibration (blue), neutron calibration (green) and blind data set (red) in logarithmic and in linear representation. The measurement time is normalized to one hour after rate and stability cut. A conversion factor of 5% from $\mathrm{keV_{ee}}$ to keV real energy deposition is assumed. A different factor will scale the x-axis linearly, e.g., 1% reduces all energies by a factor 5.

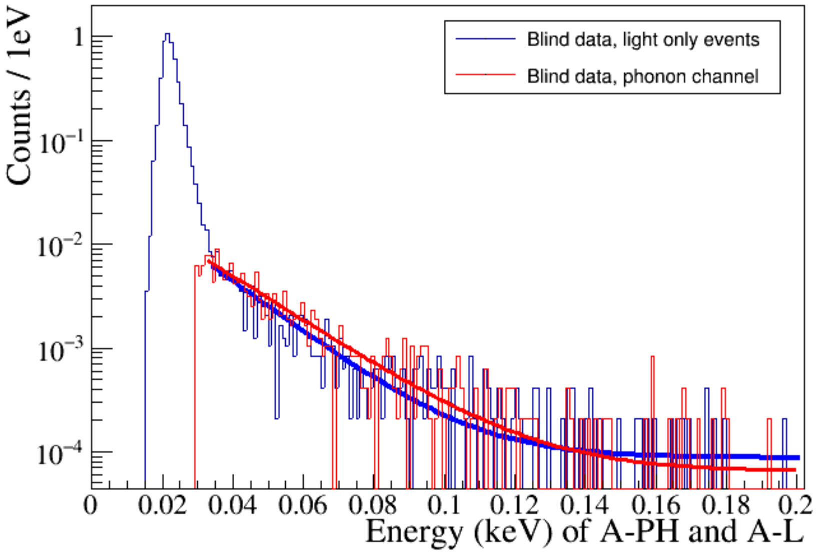

Figure 5.18: Comparison of the energy spectrum of light only events in detector module A, blind data set, to the excess in the phonon detector. A conversion factor from keVee to keV real energy deposition of 5% for the light channel is assumed. Spectra scaled to one hour of measurement time. Survival probabilities can be different by about a factor of two. Given the unknown survival probability for the light detector and that the 5% conversion factor being somewhat arbitrary, the displayed fits of exponential decay plus constant only serve illustrative purposes.

light detector. It is comparable to the rise of the excess in the phonon detector. However, the displayed data assumes the speculative 5% conversion factor from keV_{ee} to keV.

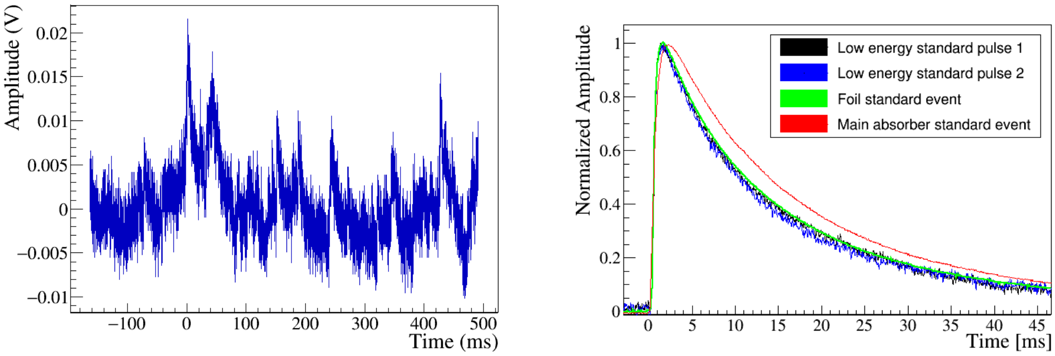

(a) (b)

Figure 5.19: a Example for the disturbed baseline of a very low energy light only event. It is not clear if the several visible "pulse signals" in the record window are random noise, electronic interference or frequent, small energy depositions. However, standard pulses built from such low energy events consistently match the pulse shape of a direct light detector hit. In b) they are compared to a foil standard event (green) and the standard event for main absorber hits. Foil events produce a faster signal than the scintillation light from the main absorber with a longer scintillation time.

At even lower energies a much stronger rise in the number of events sets in. The light detector appears to trigger in the "noise" e.g. shown in figure 5.19a. However, building standard pulses by averaging over randomly chosen subsamples of the event population at threshold consistently produces standard pulses as shown in figure 5.19b. They have the pulse shape of a direct, fast energy position in the light channel (compare section A.8.5). The pulse shape excludes an origin from the light sticks, which leads to a much slower pulse (compare section A.8.4). It hence seems that there exists a high rate of very small energy depositions to the light channel. Their origin is unclear, possibly scintillation light from long lived states. However, their rate is too high and their energy too low to be a direct explanation for the excess in the phonon detector.

Neutron and γ calibration show a greatly enhanced number of low energy light only events compared to the blind data set. However energy scales and particle types obviously vary, therefore a direct comparison is not possible. The neutron calibration also has a similar or higher event rate in γ events than the γ calibration, especially at low energies.

In summary, the analyses of direct hits of the light detector does not exclude a possible surface related origin of the excess events. However, any conclusion has to remain highly speculative without a real energy calibration of the light detector.

5.2.5 Comparison to the Gamma Calibration

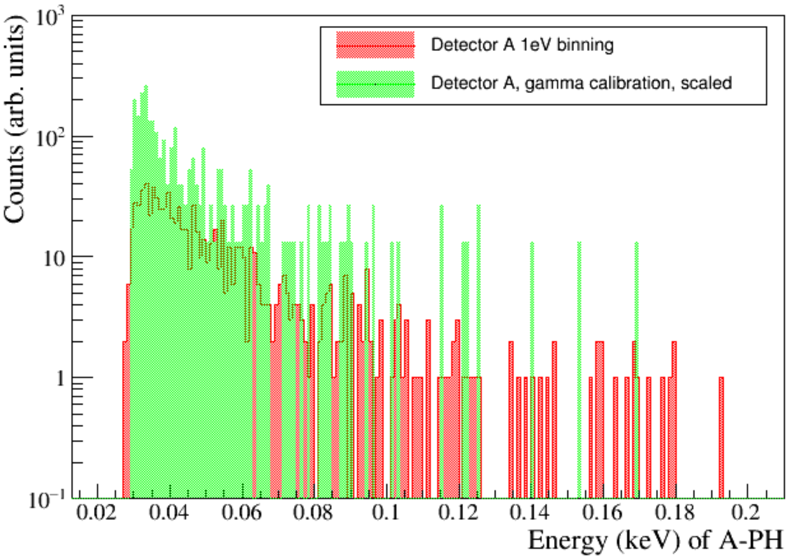

Figure 5.20: Comparison of the energy spectra of events with light yield ±10 (β/γ and nuclear recoils) of the γ calibration and the blind data set of detector A. The γ calibration spectrum is scaled to the exposure of the blind data set.

An excess spectrum with a similar spectral shape as in the blind data set is also visible in the γ calibration measurement. The measurement has about a factor 14 less exposure and a much higher overall event rate due to the calibration source. However, the events from the calibration are concentrated at higher energies, therefore a comparison of low energy events with a light yield within [-10,10] is possible and is shown in figure 5.20. The γ calibration spectrum has been scaled to match the exposure of the blind data. It clearly shows an increased rate by a factor 3-4 for the low energy events compared to the blind data set. This is similar to the factor 4 observed for the light detector (compare section 5.2.4.2). For comparison, the total rate of main absorber events is about 40 times higher in the γ calibration than in the blind data set. No detailed analysis of the survival probability in the γ calibration has been performed, but the applied data selection criteria are the same, except for the rate cut. From removed time periods of the rate and stability cut, a difference of only 7 % is expected in survival probability. If the low energy events in the γ calibration are attributed to the same background as seen in the blind set, this would imply that the background can be induced to some extent by the high energy γs of the calibration source.

5.2.6 Comparison to other Detector Modules

Assuming, that the low energy excess of events is caused by a common external source, all detector modules are expected to observe the same spectrum. If the excess is caused by internal contamination or other effects, different rates and possibly energy scales are expected for different modules.

5.2.6.1 Detector Module E

For detector E-phonon the 11.27 keV line and the 2.6 keV line cannot be brought into agreement. Fixing one line at the literature value of the energy, the other line is always off by about 10%. The main interest for the present considerations lies on the low energy region. Therefore, for the data presented in this section, the energy scale was adjusted to the 2.6 keV line after unblinding although this violates the blinding scheme.

The data set is based on the continuous acquisition and triggering scheme. The average survival probability is estimated to $(30 \pm 5)\%$ from a simple empty baseline simulation, compare section 3.4.2. The threshold of detector E is about 60 eV.

The resulting spectrum is shown in figure 5.21 in comparison with detector A-phonon. The survival probability of detector E is about half of the survival probability of detector A. This was taken into account by choosing double the bin size (2 eV vs 1 eV) for detector E in the plot. Detector E also shows an exponential excess at low energies. However, the decay constant is about half compared to detector A.

Additionally, the constant background from the β/γ band is significantly larger. Between 3 keV to 9 keV detector E shows a rate of β/γ events of $14 \pm 1(stat) \pm 3.7(sys)$counts/(keV kg d). A 10% systematical uncertainty from the energy calibration, a 15% systematical uncertainty from the survival probability and a 1 %-2 % uncertainty from varying the TPA offset in the energy calibration are included. The rate is about a factor 2 higher than observed for detector A-phonon in a similar range.

The same factor two is observed in the range between the threshold of detector E and 100 eV. This hints towards a possible connection between the excess and β/γ backgrounds. Still, this would not explain the different decay constants. However, significant systematic errors have to be taken into account for this comparison.

The shape of the energy spectrum is not influenced by the error on the approximately constant survival probability. The energy calibration, on the other hand, does have significant influence. Most notably, varying the offset on the injected energy introduced in section 5.1.5 by ±100% varies the threshold from 40 eV to 80 eV. Thereby the spectrum gets stretched or compressed. Visually, the excess of detector A and E can be brought into agreement with a reasonable choice of (offset) parameters while keeping the 2.6 keV peak at the correct position. A more detailed study of fitting a dark matter spectrum to the observed excess however reveals that the results still cannot be explained by a common, external, dark matter like component on a flat background (see section 5.2.7).

The lowest heater pulse corresponds to an energy of about 100 eV. A systematic error on the energy calibration due to a change in slope of the TES transition at lowest energies is therefore unlikely.

In total there appears to be a disagreement in the measured spectra of detector modules A and E. This disfavors a common, external origin as a full explanation for the excess.

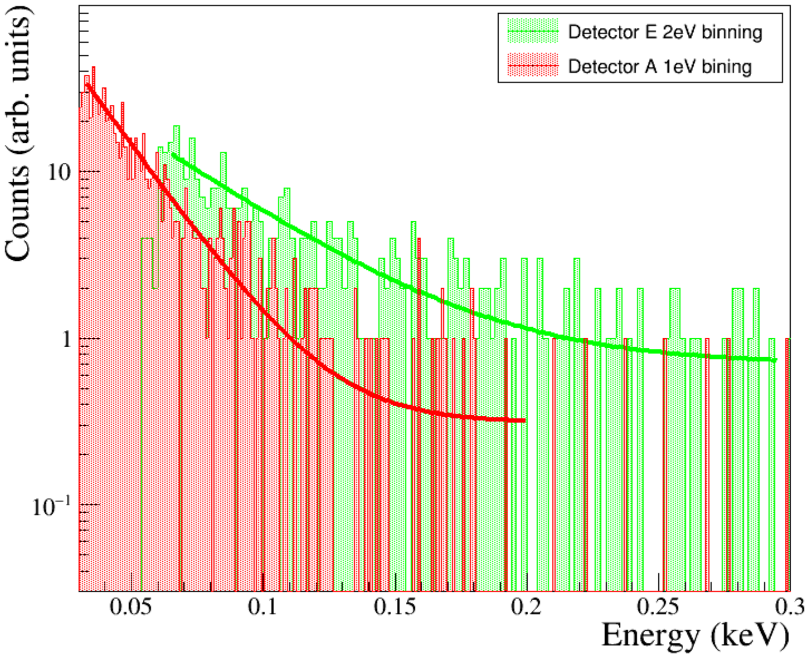

Figure 5.21: Comparison of the energy spectra of events with light yield ±10 (electron γ and nuclear recoils) of detectors A (red) and E (green), phonon. Differences of about a factor two in survival probabilities are taken into account by a different binning. An exponential decay plus a constant is fitted to both spectra in the displayed ranges. The obtained decay constants are $-50\,\mathrm{keV}^{-1}$ (A) and $-24\,\mathrm{keV}^{-1}$ (E) respectively.

5.2.6.2 Detector Module J

Detector module J nominally has a comparably low threshold of 60 eV to 70 eV in the analysis at hand. However, its analysis poses several challenges. First, the working point was changed after about one third of MCIII-1 due to unstable operating conditions. Therefore, only part of the data can be used. Second, detector J, phonon has a significant number of baseline jumps. Third, there is an unexplained background with low light yield starting at 6.6 keV extending down to threshold. Those three problems are briefly discussed in the following before comparing the measured spectra to detector A. Survival probabilities are derived from a simple empty baseline simulation (compare section 3.4.2).

Change of operating point: Only the data collected in the final operating point is analyzed, reducing the raw exposure of detector module J to 4.11 kg d. The γ calibration for the determination of the energy scale was performed with another operating point. However, as the heater has not changed, the CPE factor is expected to remain the same. The calibration after operation point change is checked with the unexplained 6.6keV line. The 2.6keV line is not significant enough for a recalibration.

Baseline jumps: For detector J-phonon the rate cut is not sufficient to remove the baseline jumps. Therefore, in addition, a selection on the optimum filter minimum as discussed in section 5.1.3.3 is applied. Nonetheless some events possibly originating from the jumps remain. Similar to figure 5.16 for detector A, in figure 5.22a the final spectrum observed for detector J is compared to the spectral shape of the jump events. The jump events are obtained from a dedicated selection on the MinOF parameter but with the rate cut already applied. Unlike detector A, baseline jump events and remaining events cannot be separated in terms of spectral shape. Visual inspection of the events in the final particle spectrum indicate that at least part of the events are due to misidentified baseline jumps.

Selection criteria are considerable tightened at low energies to remove the baseline jumps. As a side effect, the applied approximation of a constant survival probability down to threshold is not completely valid anymore. It potentially underestimates the lowest end of the energy spectrum by up to one third, as estimated from simulated data.

Unexplained background at 6.6 keV: The background is shown in figure 5.22b. The events identified with a selection indicated in figure 5.22c in terms of rise time vs fitted amplitude are displayed in red. Here, the rise time was determined by a parametric fit with the analytical pulse model leaving only the rise time parameter free (compare section 2.2.3 and 3.2.2.1). It can be seen that the majority of the unexplained events have a different rise time. They can therefore be removed arguing that a different pulse shape disqualifies them as potential standard nuclear recoil dark matter events. No parameter was found to discriminate the remaining unexplained background from nuclear recoils. This leaves detector module J as an unsuitable candidate for a dark matter search.

Nonetheless, the spectrum at low energies with light yield in between [-10,10] can be compared to detector A and E, see figure 5.23. It is observed that detector module J shows a similar rise at low energies. The survival probability at low energies is about 30%, compensated by a 2 eV binning compared to the 1 eV binning of the detector A data.

No meaningful uncertainty could be estimated. The systematics from the energy recalibration by the not understood 6.6 keV line are unknown. The contribution of jump events to the spectrum at low energies could not be quantified. Additionally the error sources discussed for detector E would apply, too.

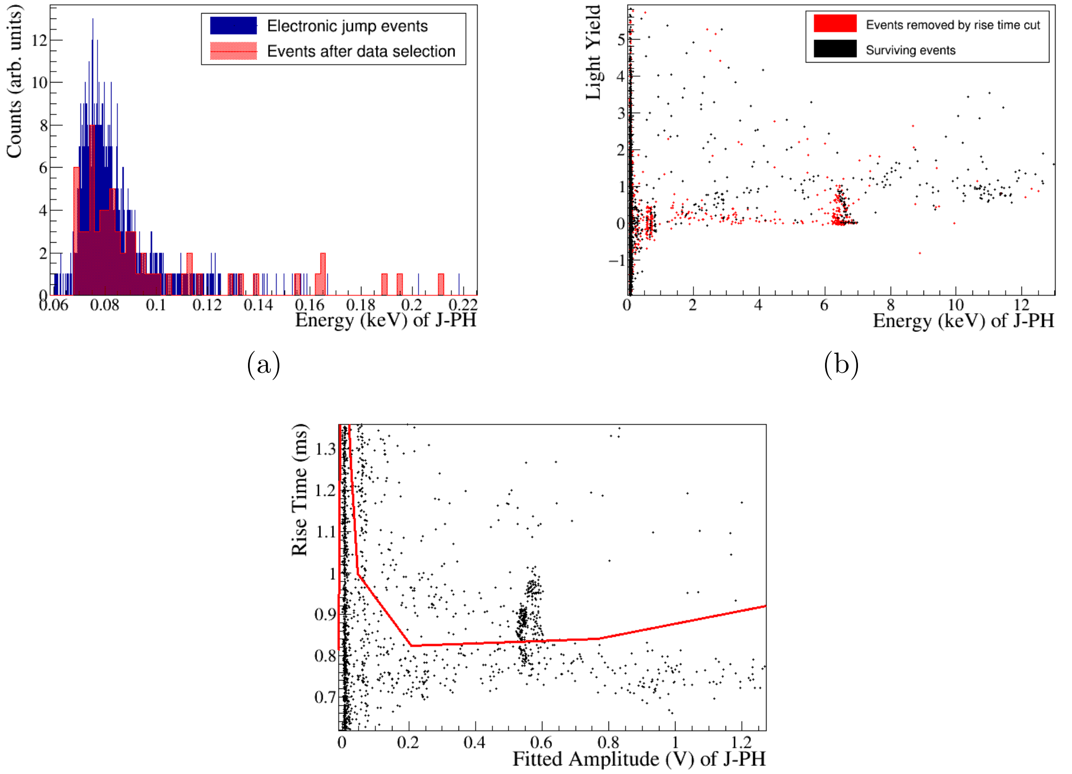

(a)

(b)

(c)

Figure 5.22: a) Energy spectrum of baseline jumps (blue) compared to the energy spectrum of events after data selection (red). The baseline jumps are identified by a selection on the MinOF parameter. Unlike for detector module A, the baseline jumps cannot be separated in terms of spectral shape. This leaves serious doubt about the nature of the observed low energy events after data selection. Binning is adjusted to obtain visually comparable spectra. b) Detector module J observes an unexplained event population starting at about 6.6 keV. It reaches down to low energies in the nuclear recoil band and featuring a triple line slightly below 1 keV. Part of it (red) can be removed with a selection on the rise time, displayed in c). The rise time is determined by a parametric fit.

5.2.6.3 Detector Modules B,C,D

For detector B-phonon survival probabilities at low energies are in the 30-45% range. The threshold is at about 100 eV, too high for conclusive results regarding the excess seen in detector A. The CPE factor of detector B was adjusted with the help of the 8 keV copper fluorescence line from the γ calibration. The strong 2.6 keV line fits with an error below 1%. Detector B-phonon shows a strong time variation in sensitivity. Therefore, the threshold is not sharp in reconstructed energy, complicating the decision where to fit an exponential. A rise at threshold is observed as shown in figure 5.24a. The displayed fit includes a flat background,

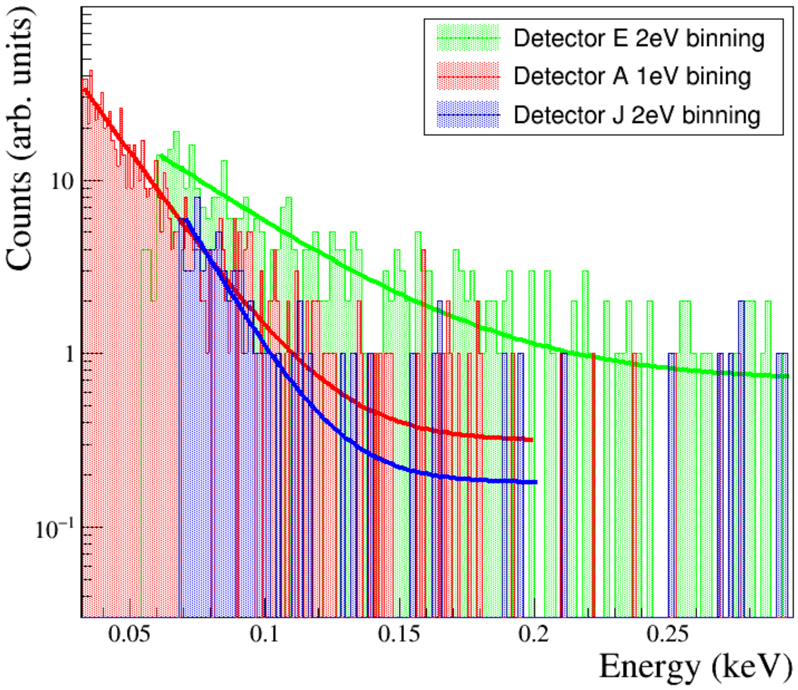

Figure 5.23: Comparison of the low energy spectra of detectors A (red), E (green) and J (blue), phonon. Different survival probabilities are taken into account by different binning. The lowest energy bins of detector J, phonon are on the one hand underestimated due to energy dependent survival probability but on the other hand have an unknown contribution from baseline jumps.

a Gaussian at the position of the 2.6 keV line and an exponential at low energies. The exponential is for illustrative purposes only as the small number of events does not allow for a meaningful determination of a decay constant.

A sufficient energy calibration is possible for detector module C with the presence of the 11.2 keV and 2.6 keV lines. However, the detector is dominated over the whole of MCIII-1 by noise on the baseline, compare figure 5.24b. The noise reaches up to about 400 eV. Detector module C is therefore not sensitive to the relevant energies.

Similarly, Detector D, phonon shows strong baseline fluctuations in addition to the baseline jumps (compare figure 5.24c). The combination makes any meaningful analysis below 400 eV impossible.

5.2.7 Likelihood Compatibility Check

To check for the compatibility of the different spectra observed in detector modules A, E, J and the light detector of detector A, a simplified dark matter likelihood analysis has been performed. It follows the likelihood analysis method described

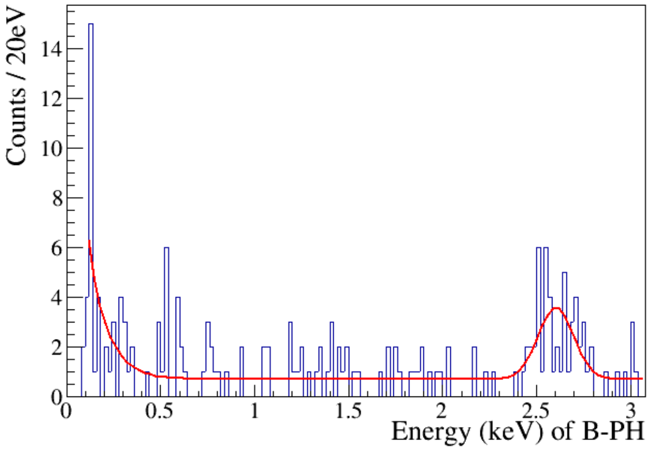

(a)

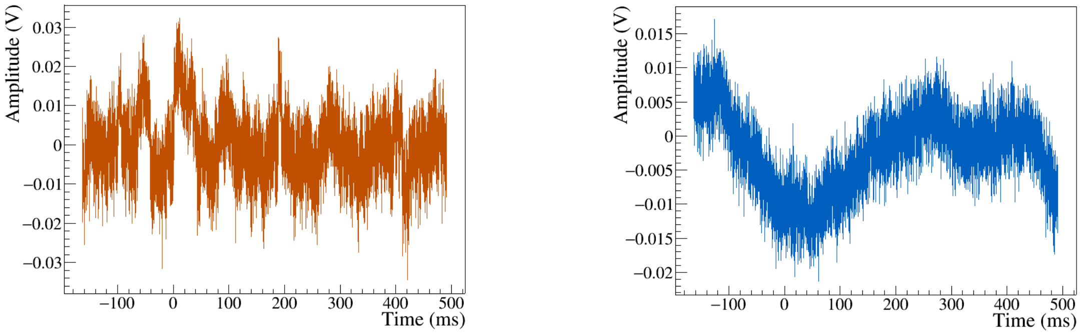

(b) (c)

Figure 5.24: Results for detector modules B, C and D; a) Energy spectrum observed for detector B-phonon. The 2.6 keV peak is visible at the correct energy as well as a rise at energies of about 100 eV. The fit of an exponential at lowest energies is for illustrative purposes only, as the number of observed events and the close by threshold do not allow for a meaningful determination of the decay constant. b) Typical baseline of detector C-phonon. Heavy disturbances make a low energy analysis impossible. c) In addition to a dominating number of baseline jumps (not shown), detector D-phonon also shows strong oscillations on the baseline. The combination makes discrimination of the baseline jumps and thereby a low energy analysis impossible.

in section 3.7.4 for a binned 1D energy spectrum. Included in the likelihood are a flat background and the dark matter spectrum calculated with standard assumptions as presented in section 3.7.1. The survival probabilities are approximated as constant. The likelihood takes into account the measured energy spectra of events with a light yield within $[-10, 10]$ starting from slightly above the detector thresholds. This choice of light yield includes the approximately flat β/γ band which justifies the flat background assumption. The exact values of survival probability, resolution, exposure and energy interval for the likelihood calculation are summarized in table 5.3. The 90 % confidence islands for the best dark matter fits are displayed in figure 5.25 with the exclusion limits from figure 5.13 in the background. In addition, also the exclusion limit for detector E, calculated by [145], is displayed.

Detector	Survival probability (%)	Resolution (eV)	Exposure (kg d)	Energy interval (keV)
A	64	4.6	5.594	[0.032,2]
A Light	30	6	0.151	[0.04,1]
	50	6	0.151	[0.04,1]
E	30	9.4	5.808	[0.065,2]
E TPA offset=0	30	9.4	5.808	[0.081,2]
E TPA offset=4 mV	30	9.4	5.808	[0.043,2]
J	30	13	5.666	[0.07,0.6]

Table 5.3: Summary of choices for the dark matter likelihood fit. Given the lack of a full survival probability simulation, the light detector of module A is fitted with a survival probability of 50 % and 30 %. To check the effect of known possible systematic errors, the default testpulse offset of 2 mV in the energy calibration of detector E is varied by 100 %.

For the dark matter calculation of detector E, the calibration based on the 2.6 keV is used for the calculation. In addition, the offset on the testpulse amplitude discussed in section 5.1.5 is varied by ±100 % which roughly varies the threshold between 40 eV and 80 eV. For the light detector, the 5 % conversion factor from *keVee* to *keV* is assumed, compare section 5.2.4. The Al_2O_3 bulk of the light detector has a mass of about 0.64 g [148]. The calculation for the light detector is performed with survival probabilities of 50 % and 30 %, where 50 % corresponds to the maximum possible survival probability due to the selection on a phonon channel amplitude below zero and 30 % to an realistic estimate of a 60 % survival probability for the other selection criteria. It only includes the high energy tail above 40 eV, compare figure 5.18.

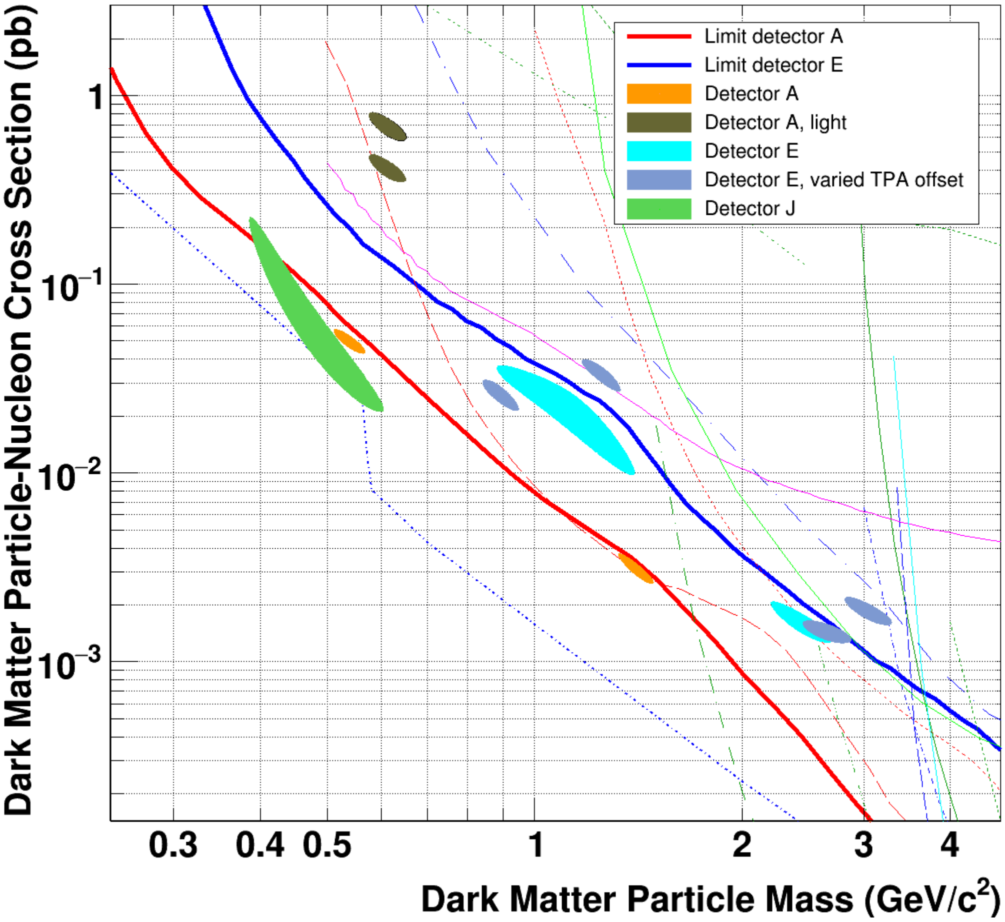

Figure 5.25: Dark matter 90 % confidence islands from a likelihood analysis assuming the excess observed in MCIII-1 is caused by a dark matter signal on top of a flat background. The islands of the different detectors do not overlap, hence a dark matter only interpretation of the excess can be excluded. The limits calculated for detectors A and E are shown in red and blue. In the background, the other limits shown in figure 5.13 are visible for orientation but are not labeled.

The resulting 90 % confidence islands for the different detectors in terms of dark matter mass and interaction cross section can be seen in figure 5.25. There is a clear disagreement between the detectors. This strongly suggests that the observed excess is not caused by a unique, external source. The effect of the significant systematic uncertainties included via the offset variation for detector E is not capable of explaining the differences. As the energy scale of the light detector hits is not fixed by a calibration, it is possible to align them in terms of dark matter mass to the higher mass result for detector A. However, it is not possible to reconcile the different rates leading to incompatible expectations for the cross-section.

5.2.8 Detector Module related Event Types

A detailed analysis of all expected event types in a CRESST-III detector module is given in appendix A. It focuses in detector A, but the event types do appear in all investigated detector modules. The results of this analysis with respect to the low energy excess are summarized in the following. None of the investigated event types appear to be a direct candidate for the excess. The investigated event types are:

- Nuclear and electron recoils in the main absorber (compare appendix A.8.2).
- iStick events caused by an energy deposition in the instrumented holding sticks (compare appedix A.8.3).
- Light stick events caused by an energy deposition in the non-instrumented holding sticks of the light detector (compare appendix A.8.4).
- Foil events caused by an energy deposition in the reflective, scintillating foil (compare appendix A.8.5).
- Direct light detector hits (compare appendix A.8.6).

The analysis includes a comparison of event rates above 100 eV in both phonon and light channel. First, the general results are given, then some considerations concerning specific event classes and their relation to the observed low energy excess are presented.

5.2.8.1 Results concerning Light Detection in the Phonon Channel

It appears that the phonon detector can also detect scintillation light form the scintillating holding structure and the foil. This is not fundamentally surprising with the absorber crystal not being completely transparent [128][138]. However, it has not been observed so clearly in previous CRESST measurements.

One question in this regard is, whether the light is absorbed in the $CaWO_4$ absorber crystal or directly in the dark TES. The sources of light in the detector module are either $CaWO_4$ or the scintillating foil. Both scintillate in the

400 nm [149, 150] range where the crystal is largely transparent with an attenuation length of around 10 cm [138]. The rise times observed for different event classes offers some additional information concerning the question of absorption in the TES vs the absorber crystal. If the photons were absorbed directly in the TES, the ms collection time of the phonon detector would have no impact and the rise time would be dominated by the time constant of the incoming light. However, the fast scintillation of the scintillating foil as well as from the sapphire of the light detector lead to rise times in the phonon channel similar to main absorber events, compare appendices A.8.2, A.8.5 and A.8.6. Therefore, it can be concluded, that the light is indeed absorbed in the crystal with expected collection times.

For completeness, it should be mentioned that in case of a different mechanism, e.g., absorption in the TES, a very high sensitivity to the light component is expected. In an extreme case, this could lead to a stronger total signal in the phonon channel when more scintillation light is produced, contrary to what is expected in the phonon anti-quenching correction to the energy calibration (compare section 3.5.5.1).

As already discussed with the light detector analysis, the detection of light in the main absorber crystal opens up the possibility of a photon induced excess.

5.2.8.2 Electron/Gamma and Neutron Events as Excess Candidates

The β/γ spectrum appears to be relatively flat above 100 eV, compare figure 5.12c. A γ line at threshold would be much better resolved (resolution about $5-10$eV at threshold) than the observed exponentially decaying excess and follow a different spectral shape. There is no specific motivation to attribute the excess to an exponential increase of β or γ radiation from radioactive contamination of unknown origin.

A low energy neutron population could explain the excess. It could be produced by the moderating plastic in the shielding from incident higher energy neutrons.

There exist several measurements of neutron backgrounds e.g. summarized in [98]. In total a flux of about $4\times10^{-6}/(\mathrm{cm}^2\,\mathrm{s})$ is measured/predicted. Scaling to the size of the detector surface, $8\,\mathrm{cm}^2$, a measurement time of 5000 h, 65 % survival probability and 100 % interaction above threshold in the main absorber crystal, this could still only explain $\sim$ 400 of the $\sim$ 800 events observed at low energies. For realistic numbers, a simulation taking the shielding into account is required.

5.2.8.3 Instrumented Stick Events as Excess Candidates

A population of unidentified phonon-only events in the iSticks could explain the excess. In general, for iStick events with a light signal, the light detector is a sufficient veto. If a light signal is detected, the iStick events have a light yield far above the region of interest for a dark matter search. For iStick events without a light signal inside the detector module, the pulse shape is very different (compare figure A.8). This difference should be clearly visible for the ~100 eV events of

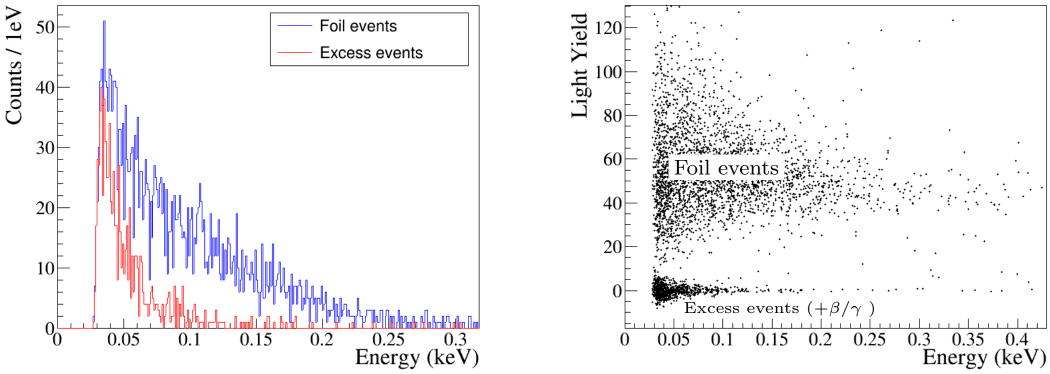

(a) (b)

Figure 5.26: Observed excess spectrum at low energies without region of interest selection compared to the observed foil events in the blind data set after data selection. Foil events have a similar pulse shape and are not specifically targeted by any selection criterion, therefore survival probabilities are expected to be the same as for main absorber events. a) Energy spectrum of low energy events with light yield below ten compared to foil events. The number of β/γ events in the excess spectrum is negligible. b) Foil events and β/γ + excess events are separated in light yield down to threshold.

the excess, excluding the iSticks as an explanation for the excess at least in this regime.

5.2.8.4 Light Detector holding Stick Events as Excess Candidates

Energy depositions in or on the holding sticks of the light detector are shifted far out of the region of interest by the light detector. They are discussed in more detail in appendix A.8.4.

5.2.8.5 Foil Events as Excess Candidates

Foil events are similar to the excess in terms of spectral distribution and number of events in the blind data, see figure 5.26a. They also have a phonon pulse shape that does not differ from main absorber events (compare appendix A.8.5). However, they are clearly separated from the excess events down to threshold in terms of light yield, see figure 5.26b. This implies, that hypothetical foil events that do not produce a signal in the light detector might be a candidate for the excess. However, as already visible in figure 5.26b, at least the spectral shape of foil events with light does not match the excess. This reasonably excludes the possibility of an opaque crystal where light from foil events on the far side does not reach the light detector. Furthermore, more mixed events with a light yield in-between the foil events and zero would be expected for an opaque crystal.

Foil events are discussed in more detail in appendix A.8.5.

5.3 Summary and Conclusions

The detector module of MCIII-1 with the lowest threshold (30 eV, module A) has been analyzed in detail. New limits on dark matter nucleon interaction cross-sections at low dark matter particle masses have been set. The results have been published in [80].

An exponentially rising excess of events below 200 eV of unknown origin is observed. This is severely limiting the sensitivity to dark matter at the lowest energies. Several origins for the excess could be excluded during the analysis.

A similar excess spectrum is also observed in detector A-light. However, calibration factors for direct energy depositions in the light detector can only be guessed.

An excess of events at lowest energies is also visible in the other detector modules that reach the required sensitivity (E,J). However, tensions arise in spectral shape between detector module A and E. Calculating values for the dark matter parameters required to produce the single detector spectra yields incompatible results.

The discussion of the results of an event classes analysis described in appendix A did not offer an obvious explanation for the excess. This analysis includes all event classes that are expected from energy depositions in the different parts of the CRESST-III detector modules. It showed that the phonon detector is also sensitive to scintillation light. This offers the possibility of a light induced excess. Notably, the population of light only events induced by the scintillation of the foil is close to the rate and energy range of the excess in the phonon channel. They are, however, not directly a candidate for the excess as they are reliably shifted far out of the region of interest by the light detector.

Chapter 6
Summary and Outlook

Two major analyses have been performed in the present work. The α analysis of the CRESST-II phase 2 measurement campaign yielded precise values for the internal radioactive contamination of the employed crystals. A preliminary version of those results had already been successfully deployed in recent background simulations. Furthermore, dedicated analysis methods have been developed that can be of use for upcoming analyses.

The major challenge of the α analysis came from the high energy deposition of αs ($\mathcal{O}(1\,\mathrm{MeV})$) compared to the keV energies the setup was optimized for. α pulses exceed the dynamic range of the detectors, saturating their output, making an energy reconstruction challenging. In addition, flux quantum losses appear from the SQUID read-out. Both effects cannot be simulated, therefore also a simulation based approach to obtain the survival probabilities of α events is not feasible.

As a solution to the energy reconstruction, a combination of parameters centered around a truncated standard event fit was exploited to get an energy proportional parameter with sufficient resolution. The α lines were identified by their characteristic pattern and the final calibration based on the position of two well identifiable lines. This allowed to clearly identify all expected α lines.

Concerning the survival probability, a careful analysis allowed to extract lower and upper bounds on the α rates as well as a rate based on an average, data driven survival probability. The methodology for energy calibration, identification of α lines and rate calculations was described in detail.

The results were compared to a previous, published α analysis based on a subset of the data analyzed in this work. Compared to the previous work, the resolution of the energy reconstruction could be significantly improved, allowing for a better separation of the α lines. Furthermore, γ escape lines, where a γ from the α decay escapes the detector, could be identified that had not been taken into account before.

The dark matter analysis of the CRESST-III Phase 1 data yielded new, published limits on the spin-independent dark matter particle - nucleon scattering cross section at low WIMP-like dark matter masses down to $160\,\mathrm{MeV}/c^2$. It focused on the best performing of ten geometrically identical detector modules. This module had an energy threshold of $30.0^{+4.8}_{-6.5}(sys.) \pm 0.2(stat.)$eV.

This is the first analysis based on the newly installed continuous data acquisition of CRESST. A major improvement compared to the previous dark matter analyses is the continuous simulation. It allows to obtain the survival probability of a potential dark matter interaction into the final data set in a consistent manner, eliminating some long standing, known issues of the previous methods. For the continuous simulation, the dark matter events are simulated on the stream and undergo the full analysis, including triggering and event building.

The analysis revealed an exponentially rising background excess starting at about 200 eV, severely limiting the sensitivity down to the 30 eV threshold of the detector. The excess events show no light signal. This would be the expected behavior of nuclear recoils but also β/γ events at these low energies. Great effort has been dedicated to understanding the origin of these events.

Comparison with two more detector modules as well as direct hits on the light detector revealed similar but ultimately incompatible excess spectra. This was shown by extracting the 90 % confidence parameter spaces for a dark matter explanation of the observed excess for the detectors independently of each other and comparing them.

The efforts on the understanding of the origin of the excess included a precise understanding of the expected event types from the detector geometry. To this end, an analysis very different from the dark matter analysis was required of which the results were discussed briefly with regard to the excess events. The new detector module design of CRESST-III phase 1 with the partially instrumented holding structure (iSticks) offers unique possibilities in this regard. Event types originating from all parts of the holding structure could be identified.

A striking feature from this analysis was the clear presence of a light component detected in the phonon channel either by absorption in the main absorber crystal or the TES structure. The analysis underlines the importance of the light detector for background identification and reduction.

None of the investigated event types appeared to be viable candidates for producing the excess events. Hence, no conclusive verdict could be reached in their origin.

The observed excess will prevent an increase of sensitivity of the CRESST experiment at low energies in terms of interaction cross-section. Accordingly, identifying the origin of these events and subsequently removing them has to be the primary concern of further developments. A new measurement campaign with modified CRESST-III Phase 1 detector modules has been performed between September 2018 and September 2019. Another measurement campaign with further, complementary modifications is underway. The modification did and will include for example:

- differently polished crystals to investigate surface effects;
- different orientations of the TES to investigate magnetic effects, especially concerning the baseline jumps. In addition, coils and a magnetometer have been installed around the cryostat. They are used to compensate changes in the external magnetic fields;
- replacing the instrumented holding sticks by copper sticks can remove any backgrounds from energy depositions within the sticks;

- removing all scintillating holder parts allows to remove scintillation light based backgrounds. However, the $CaWO_4$ main absorber is still scintillating;
- replacing the $CaWO_4$ absorber by a Al_2O_3 or Si crystal allows to investigate material related effects;
- a newly developed $LiAlO_2$ neutron detector can investigate the neutron background;

Combining the results of these measurements with the understanding of event types developed in this thesis will hopefully allow to decipher the origin of the excess events.

Another step towards understanding is the improvement of background simulations currently under way, especially concerning neutrons. Furthermore, a specialized setup for α measurements of CRESST crystals operated as cryogenic detectors is currently being tested at TU München that should avoid the major challenges discussed in the α analysis in this work.

Appendix A
Event Class Analysis

A detailed analysis of the event classes expected in the MCIII-1 detector modules has been performed. Motivation and introduction to the general idea are given in section A.1. Sections A.2 to A.7 largely follow the analysis steps outlined in chapter 3. The different event classes can be found in section A.8. For each class, the origin, energy transport, identification, rates and signal shape are presented. The findings are discussed in section 5.2.8 as part of the dark matter analysis and the extracted event rates are only briefly summarized in section A.9.

A.1 Introduction and Motivation

The MCIII-1 detectors consist of several instrumented, active and passive parts (compare section 2.2). The parts relevant for the event class analysis are marked in the schematic module drawing in figure A.1. All parts with a direct line of sight to the main absorber crystal are at least active, i.e., scintillating.

Incoming particles can deposit energy in any of those parts. Different combinations of particles and detector parts lead to a multitude of different event classes. Each class produces a distinct signatures in the three read out channels. Identifying all expected event classes is crucial for the understanding and rejection of backgrounds as well as for confidence in a potential dark matter signal. Furthermore, understanding can lead to improvement in the detector design for upcoming measurements and verification of simulation efforts.

A.2 Pre-Analysis Knowledge

The event class analysis is based on the same data sets as described in section 5.1.1 for the dark matter analysis. A combination of data from γ and neutron calibration as well as the training and blind set is used. This allows to compare rates of event classes in the presence of different backgrounds. The analysis focuses on detector module A. Presented plots are taken from the neutron calibration if not stated otherwise.

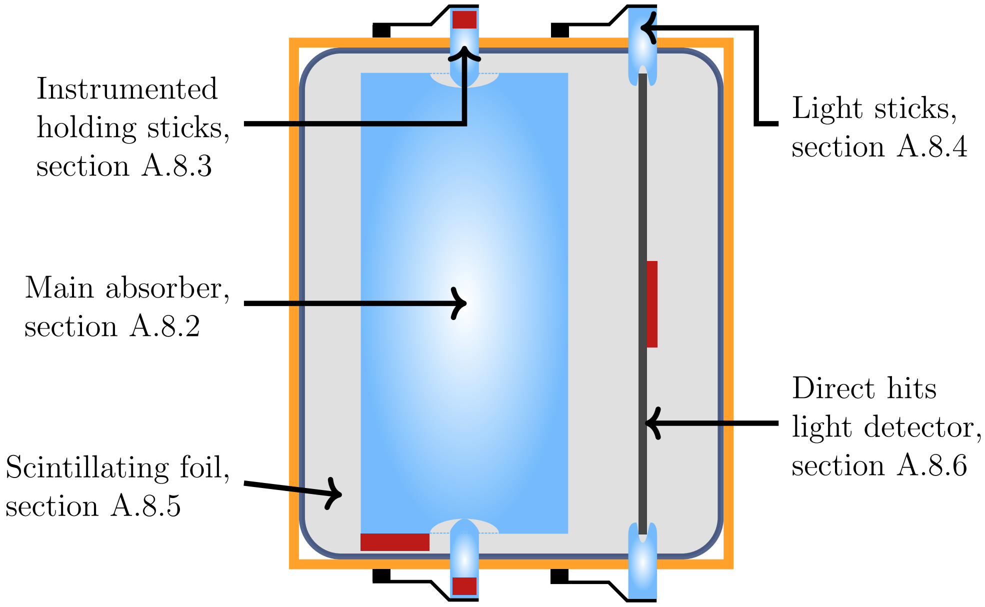

Figure A.1: Schematic drawing of a CRESST-III Phase 1 detector module with the origins of the different possible event classes marked.

A.3 Parameter Gathering

A.3.1 Basic Parameters

Parameters of importance are the peak position for the removal of unwanted events and the pulse height for the classification of events. Furthermore, the peak position minus onset parameter is taken as an estimate of the rise time of a pulse signal. Empirically, It shows a more consistent performance and better separation of event classes than the rise time parameter. For simplicity, in the following, the peak position minus onset parameter is often referred to as rise time. For the classification of FQLs and SQUID resets the right minus left baseline parameter is required.

A.3.2 Template Event Fit and Optimum Filtering Parameters

The classification of events requires a parameter that is proportional to the signal strength also in the saturated range of the TESs. Unlike for the dark matter analysis, a direct proportionality or good resolution is not necessary. However, the dynamic range of the parameter has to reliably cover events up to several hundred keV. Events should not be misidentified or not considered in the analysis due to a failed or wrong parameter determination.

This can be achieved with a truncated standard event fit with a high truncation limit above the linear range. An example of a pulse fitted with the high truncation limit can be seen in figure A.2. The fitted standard event no longer fully describes the observed pulse trace. Nonetheless, it produces a fitted amplitude proportional to the signal strength. The high truncation limits compared to the standard truncation limits are listed in table A.1. This method also works well for event classes with a slightly different pulse shape, even without changing the standard event.

The phonon and light channel standard event fits are based on the same standard events as the dark matter analysis. For the iStick channel, standard events are created by averaging over a number of pulses (compare section 3.2.2.1).

The optimum filter is only required for triggering.

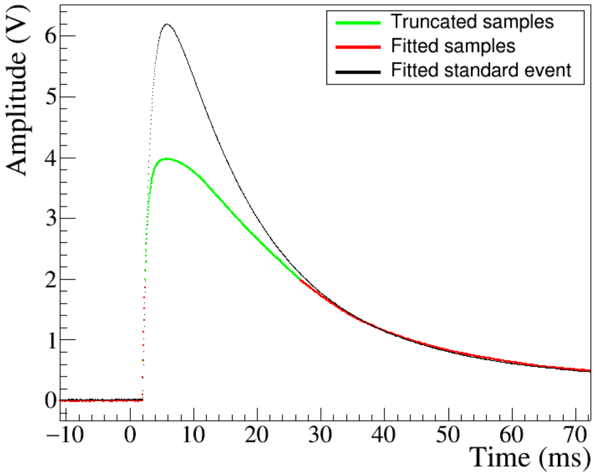

Figure A.2: High truncation fit of a pulse in detector A, phonon. Samples in green are above the truncation limit of 2 V. They are not considered for the standard event fit shown in black. The fit does not fully describe the fitted part of the pulse record (red). It nonetheless produces a fitted amplitude that is proportional to the signal strength.

Detector	Dark matter analysis truncation limit (V)	High truncation limit (V)
A-PH	0.6	2
A-L	0.16	0.3

Table A.1: Truncation limits for detector A, phonon and light for the high truncation standard event fit. The truncation limits for the dark matter analysis are given for comparison.

A.4 Data Selection

The goal of the data selection criteria applied in this section is to remove non-particle induced artifacts. Special attention is given to keeping all events that could belong to one of the searched for event classes. The identification scheme for a specific event class is discussed in the corresponding event class sections.

A.4.1 Pre-selection on Files and Time Periods

The same selection of files, rate and stability cuts as for the dark matter analysis are applied (compare section 5.1.3.2). The rate cut was adjusted to the higher overall rate in the neutron and γ calibration each. The raw measurement times after rate and stability cut are summarized in table A.2.

Measurement	Raw measurement time (h)
Neutron calibration	565
γ calibration	364
Training data	600
Blind data	4 821

Table A.2: Raw measurement times after rate and stability cut for detector A and different data sets.

A.4.2 Basic Selection for the Event Class Analysis

Many of the event classes discussed in the following are considered an undesired background for the dark matter analysis. Therefore, their survival probability can be very low with the data selection considered in section 5.1.3. Hence, the event class analysis requires a different set of selection criteria. To avoid elaborate efficiency considerations, only the following basic scheme scheme is applied after rate and stability cut:

- A selection on the peak position parameter is applied to the phonon channel to remove the main artifact population, i.e., the decaying baselines (compare 3.3.2.1).
- A selection on the pulse height corresponding to about >100 eV energy deposition is applied. This is above threshold and ensures that the measured rates are not spoiled by threshold effects or the baseline jump events discussed in section 5.1.3.1.
- The same selection criteria are applied to the light detector but also starting from the full data set. The energy cutoff of is set to 2 keVee. Assuming a total of 5 % for scintillation and detection efficiency, this corresponds to a 100 eV energy deposition, too.
- The resulting phonon and light sets are merged. That way, all events with at least one proper pulse are kept for further analysis.

A.4.3 SQUID Resets and Flux Quantum Losses

There is one category of artifacts specifically relevant for the rate analysis below, namely SQUID resets and flux quantum losses. They are induced by real particle interaction. Therefore, they cannot be removed without further consideration when considering a rate calculation. They survive the basic data selection scheme described above and can subsequently be separated by the right minus left baseline parameter from the other events. Table A.3 summarizes the rate of such events relative to the total number of events. While their influence overall is small they are not necessarily equally distributed over all event types and can be a major contribution to a specific event type. Fortunately, for the most part, they can be assigned to the correct event classes by applying an adapted identification scheme.

Measurement	FQLs and resets
Neutron calibration	13.8 %
γ calibration	2.5 %
Training data	10.7 %
Blind data	11.9 %

Table A.3: Percentage of flux quantum losses and SQUID resets compared to the total event rate for the different data sets, detector A.

A.5 Survival Probabilities

The number of different event types and their more complicated behavior compared to the main absorber events makes a simulation based approach for the survival probability impractical. Above the artificial analysis threshold of 100 eV, the different event classes can be very well separated by a combined selection on several parameters. This allows to apply only a loose selection on each individual parameter. It is assumed that the losses from these loose selection criteria are negligible for the following considerations and no survival probability is derived. A more detailed treatment is beyond the scope of this appendix.

There is a DAQ dead time of about 2% of the raw measurement times given in table A.2 due to test and control pulses. This is negligible for the rate considerations in this chapter.

A.6 Energy Calibration

For the most part, no energy calibration is required for the considerations in this chapter. Where necessary, a linear, peak based calibration, compare section 3.5.2, is applied.

A.7 Light Yield, Band fits and Limit Calculation

The light yield, band fits and limit calculation are not relevant for the event class analysis. Particle identification based on the ratio between phonon and light signal are directly defined in the phonon vs light pulse height or fitted amplitude plane.

A.8 Event Classes

A.8.1 Total Event Population

A quantitative analysis requires comparison of event rates in the presence or absence of calibration sources. That way, correlation between the rate of a certain event type to the γ , neutron and total background can be extracted. The correlation can give valuable hints towards the origin of certain event classes.

To obtain the observed rates, only the basic selection criteria as described in section A.4.2 are applied. The remaining number of events is divided by the raw measurement times of table A.2 to obtain an hourly event rate. The measured total event rates are given in table A.4.

Measurement	Rate (cts/h)
Neutron calibration	133
γ calibration	54
Training data	2.8
Blind data	2.8

Table A.4: Total observed event rates for detector module A and different data sets.

A.8.2 Main Absorber Events

Electron and nuclear recoils in the main absorber make up the bulk of events. They are the intended way of detecting a particle. As discussed in section 3.6, detectable electron recoils are caused by β and γ particles. Nuclear recoils stem mainly from neutrons and therefore appear almost exclusively in the neutron calibration.

Energy Transport When an electron or nuclear recoil in the main absorber takes place, a phonon population is excited and scintillation light is emitted. Both can be detected in the phonon channel. Furthermore, the scintillation light is detected in the light channel. Phonons can be transmitted to the iSticks through the contact point. This enabled the α analysis in [138] but is of no further interest here. A schematic view is shown in figure A.3a.

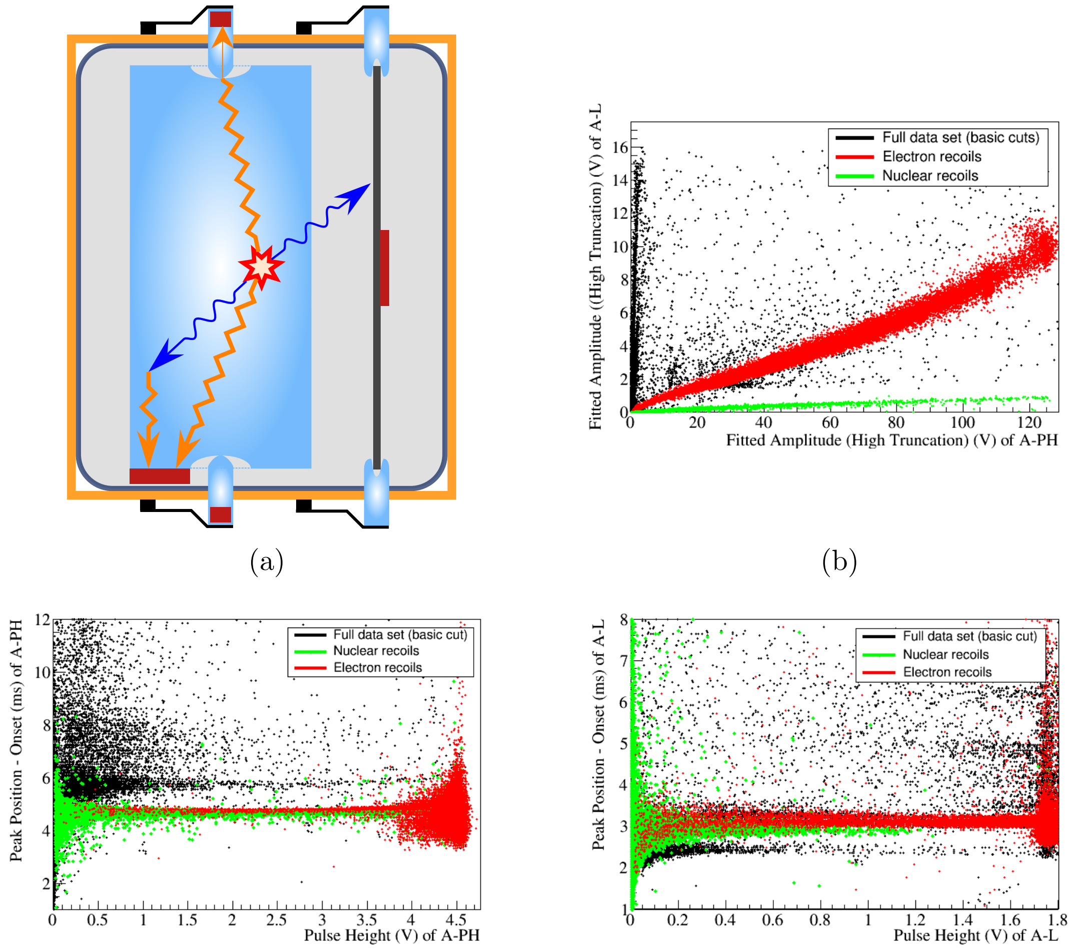

(a) (b)

(c) (d)

Figure A.3: Electron and nuclear recoil events in the main absorber. a) Schematic representation; interaction location (star) and transmission via phonons (orange) and light (blue). b) Position of electron recoils (red) and nuclear recoils (green) in the fitted light vs phonon amplitude plane of the high truncation standard event fit. The remaining events are shown in black. c) Rise time of electron and nuclear recoil events in the phonon channel. d) Rise time of electron and nuclear recoil events in the light channel.

Identification Electron and nuclear recoils can be identified by the bands they form in the light pulse height vs phonon pulse height or fitted amplitude planes. Their energy range extends into the fully saturated regime for both channels. Therefore, the fitted amplitude with the high truncation limit is the best parameter for identification purposes. It allows a clear identification of the electron and nuclear bands up to the highest energies (see figure A.3b). Events with FQLs get fitted in a way that leads to a shift in the position of the bands. They can be categorized accordingly (not shown).

The bands start to overlap at low energies. Some misclassified events at low energies are removed by an additional selection on the rise time and the iStick pulse height.

Rates Nuclear and electron recoil event rates are summarized in table A.5. A significant amount of nuclear recoils can only be observed in the presence of the neutron calibration source. The neutron calibration also yields the highest rate of γs at low (<50 keV) energies. The γ calibration has its main γ rate at higher energies below the 122 keV peak.

	Rate (cts/h)		Fraction of total rate (%)	
Measurement	e^-	n	e^-	n
Neutron calibration [cts/h]	84	14.6	63	11
γ calibration [cts/h]	41	–	77	–
Training data [cts/h]	0.97	–	34	–
Blind data [cts/h]	1.0	–	36	–

Table A.5: Relative and absolute electron and nuclear recoil event rates for detector A and different measurements.

Signal Shape The phonon pulse shape of nuclear and electron recoil events follows the model for an energy deposition in the main absorber, compare section 2.2.3. A slight difference in rise time in the sub ms range is observed between nuclear and electron recoils. The nuclear recoils are faster, i.e., have a lower rise time. This is illustrated in figure A.4.

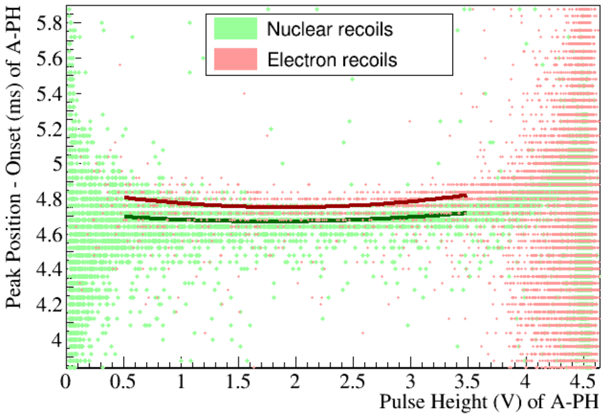

Figure A.4: Comparison of the rise time of nuclear (green) and electron (red) recoil events in the phonon channel. A polynomial of second degree is fitted to both populations. The fit uses a least trimmed square regression to minimize the effect of the obvious outliers. Nuclear recoil events show a faster rise time than electron recoils.

In the light channel, the observed rise time is a combination of the intrinsic rise time of the light detector and the 0.36 ms [149] scintillation time of the $CaWO_4$ main absorber. The scintillation from nuclear recoils is thereby slightly faster, leading to a slightly ($< 10\%$) faster signal in the light channel (see figure A.3d). Details about the corresponding scintillation mechanism can be found in [101].

The main difference between electron and nuclear recoils lies in their different light yield. Overall, their light to phonon signal ratio is the smallest of all the event classes considered, compare figure A.3b.

A.8.3 iStick Events

The iStick events stem from an energy deposition in one of the three instrumented $CaWO_4$ holding sticks of the main absorber crystal. This is the kind of events the iStick veto system is intended to identify.

Energy Transport When an incident particle deposits energy in an iStick, a phonon population is excited. It is primarily detected by the iStick TES. Some of it is transmitted via the contact point to the main absorber crystal where it is picked up by the phonon channel.

Furthermore, scintillation light is produced. The iSticks extend to the outside of the detector housing. Therefore, the amount of light that is detected by the phonon and the light channel depends on the position of the interaction. For energy deposition on the outside, most of the light escapes outside the housing. For energy deposition on the inside, the light signal is expected to behave the same as scintillation light from an energy deposition in the $CaWO_4$ main absorber. Where the distinction is relevant, those events are referred to as “inside iStick events” and “outside iStick events” in the following. A schematic drawing is shown in figure A.5a.

Identification The iStick events can be identified by their signal in the iStick channel. Some care has to be taken as very high energetic events in the main absorber also transmit a signal in there. The three iSticks are read out by a single readout channel (compare section 5.1.1). Nonetheless, they can be distinguished by their different TES sensitivities and saturation limits (see figure A.6). A separation by their different decay times is possible at high energies (not shown). Inside and outside iStick events can then be subsequently identified in a plot of light channel fitted amplitude vs iStick fitted amplitude (compare figure A.7). Attributing the visible bands to energy depositions in- and outside the housing and not to electron vs nuclear recoil events is based on having the same bands clearly visible in the γ calibration. The iSticks will be labeled 1,2 and 3 in the following as indicated in figure A.6.

Rates The iStick event rates are summarized in table A.6. They make up about

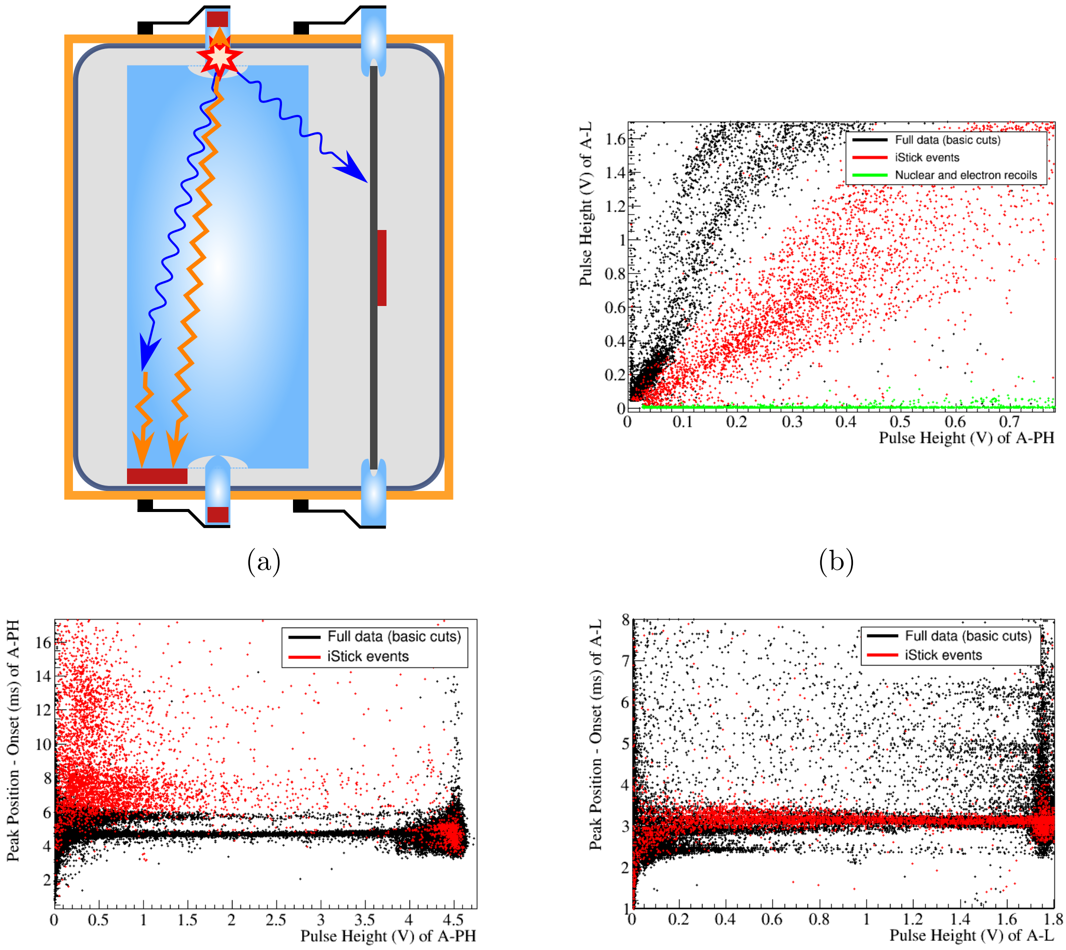

(a) (b)

(c) (d)

Figure A.5: Summary of iStick events. a) Schematic representation; interaction location (star) and transmission via phonons (orange) and light (blue). b) iStick events (red) in the light vs phonon pulse height plane. For comparison, the main absorber events identified in section A.8.2 are marked in green. Shown is a zoom into the low pulse height region of both, phonon and light channel compared to figure A.3b (pulse height and fitted amplitude are interchangeable in this region for the discussed analysis). c) Rise time of iStick events in the phonon channel. d) Rise time of iStick events in the light channel.

10 % of the total event rate in all data sets. Their relative rate in the calibration data is smaller than in the training and blind data.

Signal Shape The pulse shape observed in the iStick channel for iStick events strongly depends on the specific iStick's TES and coupling to the heat bath. It is of no further interest here.

The iSticks are made of CaWO4 and show the same scintillation properties and light signal shape as the main absorber. This is visible in the rise time parameter

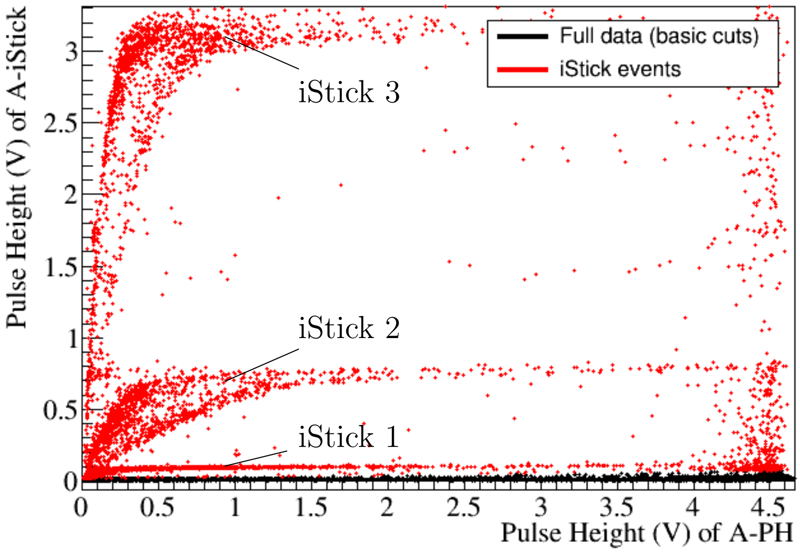

Figure A.6: iStick vs phonon pulse height plot used to identify the iStick events (red) and separate between the three iSticks (labels). The iStick TESs are read out by only one read-out channel. Nonetheless, they can be separated by the different sensitivities and dynamic ranges of the TESs. The labels (iStick 1-3) are not related to the physical position of the sticks within the detector module.

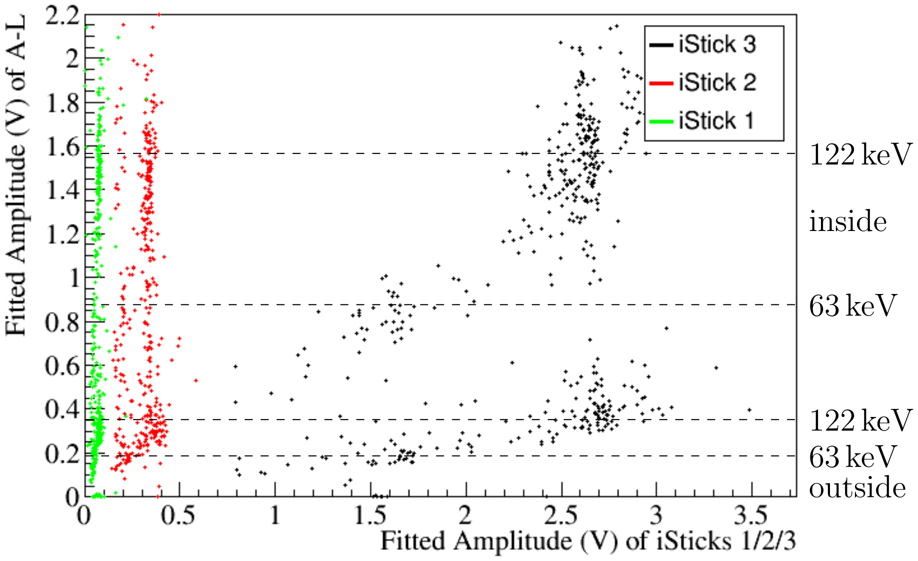

Figure A.7: Calibration peaks of iStick events in the γ calibration measurement. Each iStick is fitted with its own standard event. iSticks show different sensitivities but similar light signals for the 63 keV and 122 keV calibration lines. More light is visible in the light channel for iStick events inside the module housing.

Measurement	Rate (cts/h)	Percentage of total Rate (%)
Neutron calibration	9.5	7.2
γ calibration	3.9	7.3
Training data	0.35	12.3
Blind data	0.33	12.0

Table A.6: Relative and absolute iStick event rates for detector A and different data sets.

in figure A.5d. The amount of detected light however depends strongly on the position of the interaction.

The phonon channel shows a more complicated behavior. The iStick events have a broad distribution in the rise time (see figure A.5c). The light and the heat component in the phonon channel have very different pulse shapes. This can be derived from events with energy depositions in- and outside the copper housing (compare figure A.8).

The heat transmitted from the iStick results in a very slow, no longer calorimetric pulse. It appears that the time constant of the energy input actually exceeds the decay time of the thermal component (compare figure A.8a). The light detected by the phonon detector leads to a faster component (compare figure A.8c). It is similar to what is discussed for the light stick events in section A.8.4. Both components contribute about equally to the pulse height of iStick events inside the housing.

Of the three holder related event classes (iStick, Light stick and Foil), the iSticks have the lowest light to phonon ratio, see figure A.5b. This is due to the phonon channel seeing both, the light and a direct thermal component while the light channel only sees the light component.

A.8.4 Light Stick Events

Energy depositions can also happen in the $CaWO_4$ sticks holding the light detector. This leads to a situation analogous to the iStick events but an inverted role of light and phonon detector.

Energy Transport When an incident particle deposits energy in one of the sticks holding the light detector, a phonon population is excited that is partially transmitted to the light detector. Furthermore, scintillation light is produced that is picked up by both, the light and the phonon detector. Similar to the iStick events, the interaction can happen in or outside the detector housing leading to a more or less pronounced light signal. A schematic representation is shown in figure A.9a.

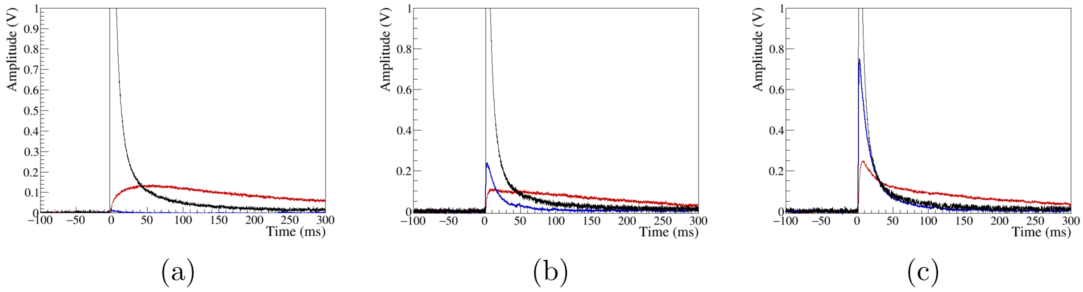

Figure A.8: Three events in iStick 3 of detector module A with the same iStick pulse height, i.e., similar energies. They differ in the amount of light visible inside the module. Red: Phonon channel; Blue: Light channel; Black: iStick channel. a) iStick event with almost no light visible to the phonon and light detector. Possibly a nuclear recoil in the iStick, outside the housing. Only a slow component is visible in the phonon channel. b) iStick event with a medium amount of light visible in the phonon and light channel. Possibly an electron recoil in the iStick, outside of the housing. c) iStick event with a strong light signal visible in phonon and light channel. Possibly an electron recoil in the iStick inside the housing.

Measurement	Rate (cts/h)	Percentage of total Rate %
Neutron Calibration	7.2	5
γ Calibration	5.1	10
Training Data	0.13	4
Blind Data	0.14	5

Table A.7: Relative and absolute light stick event rates for detector A and different data sets.

Identification Light stick events have the highest light yield / slope in the light vs phonon plane of the three holder related backgrounds as the directly transmitted heat component is added to the light channel. Their pulse shape in both phonon and light channel is roughly the same as for main absorber events. Therefore, they can be most easily identified plotting the amplitudes of the high truncation fit, see figure A.9b. Light stick events with almost no signal in the phonon channel, can be separated from direct light detector hits by their slower rise time, compare figures A.9d and A.11d.

Rates The rates of light stick events are summarized in table A.7. No significant contribution of light channel FQLs to the light stick events could be found.

Signal Shape The rise time of light stick events in the phonon channel is slightly slower than for main absorber events, see figure A.9c. This is due to the 0.36 ms scintillation time of the $CaWO_4$ compared to an instantaneous energy deposition.

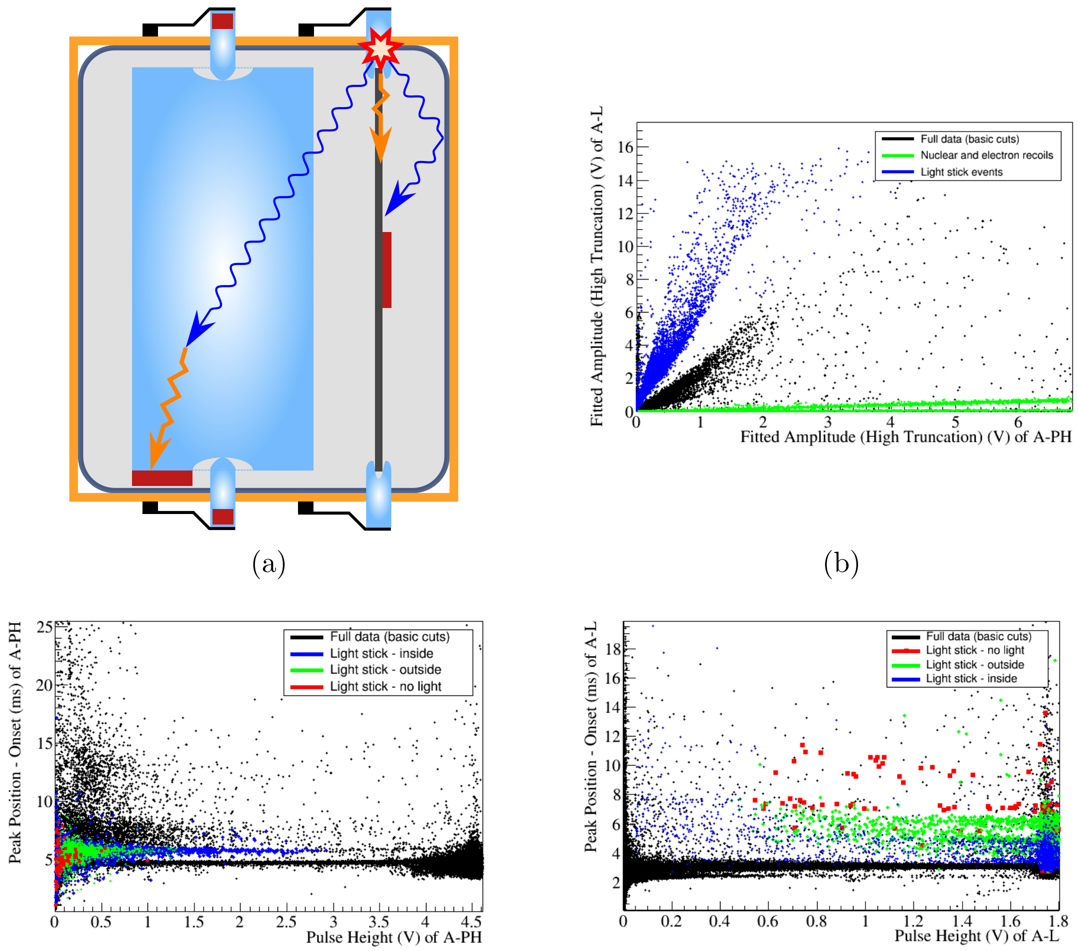

(a) (b)

(c) (d)

Figure A.9: Summary of light stick events. a) Schematic representation; interaction location (star) and transmission via phonons (orange) and light (blue). b) Light stick events (blue) in the light vs phonon fitted amplitude (high truncation) plane. For comparison, the main absorber events identified in section A.8.2 are marked in green. c) Rise time of light stick events in the phonon channel. The light stick events are further separated into events inside (blue) and outside (green) of the housing as well as events completely without a visible light component (red), presumably from nuclear recoils outside the housing. d) Rise time of light stick events in the light channel with the same colorcoding as in figure A.9c.

The spatial origin and amount of light (outside or inside light stick events, nuclear or electron recoil) on the other hand does not affect the shape, only the signal height.

In the light channel, light stick events are slower than main absorber events. This is due to the slow, directly transmitted thermal component. A rough separation between three subclasses, events with more light, less light and almost no light is possible. The amount of light is derived from the phonon channel signal. The first two subclasses can again be attributed to interactions in- and outside the housing. The low number of observed events does not allow for a final conclusion on whether the third subclass consists of nuclear recoils or another geometrical effect. All three subclasses are marked separately in the rise time plots of figure A.9c and A.9d.

As already introduced for the identification, light stick events have the highest light to phonon signal ratio of the holder related event classes. It is not possible to separate the different holding sticks as they are not instrumented.

A.8.5 Low Energy Excess Light / Foil events

Foil events from the scintillating foil make up the third class of holder related events. Their signature is a light signal in both, the phonon and the light channel, but no direct thermal component. Hence, they are expected to appear in the pulse height plot in-between the iStick and the light stick bands.

Energy Transport Energy depositions in the foil surrounding the phonon and light detector lead to the production of scintillation light. Observationally, foil events appear to be restricted to low energies (<1 keVee). Some more detailed investigation into the scintillation properties of the foil can be found in [150] and the appendix of [138]

A schematic view of the energy transport of foil events is shown in figure A.10a.

Identification The foil events are identified by a wide selection on the corresponding band in the light vs phonon amplitude plane of the high truncation fit. The iStick events that leak into this region are removed by a selection on the iStick pulse height. The light stick events that leak into this region are removed by a cut on their slower rise time in the light channel. Direct light detector hits cannot be separated from foil events at very low energies but have a negligible rate in comparison. The identified foil events are marked in the light vs phonon amplitude plane in figure A.10b.

Rates The rates of foil events are summarized in table A.8. The neutron calibration shows a much enhanced rate compared to the blind data set. Surprisingly, the γ calibration shows only a 10 % increase compared to the blind data set. This is despite a factor 20 difference in overall rate. It is not possible to determine whether the increase for the neutron calibration is due to the neutrons or the much more abundant low energy γs not found in the γ calibration.

Signal Shape Foil events have the same rise time in the phonon channel as main absorber events, see figure A.10c. The foil is made out of a plastic scintillator, Polyethylenenaphthalate (PEN) [150]. The timescale of the PEN scintillation is in the ≈ 100 ns range [151]. This results in a practically instantaneous energy deposition compared to the ms timescale of the detector response, similar to absorber events.

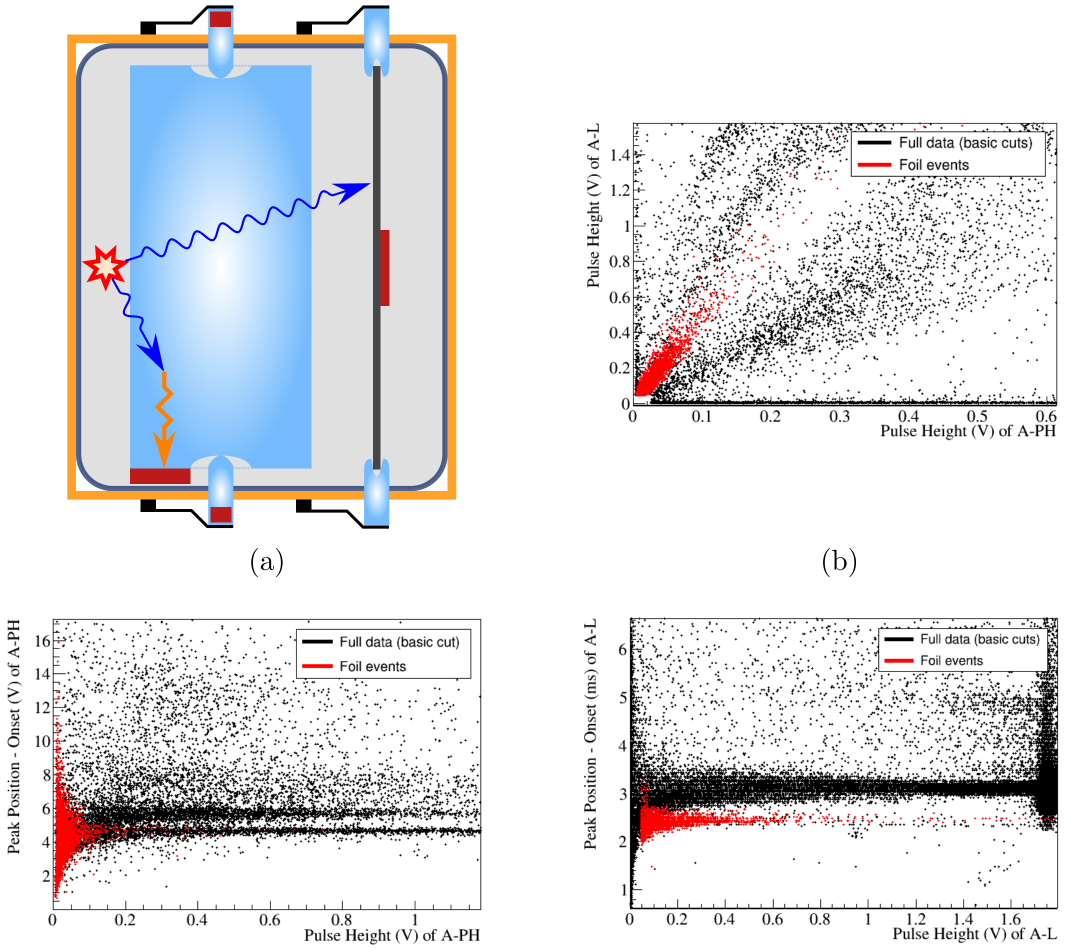

(a) (b)

(c) (d)

Figure A.10: Summary of foil events. a) Schematic representation; interaction location (star) and transmission via phonons (orange) and light (blue). b) Foil events (red) in the light vs phonon pulse height plane. Shown is a zoom into the lower pulse height region compared to figure A.3b. c) Rise time of foil events in the phonon channel (red). d) Rise time of foil events (red) in the light channel.

Measurement	Rate (cts/h)	Percentage of total Rate %
Neutron Calibration	5.4	4
γ Calibration	0.87	1.6
Training Data	0.77	27
Blind Data	0.72	26

Table A.8: Relative and absolute foil event rates for detector A and different data sets.

In the light channel a signal faster than for main absorber events is observed, see figure A.10d. It has the same rise time as direct hits to the light detector, compare section A.8.6. Again, this is explained by the fast scintillation of the foil.

As introduced for the identification, the light to phonon ratio is in between the iStick events and the light stick events, see figure A.10b.

A.8.6 Direct Light Detector Hits

Similar to events in the main absorber, also the light detector can be directly hit by a particle.

Energy Transport Direct interactions of incident particles with the light detector predominantly cause a signal therein. Furthermore, the sapphire of the silicon-on-sapphire light detector can be scintillating, albeit with a much lower scintillation yield than $CaWO_4$. This light can be picked up by the phonon detector. A schematic representation can be found in figure A.11a.

Measurement	Rate (cts/h)	Percentage of total Rate %
Neutron Calibration	3	2
γ Calibration	0.8	2
Training Data	0.1	4
Blind Data	0.1	3

Table A.9: Relative and absolute direct light detector hit event rates for detector A and different measurements.

Identification Direct hits to the light detector can be identified as almost light only in the light vs phonon pulse height / amplitude plane, compare figure A.11b. Their faster rise time allows to discriminate them from no-light light stick events.

Due to their fast rise time and very high energy deposition, direct light detector hits are dominated by FQLs. They can be discriminated from other event types with FQLs in the phonon pulse height vs light right minus left baseline plane (not shown).

Rates The rates of direct light detector hits are summarized in table A.8.

Signal Shape Direct light detector hits show a fast rise in the light channel due to immediate energy deposition in there, see figure A.11d, also discussed in [152].

The sapphire appears to scintillate. This leads to a strongly suppressed signal in the phonon channel with a fast rise time, see figure A.11c. Similar to events in the main absorber crystal, the scintillation allows to distinguish nuclear and

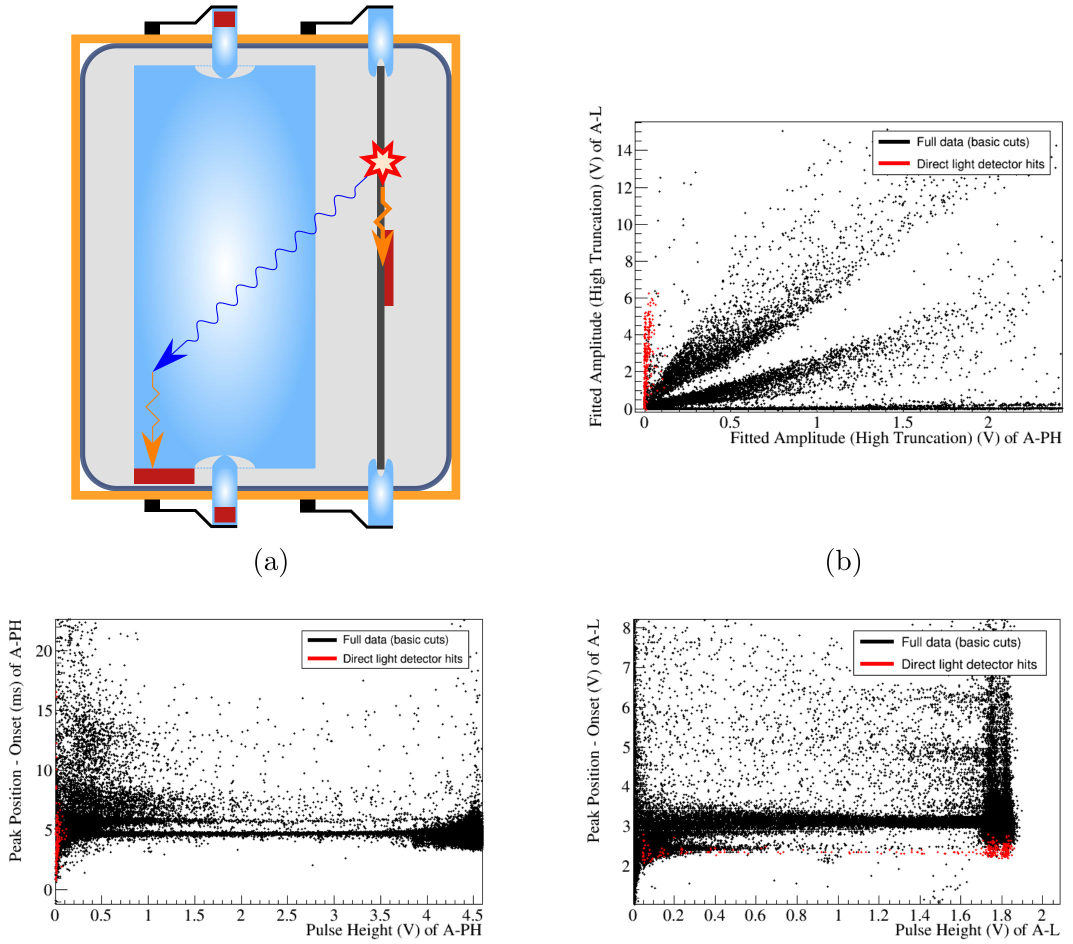

(a) (b)

(c) (d)

Figure A.11: Summary of direct light detector hits. a) Schematic representation; interaction location (star) and transmission via phonons (orange) and light (blue). b) Direct light detector hits (red) in the light vs phonon fitted amplitude (high truncation) plane. Shown is a zoom into the low amplitude region compared to, e.g., figure A.3b. c) Rise time of direct light detector hits in the phonon channel. d) Rise time of direct light detector hits in the light channel.

electron recoils. This is demonstrated in figure A.12 by comparing neutron and γ calibration data.

A.9 Summary of the observed Event Rates

Rates in terms of cts/h are calculated for all events types only taking into account events with an energy depositions in the main absorber and/or light detector above 100 eV. The rates are summarized in table A.10 and discussed in the following. Relative rates between the different components and for different background situations can serve as valuable input to simulation efforts.

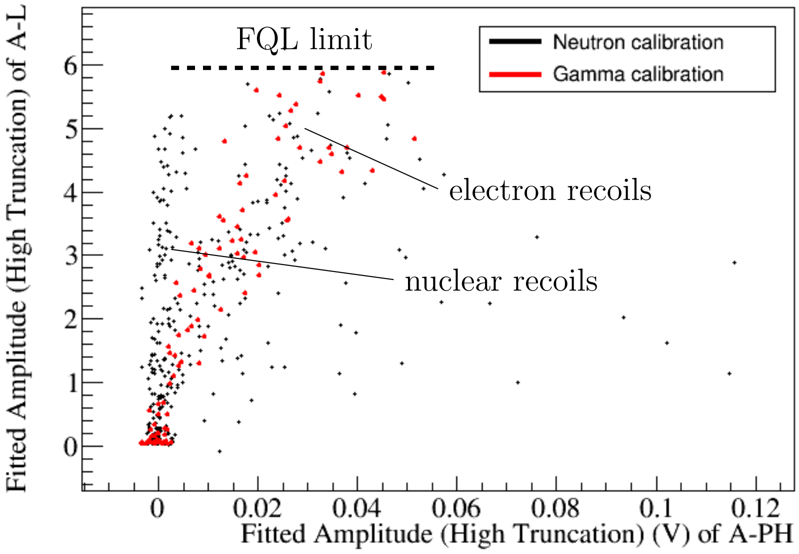

Figure A.12: Particle discrimination for direct light detector hits. The sapphire of the light detector is scintillating. The scintillation light is detected in the phonon channel via absorption of the light in the main absorber crystal. Direct hits deposit comparably high energies in the light detector and have a fast rise time. This leads to almost all events above the indicated "FQL limit" suffering from FQLs.

Measurement	Total rate	Absorber electron	Absorber nuclear	iStick	Light stick	Foil	Light detector
Neutron calibration [cts/h]	133	84/63 %	14.6/11 %	9.5/7.2 %	7.2/5 %	5.4/4 %	3/2 %
γ calibration [cts/h]	54	41/77 %	–	3.9/7.3 %	5.1/10 %	0.87/1.6 %	0.8/2 %
Training data [cts/h]	2.8	0.97/34 %	–	0.35/12.3 %	0.13/4 %	0.77/27 %	0.1/4 %
Blind data [cts/h]	2.8	1.0/36 %	–	0.33/12.0 %	0.14/5 %	0.72/26 %	0.1/3 %

Table A.10: Summary of event rates of detector A for the different event types and measurements investigated. Given is the absolute rate in cts/h as well as the rate relative to the total rate in %.

For interpretation of the different (relative) rates, the different energy spectra of γ and neutron calibration as well as the dark matter data have to be kept in mind. The neutron calibration extends to high energies but with the majority of events at low energies. The γ calibration has most of its events occurring at energies around the 136 keV, 122 keV and 63 keV lines. The training and blind data show a flat spectrum with a slow rise towards low energies. The analysis threshold of 100 eV in phonon and light channel translates to possibly much higher thresholds to energy depositions in any of the other parts of the holding structure. Hence, low energy depositions in those parts can be suppressed by this choice of threshold.

This is expected to primarily affect the neutron calibration. The excess events themselves are largely excluded in the event classes analysis.

Looking at the rates there are several things to notice:

- The neutron calibration is dominated by electron recoils, not nuclear recoils.
- The investigated event classes cover almost 100 % of events for the calibration measurements but only about 80 % for the blind data set. It can be estimated from the α analysis in [138] that at least half of the unidentified events are αs.
- About $\frac{3}{4}$ of the events in the calibration measurements happen in the main absorber. For the blind data set it is only about one third up to one half if the unidentified events are considered. The foil events have a much higher relative abundance. It follows, that the backgrounds observed in the blind data set are not dominated as much by external γs and neutrons as in the calibration measurements.
- The iSticks have a total mass of about 1 g, which is about 4 % of the mass of the 24 g absorber crystal. Therefore, the ratio between iStick and absorber events is expected to be similar. The event rate in the calibration measurements is dominated by the external calibration sources. A relative rate of 9.5 %/9.7 % is observed instead, more than double what than the expected 4 %. Input from simulations is required to investigate whether this has geometrical or other reasons. In the dark matter data, iSticks events have a relative rate of about one third of the absorber event rate. Possible explanations are a higher intrinsic contamination, extension into the less shielded/ none-active outer parts of the detector module or a misidentified artifact population with significant effect due to the low overall rate.
- Direct light detector hits in the calibration measurements are very rare, about 2 % to 3 % compared to the main absorber. This is expected from its 2 % mass compared to the main absorber. However, while the mass is small, the light detector has half the surface of the main absorber crystal and one third of the instrumented surfaces facing the walls of the module. For the dark matter data, the rate relative to the main absorber is about 10 %. Whether this increase is due to intrinsic contamination or due to an event class scaling with the surface cannot be distinguished.
- Foil events show their by far highest rate in the neutron calibration measurement. Whether this is due to the high cross section for neutrons of the hydrogen contained in the plastic or the generally increased low energy background has to be investigated by simulation. The γ and blind data show almost the same absolute foil event rate. This is expected as the high energy γs of the γ calibration source will not be stopped or scattered by the thin foil. An important aspect is the very high relative rate of the foil events

which are almost as abundant as absorber events in the dark matter data. If whatever causes these events has a chance to also reach the phonon detector without depositing energy and producing light in the foil, it would be a viable candidate for the observed excess events.

Appendix B

Basic Event and Pulse Parameters

This appendix contains the description and, if applicable, the c++ code for the basic parameters introduced in sections 3.2.1 as found in the analysis software "OxRop". For the c++ code, the variables were renamed and the code partially rearranged and shortened to improve readability. The parameter calculation requires a number of settings summarized in table B.1.

Parameter	Variable name in code	MCII-2 value	MCIII-1 value
Record length	recordLength	8192 samples	16384 samples
Sampling time base	timeBase	0.04 ms/sample	0.04 ms/sample
Pre-trigger parameter calculation range, percentage of pre-trigger	[pretriggerCalculationRangeStart, pretriggerCalculationRangeStop]	[0%,95%]	[0%,95%]
Pre-trigger range in 1/8th of record lenght	DaqPretrigger	2	2
Number of samples in the pre-trigger region	$numberOfSamplesPretrigger = \frac{DaqPretrigger}{8} * recordLength$	2048	4096
Number of samples in the moving average	movingAverageN	50	50

Table B.1: Variables required for the parameter calculation, their name in the presented code and their values for the measurements analyzed in this work.

B.1 Event Number

The event number is the position of an event in the time ordered list of events of the currently loaded measurement. Accordingly the event number can only be compared between different analyses if exactly the same data were loaded. Otherwise events are better identified by their absolute time stamp.

B.2 Time since Start

The time since start is the difference between the time of triggering for the event and the start of the first loaded file. If multiple detectors triggered simultaneously and are grouped to an event, depending on the setting, either the first or a selected detector channel defines the timestamp of the event. An absolute Unix time stamp is also available. It does not depend on the loaded files and allows to unambiguously identify an event.

B.3 Light Yield

The light yield is the ratio between the energy measured in the light channel and the energy measured in the phonon channel. In the standard CRESST energy calibration scheme as discussed in section 3.5, it is normalized to one for electron and γ events at the energy of the calibration peak. The light yield is the primary parameter for particle identification and background rejection in CRESST, see section 3.6.

B.4 Testpulse Amplitude

Heater pulses injected via the ohmic heaters, compare section 2.2.2, are identified by the testpulse amplitude parameter (TPA). If a heater pulse triggers the data acquisition, the TPA is set to a value corresponding to the heater voltage. The TPA is set to zero for events without a heater pulse. Empty baselines are marked by a TPA of -1.

B.5 Trigger Delay

The trigger delay is the time difference between the triggering in the given channel and the triggering in the event defining channel. The event defining channel can either be the first channel that triggered or a designated channel that was chosen beforehand. In the first case the trigger delay can only take positive values. If the channel did not trigger within the post trigger length, the end of the post trigger length is assigned to the trigger delay.

B.6 Pulse Number

Pulses are numbered in chronological order starting from the first loaded file. Accordingly, similar to the event number, this is not an absolute identifier of an event as it depends on the loaded data.

B.7 Baseline Offset

The baseline offset is the constant output voltage of the read-out system when there is no additional energy deposition. It is constant due to the stabilization of the TES at a fixed working point but can change by discreet values when the SQUID read-out loses a flux quantum or resets (compare section 2.3.2).

The baseline offset is calculated for each pulse from part of the pre-trigger region by averaging over all samples. The default value for this part is the [0%, 95%] interval of the pre-trigger but other values can be chosen. It is not guaranteed that the trigger will be set right at the onset of the pulse because of trigger walk. Therefore, a safety margin is required in order to calculate the baseline offset from an undisturbed baseline region.

```
Int_t baselineStart = int(numberOfSamplesPretrigger *pretriggerCalculationRangeStart );
Int_t baselineStop = int(numberOfSamplesPretrigger * pretriggerCalculationRangeStop);

Float_t sumOfSamples(0);

for (Int_t i=baselineStart; i<baselineStop; ++i)
        sumOfSamples += pulseRecord[i];

Float_t numberOfSamples = float(baselineStop - baselineStart);

Float_t baselineOffset = sumOfSamples/numberOfSamples
```

B.8 Pulse Height and Peak Position

The pulse height is the value of the highest sample in a pulse record minus the baseline offset. The peak position is the position of this sample relative to the start of the pulse record.

Ideally, the pulse height is a measure of the energy deposition in the detector. As a pure maximum search it is susceptible to upwards fluctuations around the peak of the slow particle induced pulses. Therefore, it systematically overestimates the signal amplitude. To reduce this effect, a running average is applied with a default value of 50 samples before the maximum search. Nonetheless the pulse height is not suitable for a precise energy calibration.

```
Float_t movingAverageValue(0);

Int_t posMaximum = movingAverageN;
Int_t searchEnd(recordLenght);

for (Int_t i=0; i<movingAverageN; ++i)
        movingAverageValue += pulseRecord[i];

Float_t maximum(movingAverageValue);
```

```
for (Int_t i=movingAverageN; i<recordLength; ++i)
{
    movingAverageValue += pulseRecord[i] - pulseRecord[i-movingAverageN];
    if (movingAverageValue > maximum)
    { // found new maximum
        maximum = movingAverageValue;
        posMaximum = i;
    }
}

 PeakPositionSamples = float(posMaximum) - 0.5 * float(movingAverageN);
 PeakPosition=PeakPositionSamples*timebase;

 Pulse Height = maximum/float(movingAverageN) - baselineOffset;
```

B.9 (Plain) FWHM of Baseline

The (plain) **F**ull **W**idth **H**alf **M**aximum (FWHM) of the baseline is a measure for the noise. It is calculated from part of the pre-trigger region, analogous to the baseline offset. The (plain) FWHM parameter is calculated (without) applying a running average beforehand. The formula for calculating the full width half maximum of a normal distribution with a non-zero expectation value is:

$$FWHM = 2\sqrt{2ln2} * \sqrt{E[y^2] - (E[y])^2} \tag{B.1}$$

where E denotes the expectation value and y the value of the measured quantity.

The baseline noise only follows a normal distribution in amplitude in the case of white noise. Noise in CRESST is not fully white, e.g., there is a 50 Hz component from the power grid. Therefore, this parameter loses its clear meaning, but is still a useful measure for the noise.

FWHM with running average (default):

```
Int_t baselineStart = int(numberOfSamplesPretrigger *pretriggerCalculationRangeStart );
Int_t baselineStop = int(numberOfSamplesPretrigger * pretriggerCalculationRangeStop);

Double_t sumOfSquare(0), sum(0), movingAverageValue(0);
Float_t FWHM = 0;

Int_t nSamplesAfterAveraging = baselineStop - baselineStart - movingAverageN;

if (nSamplesAfterAveraging > 0)
{
        for (Int_t i=baselineStart; i<baselineStart+movingAverageN; ++i)
                movingAverageValue += pulseRecord[i];

        for (Int_t i=baselineStart+movingAverageN; i<baselineStop; ++i)
        {
                movingAverageValue += pulseRecord[i] - pulseRecord[i-movingAverageN];
```

```
                sum += movingAverageValue;
                sumOfSquare += movingAverageValue*movingAverageValue;
        }

        Double_t squaredSum=sum * sum;
        Double_t expectationDifference= sumOfSquare * Double_t(nSamplesAfterAveraging)-squaredSum;
        FWHM = 2.35482 * sqrt(expectationDifference) / Double_t(nSamplesAfterAveraging * movingAverageN);
}
```

FWHM without running average (plain):

```
Int_t baselineStart = int(numberOfSamplesPretrigger *pretriggerCalculationRangeStart );
Int_t baselineStop = int(numberOfSamplesPretrigger * pretriggerCalculationRangeStop);

Double_t sumOfSquare(0), sum(0);

Int_t nSamples = baselineStop - baselineStart;


for (Int_t i=baselineStart; i<baselineStop; ++i)
{
        sum += pulseRecord[i];
        sumOfSquare += pulseRecord[i] * pulseRecord[i];
}

Double_t squaredSum=sum * sum;
Double_t expectationDifference=sumOfSquare*Double_t(nSamples)-squaredSum
plainFWHM = 2.35482 * sqrt(expectationDifference) / Double_t(nSamples);
```

B.10 Peak Onset

The peak onset is the position in the pulse record where it starts rising above the baseline noise. It gives an estimate of the signal position in the record independent of the trigger. It is calculated by moving back in time from the peak position(B.8) until a sample of the pulse record is below the FWHM of the baseline plus baseline offset. Again the pulse record is filtered with a running average beforehand.

The variable *PeakPositionSamples* is taken from the Pulse Height and Peak Position calculation B.8:

```
movingAverageValue = 0;

Int_t movingAverageStart = (PeakPositionSamples+movingAverageN < recordLength) ?
         PeakPositionSamples : recordLength-movingAverageN;

for (Int_t i=movingAverageStart; i<movingAverageStart+movingAverageN; ++i)
        movingAverageValue += pulseRecord[i];

Float_t peakOnset = Float_t(movingAverageStart + movingAverageN/2);
```

```
Float_t cutoff = (baselineOffset+FWHM) * movingAverageN;

for (Int_t i=movingAverageStart-1; i>=0; --i)
{
      peakOnset = Float_t(i + movingAverageN/2);
      movingAverageValue += pulseRecord[i] - pulseRecord[i+movingAverageN];

      if (movingAverageValue < cutoff)
        break;
}

peakOnset*=timebase;
```

B.11 Peak Position - Onset

Peak position minus onset is the difference between the peak position parameter and the peak onset parameter in units of ms. It is the time the signal in a pulse requires to rise from its start to its maximum.

B.12 Risetime

There are two risetime parameters calculated in OxRop, the 10 to 50% risetime and the 10 to 70% risetime. As the name suggests it is the time the signal needs to rise from 10% to 50/70% of its maximum value. The calculation is done by moving sample wise backwards in time from the peak position until the pulse record falls below 70/50/10% of the pulse height plus baseline offset. No running average is applied.

The variable *PeakPositionSamples* is taken from the Pulse Height and Peak Position calculation B.8:

```
Float_t signalValue_10_percent = 0.1 * pulseHeight + baselineOffset;
Float_t signalValue_50_percent = 0.5 * pulseHeight + baselineOffset;
Float_t signalValue_70_percent = 0.7 * pulseHeight + baselineOffset;

  Int_t samplePosition = int(PeakPositionSamples);

  while (samplePosition > 0)
        if (pulseRecord[samplePosition--] < signalValue_70_percent)
                break;
  Float_t seventyPercentPosition = float(samplePosition+1);


  while (samplePosition > 0)
        if (pulseRecord[samplePosition--] < signalValue_50_percent)
                break;
  Float_t fiftyPercentPosition = float(samplePosition+1);
```

```
while (samplePosition > 0)
      if (pulseRecord[samplePosition−−] < signalValue_10_percent)
              break;
Float_t tenPercentPosition = float(samplePosition + 1);

Float_t Risetime_10to50=timebase∗(fiftyPercentPosition − tenPercentPosition);
Float_t Risetime_10to70=timebase∗(seventyPercentPosition − tenPercentPosition);
```

B.13 Decaytime

The decay time is the time required for the signal to decrease to $1/e$ of its maximum value given by the pulse height parameter. The calculation is done by moving sample wise forward in time from the peak position until the pulse record falls below $\frac{1}{e} \approx 0.36788$ of the pulse height plus baseline offset. No running average is applied.

The variable *PeakPositionSamples* is taken from the Pulse Height and Peak Position calculation B.8:

```
Float_t signalValue_oneOverE = 0.36788 ∗ pulseHeight + baselineOffset;
Int_t samplePosition = int(PeakPositionSamples);

while (samplePosition < recordLength)
        if (pulseRecord[samplePosition++] < signalValue_oneOverE)
                break;

decaytime=timebase∗(float(samplePosition−1) − PeakPositionSamples);
```

B.14 Right - Left Baseline

The right - left baseline parameter is the difference between the start and the stop of the pulse record. It is based on the same running average as previous parameters, i.e., it is calculated as the difference of the average of the first and last N samples.

```
sum = 0;
for (Int_t i=0; i<movingAverageN; ++i)
      sum += pulseRecord[recordLength−i−1] − pulseRecord[i];

Float_t rightMinusLeft = sum/movingAverageN;
```

B.15 Integral over PH

The integral over the pulse height is calculated by adding up all sample values minus the baseline offset and dividing the result by the pulse height (PH). Noise components should average to zero in the integral leaving only the signal component of the pulse. The signal shape of events with the same origin is fixed by thermal couplings and just scales with the deposited energy. By normalizing with the pulse height, the Integral over PH parameter is sensitive to differences in the signal shape without further prior knowledge of it. This parameter in general has only little relevance for the analysis as the pulse shape is known in most cases and pulse shape discrimination can be based on the parameters presented in section 3.2.2.

```
sum = 0;
for (Int_t i=0; i<recordLength; ++i)
        sum += pulseRecord[i] − baselineOffset;

Float_t integralOverPH = timebase ∗ sum / pulseHeight;
```

B.16 Baseline Gradient

The baseline gradient is the slope of the baseline before the trigger. It is calculated by fitting a linear function ($y = A0 + A1 * x$) to part of the pretrigger region of the pulse, usually the first 95%. A slope far away from zero implies that the detector was still cooling down from a previous, large event and was therefore not back to its operation point.

```
Int_t baselineStart = int(numberOfSamplesPretrigger ∗pretriggerCalculationRangeStart);
Int_t baselineStop = int(numberOfSamplesPretrigger ∗ pretriggerCalculationRangeStop);


 // Fit (y = A0 + A1*x) to pre-trigger baseline

  Double_t Sx(0.0), Sy(0.0), Sxx(0.0), Sxy(0.0);
  for (Int_t i=baselineStart; i<baselineStop; ++i) {
    Sx += double(i);
    Sy += pulseRecord[i];
  }
  if (baselineStop > baselineStart) {
    Sx /= double(baselineStop − baselineStart);
    Sy /= double(baselineStop − baselineStart);
  }
  for (Int_t i=baselineStart; i<baselineStop; ++i) {
    const Double_t brak = double(i) − Sx;
    Sxx += (brak ∗ brak);
    Sxy += (brak ∗ (pulseRecord[i] − Sy));
  }

  const Double_t A1 = (Sxx != 0.0) ? (Sxy / Sxx) : 0.0;
  const Double_t A0 = Sy − (A1 ∗ Sx);
```

```
  baselineGradient=A1 * timebase; //This is a bug in the OxRop code.
                  //The correct code would be A1/timebase
```

B.17 Pile-up Voltage/RMS and Pile-up Time Width

Pile-up denotes the case when two energy depositions happen within one record window. As a result, there are two pulse signals in the pulse record with an offset relative to each other. Reconstruction of those events is challenging, therefore they are discarded or treated separately. The Pile-up Voltage/RMS parameter is designed to identify those events. It is the maximum increase in voltage when moving down from the highest sample/peak in either direction divided by the baseline RMS. No running average is applied.

The exact way this parameter is calculated assumes that the signal that triggered the event is also the first event in the record. This means that any pile up signal will come after the trigger. This is not necessarily true for the continuous trigger which will set the biggest signal as the one that triggers.

The Pile-up Time Width is the time the pulse record around the peak stays above 75% of the value of the highest sample minus the baseline offset.

The variables *RMS of the baseline*, *A0* and *A1* are taken from the calculation of the Baseline Gradient:

```
Double_t baselineRMS(0.0);

for (Int_t i=baselineStart; i<baselineStop; ++i)
{
    const Double_t diff = pulseRecord[i] - (A0 + (A1 * double(i)));
    baselineRMS += (diff * diff);
}

baselineRMS /= double(baselineStop - baselineStart - 1);
baselineRMS = TMath::Sqrt(baselineRMS);
```

Plain peak position and plain maximum, i.e. without running average:

```
Int_t plainPeakPosition(0);
Double_t plainMaximum(-1.e36);

for (Int_t i=baselineStop; i<recordLength; ++i)
{
    if (pulseRecord[i] > plainMaximum)
    {
      plainMaximum = pulseRecord[i];
      plainPeakPosition = i;
        }
}
```

Find pile-up voltage

```
  const Double_t critVoltage = 0.75 * (plainMaximum - baselineOffset);
  // for cross-talk, e.g. heater pulses can cause a fast spike at the start of
```

```
  //the pulse which is not what this parameter is looking for
  const Int_t crosstalkSamplesN(30);

  Double_t maximumDifference_Back(−10.0), minimum_Back(1.e36);
  Int_t firstBelow75percent_Back(−1);
  \\go backwards in time
for (Int_t i=plainPeakPosition; i>=0; −−i)
{
        if (i > (numberOfSamplesPretrigger + crosstalkSamplesN))
        {
                if (pulseRecord[i] < minimum_Back)
                        minimum_Back = pulseRecord[i];

                double diff = pulseRecord[i−1] − minimum_Back;

                if (diff > maximumDifference_Back)
                        maximumDifference_Back = diff;
    }
        if ((firstBelow75percent_Back < 0) && ((pulseRecord[i]−baselineOffset) < critVoltage))
        firstBelow75percent_Back = i;
}

if (firstBelow75percent_Back < 0) firstBelow75percent_Back = 0;


 Double_t maximumDifference_Forward(−10.0), minimum_Forward(1.e36);
  Int_t firstBelow75percent_Forward(−1);

for (Int_t i=plainPeakPosition; i<recordLength−1; ++i)
{
    if (pulseRecord[i] < minimum_Forward)
        minimum_Forward = pulseRecord[i];

    const Double_t diff = pulseRecord[i+1] − minimum_Forward;

    if (diff > maximumDifference_Forward)
        maximumDifference_Forward = d;

    if ((firstBelow75percent_Forward < 0) && ((pulseRecord[i]−baselineOffset) < critVoltage))
        firstBelow75percent_Forward = i;
}
  if (firstBelow75percent_Forward < 0)
        firstBelow75percent_Forward = recordLength−1;


  const Double_t pileUpVoltage = (maximumDifference_Back > maximumDifference_Forward) ?
                maximumDifference_Back : maximumDifference_Forward;
  const Double_t pileUpVoltageOverRMS = (rms > 0.0) ?
                (pileUpVoltage / baselineRMS) : 0.0;
  const Double_t pileUpTimeWidth =
        Double_t(firstBelow75percent_Forward−firstBelow75percent_Back) ∗ timebase;
```

B.18 Delta Voltage (-)/RMS

A common artifact that appears in the CRESST data are negative "spikes", likely caused by some switching process in the DAQ electronics. They are only a few samples long and have a negative value below the noise. To identify them the Delta Voltage (-)/RMS parameter is calculated. It is the biggest negative difference found between a sample and the next but one sample in the record.

The *baselineRMS* variable is taken from the Pile-up Voltage/RMS calculation.

```
  Double_t deltaMin(0.0), min(1.e308);
  for (Int_t i=2; i<recordLength; i++)
  {
        if (pulseRecord[i] < min)
        {
                min = pulseRecord[i];
        const Double_t delta =
                TMath::Min(pulseRecord[i]−pulseRecord[i−1], pulseRecord[i]−pulseRecord[i−2]);
        if (delta < deltaMin)
                deltaMin = delta;
    }
  }

const Double_t deltaVoltageOverRMS = deltaMin / baselineRMS;
```

B.19 Heater Demand

The heater demand is the control voltage applied to the heater current source of the channel. It is directly proportional to the heating power (see section 2.3.3).

B.20 Deadtime and Live Time

The trigger scheme of the hardware trigger as well as the heater pulses produce time periods where the data acquisition is not sensitive to incoming signals, mainly because the trigger is disarmed. For the calculation of (expected) event rates etc. this deadtime has to be subtracted from the measurement time to obtain the **raw live time**, i.e. the time the complete setup was sensitive to an incoming signal. In this framework the effect of data selection criteria can be taken into account as a further reduction of live time to an **effective live time**. This is further discussed in section 3.4.1.

This parameter is no longer relevant for the continuous acquisition.

A related quantity is the **(effective) exposure** which is the product of (live time) measurement time and mass of the main absorber crystal.

B.21 Trigger Amplitude (Continuous Acquisition only)

With the off-line trigger described in section 2.4.2 it is possible to also save the signal amplitude observed by the trigger algorithm. It can be slightly different from the filtered amplitude obtained from the pulse record, as the filtered window can be different.

Appendix C

Co-57 Calibration Spectrum for $CaWO_4$

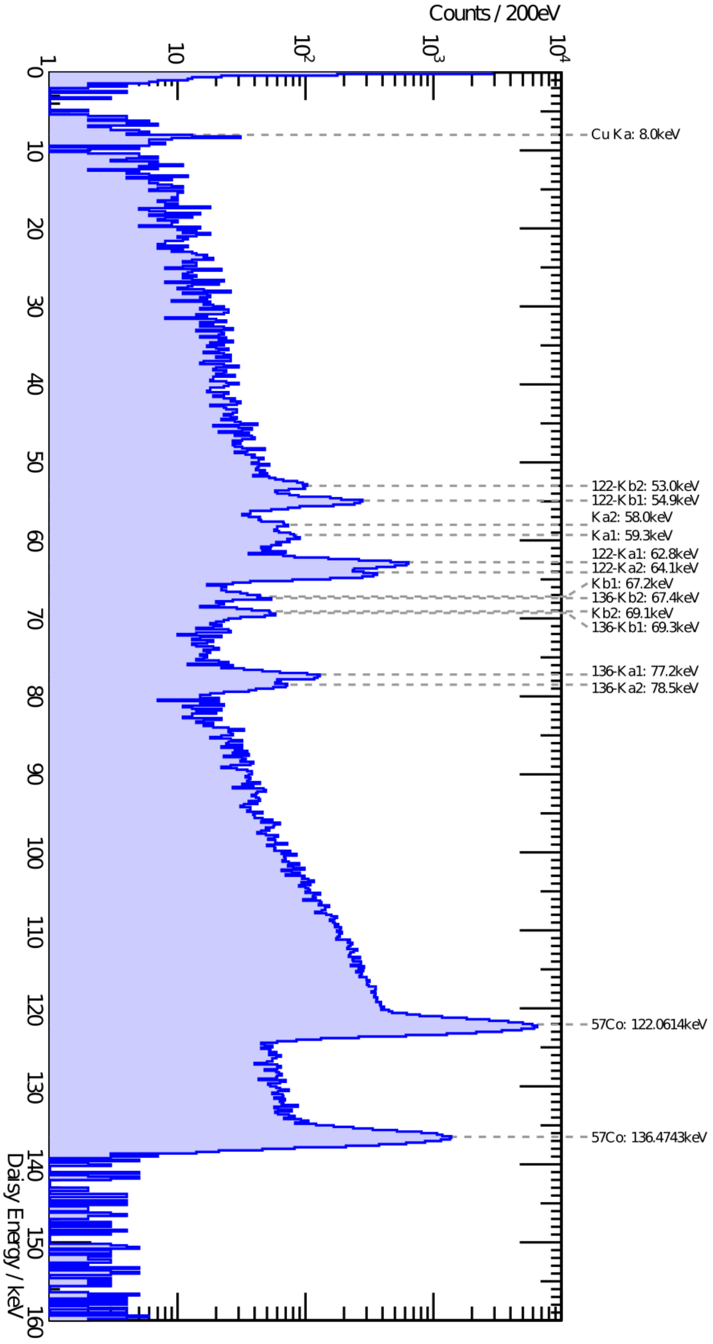

Figure C.1: Energy Spectrum in detector Daisy from one week of 57 Co calibration, directly copied from [114]. The lines are labeled according to their origin. Lines between 50 and 90 keV are tungsten escape lines.

Appendix D

Energy Patterns from internal Alpha Decays of the Natural Decay Chain

Shown are the expected energy patterns for internal α decays from the natural decay chains ${}^{238}_{92}\mathrm{U}$, ${}^{235}_{92}\mathrm{U}$ and ${}^{232}_{90}\mathrm{Th}$. Peaks that are expected to be in secular equilibrium have the same size. The displayed activities are arbitrarily chosen for visualization. The chosen resolution of 20 keV is of the same order as what has been achieved in the α analysis of chapter 4.

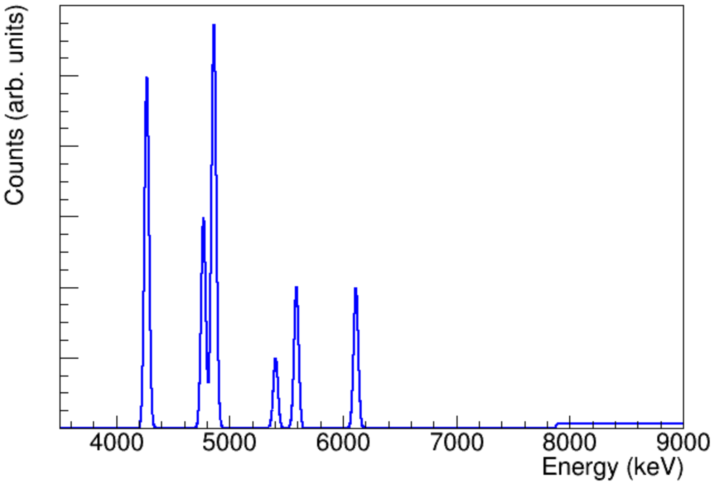

Figure D.1: Expected pattern of α peaks in a CRESST detector for the ${}^{238}_{92}\mathrm{U}$ decay chain. The displayed resolution is 20 keV. Peaks with the same height are in secular equilibrium. Absolute activities and relative activities between non-equilibrium lines are arbitrarily chosen for visualization.

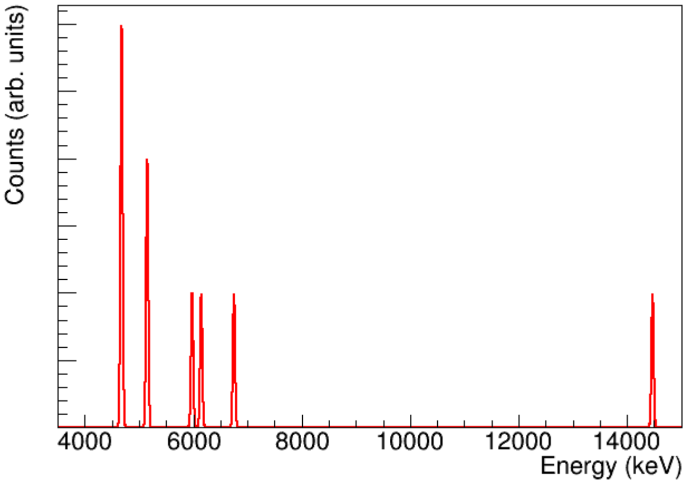

Figure D.2: Expected pattern of α peaks in a CRESST detector for the $^{235}_{92}$U decay chain. The displayed resolution is 20 keV. Peaks with the same height are in secular equilibrium. Absolute activities and relative activities between non-equilibrium lines are arbitrarily chosen for visualization.

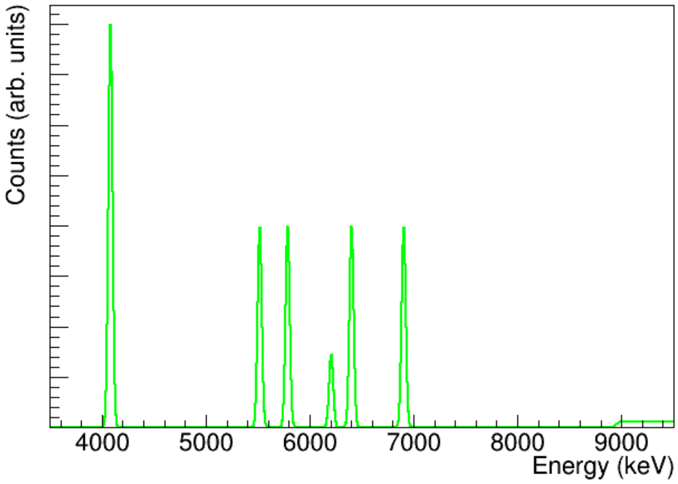

Figure D.3: Expected pattern of α peaks in a CRESST detector for the $^{232}_{90}$Th decay chain. The displayed resolution is 20 keV. Peaks with the same height are in secular equilibrium. Absolute activities and relative activities between non-equilibrium lines are arbitrarily chosen for visualization.

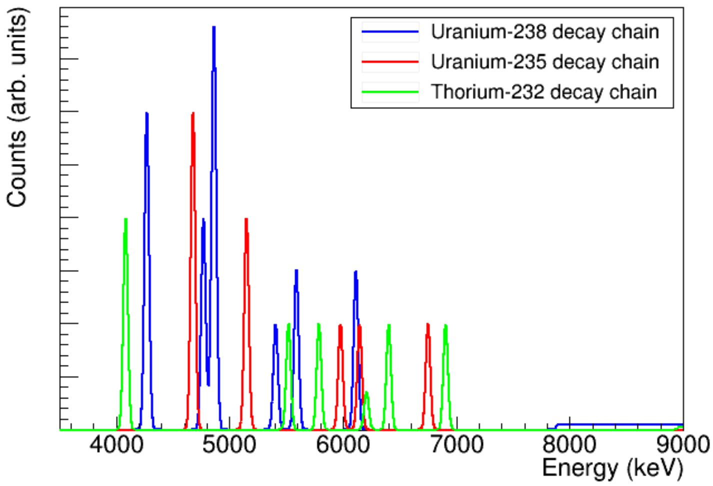

Figure D.4: Expected pattern of α peaks for a CRESST detector for the natural decay chains combining figures D.1 to D.3. The displayed resolution is 20 keV. Peaks with the same height and color are in secular equilibrium. Absolute activities and relative activities within and between decay chains are arbitrarily chosen so that all lines are well visible.

Appendix E

Alpha Analysis Data Selection Criteria

This appendix summarizes the applied data selection criteria, their values and motivation for the α analysis presented in chapter 4. In figure E.1 the different types of α events with artifacts are displayed. They have to be preserved by the first steps of the data selection to obtain the α basis. In figure E.2 several artifact types that can mimic α induced events are shown that have to be removed.

Tables E.1 (TUM40) and E.2 (Lise) contain the information about the data selection criteria. The first column indicates the selection parameter. The second column contains the selection values. Behind the selection values it is indicated whether the selected events get removed *(removed)* or are kept *(kept)* and the not selected events removed. Some data selection criteria remove potential α events that have to be recovered to the kept data. The selection criteria indicated with $\rightarrow$ and *(recovered)* are applied to events removed by the previous selection and the selected events returned to the set of good events. The last column contains the motivation for the specific data selection criterion.

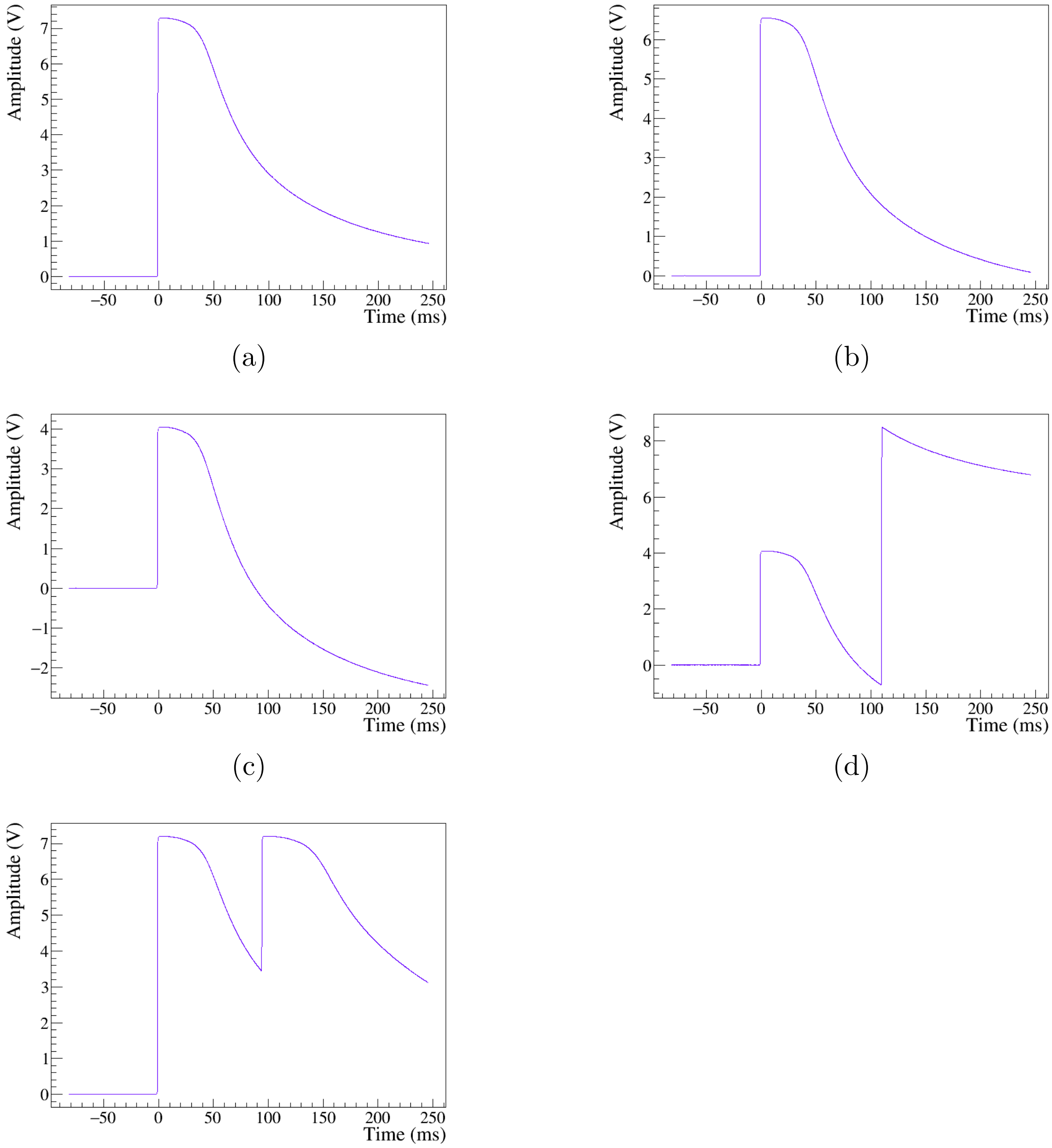

(a) (b) (c) (d) (e)

Figure E.1: Different types of α events in Lise with an energy of around 5500 keV in the initial event. All of them have to be preserved by the data selection criteria determining the α basis. Event types (b) to (e) are then removed as problematic. a) Undisturbed α event b) alpha event with one FQL leading to a left minus right baseline difference of zero c) α event with four FQLs d) aα event with four FQLs and a SQUID reset e) α-α pile-up

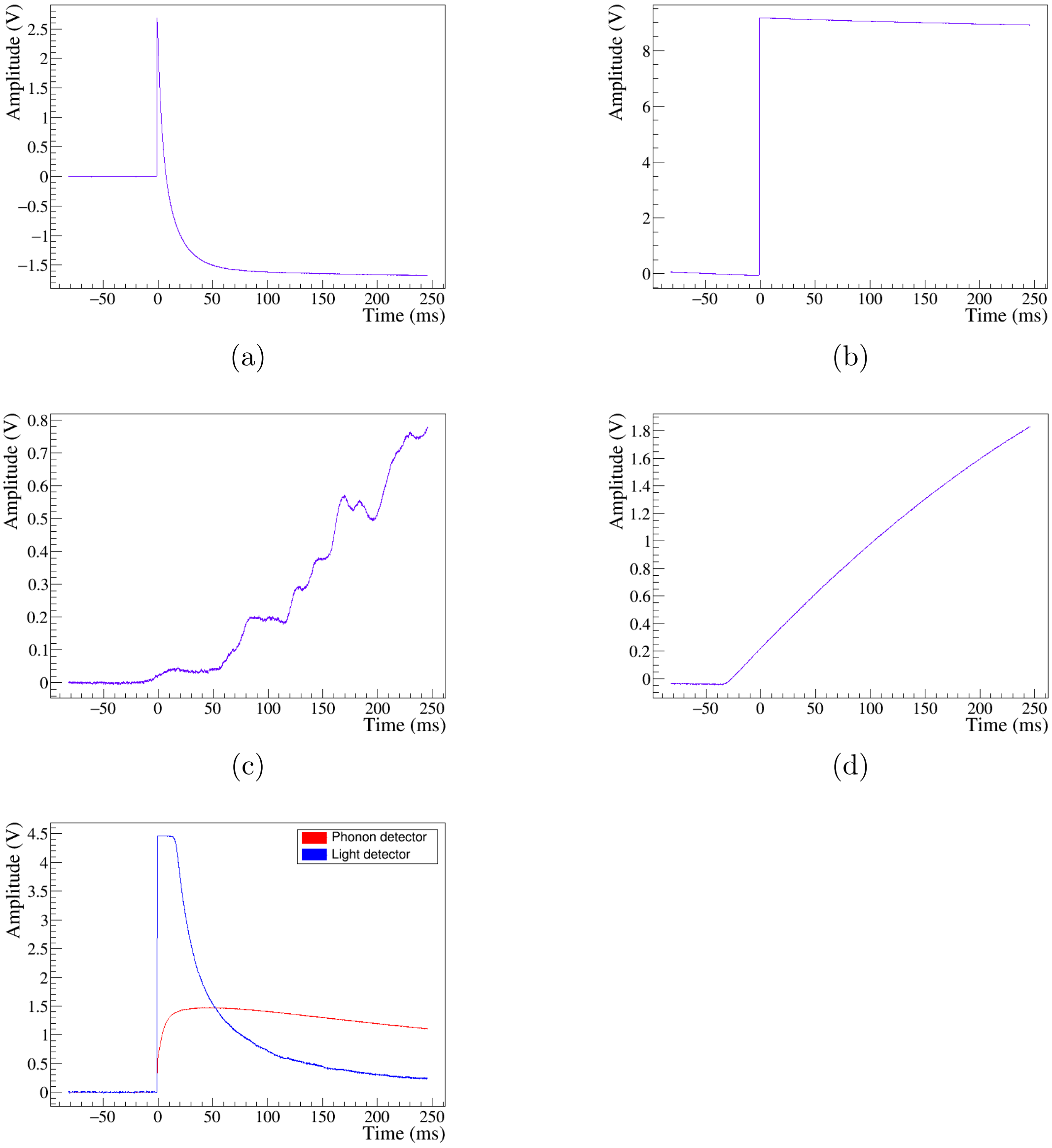

(a)

(b)

(c)

(d)

(e)

Figure E.2: Examples of events that have a right - left baseline difference bigger than expected for the bulk β/γ events but are no αs. a) carrier event with FQL. For more information on carrier events see [100]. b) SQUID reset without an α interaction in the record window c) Microphonics caused by vibrations in the cryostat. c) Rising baselines e) events in the $CaWO_4$ holding sticks, TUM40 only.

Parameter(s)	Value	Comment
α basis identification		
Trigger delay	>= 0 (kept)	Only events that triggered the phonon channel, non-triggers were set to -2500 in MCII-2
Peak position (PPos)	>= $75ms$ (kept)	Removes events in the dead-time
Right - left baseline (RL)	$[-0.2V, 0.55V]$ (removed)	Removes all events with lower energies than expected for αs
→ RL vs fitted Amplitude	custom, recovering some events removed in the last step (recovered)	Recover αs with one FQL
Pulse height (PH) vs peak position (PPos)	PPos: [326,328], PH: [-1,4] (removed)	Removes rising baselines and microphonics with the peak position at the end of the record but, unlike αs, not saturating; saturation is at $PH \approx 9V$
Light channel pulse height (PH-L)	$PH-L < 3.8$ (removed)	αs will saturate the light channel, reaching $PH-L \approx 4.5V$
→ RL light (RL-L)	$RL-L < -0.3$ or $RL-L > 0.2$ (recovered)	S smaller pulse height can appear for actually saturated pulses if there is an FQL, which are therefore recovered
Light vs phonon fitted amplitude	custom (removed)	Remove the high energy end of the e^-/γ band including the ${}^{208}_{81}$Tl line
Decay time (Decay) vs RL	RL: $[-10V, 0V]$, Decay: $[-1ms, 20ms]$ (removed)	Removes carrier events (fast decay) with FQLs
PH-L vs RL-P	RL-P: $[0V, 11V]$, PH-L: $[-0.1V, 0.4V]$ (removed)	Removes miscellaneous events that were also targeted by the previous cuts
Pile-up Voltage/RMS (PuV/RMS) vs RL	RL: $[0.9V, 1.5V]$, PuV/RMS: $[150, 5000]$ (removed)	Removes more carrier events with SQUID resets
→ Pulse Height	$PH > 8.5V$ (recovered)	Carrier events with SQUID resets due to their very fast nature usually do not get to these high pulse heights
Pulse height vs Decay Time	PH: $[0.24V, 2.6V]$, Decay: $[140ms, 250ms]$ (removed)	Removes presumably stick events that have a very slow decay leading to a big RL value despite a small pulse height / signal amplitude.
Cascade/Pile-up identification		
Right minus left baseline	$RL > 2V$	High energies/pulse signals
+ Positive delta voltage	$\Delta V(+) < 6$	Pile up, not SQUID resets which have $\Delta V(+) \approx 8$
+Peak Onset	Onset$< 83ms$	Not just a late pulse
remove problematic events		
Peak Position	PPos [83ms,95ms] (kept)	
Right minus left baseline	[0.5,2] (kept)	
Fit RMS	RMS$< 0.056[V]$ (kept)	

Table E.1: Data selection criteria with parameter, values and motivation for the α analysis of TUM40. The selected events are either removed or kept in the set of good events. Selection criteria marked with an arrow are applied to the events removed by the selection immediately before. The selected events are then recovered into the set of good events.

Parameter(s)	Value	Comment
α basis identification		
Trigger delay	>= 0 (kept)	Only events that triggered the phonon channel, non-triggers were set to -2500 in MCII-2
Peak position (PPos)	>= $80ms$ (kept)	Removes events in the dead-time
Right minus left baseline (RL)	$[-0.5V, 0.6V]$ (removed)	Removes all events with lower energies than expected for αs
→ RL vs fitted Amplitude	custom, recovering some events removed in the last step (recovered)	Recover αs with one FQL
Pulse height (PH) vs peak position (PPos)	PPos: [326.4ms,327ms], PH: [0V,5.27V] (removed)	Removes rising baselines and microphonics with the peak position at the end of the record but, unlike αs, not saturating; saturation is at $PH \approx 9V$
→ Positive Delta Voltage	> 0.04 (recovered)	Recovers some SQUID resets
Decay time (Decay) vs RL	RL: $[7.7V, 10V]$, Decay: $[-1ms, 8ms]$ (removed)	Removes SQUID resets without an α in the record window.
Decay time (Decay) vs Pulse Height (PH)	PH: [0V,4.3V], Decay: [0ms,22ms] (removed)	Removes fast carrier events with FQLs
→ Positive delta voltage	$> 5V$ (recovered)	Recovers αs with SQUID resets
→ Baseline Gradient	$< -2 * 10^{-}6$ (wrong calculation, compare B.16) (recovered)	Recovers α pulses on decaying baselines
→ Pile-up voltage /RMS	$> 90V$ (recovered)	recovers pile up events
remove problematic events		
Peak Position	PPos [80ms,95ms] (kept)	
Right minus left baseline	[0.4V,3V] (kept)	
Pile-up voltage / RMS	$< 500V$ (kept)	

Table E.2: Data selection criteria with parameter, values and motivation for the α analysis of Lise. The selected events are either removed or kept in the set of good events. Selection criteria marked with an arrow are applied to the events removed by the selection immediately before. The selected events are then recovered into the set of good events.

Appendix F

Fitted Amplitude Corrections for the Alpha Analysis

This appendix describes the amplitude corrections applied to the data of the α analysis in chapter 4 in detail. The general idea is that there are several parameters that correlate with the exact value of the fitted amplitude of the high truncation fit for α events from a nominally mono-energetic line. In the following, possible correlation inducing mechanisms are presented in section F.1 and a correction approach in section F.2. Then, the application to the α analysis of TUM40 as well as Lise and VK28 are discussed in sections F.3 and F.4.

F.1 Correlation Mechanisms

Most of the correlation is due to small variations of the operating point at the time of the events. These variations appear below the times scale and precision of the stabilization. A different operating point implies a different onset of the non-linearity effects. For a dark matter analysis the truncation limit is chosen with a safety margin below the non-linear part of the pulse. Small operating point variation therefore do not influence the fit.

In the α analysis, some of the non-linear part of the pulse is fitted. The fit therefore becomes sensitive to the operating point variations. Fitting more of the non-linear part leads to a smaller fitted amplitude and vice versa.

There are two parameters that are a direct measure of the operating point for α events: the baseline offset, modulo the flux quantum state, and the pulse height. The pulse height is a measure of the working point as discussed in 2.3.1.2 as all α events are saturated in the phonon channel. The fitted RMS is also available. It is a general measure for the fit quality and therefore sensitive to all effects changing the recorded pulse shape.

Another mechanism for a correlation of the fitted phonon amplitude, and, in that case, the fitted light amplitude is the distribution of energy between the light and the phonon channel as discussed in section 3.5.5. In this case there is an anti correlation between the reconstructed signal amplitude in the light and the phonon channel.

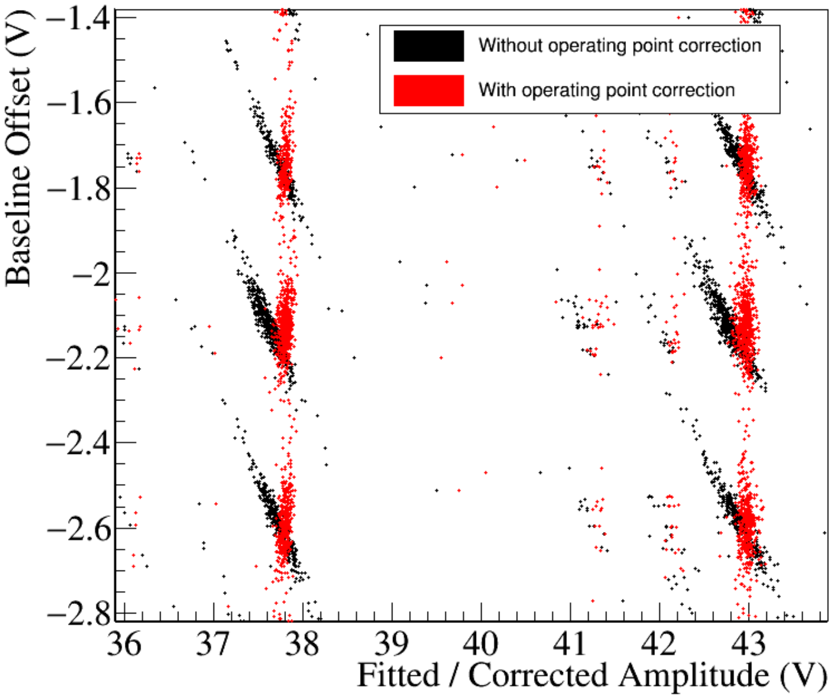

(a) Correlation between baseline offset and fitted amplitude for α lines in TUM40, phonon. The different flux quantumn levels off the SQUID show up as different mean baseline offsets. Small variations are caused by variations of the exact operating point at the moment of an event. The events in black show a strong correlation between the baseline offset and the uncorrected fitted amplitude. In red, the same events are shown after the correlation was exploited to improve the resolution as described in the text.

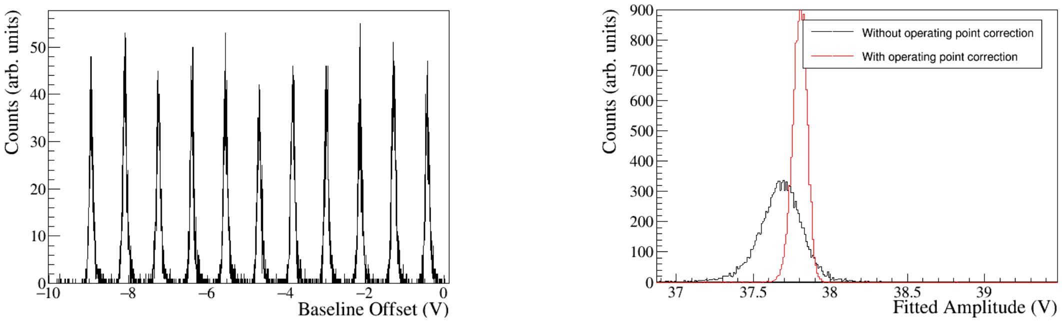

(b) The different flux quantum levels of TUM40 can be separated in a histogram of the baseline offset. Each peak corresponds to one level. This is only possible if the detector operation is very stable. Otherwise the peaks will overlap.

(c) $^{238}_{92}$U peak in TUM40. Black: Before operating point correction, Red: After operating point correction. The resolution improves by about a factor of three.

Figure F.1

F.2 Fitted Amplitude Corrections

Any such correlation can be exploited to improve the phonon energy resolution of the α analysis. To this end, the lines are rotated in the correlated parameter vs fitted amplitude space by calculating:

$$A_{cor} = A + par * m - c \tag{F.1}$$

where A_{cor} is the corrected amplitude, A is the original fitted amplitude and par the parameter value. The proportionality constant m depends on the inclination of the lines and c is an arbitrary constant that can be used to adjust the final value.

F.3 Application to the Alpha Analysis of TUM40

For the α analysis of TUM40 the relevant parameter is the baseline offset, compare figure F.1a. Applying equation F.1 is complicated by the different flux quantum levels of the SQUID. Each level corresponds to a different average baseline offset. The correction has to be applied to each flux quantum level separately. In this case, c has to be chosen for each level such that the final mean A_{cor} is the same for a given α line.

The different flux quantum levels are clearly separable in terms of baseline offset as can be seen in figure F.1b. If events are accidentally assigned to the wrong flux quantum level, their corrected amplitude will have an offset and fake lines appear in the spectrum.

The effect of the correction for TUM40 for the ${}^{238}_{92}$U peak is shown in figure F.1c. The resolution is improved by a factor of three by correcting with the baseline offset for each FQ-level. Some events had to be removed because they could not be unambiguously assigned to a flux quantum level of the SQUID. They can be identified in a plot showing pulse height vs corrected amplitude. In terms of rate estimation for the α analysis it can be assumed that all α peaks lose the same percentage of events from this.

F.4 Application to the Alpha Analysis of Lise and VK28

For the α analysis of Lise and VK28, the correction is based on the pulse height parameter. The baseline position of Lise and VK28 is not as stable in time as for TUM40. It, hence, becomes technically too challenging to assign events to the correct FQ-level and determine the necessary cs. The correlation between pulse height and fitted amplitude of Lise is shown in figure F.2a. A polynomial of the form

$$A_{cor} = A + \sum_{i=1}^{3} (a_i + (A - A_0) \cdot \alpha_i) \cdot (\mathit{\Delta} PH)^i \tag{F.2}$$

is applied to correct the fitted amplitude A and obtain A_{cor}, the operating point corrected amplitude. The coefficients are $a_{1/2/3}$ and $\mathit{\Delta} PH$ is the deviation of the pulse height from the mean saturation pulse height. As the effect changes in strength with changing signal amplitude, a linear correction $(A - A_0) * \alpha_{1/2/3}$ based on the fitted amplitude is added to the coefficients. A_0 is an arbitrary amplitude here chosen at the start of the γ lines to facilitate finding the correct values for the αs.

The correction becomes more unreliable the further the pulses deviate from the mean working point. Therefore, a cut on the difference to the mean pulse height is applied. In total the resolution is improved by about a factor two. The effect of the correction is shown in figure F.2d.

VK28 is treated analogously.

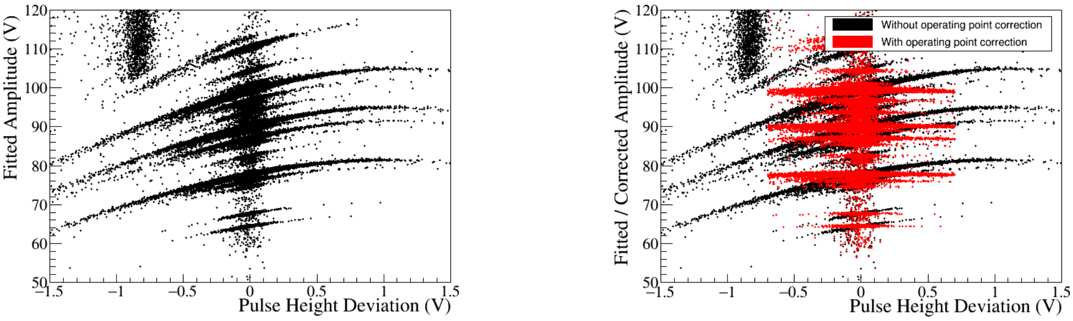

(a) Fitted amplitude vs deviation of the pulse height from the mean saturation pulse height for α events in Lise-phonon. A strong correlation is observed. The exact correlation changes with energy.

(b) The correlation can be exploited to improve the amplitude resolution based on equation F.2. Events with a large deviation are removed.

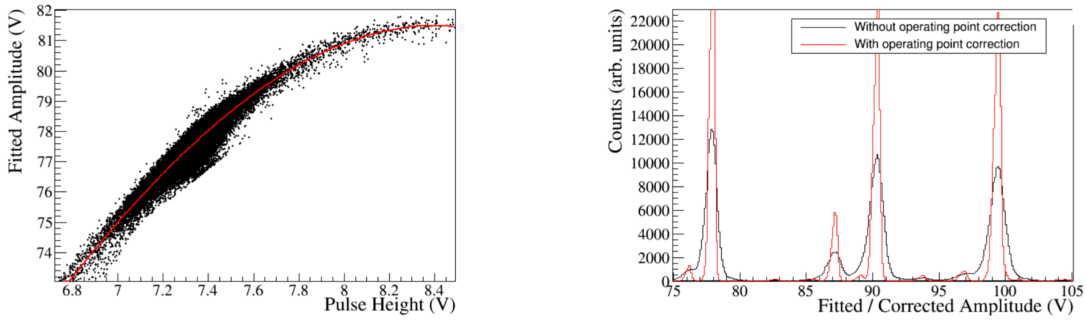

(c) Good starting values for the polynomial of equation F.2 can be obtained by fitting one or more α lines independently.

(d) The resolution is improved by a factor two for Lise, phonon. Black: Fitted amplitude before the operating point correction. Red: Corrected Amplitude for the same events.

Figure F.2

Appendix G

MCIII-1 Dark Matter Analysis Settings

Standard Event Fit Settings						
Detector channel	A-PH	A-L	B-PH	B-L	C-PH	C-L
Standard event fit truncation / Linearity limit (V)	0.6	0.16	0.7	0.4	0.6	0.08
Search range heater pulse (ms)	[−4,7]	[−2,7]	[−3,5]	[−3,4]	[−1,5]	[−5,5]
Search range particle pulse (ms)	±0.5	±0.5	±0.5	±0.5	±0.5	±0.5
Baseline shape	cubic	cubic	cubic	cubic	cubic	cubic
Filter peak search interval around zero (ms)	$[-8, 20]$	–	$[-8, 20]$	–	$[-8, 20]$	–
Filter close RMS range around peak (ms)	30	–	30	–	30	–

Detector channel	D-PH	D-L	E-PH	E-L	J-PH	J-L
Standard event fit truncation / Linearity limit	0.7	0.4	0.6	0.1	0.6	0.2
Search range heater pulse (ms)	[−4,1]	[−1.5,1]	[−4,4]	[−5,3]	[−4,4]	[−1,2]
Search range particle pulse (ms)	±0.5	±0.5	±0.5	±0.5	±0.5	±0.5
Baseline shape	cubic	cubic	cubic	cubic	cubic	cubic
Filter peak search interval around zero (ms)	$[-8, 20]$	–	$[-8, 20]$	–	$[-8, 20]$	–
Filter close RMS range around peak (ms)	30	–	20	–	20	–

Table G.1: Settings for Standard event fit and optimum filter. A correlated standard event fit is applied to the particle events and an uncorrelated standard event fit to the injected heater pulses.

Selection Parameter	Data Selection Criteria					
	Detector Module					
	A	B	C	D	E	J
Rate cut (Counts/0 5h), resulting time periods shorter than 5 h are also removed	160	105	—	60	220	80
Stability cut, set point and maximum deviation (V)	PH: 4.5 ± 0.1 L: 1.4 ± 0.04	PH: 4.5 ± 0.3 L: 0.95 ± 0.015	PH: 3.35 ± 0.07 L: 0.17 ± 0.03	PH: 4.55 ± 0.05 L: 1.7 ± 0.1	PH: 3.0 ± 0.1 L: 0.35 ± 0.05	PH: 5.35 ± 0.03 L: 1.1 ± 0.01
Peak position (ms)	[160,200]	[160,220]	[160,260]	[160,180]	[165,176]	[160,200]
Right-left baseline (V)	[-0.1,1]	[-0.2,2]	[-0.2,1]	[-0.2,0.5]	[-0.1,0.3]	[-0.1,0.4]
Right-left baseline Light (V)	[-0.02,0.03]	[-0.02,0.05]	[-0.2,0.2]	[-0.2,0.2]	[-0.004,0.6]	[-0.1,0.4]
Delta voltage / RMS	[-6,-1]	> -5.5	[-10,0]	[-15,-0.4]	[-8,-0.5]	[-11.5,-0.9]
iStick pulse height (V)	< 0.015	< 0.06	—	< 0.03	< 0.05	< 0.15
Muon veto (distance to next veto (ms))	[-10,5]	[-10,5]	[-10,5]	[-10,5]	[-10,5]	[-10,5]
Trigger delay phonon	== 0	== 0	== 0	== 0	== 0	== 0
Coincidence to other detectors (ms, removed)	±10	—	—	—	±10	—
Fit RMS	graphical 2D cut					
Fit RMS light channel	graphical 2D cut					
Close RMS optimum filter	graphical 2D cut					
Minimum optimum filter	–	–	—	—	—	graphical 2D cut
Trigger amplitude vs optimum filter amplitude	graphical 2D cut					
Filtered amplitude (trigger) (V)	< 3	< 4	—	—	< 2.5	< 4
Fitted amplitude light channel (V)	< 1.1	< 1.05	—	—	< 0.37	< 1.06

Table G.2: Data selection criteria. Unless stated explicitly all cuts are applied to the phonon channel of the detector module.

<table>
<tr><th colspan="2">Standard Event Fit Settings, Light Detector Analysis</th></tr>
<tr><td>Standard Event Fit Truncation / Linearity Limit (V)</td><td>PH: 0.6 L: 0.16</td></tr>
<tr><td>Search Range Particle Pulse (ms)</td><td>±0.5</td></tr>
<tr><td>Baseline Shape</td><td>cubic</td></tr>
<tr><th>Selection Parameter</th><th>Selection Value</th></tr>
<tr><td>Stability and rate cut</td><td>Same time periods removed as in the main analysis</td></tr>
<tr><td>Peak Position (ms)</td><td>[160,175]</td></tr>
<tr><td>Right-Left Baseline (V)</td><td>[-0.1,0.1</td></tr>
<tr><td>Right-Left Baseline Phonon (V)</td><td>[-0.05,1]</td></tr>
<tr><td>Delta Voltage / RMS</td><td>[-8,0]</td></tr>
<tr><td>iStick Pulse Height (V)</td><td>< 0.015</td></tr>
<tr><td>Trigger Delay</td><td>== 0</td></tr>
<tr><td>Rise Time Cut vs Light Stick Events</td><td>graphical 2D cut</td></tr>
<tr><td>Fitted Amplitude Phonon (V)</td><td>< 0</td></tr>
</table>

Table G.3: Fit and data selection parameters for the analysis of detector A-light, light only events. All the fit parameters refer to a dedicated fit with a standard event build from foil events. Data selection criteria refer to the light channel if not explicitly stated.

Bibliography

[1] Gianfranco Bertone et al. “History of dark matter”. In: *Rev. Mod. Phys.* 90 (4 2018), p. 045002. DOI: `10.1103/RevModPhys.90.045002`.

[2] Planck Planck Collaboration et al. “Planck 2018 results. I. Overview and the cosmological legacy of Planck”. 2018. arXiv: `1807.06205`.

[3] R. Clausius. “Ueber einen auf die Wärme anwendbaren mechanischen Satz”. In: *Annalen der Physik und Chemie* 217.9 (1870), pp. 124–130. DOI: `10.1002/andp.18702170911`.

[4] F. Zwicky. “Die Rotverschiebung von extragalaktischen Nebeln”. In: *Helv. Phys. Acta* 6 (1933), pp. 110–127. DOI: `10.1007/s10714-008-0707-4`.

[5] F. Zwicky et al. “On the Masses of Nebulae and of Clusters of Nebulae”. In: *The Astrophysical Journal* 86 (1937), p. 217. DOI: `10.1086/143864`.

[6] Yoshiaki Sofue et al. “Rotation Curves of Spiral Galaxies”. In: *Annual Review of Astronomy and Astrophysics* 39.1 (2001), pp. 137–174. DOI: `10.1146/annurev.astro.39.1.137`.

[7] Yoshiaki Sofue. “Rotation and mass in the Milky Way and spiral galaxies”. In: *Publications of the Astronomical Society of Japan* 69.1 (2016). DOI: `10.1093/pasj/psw103`.

[8] Edvige Corbelli et al. “The extended rotation curve and the dark matter halo of M33”. In: *Monthly Notices of the Royal Astronomical Society* 311.2 (2000), pp. 441–447. DOI: `10.1046/j.1365-8711.2000.03075.x`.

[9] Mario De Leo. “Rotation curve of spiral galaxy Messier 33 (Triangulum)”. licensed under the Creative Commons Attribution-Share Alike 4.0 International license. 2018. URL: `https://commons.wikimedia.org/wiki/File:Rotation_curve_of_spiral_galaxy_Messier_33_(Triangulum).png`.

[10] A Einstein. “Lens-Like Action of a Star by the Deviation of Light in the Gravitaional Field.” In: *Science (New York, N.Y.)* 84.2188 (1936), pp. 506–7. DOI: `10.1126/science.84.2188.506`.

[11] Matthias Bartelmann et al. “Weak gravitational lensing”. In: *Physics Reports* 340.4 (2001), pp. 291 –472. DOI: `https://doi.org/10.1016/S0370-1573(00)00082-X`.

[12] Henk Hoekstra et al. “Masses of Galaxy Clusters from Gravitational Lensing”. In: *Space Science Reviews* 177.1 (2013), pp. 75–118. DOI: `10.1007/s11214-013-9978-5`.

[13] TallJimbo. “Weak gravitational lensing of galaxies in astronomy.” Creative Commons Attribution-Share Alike 3.0 Unported license and GNU Free Documentation License. 2008. URL: `https://commons.wikimedia.org/wiki/File:Shapenoise.svg`.

[14] Douglas Clowe et al. “A Direct Empirical Proof of the Existence of Dark Matter”. In: *The Astrophysical Journal* 648.2 (2006), pp. L109–L113. DOI: `10.1086/508162`.

[15] NASA. “The Matter of the Bullet Cluster”. Image Credit: X-ray: NASA/CXC/CfA/M.Markevitch et al.; Optical: NASA/STScI; Magellan / U.Arizona / D.Clowe et al.; Lensing Map: NASA/STScI; ESO WFI; Magellan / U.Arizona / D.Clowe et al. 2017. URL: `https://apod.nasa.gov/apod/ap170115.html`.

[16] J. Merten et al. “Creation of cosmic structure in the complex galaxy cluster merger Abell 2744”. In: *Monthly Notices of the Royal Astronomical Society* 417.1 (2011), pp. 333–347. DOI: `10.1111/j.1365-2966.2011.19266.x`.

[17] Bharat Ratra et al. “The Beginning and Evolution of the Universe”. 2007. DOI: `10.1086/529495`.

[18] Dorothea Samtleben et al. “The Cosmic Microwave Background for Pedestrians: A Review for Particle and Nuclear Physicists”. In: *Annu. Rev. Nucl. Part. Sci.* (2008). DOI: `10.1146/annurev.nucl.54.070103.181232`.

[19] C. L. Bennett et al. “4-Year COBE DMR Cosmic Microwave Background Observations: Maps and Basic Results”. In: *The Astrophysical Journal* (1996). DOI: `10.1086/310075`.

[20] C. L. Bennett et al. “Nine-Year Wilkinson Microwave Anisotropy Probe (WMAP) Observations: Final Maps and Results”. In: *The Astrophysical Journal Supplement Series* (2013). DOI: `10.1088/0067-0049/208/2/20`.

[21] M. Tanabashi et al. “Review of Particle Physics”. In: *Physical Review D* 98.3 (2018), p. 030001. DOI: `10.1103/PhysRevD.98.030001`.

[22] Planck Planck Collaboration et al. “Planck 2018 results. VI. Cosmological parameters”. 2018. arXiv: `1807.06209`.

[23] R. Adam et al. “<i>Planck</i> 2015 results”. In: *Astronomy & Astrophysics* 594 (2016). DOI: `10.1051/0004-6361/201527101`.

[24] ESA et al. “Planck Image Gallery”. Image Credits: ESA and the Planck Collaboration, 2015/18 Results. 2018. URL: `https://www.cosmos.esa.int/web/planck/picture-gallery`.

[25] Jonathan L. Feng. “Dark Matter Candidates from Particle Physics and Methods of Detection”. In: *Annual Review of Astronomy and Astrophysics* 48.1 (2010), pp. 495–545. DOI: `10.1146/annurev-astro-082708-101659`.

[26] Howard Baer et al. “Dark matter production in the early Universe: Beyond the thermal WIMP paradigm”. In: *Physics Reports* 555 (2015), pp. 1 –60. DOI: `10.1016/j.physrep.2014.10.002`.

[27] Marco Battaglieri et al. “US Cosmic Visions: New Ideas in Dark Matter 2017: Community Report”. 2017. arXiv: `1707.04591`.

[28] Peter W. Graham et al. “Experimental Searches for the Axion and Axion-Like Particles”. In: *Annual Review of Nuclear and Particle Science* 65.1 (2015), pp. 485–514. DOI: `10.1146/annurev-nucl-102014-022120`.

[29] Stefano Giagu. “WIMP Dark Matter Searches With the ATLAS Detector at the LHC”. In: *Frontiers in Physics* 7 (2019), p. 75. DOI: `10.3389/fphy.2019.00075`.

[30] Antonio Boveia et al. “Dark Matter Searches at Colliders”. In: *Annual Review of Nuclear and Particle Science* 68.1 (2018), pp. 429–459. DOI: `10.1146/annurev-nucl-101917-021008`.

[31] ATLAS ATLAS Collaboration. “Constraints on mediator-based dark matter and scalar dark energy models using $\sqrt{s} = 13$ TeV \$pp\$ collision data collected by the ATLAS detector”. In: *Journal of High Energy Physics* (2019). DOI: `10.1007/JHEP05(2019)142`.

[32] The ATLAS Collaboration et al. “The ATLAS Experiment at the CERN Large Hadron Collider”. In: *Journal of Instrumentation* 3.08 (2008), S08003–S08003. DOI: `10.1088/1748-0221/3/08/S08003`.

[33] The CMS Collaboration et al. “The CMS experiment at the CERN LHC”. In: *Journal of Instrumentation* 3.08 (2008), S08004–S08004. DOI: `10.1088/1748-0221/3/08/S08004`.

[34] Jennifer M. Gaskins. “A review of indirect searches for particle dark matter”. In: *Contemporary Physics* 57.4 (2016), pp. 496–525. DOI: `10.1080/00107514.2016.1175160`.

[35] Marco Cirelli. “Status of Indirect (and Direct) Dark Matter searches”. 2015. arXiv: `1511.02031`.

[36] M. Klasen et al. “Indirect and direct search for dark matter”. In: *Progress in Particle and Nuclear Physics* 85 (2015), pp. 1 –32. DOI: `https://doi.org/10.1016/j.ppnp.2015.07.001`.

[37] W. B. Atwood et al. “THE LARGE AREA TELESCOPE ON THEFERMI GAMMA-RAY SPACE TELESCOPEMISSION”. In: *The Astrophysical Journal* 697.2 (2009), pp. 1071–1102. DOI: `10.1088/0004-637x/697/2/1071`.

[38] Juan Cortina et al. “Technical Performance of the MAGIC Telescopes”. 2009. arXiv: `0907.1211`.

[39] V. Lefranc et al. “Dark matter search in the inner Galactic halo with H.E.S.S. I and H.E.S.S. II”. 2015. arXiv: `1509.04123`.

[40] A.U. Abeysekara et al. “A search for dark matter in the Galactic halo with HAWC”. In: *Journal of Cosmology and Astroparticle Physics* 2018.02 (2018), pp. 049–049. DOI: `10.1088/1475-7516/2018/02/049`.

[41] The Pierre Auger The Pierre Auger Collaboration et al. “Multi-Messenger Physics with the Pierre Auger Observatory”. In: *Frontiers in Astronomy and Space Sciences* (2019). DOI: `10.3389/fspas.2019.00024`.

[42] Katarzyna Frankiewicz et al. “Dark matter searches with the Super-Kamiokande detector”. In: *Journal of Physics: Conference Series* 888.1 (2017), p. 012210. DOI: `10.1088/1742-6596/888/1/012210`.

[43] M.G. Aartsen et al. “The IceCube Neutrino Observatory: instrumentation and online systems”. In: *Journal of Instrumentation* 12.03 (2017), P03012–P03012. DOI: `10.1088/1748-0221/12/03/p03012`.

[44] Lisa Goodenough et al. “Possible Evidence For Dark Matter Annihilation In The Inner Milky Way From The Fermi Gamma Ray Space Telescope”. 2009. arXiv: `0910.2998`.

[45] Tansu Daylan et al. “The characterization of the gamma-ray signal from the central Milky Way: A case for annihilating dark matter”. In: *Physics of the Dark Universe* 12 (2016), pp. 1 –23. DOI: `https://doi.org/10.1016/j.dark.2015.12.005`.

[46] Rebecca K. Leane et al. “Dark Matter Strikes Back at the Galactic Center”. 2019. arXiv: `1904.08430`.

[47] Daniel Carney et al. “Gravitational Direct Detection of Dark Matter”. 2019. arXiv: `1903.00492`.

[48] F. Donato et al. “Effects of galactic dark halo rotation on WIMP direct detection”. In: *Astroparticle Physics* 9.3 (1998), pp. 247–260. DOI: `10.1016/S0927-6505(98)00025-5`.

[49] J.D. Lewin et al. “Review of mathematics, numerical factors, and corrections for dark matter experiments based on elastic nuclear recoil”. In: *Astroparticle Physics* 6.1 (1996), pp. 87–112. DOI: `10.1016/S0927-6505(96)00047-3`.

[50] Gintaras Dūda et al. “Model-independent form factors for spin-independent neutralino–nucleon scattering from elastic electron scattering data”. In: *Journal of Cosmology and Astroparticle Physics* 2007.04 (2007), pp. 012–012. DOI: `10.1088/1475-7516/2007/04/012`.

[51] Richard H. Helm. “Inelastic and Elastic Scattering of 187-Mev Electrons from Selected Even-Even Nuclei”. In: *Physical Review* 104.5 (1956), pp. 1466–1475. DOI: `10.1103/PhysRev.104.1466`.

[52] J. I. Read. “The Local Dark Matter Density”. In: *J. Phys. G: Nucl. Part. Phys.* (2014). DOI: `10.1088/0954-3899/41/6/063101`.

[53] Alejandro Ibarra et al. “Optimized velocity distributions for direct dark matter detection”. In: *Journal of Cosmology and Astroparticle Physics* 08 (2017), pp. 039–039. DOI: `10.1088/1475-7516/2017/08/039`.

[54] Jianglai Liu et al. “Current status of direct dark matter detection experiments”. In: *Nature Physics* 13.3 (2017), pp. 212–216. DOI: `10.1038/nphys4039`.

[55] D. S. Akerib et al. “Results from a Search for Dark Matter in the Complete LUX Exposure”. In: *Phys. Rev. Lett.* 118 (2 2017), p. 021303. DOI: `10.1103/PhysRevLett.118.021303`.

[56] Masahiro Ibe et al. “Migdal effect in dark matter direct detection experiments”. In: *Journal of High Energy Physics* 2018.3 (2018), p. 194. DOI: `10.1007/JHEP03(2018)194`.

[57] E. Aprile et al. “Search for Light Dark Matter Interactions Enhanced by the Migdal Effect or Bremsstrahlung in XENON1T”. In: *Phys. Rev. Lett.* 123 (24 2019), p. 241803. DOI: `10.1103/PhysRevLett.123.241803`.

[58] D. S. Akerib et al. “Results of a Search for Sub-GeV Dark Matter Using 2013 LUX Data”. In: *Phys. Rev. Lett.* 122 (13 2019), p. 131301. DOI: `10.1103/PhysRevLett.122.131301`.

[59] E. Aprile et al. “Dark Matter Search Results from a One Tonne Year Exposure of XENON1T”. In: *Phys. Rev. Lett.* (2018). DOI: `10.1103/PhysRevLett.121.111302`.

[60] XENON100 XENON100 Collaboration et al. “The XENON100 Dark Matter Experiment”. In: *Astroparticle Physics* (2011). DOI: `10.1016/j.astro\-partphys.2012.01.003`.

[61] B. J. Mount et al. “LUX-ZEPLIN (LZ) Technical Design Report”. 2017. arXiv: `1703.09144`.

[62] Xiangyi Cui et al. “Dark Matter Results from 54-Ton-Day Exposure of PandaX-II Experiment”. In: *Phys. Rev. Lett.* 119 (18 2017), p. 181302. DOI: `10.1103/PhysRevLett.119.181302`.

[63] P. Agnes et al. “DarkSide-50 532-day dark matter search with low-radioactivity argon”. In: *Phys. Rev. D* 98 (10 2018), p. 102006. DOI: `10.1103/PhysRevD.98.102006`.

[64] P. Agnes et al. “Low-Mass Dark Matter Search with the DarkSide-50 Experiment”. In: *Phys. Rev. Lett.* 121 (8 2018), p. 081307. DOI: `10.1103/PhysRevLett.121.081307`.

[65] David Malling et al. licensed under the Creative Commons Attribution 3.0 Unported, Attribution: User:Gigaparsec, no changes. 2013. URL: `https://en.wikipedia.org/wiki/File:LUXEvent.pdf`.

[66] A. Aguilar-Arevalo et al. “The DAMIC dark matter experiment”. 2015. arXiv: `1510.02126`.

[67] A. Aguilar-Arevalo et al. “Search for low-mass WIMPs in a 0.6 kg day exposure of the DAMIC experiment at SNOLAB”. In: *Phys. Rev. D* 94 (8 2016), p. 082006. DOI: `10.1103/PhysRevD.94.082006`.

[68] Q. Arnaud et al. “First results from the NEWS-G direct dark matter search experiment at the LSM”. In: *Astroparticle Physics* 97 (2018), pp. 54 –62. DOI: `https://doi.org/10.1016/j.astropartphys.2017.10.009`.

[69] Q. Arnaud et al. “Spherical Proportional Counter: A review of recent developments”. In: *Journal of Physics: Conference Series* 1029.1 (2018), p. 012006. DOI: `10.1088/1742-6596/1029/1/012006`.

[70] C. Amole et al. “Dark Matter Search Results from the PICO−60 C_3F_8 Bubble Chamber”. In: *Phys. Rev. Lett.* 118 (25 2017), p. 251301. DOI: `10.1103/PhysRevLett.118.251301`.

[71] C. Amole et al. “Dark matter search results from the complete exposure of the PICO-60 C_3F_8 bubble chamber”. In: *Phys. Rev. D* 100 (2 2019), p. 022001. DOI: `10.1103/PhysRevD.100.022001`.

[72] R. Agnese et al. “Results from the Super Cryogenic Dark Matter Search Experiment at Soudan”. In: *Phys. Rev. Lett.* 120 (6 2018), p. 061802. DOI: `10.1103/PhysRevLett.120.061802`.

[73] R. Agnese et al. “Projected sensitivity of the SuperCDMS SNOLAB experiment”. In: *Phys. Rev. D* 95 (8 2017), p. 082002. DOI: `10.1103/PhysRevD.95.082002`.

[74] R. Agnese et al. “First Dark Matter Constraints from a SuperCDMS Single-Charge Sensitive Detector”. In: *Phys. Rev. Lett.* 121 (5 2018), p. 051301. DOI: `10.1103/PhysRevLett.121.051301`.

[75] R. Agnese et al. “Search for low-mass dark matter with CDMSlite using a profile likelihood fit”. In: *Phys. Rev. D* 99 (6 2019), p. 062001. DOI: `10.1103/PhysRevD.99.062001`.

[76] E. Armengaud et al. “Performance of the EDELWEISS-III experiment for direct dark matter searches”. In: *Journal of Instrumentation* 12.08 (2017), P08010–P08010. DOI: `10.1088/1748-0221/12/08/p08010`.

[77] B. S. Neganov et al. “Colorimetric method measuring ionizing radiation”. In: *Otkryt. Izobret.* 146 (1985), p. 215.

[78] P. N. Luke. “Voltage-assisted calorimetric ionization detector”. In: *Journal of Applied Physics* 64.12 (1988), pp. 6858–6860. DOI: `10.1063/1.341976`.

[79] G. Angloher et al. “Results from 730 kg days of the CRESST-II Dark Matter search”. In: *European Physical Journal C* 72.4 (2012), pp. 1–22. DOI: `10.1140/epjc/s10052-012-1971-8`.

[80] CRESST CRESST Collaboration et al. “First results from the CRESST-III low-mass dark matter program”. 2019. arXiv: `1904.00498`.

[81] G. Angloher et al. “Results on MeV-scale dark matter from a gram-scale cryogenic calorimeter operated above ground”. In: *The European Physical Journal C* 77 (2017). DOI: `10.1140/epjc/s10052-017-5223-9`.

[82] G Angloher et al. “Results on light dark matter particles with a low-threshold CRESST-II detector”. In: *European Physical Journal C* 76.1 (2016), pp. 1–8. DOI: `10.1140/epjc/s10052-016-3877-3`.

[83] G. Angloher et al. “Results on low mass WIMPs using an upgraded CRESST-II detector”. In: *The European Physical Journal C* 74.12 (2014), p. 3184. DOI: `10.1140/epjc/s10052-014-3184-9`.

[84] H. Jiang et al. “Limits on Light Weakly Interacting Massive Particles from the First 102.8 kg x day Data of the CDEX-10 Experiment”. In: *Physical Review Letters* 120.24 (2018), p. 241301. DOI: `10.1103/PhysRevLett.120.241301`.

[85] Z. Z. Liu et al. “Constraints on Spin-Independent Nucleus Scattering with sub-GeV Weakly Interacting Massive Particle Dark Matter from the CDEX-1B Experiment at the China Jinping Underground Laboratory”. In: *Phys. Rev. Lett.* 123 (16 2019), p. 161301. DOI: `10.1103/PhysRevLett.123.161301`.

[86] R. Agnese et al. “Search for Low-Mass Weakly Interacting Massive Particles with SuperCDMS”. In: *Physical Review Letters* 112.24 (2014), p. 241302. DOI: `10.1103/PhysRevLett.112.241302`.

[87] L. Hehn et al. “Improved EDELWEISS-III sensitivity for low-mass WIMPs using a profile likelihood approach”. In: *The European Physical Journal C* 76.10 (2016), p. 548. DOI: `10.1140/epjc/s10052-016-4388-y`.

[88] E. Armengaud et al. “Searching for low-mass dark matter particles with a massive Ge bolometer operated above ground”. In: *Physical Review D* 99.8 (2019), p. 082003. DOI: `10.1103/PhysRevD.99.082003`.

[89] J. I. Collar. “Search for a nonrelativistic component in the spectrum of cosmic rays at Earth”. In: *Phys. Rev. D* 98 (2 2018), p. 023005. DOI: `10.1103/PhysRevD.98.023005`.

[90] Govinda Adhikari et al. “An experiment to search for dark-matter interactions using sodium iodide detectors”. In: *Nature* 564.7734 (2018). [erratum: Nature566,no.7742,E2(2019)], pp. 83–86. DOI: `10.1038/s41586-018-0739-1,10.1038/s41586-019-0890-3`.

[91] E. Aprile et al. “Low-mass dark matter search using ionization signals in XENON100”. In: *Phys. Rev. D* 94 (9 2016), p. 092001. DOI: `10.1103/PhysRevD.94.092001`.

[92] A. Gütlein et al. “Impact of coherent neutrino nucleus scattering on direct dark matter searches based on CaWO4 crystals”. In: *Astroparticle Physics* 69 (2015), pp. 44 –49. DOI: `https://doi.org/10.1016/j.astropartphys.2015.03.010`.

[93] INFN LNGS. [...] The 1400 metre-rock thickness above the Laboratory represents a natural coverage that provides a cosmic ray flux reduction by one million times; [...] URL: `https://www.lngs.infn.it/en/lngs-overview`.

[94] G Bellini et al. "Cosmic-muon flux and annual modulation in Borexino at 3800 m water-equivalent depth". In: *Journal of Cosmology and Astroparticle Physics* 2012.05 (2012), pp. 015–015. DOI: `10.1088/1475-7516/2012/05/015`.

[95] F. Bellini et al. "Monte Carlo evaluation of the external gamma, neutron and muon induced background sources in the CUORE experiment". In: *Astroparticle Physics* 33.3 (2010), pp. 169 –174. DOI: `https://doi.org/10.1016/j.astropartphys.2010.01.004`.

[96] M. Ambrosio et al. "Vertical muon intensity measured with MACRO at the Gran Sasso laboratory". In: *Physical Review D* 52.7 (1995), pp. 3793–3802. DOI: `10.1103/PhysRevD.52.3793`.

[97] Rafael F Lang et al. "Search for dark matter with CRESST". In: *New Journal of Physics* 11.10 (2009), p. 105017. DOI: `10.1088/1367-2630/11/10/105017`.

[98] H. Wulandari et al. "Neutron flux at the Gran Sasso underground laboratory revisited". In: *Astroparticle Physics* 22.3-4 (2004), pp. 313–322. DOI: `10.1016/J.ASTROPARTPHYS.2004.07.005`.

[99] P. Belli et al. "Deep underground neutron flux measurement with large BF3 counters". In: *Il Nuovo Cimento A* 101.6 (1989), pp. 959–966. DOI: `10.1007/bf02800162`.

[100] Andreas Josef Zöller. "Artificial Neural Network Based Pulse-Shape Analysis for Cryogenic Detectors Operated in CRESST-II". Dissertation. München: Technische Universität München, 2016.

[101] Sabine Roth. "The Potential of Neganov-Luke Amplified Cryogenic Light Detectors and the Scintillation-Light Quenching Mechanism in $CaWO_4$ Single Crystals in the Context of the Dark Matter Search Experiment CRESST-II". Dissertation. München: Technische Universität München, 2013.

[102] R Strauss et al. "Results of Quenching Factor Measurements of CaWO 4 at mK Temperatures for the Direct Dark Matter Search Experiment CRESST". In: *J Low Temp Phys* 176.176 (2014). DOI: `10.1007/s10909-013-1075-3`.

[103] M. Bravin et al. "The CRESST dark matter search". In: *Astroparticle Physics* 12.1 (1999), pp. 107 –114. DOI: `https://doi.org/10.1016/S0927-6505(99)00073-0`.

[104] A. H. Abdelhameed et al. "First results on sub-GeV spin-dependent dark matter interactions with $$ˆ{7}$$ 7 Li". In: *The European Physical Journal C* 79.7 (2019), p. 630. DOI: `10.1140/epjc/s10052-019-7126-4`.

[105] F. Pröbst et al. “Model for cryogenic particle detectors with superconducting phase transition thermometers”. In: *Journal of Low Temperature Physics* 100.1-2 (1995), pp. 69–104. DOI: `10.1007/BF00753837`.

[106] Anja Tanzke. “Low-Threshold Detectors for Low-Mass Direct Dark Matter Search with CRESST-III”. PhD thesis. Technische Universitaet Muenchen, 2016.

[107] Florian Reindl. “Exploring Light Dark Matter With CRESST-II Low-Threshold Detectors”. Dissertation. München: Technische Universität München, 2016.

[108] G. Angloher et al. “Performance of a CRESST-II Detector Module with True 4π-veto”. 2017.

[109] J. Schmaler et al. “Status of the CRESST Dark Matter Search”. In: (2009). DOI: `10.1063/1.3292420`.

[110] R. Strauss et al. “A detector module with highly efficient surface-alpha event rejection operated in CRESST-II Phase 2”. In: *European Physical Journal C* 75.8 (2015). DOI: `10.1140/epjc/s10052-015-3572-9`.

[111] Nahuel Iachellini Ferreiro. “Increasing the sensitivity to low mass dark matter in CRESST-III with a new DAQ and signal processing”. Dissertation. München: Technische Universität München, 2018.

[112] Andrew Brown. “Analysis and Modelling for CRESST-II”. PhD thesis. University of Oxford, 2014.

[113] Richard McGowan. “Data Analysis and Results of the Upgraded CRESST Dark Matter Search”. PhD thesis. University of Oxford, 2008.

[114] Rafael Florian Lang. “Search for Dark Matter with the CRESST Experiment”. Dissertation. München: Technische Universität München, 2008.

[115] E. Gatti et al. “Processing the signals from solid-state detectors in elementary-particle physics”. In: *La Rivista del Nuovo Cimento* 9.1 (1986). DOI: `10.1007/BF02822156`.

[116] Sunil Ramanlal Golwala. “Golwala-Thesis”. PhD thesis. UNIVERSITY of CALIFORNIA at BERKELEY, 2000, pp. 1–489. URL: `papers2://publication/uuid/61C38EA1-F8B4-4115-B8E4-3429AF654CE6`.

[117] Manuela Jelen. “The CRESST Dark Matter Search - Background Considerations and Data Analysis”. Diploma Thesis. Technische Universität München, 2006.

[118] Johannes Rothe. “Achieving Low Thresholds: Cryogenic Detectors for Low-Mass Dark Matter Searches”. MA thesis. München: Technische Universität München, 2016.

[119] R. Strauss et al. “The ν-cleus experiment: a gram-scale fiducial-volume cryogenic detector for the first detection of coherent neutrino–nucleus scattering”. In: *The European Physical Journal C* 77.8 (2017), p. 506. DOI: `10.1140/epjc/s10052-017-5068-2`.

[120] Jens Schmaler. “The CRESST Dark Matter Search – New Analysis Methods and Recent Results”. Dissertation. München: Technische Universität München, 2010.

[121] Laboratoire National Henri Becquerel / Decay Data Evaluation Project. “Nucléide - Lara”. Last update: 2017-03-03 (data), 2018-09-07 (code). URL: `http://www.lnhb.fr/nuclear-data/module-lara/`.

[122] International Atomic Energy Agency Nuclear Data Services. “Live Chart of Nuclides”. URL: `https://www-nds.iaea.org/relnsd/vcharthtml/VChartHTML.html`.

[123] R.D. Deslattes et al. “X-ray Transition Energies (version 1.2)”. URL: `http://physics.nist.gov/XrayTrans`.

[124] R.B. Firestone et al. “The Lund/LBNL Nuclear Data Search”. URL: `http://nucleardata.nuclear.lu.se/toi/index.asp`.

[125] Kenneth D. Sevier. “Atomic electron binding energies”. In: *Atomic Data and Nuclear Data Tables* 24.4 (1979), pp. 323–371. DOI: `10.1016/0092-640X(79)90012-3`.

[126] R. Strauss et al. “Beta/gamma and alpha backgrounds in CRESST-II Phase 2”. In: *Journal of Cosmology and Astroparticle Physics* 2015.6 (2015), pp. 030–030. DOI: `10.1088/1475-7516/2015/06/030`.

[127] A. H. Abdelhameed et al. “Geant4-based electromagnetic background model for the CRESST dark matter experiment”. In: *The European Physical Journal C* 79.10 (2019), p. 881. DOI: `10.1140/epjc/s10052-019-7385-0`.

[128] M. Kiefer et al. “In-situ study of light production and transport in phonon/-light detector modules for dark matter search”. In: *Nuclear Instruments and Methods in Physics Research Section A: Accelerators, Spectrometers, Detectors and Associated Equipment* 821 (2016), pp. 116 –121. DOI: `https://doi.org/10.1016/j.nima.2016.03.035`.

[129] C. Arnaboldi et al. “CdWO4 scintillating bolometer for Double Beta Decay: Light and heat anticorrelation, light yield and quenching factors”. In: *Astroparticle Physics* 34.3 (2010), pp. 143–150. DOI: `10.1016/j.astropartphys.2010.06.009`.

[130] Daniel Schmiedmayer. “Calculation of dark-matter exclusions-limits using a maximum Likelihood approach”. urn:nbn:at:at-ubtuw:1-122743. Diploma Thesis. Wien: TU Wien, 2019.

[131] S. Yellin. “Finding an upper limit in the presence of an unknown background”. In: *Physical Review D - Particles, Fields, Gravitation and Cosmology* 66.3 (2002), p. 7. DOI: `10.1103/PhysRevD.66.032005`.

[132] S. Yellin. "Extending the optimum interval method". 2007. arXiv: `0709.2701`.

[133] Steven J. Yellin. "Optimum Interval Software". URL: `http://titus.stanford.edu/Upperlimit/`.

[134] S. S. Wilks. "The Large-Sample Distribution of the Likelihood Ratio for Testing Composite Hypotheses". In: *The Annals of Mathematical Statistics* 9.1 (1938), pp. 60–62. DOI: `10.1214/aoms/1177732360`.

[135] Glen Cowan et al. "Asymptotic formulae for likelihood-based tests of new physics". In: *The European Physical Journal C* 71.2 (2011), p. 1554. DOI: `10.1140/epjc/s10052-011-1554-0`.

[136] Cenk Turkoglu. "Development of a Geant4 Based Electromagnetic Background Model for the CRESST Experiment". PhD thesis. TU Wien, 2018.

[137] A. Münster et al. "Radiopurity of CaWO4 crystals for direct dark matter search with CRESST and EURECA". In: *Journal of Cosmology and Astroparticle Physics* 2014.5 (2014). DOI: `10.1088/1475-7516/2014/05/018`.

[138] Andrea Ruth Münster. "High-Purity $CaWO_4$ Single Crystals for Direct Dark Matter Search with the CRESST Experiment". Dissertation. München: Technische Universität München, 2017.

[139] Irina Bavykina. "Investigation of ZnWO 4 and CaMoO4 as Target Materials for the CRESST–II Dark Matter Search". Dissertation. Ludwig-Maximilians-Universität München, 2009.

[140] National Institute of Standards et al. "NIST". URL: `https://physics.nist.gov/PhysRefData/XrayMassCoef/ElemTab/z74.html`.

[141] C. Cozzini et al. "Detection of the natural α decay of tungsten". In: *Phys. Rev. C* 70 (6 2004), p. 064606. DOI: `10.1103/PhysRevC.70.064606`.

[142] G. Angloher et al. "Commissioning run of the CRESST-II dark matter search". In: *Astroparticle Physics* 31.4 (2009), pp. 270–276. DOI: `10.1016/j.astropartphys.2009.02.007`.

[143] National Institute of Standards et al. "NIST". URL: `https://physics.nist.gov/PhysRefData/XrayMassCoef/ElemTab/z14.html`.

[144] M. Mancuso et al. "A Low Nuclear Recoil Energy Threshold for Dark Matter Search with CRESST-III Detectors". In: *Journal of Low Temperature Physics* 193.3-4 (2018), pp. 441–448. DOI: `10.1007/s10909-018-1948-6`.

[145] Martin Stahlberg. "Data Analysis for the CRESST Experiment (preliminary title)". Dissertation. Wien: TU Wien, 2020.

[146] HEPHY Task group in Vienna. "Band fit and limit calculation for MCIII-1, collaboration internal work". 2019.

[147] C. E. Aalseth et al. "CoGeNT: A search for low-mass dark matter using *p*-type point contact germanium detectors". In: *Phys. Rev. D* 88 (1 2013), p. 012002. DOI: `10.1103/PhysRevD.88.012002`.

[148] J. Rothe et al. “TES-Based Light Detectors for the CRESST Direct Dark Matter Search”. In: *Journal of Low Temperature Physics* 193.5-6 (2018), pp. 1160–1166. DOI: `10.1007/s10909-018-1944-x`.

[149] V. B. Mikhailik et al. “Performance of scintillation materials at cryogenic temperatures”. In: *physica status solidi (b)* 247.7 (2010), pp. 1583–1599. DOI: `10.1002/pssb.200945500`.

[150] Alexander Langenkämper. “Investigation of reflective and scintillating foils and Neganov-Trofimov-Luke amplified cryogenic light detectors for the CRESST experiment”. PhD thesis.

[151] Y. Efremenko et al. “Use of poly(ethylene naphthalate) as a self-vetoing structural material”. In: *Journal of Instrumentation* 14.07 (2019), P07006–P07006. DOI: `10.1088/1748-0221/14/07/p07006`.

[152] Patrick Huff. “The Detector Parameters Determining the Sensitivity of the CRESST-II Experiment”. PhD thesis. Technische Universität München, 2010.